A Novel Methodology to Parameterise Lithium-ion Cell Models for Low Temperature Applications

By

Yashraj Tripathy

A thesis submitted in partial fulfilment of the requirements for the degree of

Doctor of Philosophy

Warwick Manufacturing Group (WMG)

University of Warwick

September 2020

Table of Contents

List of Figures

List of Tables

Acknowledgements

The last few years have been like a journey into the unknown but the destination was never lost from sight due to the efforts of the people around me, sometimes helping me shine a torch and at times, being a lighthouse guiding me through. If any one of them would not have given me the right direction at the right time, this journey would have ended in failure, lost at sea.

First of all, I am immensely grateful to WMG and the University of Warwick for providing me with a career, and a safe place to cultivate my aspirations into reality. I would like to thank my supervisors, Dr Andrew McGordon, Dr John Low, and Dr Anup Barai for their patience and timely support all throughout – their contributions have been immense. Andy always provided me with the right level of feedback which allowed me to learn from my mistakes. John helped me improve my technical writing skills and publish my first journal paper. Anup's take on my research has been refreshing, allowing me to gain perspective on my work and make it better. I thank Prof Stuart Barnes, Prof Sujit Banerjee, Prof Barbara Shollock and Prof Paul Jennings, for inspiring me to pursue research – Stuart, I cannot thank you enough!

Line managers can make or break your career progression. I am extremely lucky that Mr Mark Amor-Segan was my first line manager. He always understood when I needed some time off, especially when I was working days and writing my thesis during the evenings and the weekends. Success at work is what kept me going through the tough times in my PhD.

I would like to thank Prof James Marco, Dr W. Dhammika Widanalage and Prof Snehasis Tripathy, for critical feedback on my work that helped me grow as a researcher. I also thank Prof Yue Guo and Mr John Palmer, without whom working in the Energy Innovation Centre (EIC) at WMG, would have been a thousand times more arduous and not half as enjoyable. I am grateful to all the technicians within EIC, especially Mr Adrian Taylor, Mr Asif Rahman and Ms Ehman Altaf, for helping me with the experimental setup and other unforeseen issues with battery testing. I am endlessly grateful to Mithun and Jack for help during various stages of the PhD, allowing me to maintain the balance between work-work and PhD-work. I would like

to thank Dr Quirin Kellner and Dr Romeo Malik for sharing their PhD experience with me and for their words of encouragement when it mattered the most. Needless to say, this PhD would not have ended successfully without the support from Dr Darren Hughes, my examination chair, and Ms Karolina Spytek from WMG Research Degrees Office.

Immeasurable gratitude to my parents, Mrs Susmita and Prof Subhasish Tripathy, for providing me with the privileged life I have had and silently preparing me for the life yet to come. They have been my safety net, my role models and everything in between. Thank you mummy and nana, for always believing in me. A huge thanks, to my younger sister, Aditi, for being there for me when the waters were too deep and the tide too strong. Aditi, you are my pride and my joy. A special thanks (or bow-wow!) to Dexter, for being my best friend.

Finally, I am indebted to Neha, my support system, and the best sounding board one could find. I cannot thank her enough for enduring my frustrations, for making me a better researcher/person, for always inspiring me, and for sharing her life with me.

I dedicate this to my grandparents –

To Mama, Bapa, and Ai. You live on in me, wherever you are.

To Aja. I hope I can make you proud.

Declaration

This thesis is presented in accordance with the regulations for the degree of Doctorate of Philosophy. It has been written and compiled by myself and has not been submitted anywhere else. The work in this thesis has been undertaken by me except where otherwise stated.

Signed: Date:

Yashraj Tripathy

List of Publications

Journal Publications

J.1 **Y. Tripathy**, A. McGordon, A. Barai, Improving Accessible Capacity Tracking at Low Ambient Temperatures for Range Estimation of Battery Electric Vehicles, Energies. 13 (2020) 2021. doi:10.3390/en13082021.

J.2 **Y. Tripathy**, A. McGordon, C.T.J. Low, A New Consideration for Validating Battery Performance at Low Ambient Temperatures, Energies 2018, Vol. 11, Page 2439. 11 (2018) 2439. doi:10.3390/en11092439.

J.3 **Y. Tripathy**, A. McGordon, A. Barai, Optimising Experimental Approaches to Parameterise Lithium-ion Cells for Automotive and Aerospace Applications at Low Ambient Temperatures. *Review article (draft version) will be submitted to Renewable and Sustainable Energy Reviews.*

In the following two publications, I contributed to developing isothermal test conditions and procedure for lithium-ion cells following the methodology developed as part of the research presented in this thesis:

J.4 S.-A. Amamra, **Y. Tripathy**, A. Barai, A.D. Moore, J. Marco, Electric Vehicle Battery Performance Investigation Based on Real World Current Harmonics, Energies. 13 (2020) 489. doi:10.3390/en13020489.

J.5 Y. Yu, E. Vergori, D. Worwood, **Y. Tripathy**, A. Soma, D. Greenwood, J. Marco, Distributed Thermal Monitoring of Lithium Ion Batteries with Optical Fibre Sensors, Energy, *Submitted April '20 - Under Review*.

In the following publication, I contributed to research in a separate project that adopted the equivalent circuit model, parameterised at low temperatures, and developed as part of the research presented in this thesis:

J.6 J. Jeffs, A. McGordon, A. Picarelli, S. Robinson, **Y. Tripathy**, W. Widanage, Complex Heat Pump Operational Mode Identification and Comparison for Use in Electric Vehicles, Energies. 11 (2018) 2000. doi:10.3390/en11082000.

Conference Proceedings

C.1 **Y. Tripathy**, A. McGordon, C.T.J. Low, J. Marco, Internal temperature prediction of Lithium-ion cell using differential voltage technique, in: 2017 IEEE Transportation Electrification Conference and Expo, IEEE, 2017: pp. 464–467. doi:10.1109/ITEC.2017.7993315.

C.2 **Y. Tripathy**, A. McGordon, C.T.J. Low, J. Marco, Low Temperature Performance of Lithium-ion Batteries for Different Drive Cycles, in: Electr. Veh. Symp. (EVS 29), Montréal, Québec, 19-21 Jun 2016, 2016: pp. 1–12.

C.3 J. Everson, **Y. Tripathy**, A. Barai, M. Amor-Segan, Thermal Runaway Suppression Capability of State-of-the-Art Coolant Fluids for Lithium-Ion Battery Applications, in: ECS Meeting Abstracts, 2019. doi:10.1149/MA2019-04/10/0492.

Abstract

Electrification of road transportation is widely recognised as a necessary solution to reduce global warming. However, the mass market adoption of electric vehicles (EVs) has been hindered by reduced battery performance in cold weather conditions leading to warranty limitations coupled with inaccurate range estimation that exacerbates customer range anxiety. Today's market leading EVs driven on typical UK motorways have a range estimation error up to 27% at an ambient temperature of 10 °C, and due to slower battery kinetics it worsens to 45% at −15 °C. The range estimation accuracy depends upon the performance of models embedded in the Battery Management System (BMS) which estimates battery states (viz. State-of-Charge (SOC) and State-of-Energy (SOE)). The performance of the models fundamentally depends upon experimentally obtained parameters at different operating temperatures and currents, and validation exercises against legislative drive cycles. The experiments are usually performed in isothermal conditions by using state-of-the-art climatic chambers that maintain a pre-set temperature by forced air convection. Unfortunately, isothermal conditions are not adhered to as the battery operating temperature deviates significantly from the predefined chamber temperature, especially when battery characterisation is undertaken at low ambient temperatures (≤10 °C). The aim of this thesis is to propose a novel experimental methodology and alternative modelling approaches to improve the range estimation accuracy of EVs at low ambient temperatures by addressing these shortcomings in existing characterisation methodology.

A novel experimental methodology is developed to ensure isothermal conditions using immersed oil baths that provides more accurate usable capacity and energy characteristics of lithium-ion cells, especially at low temperatures, by eliminating the effect of rapid heat generation during battery operation. For the first time, it is shown that model parameterisation using oil-based rather than air-based experiments leads to more accurate estimation of battery states (SOC and SOE). The findings in this thesis suggest that the absolute SOC error is reduced from 13.5% to 5.1% and the absolute SOE error is reduced from 20.6% to 4.3% at −15 °C ambient temperature.

A detailed study of heat generation using a battery model utilising the polarisation currents demonstrated improved modelled surface temperature and terminal voltage estimates. These results along with accurate parameterisation data, estimated the battery states and terminal voltage better at low ambient temperatures. A power control approach to battery characterisation ensures that the operating current responds dynamically to the changing cell voltage. A comparison based on energy throughput and peak power demand at low temperatures showed that power control is more representative of real-world applications as compared to current control. Therefore, it is recommended that power control be employed as the primary approach to obtain validation data for cell models.

The work demonstrates and provides insight on new aspects for improving the range estimation accuracy of EVs operating under cold weather conditions. Advances from this work enable increased adherence to the rigid environmental conditions necessary for global lithium-ion battery testing standards and battery modelling, leading to the increased uptake of EVs.

List of Abbreviations

Abbreviation	Meaning
AC	Alternating Current
Ah	Ampere Hour
BEV	Battery Electric Vehicle
BMS	Battery Management System
BMW	Bayerische Motoren Werke AG
CCCV	Constant Current Constant Voltage
Co	Cobalt
C	Carbon
CO_2	Carbon Dioxide
DC	Direct Current
DEC	Diethyl Carbonate
DMC	Dimethyl Carbonate
EC	Ethylene Carbonate
ECE	Environmental Commission for Europe
ECM	Equivalent Circuit Model
EIS	Electrochemical Impedance Spectroscopy
EMC	Ethylmethyl Carbonate
ESS	Energy Storage System
EU	European Union
EUCAR	European Council for Automotive Research & Development
EV	Electric Vehicle
FFT	Fast Fourier Transform
GHG	Green House Gas
GITT	Galvanometric Intermittent Titration Technique
HEV	Hybrid Electric Vehicle
IC	Current Control
ICE	Internal Combustion Engine
IEC	International Electrical Commission
LFP	Lithium Iron Phosphate
Li	Lithium
$LiPF_6$	Lithium Hexafluorophosphate

LTO	Lithium Titanate
Mn	Manganese
NEDC	New European Drive Cycle
Ni	Nickel
NiMH	Nickel Metal Hydride
NMC	Nickel Manganese Cobalt
NTC	Negative Temperature Coefficient
O	Oxygen
ODE	Ordinary Differential Equation
OECD	Organisation for Economic Cooperation and Development
OEM	Original Equipment Manufacturer
PC	Power Control
PHEV	Plug-in Hybrid Electric Vehicle
PPC	Pulse Power Characterisation
Pt	Platinum
RC	Resistor-Capacitor
RMSE	Root Mean Squared Error
SEI	Solid Electrolyte Interphase
SLI	Starting Lighting Ignition
UDDS	Urban Dynamometer Driving Schedule
UK	United Kingdom
UN	United Nations
US	United States
USABC	United States Advanced Battery Consortium
Wh	Watt Hour
WLTC	Worldwide harmonised Light duty Test Cycle
WMG	Warwick Manufacturing Group

List of Symbols

Symbol	Meaning	Value/Units
$-$	Negative Electrode Region	N/A
$+$	Positive Electrode Region	N/A
ΔG^0	Gibbs Free Energy	kJ/mol
ΔI	Current Pulse Amplitude	A
ΔT	Temperature Change	℃
ΔV	Voltage Change	V
ΔV_0	Instantaneous Voltage Drop	V
ΔV_1	Dynamic (Non-linear) Voltage Drop	V
$\emptyset$	Phase Difference	Rad
A	Surface Area	m^2
C	Specific Heat Capacity	J/kg/K
c_{bulk}	Bulk Concentration	mol/m^3
C_D	Coefficient of Drag	0.28
C_{dl}	Double Layer Capacitance	F
C_{DYN}	Dynamic Capacity	Ah
c_e	Electrolyte-phase Lithium-ion Concentration	mol/m^3
C_{NOM}	Nominal Capacity	Ah
c_o	Concentration of Oxidant	mol/m^3
C_{P1}	First RC network Capacitance	F
C_{P2}	Second RC network Capacitance	F
C_{Pn}	n^{th} RC network Capacitance	F
c_r	Concentration of Reductant	mol/m^3
c_s	Solid-phase Lithium Concentration	mol/m^3
$c_{surface}$	Concentration of Species at the Electrode Surface	mol/m^3
DCR	Direct Current Resistance	Ω
D_e	Electrolyte-phase Diffusion Coefficient	m^2/s
D_s	Solid-phase Diffusion Coefficient	m^2/s
e^-	Electron	N/A
E_e^0	Standard Electrode Potential	V
E_{act}	Activation Energy	J/mol
E_{cell}	Cell Potential	V
E_{DYN}	Dynamic Energy	Wh

E_e	Electrode Potential	V
E^e_{anode}	Anode Potential	V
$E^e_{cathode}$	Cathode Potential	V
F	Faraday Constant	96485 C/mol
f	Frequency	Hz
f_r	Friction Coefficient	0.01
g	Gravitational Acceleration	9.81 m/s^2
G	Gear Box Ratio	7.94
H	$\overline{OCV} - OCV_{discharge}$	V
$h - value$	Convective Heat Transfer Coefficient	W/m^2/K
$h\ (SOC)$	Hysteresis State Variable	N/A
I	Current	A
I_0	Current Amplitude	A
I_{input}	Input Current	A
I_{Pn}	nth Polarisation Current	A
J	Jacobian	N/A
j_0	Exchange Current Density at Equilibrium	A/cm^2
j_{dl}	Double Layer Current Density	A/cm^2
j^{Li}	Current Density	A/cm^2
K	Transition Rate	N/A
L	Cell Width	cm
m	Mass	Kg
n	Number of Moles	N/A
OCV	Open Circuit Voltage	V
$\overline{OCV}$	Average OCV	V
OCV_{charge}	Charge OCV	V
$OCV_{discharge}$	Discharge OCV	V
P	Power	W
Q_{gen}	Joule Heating	W
R	Universal Gas Constant	8.3145 J/K/mol
r	Radial Coordinate in Spherical Particle	N/A
R_{CT}	Charge Transfer Resistance	Ω
R_{Diff}	Diffusion Resistance	Ω
RDR	Remaining Driving Range	miles
RE	Regenerative-braking Efficiency	miles
R_{int}	Internal Resistance	Ω
R_O	Ohmic Resistance	Ω

R_{P1}	First RC network Resistance	Ω
R_{P2}	Second RC network Resistance	Ω
R_{Pn}	n^{th} RC network Resistance	Ω
SOC	State of Charge	%
SOC_{NOM}	Nominal State of Charge	%
SOE	State of Energy	%
SOH	Stage of Health	%
T	Absolute Temperature	K
t	Time Elapsed	s
t_{total}	Total Time	s
t_+^0	Transference Number of Lithium-ion	N/A
T_{cell}	Cell Temperature	℃
T_{EXP}	Experimental Temperature	℃
T_∞	Ambient Temperature	℃
T_{loss}	Loss Temperature	℃
T_{MODEL}	Modelling Temperature	℃
$T_{operating}$	Operating Temperature	℃
T_{ref}	Reference Temperature (298.16 K)	℃
T_{RMSE}	Root Mean Squared Error in Modelled Surface Temperature	℃
V	Voltage	V
V_0	Voltage Amplitude	V
V_{EXP}	Experimental Voltage	V
V_{MODEL}	Modelling Voltage	V
V_{output}	Output Voltage	V
V_{P1}	1st RC Network Voltage	V
V_{P2}	2nd RC Network Voltage	V
V_{RMSE}	Root Mean Squared Error in Modelled Terminal Voltage	V
$V_{terminal}$	Terminal Voltage	V
Z	Impedance	Ω
Z'	Real Part of Impedance	Ω
Z''	Imaginary Part of Impedance	Ω
Z_0	Impedance Amplitude	Ω
α_a	Exchange Coefficient at the Anode	N/A
α_c	Exchange Coefficient at the Cathode	N/A
Δt	Change in Time	s

ε_e	Electrolyte Volume Fraction	N/A
η	Overpotential	V
η_{CT}	Charge Transfer Overpotential	V
η_{diff}	Diffusion Overpotential	V
η_{ohmic}	Instantaneous Voltage Drop	V
κ	Ionic Conductivity	S/m
ρ	Density of Air	1.225 kg/m^3
σ_s	Solid-phase Conductivity	S/m
τ_{P1}	1st RC Network Time Constant	s
τ_{P2}	2nd RC Network Time Constant	s
τ_{Pn}	nth RC Network Time Constant	s
φ_I	Phase Shift for Current	rad
φ_V	Phase Shift for Voltage	rad
φ_e	Electrolyte-phase Potential	V
φ_s	Solid-phase Potential	V
ψ	Physiochemical Property	N/A
ψ_{ref}	Property Value defined at Reference Temperature	N/A
ω	Radial Frequency	rad/s

1. Introduction

Vehicle electrification is at the forefront of technological discussions globally in the automotive industry. This is primarily due to socio-economic, environmental and geo-political factors showing that reducing fossil fuel consumption is a key solution towards reducing carbon emissions and thus, reducing global warming [1]. Towards this, electric vehicles (EVs) show promising potential for both reduction in fossil fuel consumption and to satisfy customer demands [2]. However, these promises have not translated into reality as higher cost and range anxiety of EVs (concern that the battery capacity will be insufficient to complete the journey [3]) have proven to be critical barriers to mass market uptake [4]. Key deterrents to market uptake include issues such as limited low temperature performance [5] and lack of fast charging technology/infrastructure [6]. Low temperatures also lead to inaccuracies in real time range/performance estimation of BEVs [7]. These factors, exacerbated by increased range anxiety, have forced users to consider alternatives, limiting the customer acceptance of EVs [3]. The aim of this thesis is to propose a novel experimental methodology and alternative modelling approaches to improve the range estimation accuracy of EVs at low ambient temperatures (defined as ≤ 10 °C in this thesis).

This chapter embodies an introduction to recent trends in transportation electrification, EV operation and low temperature issues and consequent research problems, followed by the aims and objectives of the current work, along with the outline of the thesis.

1.1 Recent Trends in Transportation Electrification

Recently, the UK government announced their intention to become the world's first major economy to end their contribution to global warming by 2050 [8]. In 2018, a third of the total carbon dioxide (CO_2) emissions in the UK was contributed by the transportation sector, with similar statistics worldwide. Globally, it was reported that the transportation sector was one of the biggest contributors to green-house gas (GHG) emissions with 29% share in the US and 27% share in the European Union (EU-28) in 2017 [9,10]. Moreover, it is predicted that by 2050, emissions would need to fall by around two thirds, in order to meet the long term 60% GHG emission reduction target

as set by the Paris Agreement in 2015 [10,11]. Thus, to achieve climate neutrality within the next few decades, transportation electrification is going to be a key player.

Reduction in fossil fuel consumption is a key avenue towards reducing rising worldwide carbon emissions [12]. Electric vehicles (EVs) can potentially not only help in reduction of fossil fuel consumption, but also satisfy customer demands [2]. The percentage of EVs in global light vehicle production is expected to rise from <2% in 2016 to about 6% by end of 2020, and to at least 22% by 2030 [13]. Building on the success of land based EVs, aerospace electrification is also fast emerging. Norway and Sweden have already announced plans to use electric airplanes for all short-haul flights in their airspace by 2030 [14–16].

Despite technological advancements and increased customer acceptance, electric vehicle ownership only sees an incremental rise globally [17]. A large factor behind this is the cost, as the EV battery pack cost needs to decrease from $ 250-300 per kWh to less than $ 100 per kWh to become comparable with ICE based vehicles [12,18]. Similarly, slow rollout of charging infrastructure, complicated by customer range anxiety, limits mass market uptake of electric vehicles [17]. Lastly, the environmental impact of producing electric vehicle battery packs with regards to use of rare-earth materials throws up challenges such as second life use and recycling [19,20].

1.2 Introduction to Electric Vehicles

A conventional vehicle has an internal combustion engine (ICE) as the only power source. Unlike conventional vehicles, an electric vehicle (EV), along with an ICE, uses an additional power source [21]. This secondary power source can be a battery, flywheel, or supercapacitor, which provides traction using an electric motor powertrain. As shown in Figure 1, while EVs that use both ICE and a secondary power source are called hybrid electric vehicles (HEVs), EVs that only use a battery as the primary power source are termed battery electric vehicles (BEVs). EVs show better fuel economy compared to conventional vehicles because of the optimal operation and downsizing of the ICE, and recovery of kinetic energy from regenerative braking [22].

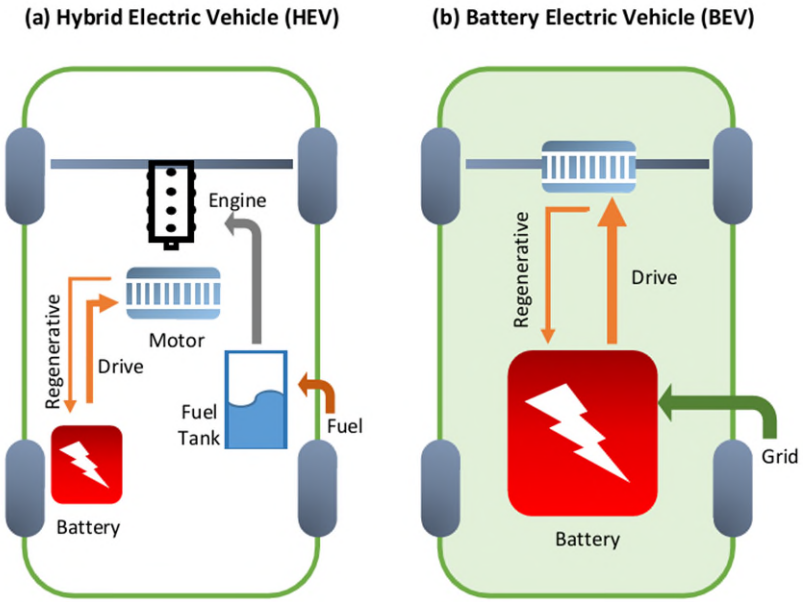

Figure 1. Layout: (a) Hybrid Electric Vehicle and (b) Battery Electric Vehicle

In an EV, the functions of the secondary power source, typically a battery, can range from mild regenerative braking to all-electric drive with grid charging capability [23]. Based on the functions of the second power source, the types of HEVs can be classified (Table 1).

Table 1. Classification of EVs based on Electric Power Source Function(s) [23,24]

Type of EV/ Function	**Micro**	**Mild**	**Full**	**Plug-in**	**BEV**
Regenerative Braking	✓	✓	✓	✓	✓
Power Assistance	✘	✓	✓	✓	✓
All-electric Drive	✘	✘	✓	✓	✓
Grid Charging	✘	✘	✘	✓	✓
No ICE	✘	✘	✘	✘	✓

Most conventional vehicles now come equipped with the ability to stop the ICE when the vehicle is at rest, known as the engine stop/start system. A micro hybrid is an HEV that shows limited regenerative braking capability when the vehicle is braking in addition to having the stop/start system [25]. An HEV is termed as a mild hybrid when the electric power source can supplement the energy from the ICE to meet driving demands. A mild hybrid also has a higher degree of regenerative braking capability

compared to a micro hybrid. Full hybrids can propel the vehicle entirely from the electric power source albeit for a limited range. This is in addition to the functions of the electric power source seen in the other types of HEVs.

Due to the ability to charge its on-board battery pack using electrical power from the grid, a Plug-in HEV (PHEV) has the option to use that electrical power preferentially. This additional flexibility allows the PHEV to function either as a full-hybrid when the electrical energy available is low, or in all-electric mode when sufficient electric energy is available. Another advantage of PHEVs is that most of the energy comes from the grid and not from fossil fuels, like in the case of other classes of HEVs. The electricity produced in the grid may be from renewable sources such as from solar or wind sources [26]. This reduces the environmental impact of a PHEV compared to other classes of HEVs. The environmental impact is reduced even further by using a battery electric vehicle (BEV), which is an EV that uses an on-board battery pack as its sole power source [27].

There are two basic architectures of HEV powertrains: series and parallel. As shown in Figure 2, in a series HEV, the ICE traction is first converted to electricity using a generator. This electrical energy is either used to charge the battery or used to provide traction at wheels via a motor. The motor is also used to charge the battery during braking events. In this case, the ICE cannot directly provide traction at the wheels. In this setup, the ICE can operate in its maximum efficiency region, since it is not directly linked to the traction demand at the wheels. But, due to inefficiencies related to multiple energy conversions and requirement of two electric machines, series hybrids can be expensive, for example, the Jaguar C-X75 [21]. Hence, series hybrids may be more suitable for urban drive cycles such as the BMW i3 Rex or the London EV Company's TX which is a purpose built hackney carriage employed for public transport [28].

In a parallel HEV, both the ICE powertrain and the electric powertrain can provide power at the wheels separately (Figure 3). Thus, a parallel HEV can deliver power using just the ICE, a combination of the ICE and the battery, or using the all-electric mode. This allows a high degree of operational flexibility as the electric drive can be the primary mode at lower speeds and the ICE at higher speeds. However, the use of

a smaller motor/inverter in a parallel HEV may limit regen-braking capability [29]. Examples of parallel HEVs are the Honda Insight, the Chevy Malibu and the Toyota Prius [28].

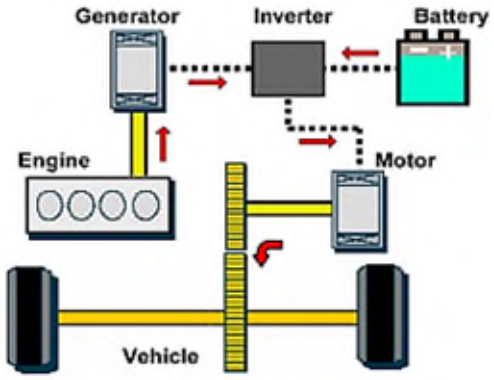

Figure 2. Basic Operation of Series Hybrid Electric Vehicle Powertrain [30]

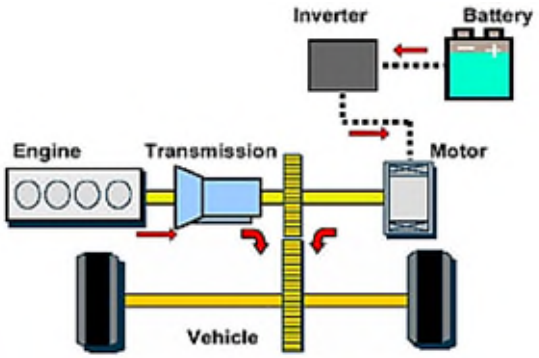

Figure 3. Basic Operation of Parallel Hybrid Electric Vehicle Powertrain [30]

1.2.1 Typical Energy and Power Requirements of Electric Vehicles

Increasing electrification of the power source in a vehicle improves its fuel economy. While a micro hybrid such as the Citroen C3 can save up to 15% of fuel, a full hybrid such as Toyota Prius can save almost 40% of fuel compared to a conventional ICE based vehicle, depending on the drive cycle [6]. However, with increasing electrification of the power source in a vehicle (from an ICE based vehicle to BEV), the energy and power demanded from the electrical source also increases (Table 2). For example, the conventional starting lighting ignition (SLI) lead-acid battery is sufficient for usage in a micro hybrid where typical power level is 3 kW and typical energy required is 0.7-1.0 kWh. However, for PHEVs and BEVs, the typical power

levels can cross 100 kW and energy levels required are 4-10 kWh and above 15 kWh, respectively. In these cases, an energy storage system (ESS) with higher energy and power density than the conventional lead-acid battery is necessary (Table 2). Furthermore, as shown in Table 2, to meet the higher power demands in PHEVs and BEVs, the typical voltage range of the energy storage system also needs to increase. This helps to mitigate thermal losses and to account for physical limits imposed by current collectors (primarily copper and aluminium) as well as safety regulations [31].

Table 2. Typical Power and Energy Requirements of the ESS [18,25]

Vehicle Type	**Typical Requirements**			**ESS Function**
	Power [kW]	**Energy [kWh]**	**Voltage [V]**	
ICE/Micro	3	1	12	Engine starting, hotel loads
Mild	5-15	1	12-48	Regenerative braking
Full	20-40	2	100-300	Power Assist
Plug-in	40-100	5-30	300-600	Main power and energy
BEV	>100	>15	300-600	Sole source of power and energy

The ESS, typically the battery, in various vehicle types, is sized to meet the peak power and energy demands of the vehicle. Batteries are chosen due to their high energy density, compact size, reliability and lifetime [32]. An automotive battery pack consists of various modules connected via bus bars [33]. For example, a 24 kWh lithium-ion battery used in the MY 2011-2015 models of the Nissan Leaf (a typical passenger BEV) consists of 48 modules [34]. Each module consists of four cells. Depending upon the requirements, the cells within a module can be connected in series, parallel or a combination of series and parallel. For example, the module in a Nissan Leaf connects two cells in parallel before connecting two such sets in series. This is commonly known as the ‘2S2P’ configuration (Figure 4). The configuration of a module and the battery pack as a whole depends on the power and energy demands of the vehicle [21]. While adding cells/modules in series means increasing the energy

capability of the battery pack (driving range), adding cell/modules in parallel means increasing the power capability (acceleration/regenerative-braking) of the battery pack [35]. However, if the pack voltage increases, the operating currents are lower for the same duty cycle power demand, and vice versa. The performance of the individual cells within a module in a PHEV/BEV battery pack are indicative of actual vehicular performance. The capacity and voltage of a single cell, its chemistry and construction, and performance under various operating conditions will translate, depending upon the pack arrangement, into driving range and performance at the vehicular level [36].

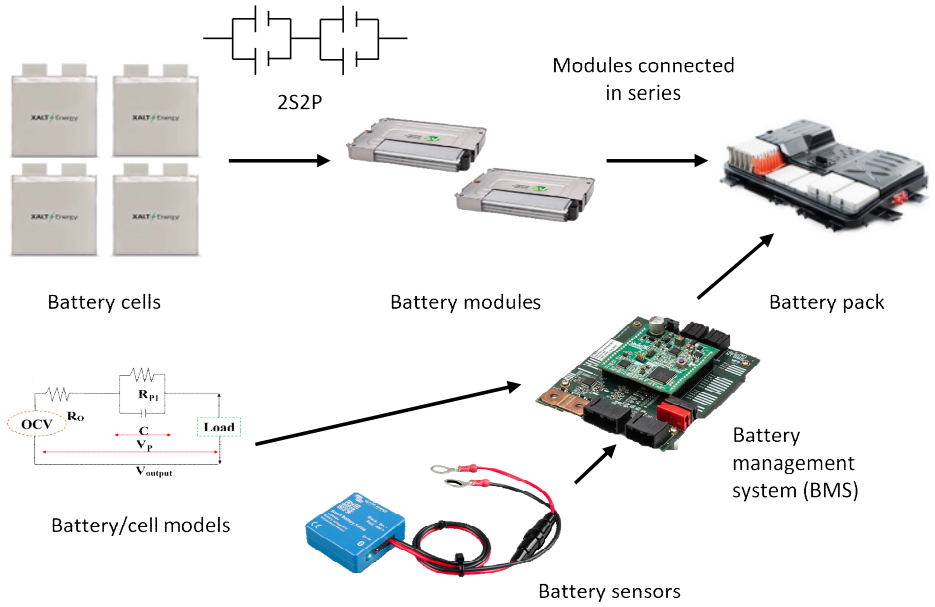

Figure 4. Block Representation of Typical Build Levels within an Automotive Battery [Individual images' source: Internet]

1.2.2 Introduction to Current Challenges with Electric Vehicles

For electric vehicles, the biggest challenge in terms of mass market acceptance is cost [12]. In an EV, the cost of the battery pack can be as much as 25% of the total cost [18]. To become cost comparable with internal combustion engines, the battery pack cost will need to decrease from around $ 200–300 per kWh presently, to around $ 100–150 per kWh by 2025, which is predicted to happen [12,37]. In the meantime, lithium-ion batteries have become the most popular energy storage technology used in EVs, due to their high gravimetric and volumetric energy densities, excellent cycling

performance and long calendar life [25]. However, most of the current EV technological challenges are related to its (lithium-ion chemistry based) battery system. As such, lithium-ion batteries, being electrochemical systems, are strongly dependent on operating temperature. Thus, studying the effect of temperature is the key to understanding battery performance, its lifetime and safety.

1.2.2.1 Issues with Low Temperature Operation

At high temperatures (≥ 35 °C), battery degradation and safety are issues owing to the presence of side reactions and volatility of its active chemicals, respectively [38,39]. However, many developed countries, viz. Norway and Sweden, and large parts of continental Europe and North America, are characterised by seasonally extreme cold weather down to −20 °C [5,34]. In these conditions, a lithium-ion battery's capacity, maximum output power and charge acceptance capability are substantially reduced. At lower temperatures (≤ 10 °C), due to slower chemical kinetics, charge transfer at the electrode-electrolyte interphase slows down, leading to higher overpotentials [40]. Furthermore, lower ionic conductivity in the electrolyte and slower diffusion, particularly in the electrodes' active material, contribute to higher voltage loss at lower temperatures [41]. These manifest as reductions in driving range and performance of EVs at low temperatures [42]. For example, the real-world range of the latest Chevy Bolt was found to be about 184 miles at −2 °C [42,43]. This is a substantial reduction of almost 30% compared to the 263 mile range advertised as per the WLTC (at 18 °C). This performance reduction is worsened by increased energy/power demands due to higher cabin heating requirements in cold weather conditions [44,45]. Various literature provide insight into energy management of BEVs and how innovative cabin heating techniques can increase passenger comfort while not increasing battery requirements substantially [44,46,47]. At low temperatures, charging current is impaired as it may damage the battery due to the potential for lithium plating; this in turn increases charging time [48]. These conditions also limit regenerative braking that further diminish the benefits of a BEV over a conventional vehicle [49]. Conversely, various lifetime studies of lithium-ion cells provide insight into charging protocol management to avoid lithium plating [50,51]. These include battery pre-heating [50], control algorithms based on limiting anode potential and avoiding regenerative braking [51].

Low temperatures also lead to large reductions in real time range/performance estimation of EVs [7,52,53]. Today's market leading EVs, driven on typical UK motorways, have real-world range estimation inaccuracy of up to 27%, at around 10 °C ambient temperature [52]. This inaccuracy worsens for lower ambient temperatures, rising up to 45% at −15 °C [54]. These factors exacerbate predisposed range anxiety and have forced users to consider alternatives, limiting the customer acceptance of EVs [3].

1.3 Research Problem

As discussed above, cold weather poses multiple challenges for battery electric vehicles. Most of these issues are related to how reliably and accurately the key performance characteristics of underlying lithium-ion cells are quantified and, in turn, modelled for low temperatures applications. Accurate modelling of lithium-ion cells is critical for reliable estimation of battery states such as State-of-Charge (SOC) and State-of-Health (SOH). Battery state estimators found in literature have adopted sophisticated algorithms and complex battery models [7,55,56]. New parameters such as State-of-Energy (SOE) have also been proposed to capture *in operando* battery behaviour more accurately [56,57]. These battery models have further expanded to include diverse operating conditions under which they are parameterised, such as at low temperatures [58,59].

Despite this, very little attention has been given to the validity of the environmental conditions under which these battery model parameterisation experiments are conducted. This is because battery testing is conducted for multiple purposes, such as, to quantify performance under different operating scenarios, to validate functional safety, and to parameterise and validate algorithms/models. These purposes come with their own requirements. In particular, the dependence of temperature on battery performance is accounted for differently. For instance, during performance testing, it is crucial that the experimental conditions replicate real-world operating conditions, such as allowing for cells to warm up, as they would in operation, to obtain the real-world performance characteristics. On the other hand, for model parameterisation, fundamental electrical parameters need to be quantified accurately whilst keeping other parameters constant; then the variation coming from a secondary (such as

thermal) effect should be included. This requires more attention especially at low temperatures, where, due to higher internal resistances, there exists a greater coupling between battery electrical and thermal phenomena. Similarly, the majority of battery testing is conducted at room temperature where certain testing and modelling assumptions are made, such as ignoring polarisation currents for heat generation estimates or using current control to obtain model validation data for legislative drive cycles. These can lead to misleading conclusions when low ambient temperatures are considered.

Thus, further insight is required into the validity of battery evaluation methods for parameterising and validating lithium-ion cell models employed for automotive applications at low operating temperatures. It is crucial to investigate any issues with existing experimental procedures, and how they can be improved.

1.4 Aim, Research Question and Objectives

The aim of this thesis is to propose a novel experimental methodology and alternative modelling approaches to improve the range estimation accuracy of EVs at low ambient temperatures (≤ 10 °C). Therefore, the research question of this thesis is defined as "**how to improve experimental evaluation methods and examine alternative approaches for parameterising and validating battery models for low temperature automotive applications?**" This will improve model performance and consequently lead to better EV range estimation at low temperatures.

Thus, to achieve the aim defined above, the following objectives have been proposed (also illustrated in Figure 5 along with relevant publications):

1. Generate a novel experimental methodology to improve the accuracy of parameterisation experiments at low temperatures.
2. Using an equivalent circuit model (ECM), compare modelling performance of existing and improved low temperature parameterisation methods.
3. Improve surface temperature and voltage error predictions through use of alternative modelling methods.
4. Quantify improvements to model performance and battery state estimation based on experimentally obtained model parameterisation data.

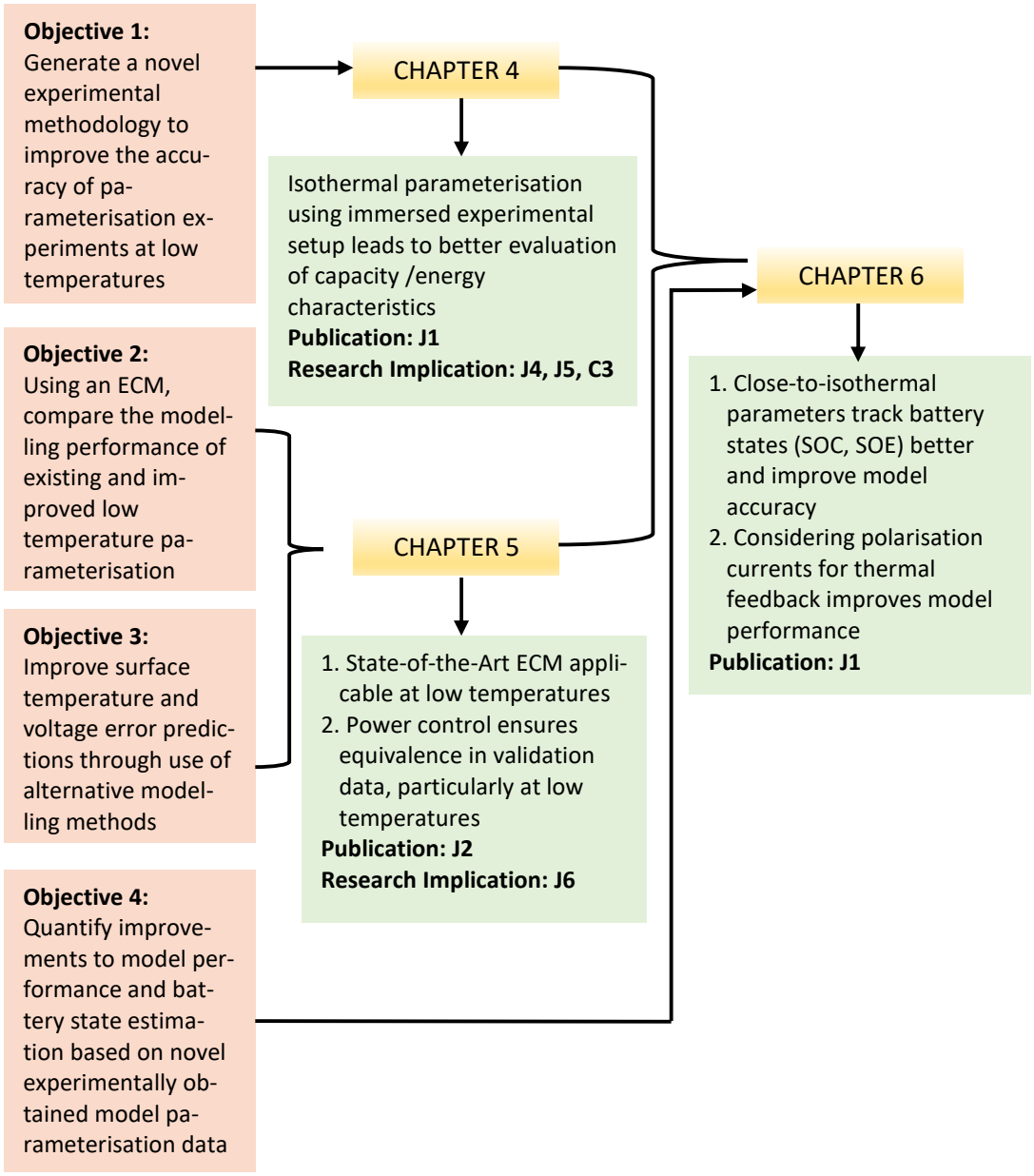

Figure 5. Graphical Representation of Research Objectives and Contributions

1.4.1 Research Novelty and Contributions to Knowledge

The novelty of this thesis is a new methodology to obtain battery model parameterisation data from experiments conducted under isothermal testing conditions.

The related contribution to knowledge is that usable capacity values obtained from experiments conducted in traditional air-based thermal chambers are inaccurate and representative of higher temperatures than the predefined temperature. Conversely, an

immersed oil-based thermal control system allows for close-to-isothermal tracking of battery usable capacity, by eliminating the effect of rapid internal heat generation, especially at low temperatures. The usable capacity of a lithium-ion cell is defined as the capacity obtained under application specific operating scenarios, such as at different operating temperatures and C-rates [60].

At the modelling stage, the contribution to knowledge is that the battery states based on close-to-isothermal capacities, particularly at low temperatures, are closer to the experimentally obtained values and lead to improved model performance when validated against legislative drive cycles. The improvements are quantified in terms of battery SOC, SOE and terminal voltage estimation.

A further contribution to knowledge is that using separate currents (allowing for inclusion of polarisation currents) rather than simply the common Ohmic current as part of the thermal feedback subsystem leads to improved estimation of modelled surface temperature and output voltage. This was validated against legislative drive cycles.

Another contribution is that power control rather than current control is a more realistic approach for characterising batteries against legislative drive cycles as it accounts for equivalence in energy throughput rather than capacity throughput across all operating conditions, especially at low temperature and lower operating voltages.

1.5 Thesis Outline

The thesis comprises of three broad sections: In Chapter 2, the state-of-the-art related to low temperature issues with automotive lithium-ion batteries are discussed and the gaps in knowledge are identified, with particular focus on battery characterisation for model parameterisation and validation. In Chapters 3-6, a novel experimental and modelling based research methodology is proposed; furthermore, the experimental and modelling evidence to achieve the aim and objectives of this thesis are presented and discussed. In Chapters 7-8, overall significance of the work is highlighted where the contributions to knowledge are presented and the future prospective of the work are suggested.

Following on from the issues with low temperature EV operation introduced earlier in this chapter, Chapter 2 presents the operating principles and background related to lithium-ion batteries and components. The effect of low temperature on lithium-ion cell internal processes are also highlighted. This leads to a discussion of existing battery testing methods followed for automotive applications and the issues with them at low temperatures. Here, it is highlighted that most battery testing takes place in air based thermal chambers which mostly fail to maintain isothermal test conditions, despite claiming to do so. To understand the effect of experimental data on model parameterisation, background information on battery modelling techniques is provided, with emphasis on equivalent circuit models. Here, the effect of parameterisation and validation data on modelling performance is highlighted. The chapter ends by summarising the gaps in research related to evaluating lithium-ion cells for modelling purposes for low temperature automotive applications.

In Chapter 3, the aims and objectives of the work are defined along with the justification for the research approach taken. This is followed by details about the research scope related to the experimental test matrix and the modelling choices made.

In Chapter 4, the shortcomings with existing testing methods in air-based thermal chambers are highlighted and confirmed based on experimental evidence. The novel experimental setup to conduct close-to-isothermal battery testing is proposed. It is shown that far-from-isothermal testing using air-based setup substantially overestimates the battery performance, particularly at low temperatures and high C-rates. Conversely, oil-based isothermal setup allows a more accurate assessment of usable battery capacity/energy, especially at low temperature and high C-rates.

In Chapter 5, a state-of-the-art equivalent circuit model (ECM), parameterised at low temperatures is developed to aid the modelling validation of the experimental findings in Chapter 4. This ECM includes alternate methods for consideration of separate (Ohmic and polarisation) currents for calculating the heat generation within a cell. The methodology adopted to obtain validation data for the ECM (based on backward facing model for legislative drive cycles) is also shown to be different. This is because power control instead of current control is used to obtain experimental validation data

for legislative drive cycles. The models developed in this chapter enables subsequent analysis in Chapter 6.

In Chapter 6, first the improvements to battery state estimation (SOC and SOE) by using oil-based parameters over air-based parameters are discussed by comparing with experimental data based on power control, for a legislative drive cycle. Then, the positive effect on output voltage accuracy for both 1^{st} and 2^{nd} order ECMs is evidenced. Following which, the improvements to modelling performance (in terms of modelling surface temperature and output voltage) by inclusion of polarisation current for calculating the heat generation from the RC branches of the ECM is presented.

In Chapter 7, the overall discussion of this research work is presented along with contributions to knowledge and potential research impact. Then, the future direction of research is also suggested. In Chapter 8, the overall conclusions related to the contributions of this research work are summarised.

1.6 Chapter Summary

Brief introductions to electric vehicle operation and issues at low temperature have been given. An introduction to the research problem was provided and the aim and objectives of this research work and associated novel contributions were highlighted. An outline for the remainder of this thesis was provided where conclusive findings will demonstrate how accuracy of battery model parameters can be improved by intervention at an experimental stage and through implementation of alternative modelling approaches, to enhance range estimation accuracy for EVs operating at low temperatures.

2. Review of Low Temperature Issues with Automotive Lithium-ion Batteries

Performance of BEVs diminishes at low temperatures (≤ 10 °C). This is primarily due to two reasons, increased cabin heating demand on the battery and diminished battery performance. While battery performance depends intrinsically on the cell chemistry, it is also affected by external factors such as battery management system (BMS) performance. The key task of the BMS is to maximise the power and energy available from the pack while ensuring battery safety. Accurate estimation of remaining driving range is also one of the key tasks within this framework and is critical to the end user.

To estimate the remaining driving range accurately, battery states such as SOC and SOE have to be inferred accurately. The accuracy of these battery states depends on the accuracy of the underlying models. The battery models rely on the quality of the experimental datasets employed in their parameterisation and validation. Hence, quality of experimental data could have a consequential effect on range estimation.

This chapter contains a review of the literature on lithium-ion battery characterisation and modelling at low temperatures and identifies the relevant knowledge gaps. This forms the basis of the research aim and objectives of this work.

The background and operating principles of lithium-ion batteries are discussed in Section 2.1, focussing on the effects of low temperature; Section 2.2 covers the review of experimental methods used in characterising battery performance at low temperatures. Particularly, in Section 2.2.6, the literature critical to the research problem is reviewed and the gaps in existing knowledge are identified. Section 2.3 presents a review of the methods to model lithium-ion batteries at low temperatures contextualising the effect of testing data. Specifically, in Section 2.3.4, the literature relevant to battery testing for model parameterisation and validation is critically examined to identify the relevant gaps in knowledge. Finally, in Section 2.4, the gaps in the literature are summarised to refine the research question for this work. The objectives originating from the research question will be detailed in Chapter 3.

2.1 Background and Operating Principles of Lithium-ion Batteries

Over the past decade, lithium-ion batteries have successfully transitioned from the consumer electronics market to the EV market. This is due to their high specific energy (or gravimetric energy density) and high specific power (gravimetric power density) [61], excellent cycling performance and long calendar life which make them ideal for automotive applications [25]. As shown in Figure 6, the latest lead-acid batteries have specific energy between 40-60 Wh/kg, and nickel metal hydride (NiMH) chemistries have around 40-110 Wh/kg, while this value increases to around 250 Wh/kg for state-of-the-art lithium-ion chemistries [62,63]. Future energy storage technologies such as lithium-sulphur, lithium-air and solid-state batteries are promising in terms of their energy densities (lithium-sulphur and lithium-air) or safety (solid-state) but are limited by low power density and cycle life [62]. The volumetric power density of lithium-ion chemistries is around 320 W/ ℓ whereas that for lithium-sulphur chemistry is about 100-200 W/ ℓ [64]. Typical lithium-ion batteries can reach up to 2000 cycles compared to ~50 cycles for latest lithium-sulphur batteries [64]. Thus, batteries based on lithium-ion chemistries are a common choice for original equipment manufacturers (OEMs) to integrate into electric vehicles (EVs). Despite these advantages, the market penetration of lithium-ion battery operated EVs is slow [65,66]. This is due to a range of technical barriers such as high cost, recycling issues, charging infrastructure, safety risks and reduced low temperature performance [67].

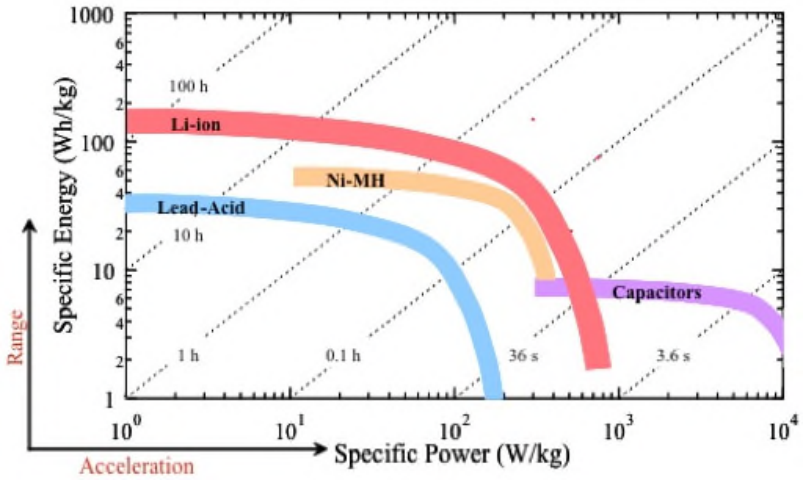

Figure 6. Ragone Plot for Contemporary Battery Chemistries [68]

To investigate the effect of low temperature on lithium-ion battery performance, the components of a lithium-ion cell (Section 2.1.1) and the underlying electrochemical principles (Section 2.1.2) are discussed in this section.

2.1.1 Lithium-ion Cell Components

A standard lithium-ion cell consists of two electrodes, two current collectors, an electrolyte and a separator. The basic constitution of a lithium-ion cell is illustrated in Figure 7. During discharge, the anode is the negative electrode and cathode is the positive electrode. The lithium ions (Li^+) diffuse and migrate through the electrolyte solution to the positive electrode active material, where they are reduced and transferred to the solid phase. The solid phase lithium (Li) then diffuses from the surface of the cathode (usually metal oxide) particles to the bulk. This process is known as intercalation.

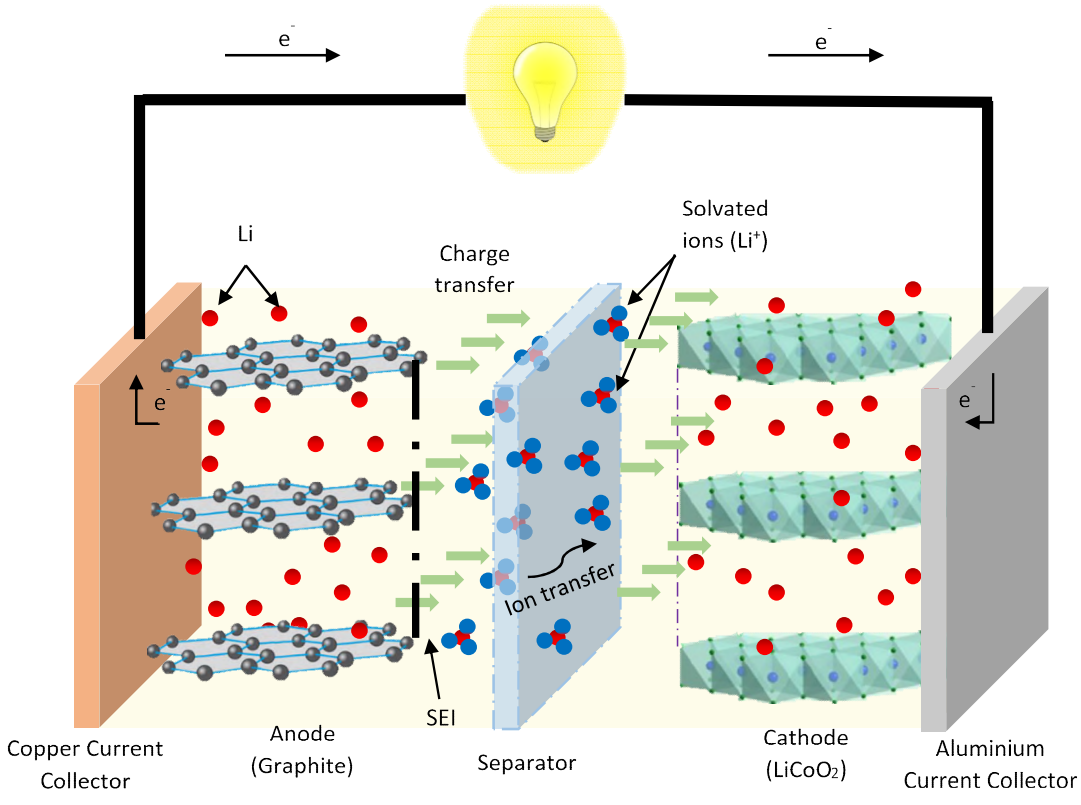

Figure 7. Schematic of the Basic Operating Principle of Secondary Lithium-ion Cell at Room Temperature (25 °C)

The reverse process (known as de-intercalation) happens at the anode, where the Li particles diffuse out of the bulk onto the surface and are oxidised into Li^+ particles. The porous separator (while ionically conducting) serves as an electronic insulator between the positive and negative electrodes to avoid internal short circuits. The separator forces the electrons to follow the opposite path to the ions, through the current collectors, to the external load.

2.1.1.1 Electrode Materials

The electrodes in a lithium-ion cell are key components that decide its capacity and energy density [69]. This is because cell voltage can be calculated from the following equation:

$$E_{cell} = E^e_{cathode} - E^e_{anode} \quad (1)$$

Thus, higher the operating voltage of the cathode and lower the operating voltage of the anode, higher is the cell voltage. Higher, the cell voltage, greater is the energy delivered for a lower operating current. For example, nickel manganese cobalt (NMC) chemistry has a 3.7 V average operating voltage, whereas for lithium iron phosphate (LFP) chemistry it is 3.2 V (Figure 8). Similarly, graphite has a low operating voltage of ~0.005 V, whereas it is ~1.5 V for a lithium titanate (LTO) anode. Amongst the popular chemistries, a lithium-ion cell with NMC cathode and graphite anode has the highest specific energy.

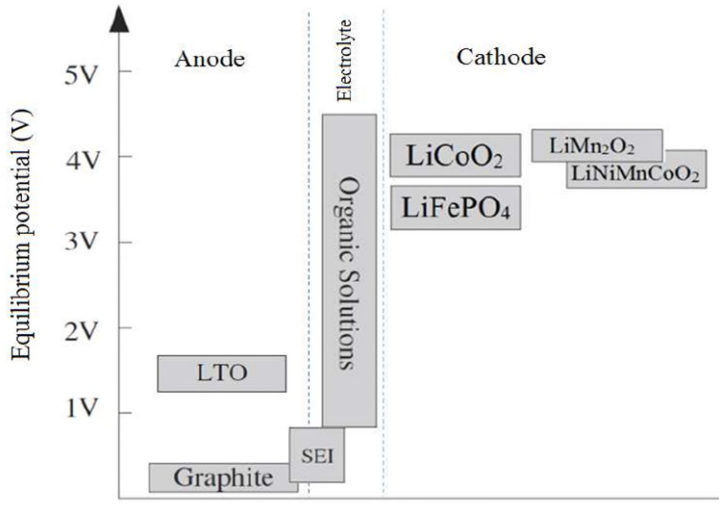

Figure 8. Stable working voltage for different cell material vs. Li/Li^+ [70]

Other factors to be considered are high electronic and ionic conductivities required to achieve high power capability, and battery safety. In this regard, cathode material based on LFP chemistry is very safe (thermal runaway onset >270 °C) and has longer cycle life and higher power capability than Nickel (Ni) based chemistries. LTO based anodes have excellent cycle life and high power capability due to a 'zero strain' intercalation mechanism in combination with a high potential of lithiation. 'Zero strain' implies that the phase change due to lithiation/de-lithiation of the electrode causes negligible change in its volume (~0.2%). The higher electrode potential of the LTO anode (1.5 V) also negates the need for a solid electrolyte interphase (SEI) layer, otherwise seen in graphite based anodes. However, a higher negative electrode potential leads to lower cell voltage reducing energy density compared to a cell with a graphite anode. This is the reason that lithium-ion cells with LTO anodes are good for high power applications. Lastly, although silicon anodes offer more than ten times the capacity than graphite, they exhibit a 270% volume change during charge/discharge leading to poor cycle life. Amongst the three anode materials considered, graphite has the highest Li diffusivity (up to 10^{-7} cm^2/s). This diffusivity (in the solid phase) is a direct function of temperature and affects the performance at low ambient temperatures [71].

2.1.1.2 Electrolyte

Ideally, in battery cells, the electrolyte is a chemically inert material with high ionic conductivity (typically 4 mS/cm [72]) and with good insulating properties for electrical charges. This forces the electrons to go through an external circuit when the cell is charged/discharged. For lithium-ion cells, the electrolytes are generally non-aqueous solutions of lithium-ion containing salts such as lithium hexafluorophosphate ($LiPF_6$) dissolved in solvent of organic liquid mixtures, such as ethylmethyl carbonate (EMC) [69,73].

The key requirement of the electrolyte is its stability (chemical inertness) within the normal operating window of the electrode reactions [72]. It should also allow the formation of a stable SEI layer to protect the electrode, prevent further decomposition of the electrolyte and only allow ionic conduction. Furthermore, the viscosity and ionic conductivity of the electrolyte decide the rate at which the ions travel from one

electrode to the other. This dictates the power capability of the cell. As temperature decreases, the viscosity of the electrolyte increases and the ionic conductivity decreases [72,74]. This will have an effect on lithium-ion cell performance. For example, the freezing point of dimethyl carbonate (DMC) is 0.5 °C.

Generally, suitable co-solvents are added to the primary electrolyte to improve low temperature performance [41], however, the composition of battery cell electrolyte is a trade secret. Generally, the electrolytes include 1.0–1.2 mol $LiPF_6$ combined with a blend of 2–3 organic solvents, such as ethylene carbonate (EC), DMC and diethyl carbonate (DEC). Despite this, the discharge capacity of lithium-ion cells using an electrolyte mixture of $LiPF_6$ and the above organic solvents combined in a 1:1:1 ratio led to discharge capacity reduction by 15% at −20 °C, even for very low C-rates such as 0.05C [41]. Since decreased ionic conductivity of the electrolyte is a major factor for poor battery performance at low temperatures, improving electrolyte properties is an open research question.

2.1.1.3 Separator and Current Collectors

The separator is a microporous layer which acts as a physical barrier between the electrodes while allowing ions to pass through from one electrode to another. Key requirements of the separator for automotive lithium-ion cells are its high mechanical stability and thickness. The thinner the separator, the lower the ionic resistance. But a thin separator can lead to cell damage in case of penetration. Most commercially available cells use polyolefin based materials as separator due to their mechanical stability, chemically inertness and low cost [70].

Current collectors transfer the current between the electrodes and the external circuit or load. Current collectors should have excellent electrical conductivity and should be chemically inactive at least with other chemicals inside the cell. In lithium-ion cells, copper and aluminium are usually the current collectors. However, aluminium cannot be used as the anodic current collector as it alloys with lithium below 0.1 V vs. Li/Li^+ [31]. Thus, copper is used as the anodic current collector and aluminium is used as the cathode current collector. While aluminium is cheap, copper is 2-3 times more expensive and increases the overall cost of a lithium-ion cell [18].

2.1.1.4 Cell Formats

Lithium-ion cells for automotive applications are manufactured in three primary formats: cylindrical, prismatic and pouch (Figure 9). Cylindrical cells housed in metallic (aluminium /steel) cans are the most common cell format and are also used in consumer electronics. For example, '21700' format cylindrical lithium-ion cells are used in the Tesla Model S battery pack. In this case, the number '21700' refers to 21 mm diameter and 70 mm length of the cylinder. Instead of cylindrical cans, if box shaped cans are utilised then these cells are called prismatic cells. If instead of a can, a layer of plastic is used, it is called a pouch cell. Due to the soft packaging, pouch cells have inherently higher energy and power densities, manufacturing flexibility and higher packing efficiency amongst all the cell formats [75]. Hence, lithium-ion pouch cells are popular amongst OEMs to be used in EVs [12].

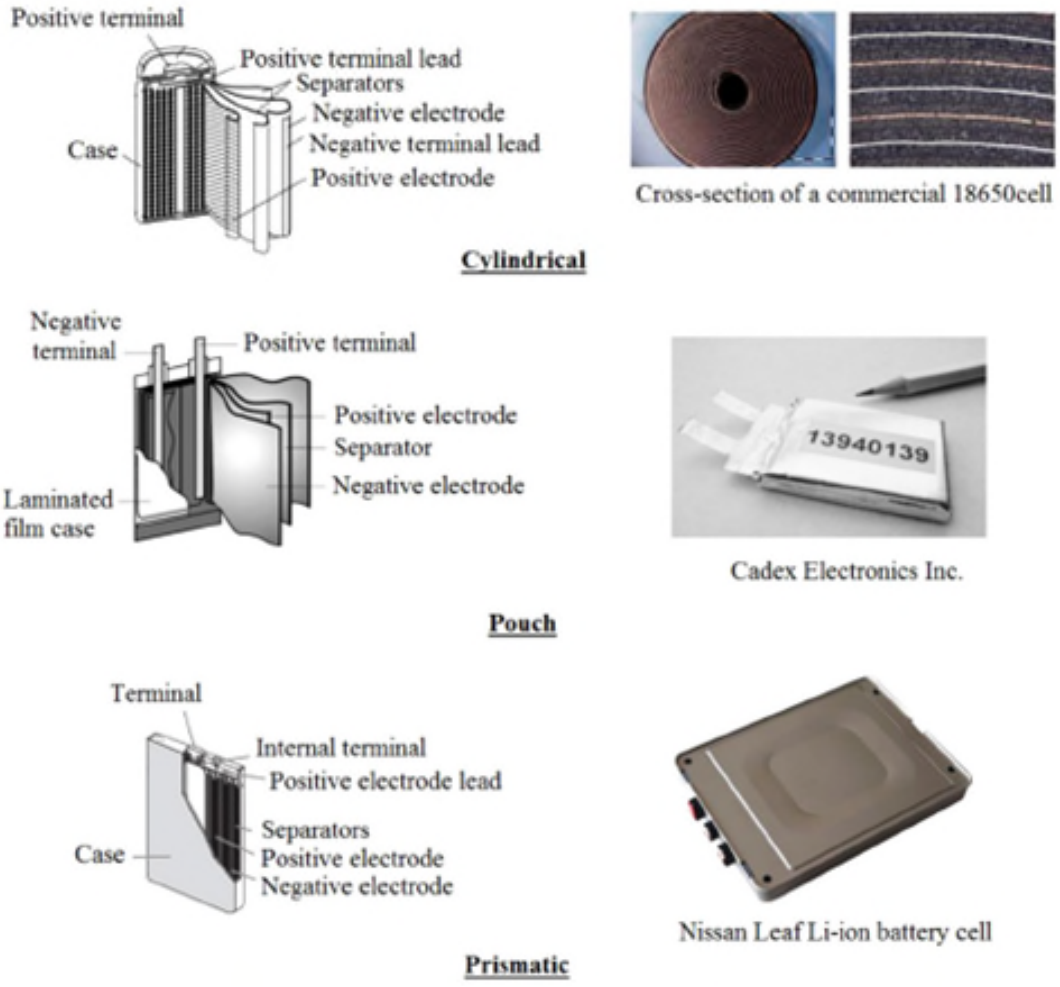

Figure 9. Battery Cell Configurations [75]

2.1.2 Operating Principles and Electrochemical Equations

Essentially, a lithium-ion cell converts stored chemical energy to electrical energy and vice versa. For example, the representative chemical reactions for a Lithium-ion cell with NMC-111 cathode ($LiNi_{0.33}Mn_{0.33}Co_{0.33}O_2$) and graphite anode would be:

At cathode:

$$Li_{1-x}(Ni_{0.33}Mn_{0.33}Co_{0.33})O_2 + xLi^+ + xe^- \overset{\Delta G^0}{\longleftrightarrow} Li(Ni_{0.33}Mn_{0.33}Co_{0.33})O_2 \quad (2)$$

At anode:

$$xLiC_6 \overset{\Delta G^0}{\longleftrightarrow} xLi^+ + xe^- + xC_6 \quad (3)$$

During discharge/charge, these redox reactions cause chemical energy to be converted to/from electrical energy as explained below:

Overall:

$$Li_{1-x}(Ni_{0.33}Mn_{0.33}Co_{0.33})O_2 + xLiC_6 \overset{\Delta G^0}{\longleftrightarrow} Li(Ni_{0.33}Mn_{0.33}Co_{0.33})O_2 + xC_6 \quad (4)$$

At each electrode, when a reaction occurs, there is a release or absorption of energy which is commonly known as the Gibbs free energy (ΔG^0) [76]:

$$\Delta G^0 = -nFE_e^0 \quad (5)$$

Here, 'n' is the number of moles transferred in the reaction. E_e^0 is the standard electrode potential for the reaction and 'F' is Faraday constant (96485 C/mol). The difference in the Gibbs free energy in the two electrode reactions is the energy supplied to/from the external circuit.

In the absence of any current flow, at a particular electrode, the electrode potential (Li in this case) with respect to the ions in the solution (Li^+ in this case) can be calculated from the Nernst equation:

$$E_e = E_e^0 + \frac{2.3RT}{nF}\log(\frac{C_o}{C_r}) \quad (6)$$

Here, R is the universal gas constant (8.3145 J/K/mol), T is the absolute temperature in Kelvin, and c_o and c_r are respectively the concentrations of the oxidant and reductant involved. As mentioned in Equation 1, based on the cathode and anode employed, the cell voltage can then be calculated from the following equation:

$$E_{cell} = E^e_{cathode} - E^e_{anode} \quad (7)$$

2.1.2.1 OCV and Overpotential

At rest, with all electrolyte and solid phase concentration gradients fully relaxed, cell terminal voltage is equal to its open-circuit voltage (OCV) [77]. As illustrated in Figure 10, any deviation in terminal cell voltage from the OCV due to current passing through the cell (either charge or discharge), causes an overpotential (η) linked to the internal resistance (R_{int}):

$$\eta = I \times R_{int} \quad (8)$$

$$V = OCV - \eta \quad (9)$$

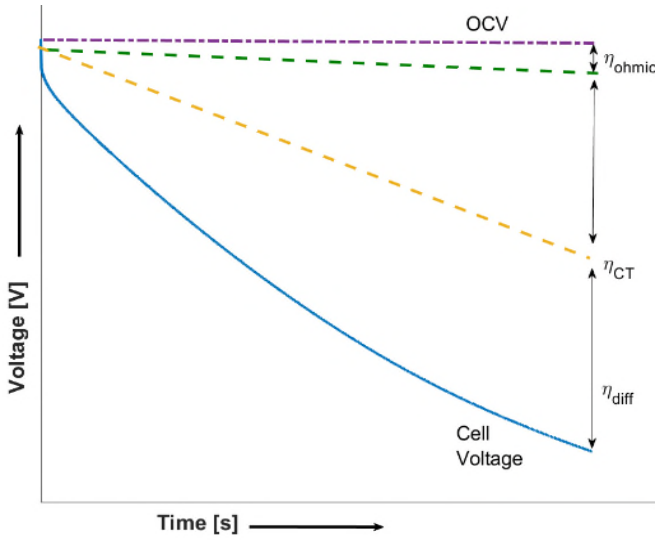

Figure 10. Cell Overpotentials

The cell overpotential consists of the following:

(a) The instantaneous voltage drop (η_{ohmic}) is due to the pure Ohmic resistance (R_O) which consists of all electronic resistances (electrodes, current collectors, and electrical contacts) and the ionic resistance of the electrolyte bulk.

The following overpotentials due to charge transfer and diffusion limitations are time dependent and tend to increase with time:

(b) The voltage drop within the first few seconds is due to resistance developing from charge transfer related potential gradients (η_{CT}) at the electrode/electrolyte interface.
(c) Any further voltage drop is due to concentration gradients developing from mass transport or diffusion limitations (η_{diff}), particularly in the solid phase.

Charge transfer related overpotential (η_{CT}) at a particular electrode is related to the potential difference between the active lithium and the lithium-ions at the solid electrode-electrolyte interphase. This is defined by:

$$\eta_{CT} = \varphi_s - \varphi_e - E_e \tag{10}$$

where, φ_s and φ_e are the potentials of the solid electrode and the electrolyte, respectively.

The η_{CT} is related to the current density (j^{Li}) through the Butler-Volmer Equation:

$$j^{Li} = j_0 \left\{ exp\left(\frac{\alpha_a F}{RT}\eta_{CT}\right) - exp\left(-\frac{\alpha_c F}{RT}\eta_{CT}\right)\right\} \tag{11}$$

where, j_0 is the exchange current density at equilibrium, and α_a and α_c are the exchange coefficients at the anode and the cathode. Note, $\alpha_a + \alpha_c = n$. To reiterate, 'n' is the number of moles transferred in the reaction.

In the low overpotential region, current density can be equated to overpotential as:

$$j^{Li} = j_0 \left(\frac{\alpha_a F}{RT}\eta_{CT}\right) \tag{12}$$

In the high overpotential region, Equation 11 simplifies to the Tafel equation:

$$j^{Li} = j_0 \times exp\left(\frac{\alpha_a \times F}{RT}\eta_{CT}\right) \tag{13}$$

At low temperatures, high overpotentials would be dominant due to increased cell resistance and sluggish dynamics.

Higher electrode current density equates to a larger overpotential based on the Butler-Volmer equation. Thus, as load currents increase, the electrode overpotentials increase causing cell voltage to decrease faster. Since cells have a manufacturer's recommended minimum voltage cut-off, for the same OCV, the terminal voltage is lower for a higher load current. Theoretically, this causes cells to prematurely reach end-of-discharge. Furthermore, higher load currents also result in higher thermal losses due to Joule heating (Q_{gen}):

$$Q_{gen} = I \times \eta \tag{14}$$

The change in potential at the electrode results in the electrode surface becoming charged. Since, the electrode surface becomes charged, oppositely charged particle are attracted towards it leading to the formation of an electrical double layer. This layer can be assumed as providing a capacitance (C_{dl}) in parallel with the charge transfer resistance at the electrode electrolyte interface producing a current (j_{dl}):

$$j_{dl} = C_{dl} \frac{d\eta_{CT}}{dt} \tag{15}$$

During sustained discharge, concentration gradients develop across the cell, particularly in the active material of the electrodes. This is principally a concentration gradient between the bulk of the active species and the surface, giving rise to an overpotential-induced due to mass transport limitations (η_{diff}):

$$\eta_{diff} = \frac{2.3RT}{nF} \log\left(\frac{c_{bulk}}{c_{surface}}\right) \tag{16}$$

Here c_{bulk} is the concentration of active species in the bulk, and $c_{surface}$ is the concentration of species at the electrode surface.

To improve the power capability of lithium-ion batteries, the active materials are built into porous electrodes, allowing for a larger surface area for chemical reactions to take place. Furthermore, both effective conductivity and diffusivity increase as the porosity of the electrodes increases and the tortuosity decreases [78]; leading to reduction in charge transfer and concentration polarisation. The area of the interface between

electrolyte and electrodes' active material depends on the particle size, electrode porosity, and available surface area.

2.1.2.2 Electrochemical Equations

Lithium/lithium-ion charge transfer and mass transport phenomena in both solid and electrolyte phases can be expressed through the following equations [65,76,77]:

Charge conservation in solid phase:

$$\frac{\partial}{\partial x}\left(\sigma_s \frac{\partial}{\partial \mathrm{x}}\varphi_s\right) - j^{Li} = 0 \tag{17}$$

Boundary condition:

$$-\sigma_{s-}\left.\frac{\partial \varphi_s}{\partial x}\right|_{x=0} = -\sigma_{s+}\left.\frac{\partial \varphi_s}{\partial x}\right|_{x=L} = \frac{I}{A}, \left.\frac{\partial \varphi_s}{\partial x}\right|_{x=\delta_-} = \left.\frac{\partial \varphi_s}{\partial x}\right|_{x=L-\delta_+} = 0 \tag{18}$$

Lithium conservation in solid phase (Fick's second law in polar form):

$$\frac{\partial c_s}{\partial t} = \frac{D_s \partial}{r^2 \partial r}\left(r^2 \frac{\partial c_s}{\partial r}\right) \tag{19}$$

Boundary condition:

$$\left.\frac{\partial c_s}{\partial r}\right|_{r=0} = 0, -D_s \left.\frac{\partial c_s}{\partial r}\right|_{r=R_s} = \frac{j^{Li}}{a_s F} \tag{20}$$

Lithium conservation in electrolyte phase:

$$\varepsilon_e \frac{\partial (c_e)}{\partial t} = \frac{\partial}{\partial \mathrm{x}}\left(D_e \frac{\partial}{\partial \mathrm{x}} c_e\right) + \frac{1-t_+^0}{F} j^{Li} \tag{21}$$

Boundary condition:

$$\left.\frac{\partial c_e}{\partial x}\right|_{x=0} = \left.\frac{\partial c_e}{\partial x}\right|_{x=L} = 0 \tag{22}$$

Charge conservation in electrolyte phase:

$$\frac{\partial}{\partial \mathrm{x}}\left(\kappa \frac{\partial}{\partial \mathrm{x}}\varphi_e + \kappa_D \frac{\partial}{\partial \mathrm{x}} ln c_e\right) + j^{Li} = 0 \tag{23}$$

Boundary condition:

$$\left.\frac{\partial \varphi_e}{\partial x}\right|_{x=0} = \left.\frac{\partial \varphi_e}{\partial x}\right|_{x=L} = 0 \quad (24)$$

Here, φ_s and φ_e are solid-phase and electrolyte-phase potentials; σ_s is solid-phase conductivity; j^{Li} is the reaction current density; c_s and c_e are solid-phase and electrolyte-phase Lithium concentrations; D_s and D_e are solid-phase and electrolyte-phase diffusion coefficients; ε_e is electrolyte volume fraction; t_+^0 is transference number of lithium-ion; κ is ionic conductivity; R is universal gas constant; T is absolute temperature in K; and F is Faraday's constant.

The equations 17-24 detailed in this section can also be used to discuss the effect of low temperatures on internal cell processes and thus, on the operation of lithium-ion cells. But before that, it is imperative to associate the effect of temperature on internal cell physiochemical parameters such as conductivity, diffusivity, etc. The Arrhenius equation can be used to explain the general dependence of physiochemical cell parameters on temperature [77]:

$$\psi = \psi_{ref} exp\left[\frac{E_{act}^{\psi}}{R}\left(\frac{1}{T_{ref}} - \frac{1}{T}\right)\right] \quad (25)$$

Here, ψ_{ref} is property value defined at reference temperature T_{ref} = 298.16 K (25 °C). The activation energy ('E_{act}') controls the temperature sensitivity of the individual physiochemical property, ψ.

Automotive lithium-ion batteries need to operate in diverse operating conditions, such as, extreme environmental conditions and aggressive power demands. Despite these challenging conditions, batteries have to supply the required power at the wheels and meet warranty conditions. Thus, rate capability, operating temperature range and lifetime considerations are critical to mass market uptake of a particular battery type. For example, at low ambient temperatures, charging current is reduced to avoid battery damage. Similarly, during driving, the power available from the battery decreases with decrease in its SOC. Quantifying the effects of different operating conditions such as for varying load currents and ambient temperatures is critical for accurately assessing performance of lithium-ion cells for automotive applications. Lithium-ion batteries, being electrochemical devices, are affected by operating temperature. Low ambient

temperatures adversely affect cell physiochemical characteristics such as a diffusivity and ionic conductivity (Figure 11). For example, as the ambient temperature decreases from 25 °C to say, 0 °C, diffusivity decreases within active material of the electrodes (Equation 25). This is seen as slower diffusion in the solid phase ($D_s \downarrow$). This is illustrated as lower number of red dots in the electrodes in Figure 11. Slower diffusion rates manifest as greater concentration gradients ($\partial c_s/\partial r \uparrow$) which contribute to increasing the overpotential of the cell for a particular current. The chemical kinetics of the redox reactions slow down at lower ambient temperatures (fewer green arrows). This manifests as an increase in the charge transfer resistance on the electrolyte/electrode interface leading to an increase in the overpotential at low temperatures. As such, cell internal resistances increase due to decreased electrolyte ionic conductivity ($\kappa \downarrow$) at lower ambient temperatures due to slower rate of ionic transfer and a higher viscosity (darker electrolyte colour).

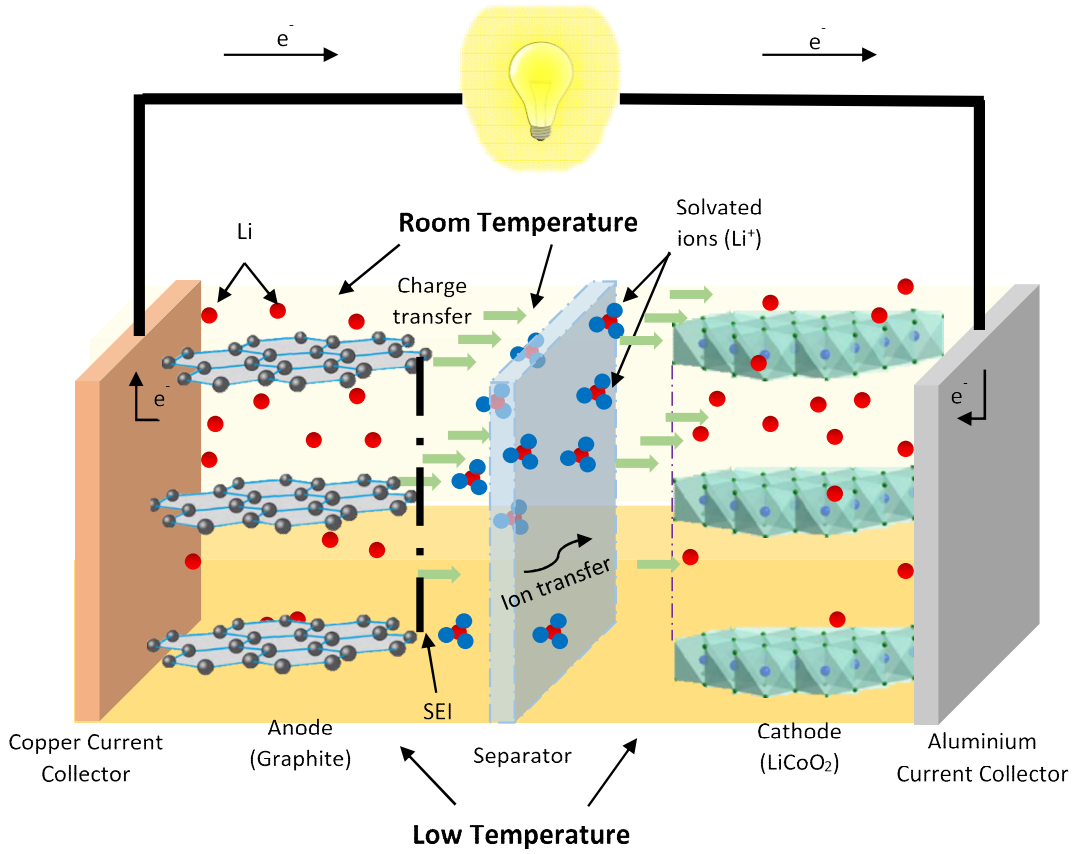

Figure 11. Schematic of the Basic Operating Principle of Secondary Lithium-ion Cell: Contrasting Effect of Low Temperature (≤ 10 °C) with Room Temperature (25 °C)

Conversely, based on Equation 25, assuming Arrhenius behaviour, high ambient temperatures (≥35 °C) lead to improved rate of internal chemical reactions along with improved physiochemical characteristics such as higher diffusivity and ionic conductivity. This leads to reduced cell internal resistances causing a suppression in cell overpotential, improving battery performance. However, higher reaction rates will cause side reactions to manifest (such as transition metal dissolution from the cathode) leading to battery degradation and potential safety risks (due to gas evolution). Contact resistances (such as those arising from copper/steel tabs and bus bars) increase as ambient temperature increases, causing cell overpotential to increase further without actually effecting any energy delivery to an external load. This is made prominent due to lower cell internal resistances at high ambient temperatures.

2.2 Review of Battery Characterisation Methods: Issues at Low Temperature

Lithium-ion batteries are characterised for primarily three purposes, (a) to benchmark against real-world operating scenarios, (b) to test operational safety, and (c) to parameterise and validate application specific models/algorithms. There exist two approaches: invasive and non-invasive. Although invasive methods (such as those employing microscopy, tomography, etc.) can draw out physical characteristics, they are complex and require battery disassembly. In particular, it is difficult to conduct them for application specific operating scenarios such as for low ambient temperature and aggressive duty cycles. Conversely, non-invasive characterisation, such as DC testing, is mainly electrical in nature and is useful to track battery performance. Essentially, the techniques employed in these tests are to measure the voltage and thermal response for various DC/AC current inputs; this is discussed in the following section. In Section 2.2.1, galvanostatic capacity tests that help capture cumulative electrical charge/energy stored will be discussed. In Section 2.2.2, dynamic capacity tests which help examine the battery's suitability for real-world automotive applications will be discussed. In Section 2.2.3, pulse power tests that help map battery instantaneous power capability at different SOCs and temperatures will be discussed. In Section 2.2.4, electrochemical impedance spectroscopy (EIS) that helps capture AC impedance response of the cells to elicit internal electrochemical phenomena will be

discussed. In Section 2.2.5, experimental techniques related to capturing cell behaviour under open circuit conditions will be discussed briefly. In Section 2.2.6, the immediate issues with these battery testing methods, particularly for low temperature applications are identified.

2.2.1 Galvanostatic Capacity Tests: Issue with Overpotential and Heat Generation at Low Temperatures

Galvanostatic (or constant current) tests are popular characterisation techniques to quantify battery performance. These tests are common in literature as well as in legislative standards. In a galvanostatic capacity test, the cells are fully charged and then discharged at different ambient temperatures and load currents until the minimum voltage cut-off is met (Figure 12). The capacity is the total electrical charge (in Ah) discharged at the end of this test. Essentially, capacity (in Ah) is a measure of the total electric charge stored in a cell and depends on the active lithium concentration in the electrodes. However, energy (in Wh) depends not just on the lithium concentration but also on the electrode potential. As such, the power delivered at the wheels of a BEV is dependent on both the current drawn from the cells as well as the operating voltage at which the current is drawn. This implies that capacity (in Ah) may not be the most appropriate method for estimating driving range of BEVs, particularly at low temperatures where voltage can decrease significantly. This will be discussed further in Section 2.2.2.

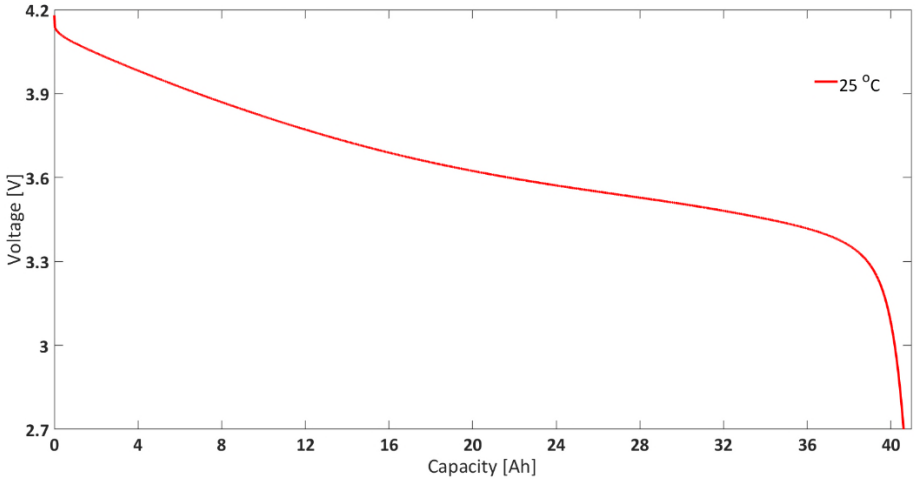

Figure 12. Typical Discharge Profile for a 1C discharge at 25 °C Ambient Temperature for a 40Ah Lithium-ion Pouch Cell

In a manufacturer's datasheet, galvanostatic (discharge) capacity is generally presented at various ambient temperatures and discharge currents for constant current continuous discharge duty cycles. It is generally seen that discharge capacity decreases with increasing discharge current and decreasing ambient temperature [79]. For example, in Figure 13 it can be seen that for 1C discharge current, the capacity decreases from ~14.6 Ah at 25 °C ambient temperature to ~12.3 Ah at −20 °C ambient temperature. Similarly, for 3C discharge current, the discharge capacity drops by almost 90% whereas for 5C discharge current, the cell fails to meet the demand. This is because of higher current demands at lower ambient temperatures. In this case, the cell internal resistances and in turn, the cell overpotentials are so high that the cut-off voltage is met without any capacity being discharged.

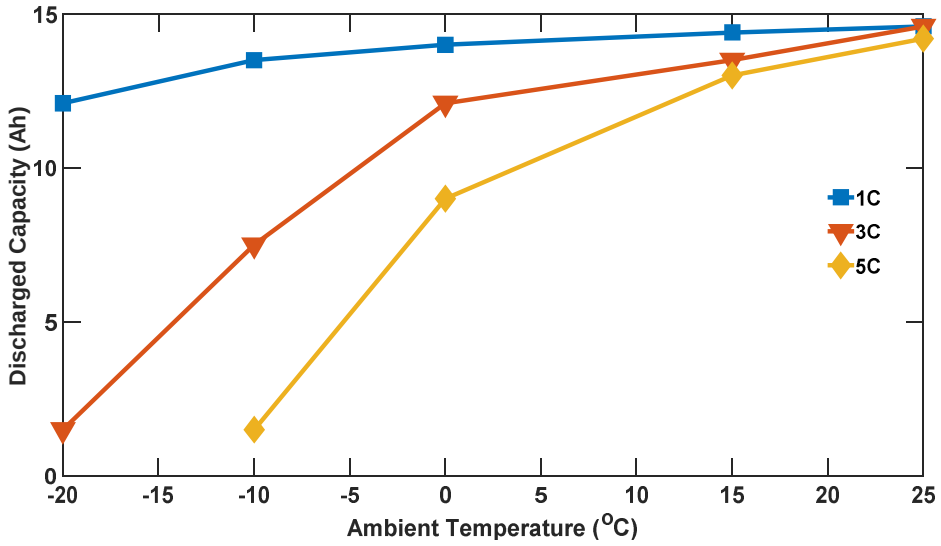

Figure 13. Effect of Low Ambient Temperature on Discharge Capacity for 14.6 Ah Lithium-ion Pouch Cell (redrawn from [79])

For the same discharge current, due to higher cell overpotential, the heat generated within the cell increases with decrease in ambient temperature [32,65,80]. This heat generated by the cell (sometimes termed as self-heating) may cause the cell internal resistances to be suppressed and in turn may cause a higher capacity being discharged from the cell than possible in isothermal conditions [80]. For example, Grandjean *et al.* recently argued that this rapid internal heat generation is a potential performance enhancement feature for lithium-ion cells operating at low ambient temperatures [81]. From −10 °C ambient temperature, towards the end of discharge at 5C, the cell surface

temperature was approximately 30 °C, a nearly 40 °C temperature rise due to rapid heat generation (Figure 14b). The thermal effect is evident in the cell voltage rise seen in the middle section of the discharge curve in Figure 14a. This is due to cell overpotentials being suppressed as the cell surface temperature increased. If the cells were not allowed to heat up, the cell voltage would have probably decreased at a faster rate and resulted in a diminished discharge capacity performance. This issue leads to a major disconnect between battery characterisation and battery operation and how the lack of distinction between them leads to issues with model parameterisation. This will be discussed further in Section 2.2.6.

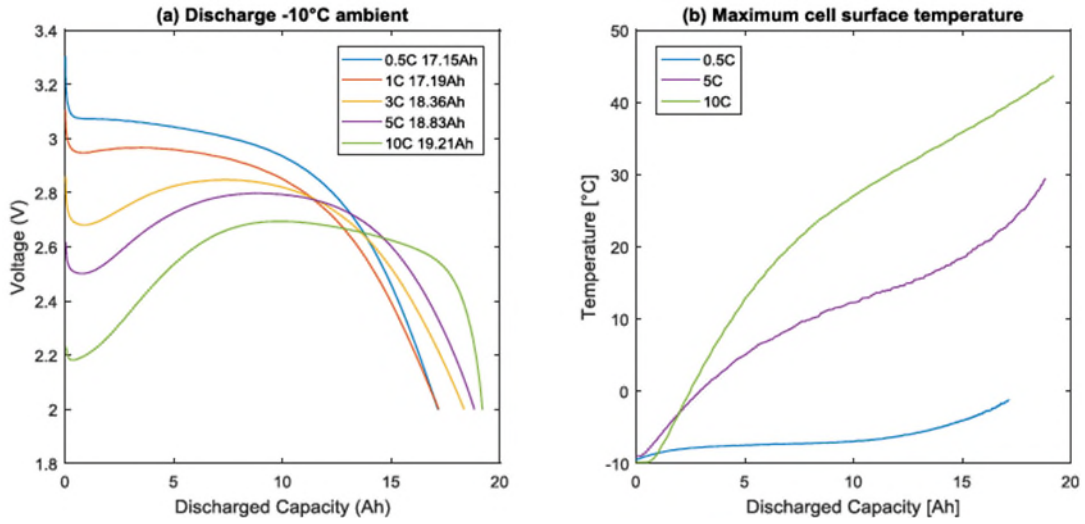

Figure 14. Effect of Different C-rates on Discharge Capacity and Surface Temperature Rise for 20 Ah Lithium-ion Pouch Cells at −10 °C Ambient Temperature: (a) Discharge Capacity and (b) Surface Temperature Evolution [82]

2.2.2 Inaccuracy of Dynamic Capacity Tests: Use of Current Control at Low Temperatures

As per International Electrical Commission (IEC) 62660-1, the dynamic capacity is defined as the capacity discharged when a fully charged cell is subjected to a dynamic power load profile (Figure 15). The capacity is usually measured until the cell reaches its minimum cut-off voltage.

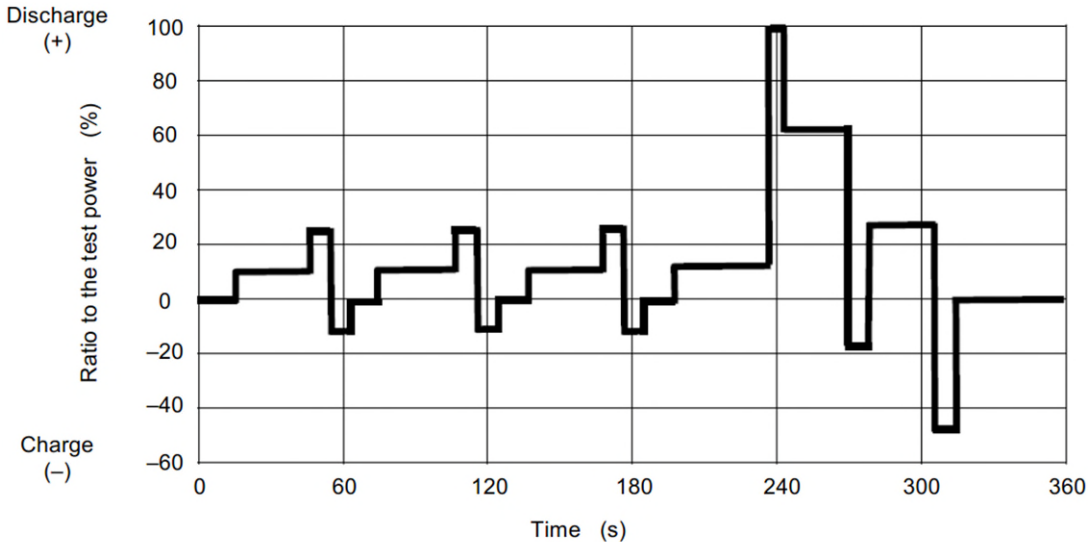

Figure 15. Typical Current Profile for Pulse Power Characterisation (IEC 62660-1)

In recent literature, Barai *et al.* argued that energy (in Wh) instead of capacity (in Ah) be adopted as an indicator of remaining driving range in electric vehicles [57]. They showed that energy (in Wh) is a more reliable indicator as it considers thermal losses as well as immediate cycling history (essentially operating voltage). They validated the hypothesis for real-world driving scenarios using the Artemis Urban/Motorway drive cycles. As ambient temperature decreases, due to higher cell overpotentials, it is expected that operating voltages will be lower and will reach cut-off voltage faster. This was also evidenced by Keil *et al.* employing the scaled-down version of the US06 legislative drive cycle to show that their cells failed to deliver the power required at ambient temperatures less than 0 °C [83]. However, they did not investigate whether the cells were able to sustain the same drive cycle when scaled using current control.

Realistic drive cycles (such as UDDS, NEDC, etc.) are also employed to capture ageing of lithium-ion cells, in which capacity fade (in Ah) is widely used as a key metric [49,84,85]. It is reasoned that capacity fade is directly related to the driving range of a BEV [35,38]. However, based on growing literature in the recent past that energy (Wh) instead of capacity (Ah) may be more representative of real-world driving range of BEVs [56,86,87], it may be prudent to consider energy throughput instead of capacity throughput as a means of quantifying lithium-ion cell ageing. In recent literature, energy fade rather than capacity has only been adopted by Zhang *et*

al. [88]. However, this methodology has not been widely adopted by other researchers [49,89].

To capture the thermal behaviour of lithium-ion cells, a similar conflict is seen in employing current control or power control as the primary metric for scaling-down vehicle level drive cycles to cell-level duty cycles. The difference between current control (calculated assuming fixed nominal voltage) and power control is illustrated in Figure 16. For example, Tourani *et al.* used Artemis legislative drive cycles (scaled-down to cell level using power control) to investigate the thermal behaviour of lithium-ion pouch cells in the −10 to 35 °C ambient temperature range [90]. On the other hand, Hosseinzadeh *et al.* employed the WLTC (Class 3) legislative drive cycle (scaled-down to cell level using current control) to validate their electrochemical-thermal model based on capacity throughput for a large format lithium-ion pouch cell between 5 and 45 °C ambient temperature range [91].

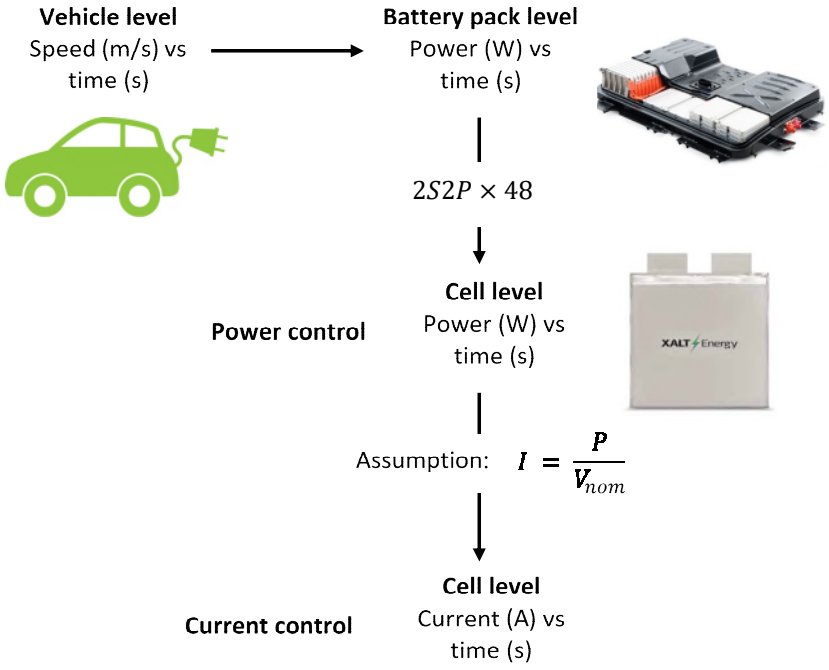

Figure 16. Backward Facing Model to obtain Cell-level Profile from Vehicle-level Speed Profile: Contrast between Power Control and Current Control (Images for EV, battery pack and cell obtained from Internet)

Over the course of the duty cycle, to compensate for the lower operating voltage, the operating current should respond to maintain consistent power delivery. So,

employing current control instead of power control (as used by Hosseinzadeh *et al.*) will intuitively lead to lower (and inaccurate) estimation of heat generation within the cells [92]. Thus, using current control (with fixed nominal voltage) for thermal characterisation of lithium-ion cells may not fully capture real-world thermal behaviour. Any thermal model thus developed may not be applicable in the real-world.

The significance of the choice between power control and current control is not an issue at higher operating temperatures (≥25 °C) where the cell resistances are lower compared to lower operating temperatures (≤10 °C) [93]. Furthermore, at higher temperatures, resistance does not increase as much with increase in current magnitude and decrease in SOC [94]. Thus, at higher temperatures, applying current control or power control for a particular duty cycle, probably will not make a substantial difference on the amount of capacity (Ah) or energy (Wh) delivered. However, at lower temperatures, particularly due to higher cell resistances at low SOC (<50%) and for high current magnitudes, the choice between current control and power control becomes more critical. In Section 2.3.4.1, the modelling implications are discussed.

2.2.3 Pulse Power Characterisation: Impact of Internal Cell Heating and Relaxation Period at Low Temperatures

The primary objective of pulse power characterisation (PPC) is to quantify the DC resistance (DCR) of a lithium-ion cell under different operating conditions. Through this, it can be estimated whether the cell will be able to meet the instantaneous duty cycle power demand. The lower the DCR at a particular operating condition, the higher the pulse power capability. The DCR (mΩ) is defined for a particular current pulse as:

$$DCR = \frac{\Delta V}{\Delta I} \tag{26}$$

Here, ΔV (V) is the change in voltage after the pulse is applied; ΔI (A) is the amplitude of the current pulse. Other factors to be considered while defining a current pulse are initial voltage (or SOC), pulse duration (usually 10 s) and current direction (charge or discharge). Although voltage response (ΔV) is assumed to be linear, as shown in Figure 17, it consists of two parts: instantaneous voltage drop (ΔV_0) assumed to be the pure Ohmic resistance of the cell and the dynamic (non-linear) voltage drop (ΔV_1)

which is based on resistances due to charge transfer resistance at the electrode electrolyte interphase and concentration polarisation due to ionic diffusion, particularly in the electrodes' active material.

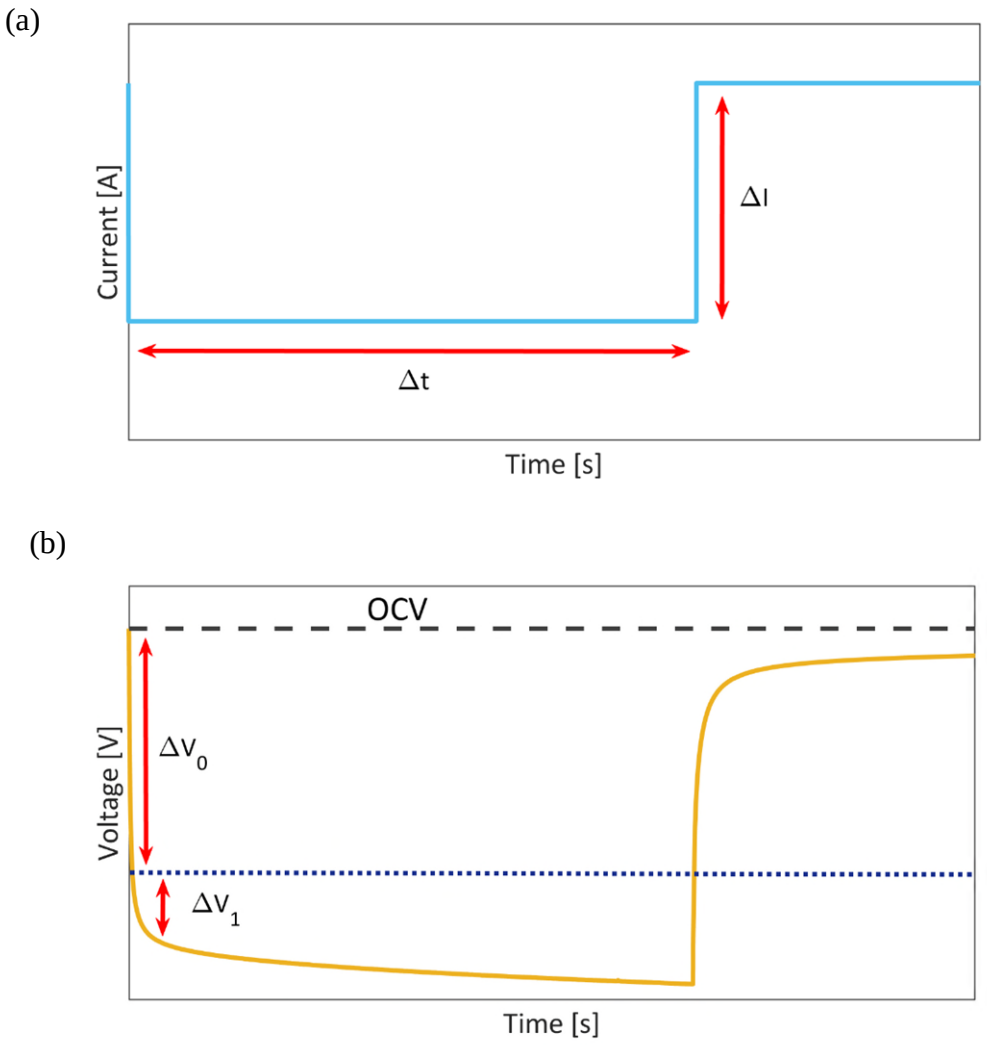

Figure 17. Schematic of (a) Current Pulse and corresponding (b) Voltage Response

The effect of temperature, SOC and charge/discharge current on DCR has been widely explored in literature [58,93,95,96]. At lower ambient temperatures (≤10 °C), due to slower chemical kinetics, charge transfer at the electrode-electrolyte interphase slows down, leading to higher overpotentials [40]. Furthermore, lower ionic conductivity in the electrolyte and slower diffusion, particularly in the electrodes' active material contribute to higher voltage loss at lower temperatures [41]. These manifest as an increase in DCR value and reduction in power capability at low ambient temperatures.

As shown in Figure 18, as ambient temperature decreases from 25 °C to 0 °C, for a 1C discharge current, the resistance increases from 1 mΩ to over 5 mΩ; a five-fold increase [93]. Furthermore, it is shown in Figure 18 that current dependency of DCR becomes more prominent as ambient temperature decreases. In particular, it is shown that DCR decreases as operating current increases at 0 °C. This is likely due to suppression of cell internal resistance due to rapid heat generation in the internal layers of the pouch cell [97].

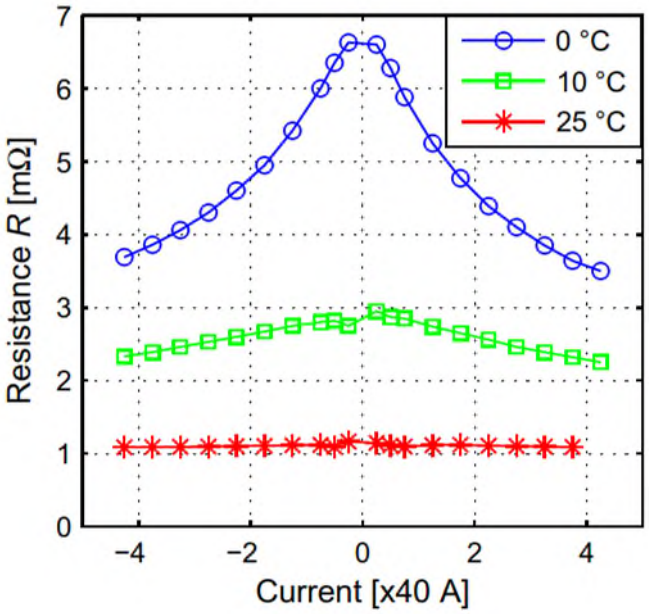

Figure 18. The Effect of Ambient Temperature and Current Magnitude on DC Internal Resistance of Lithium-ion Pouch Cells (Discharge current is positive) [93]

Recent work by Troxler *et al.* and Klein *et. al.* argued that based on the operating temperatures of the various layers within a pouch cell, there would be internal temperature and SOC gradients whose individual behaviours would affect the overall cell behaviour [97,98]. That is, within the parallel layers of the pouch cell, the layers closer to the centre would experience higher operating currents and heat up faster. This could lead to a decrease in cell resistances due to the cell operating at higher operating temperature compared to the temperature measured at the cell surface. However, most researchers assume that for a particular pulse, there is negligible change in cell temperature and SOC [99].

As such, the background electrochemical processes, and thus the internal resistances, are time dependent [100]. As illustrated in Figure 19, for an 18 s discharge pulse, while R_O (phase (i)) is time independent and is the inherent electrical resistance of the cell, R_{CT} (phase (ii)) and R_{Diff} (phase (iii)) increase with time. However, using just the voltage response, it is difficult to separate the contributions of R_{CT} and R_{Diff} to the overall resistance. Mathematical fitting can be employed to discern the contributions and modelled using an equivalent circuit model; this will be discussed in Section 2.3.

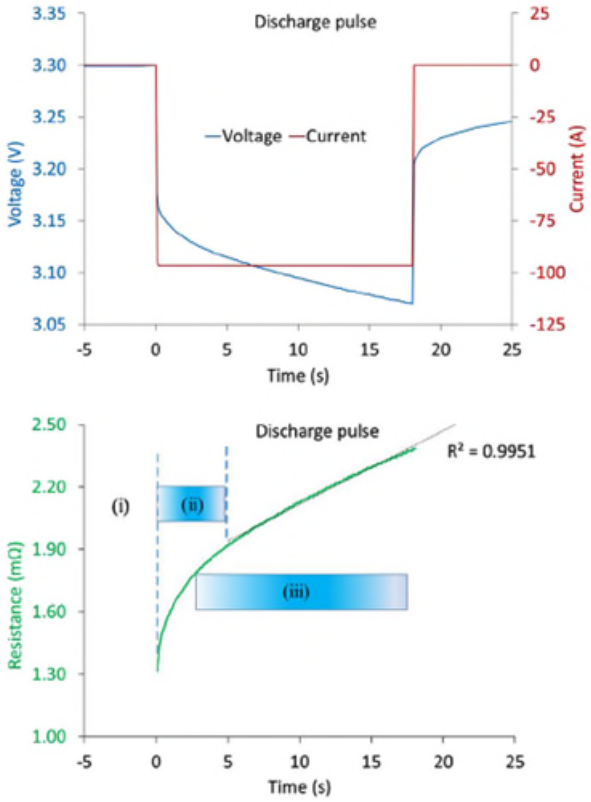

Figure 19. Voltage Response (bottom) to 18 s Discharge Pulse (top): (i) Ohmic resistance due to inherent electrical circuit, (ii) Charge transfer resistance and (iii) Diffusion resistance due to mass transport limitations [100]

The duration of the pulse should be such, so as to not change the SOC for that particular pulse response. Usually a pulse power testing regime consists of a series of predefined charge and discharge pulses (usually 10 s long) of increasing current magnitude at a particular SOC and ambient temperature [101]. As shown in Figure 20, there is a rest period between each pulse. This rest period is important to ensure that the cells are at electrochemical equilibrium before being subjected to a further current

pulse. Barai *et al.* in their investigation into relaxation times for EIS argued that at least a 4 hour period is required before any current is applied to the cells to ensure electrochemical equilibrium [102].

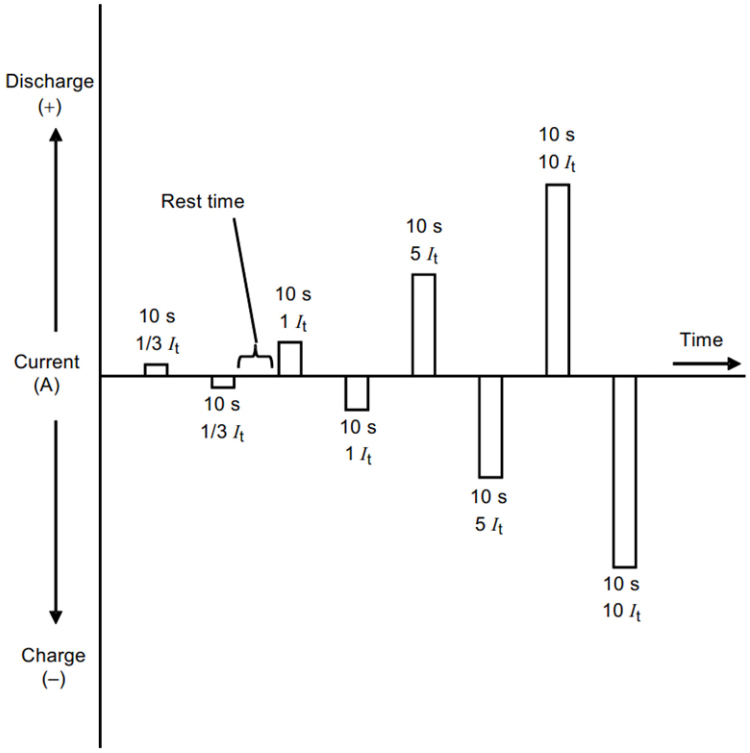

Figure 20. Typical Current Profile for Pulse Power Characterisation (IEC 62660-1)

Relaxation time is a particularly important consideration given that cell internal electrochemical processes slow down as ambient temperature decreases. The IEC 62660-1 specifies a 10 minute rest period, which is unlikely to be enough at low ambient temperatures, particularly for large pulse amplitudes [103]. Provision is given for extending relaxation times on the basis of temperature rise, which is a thermodynamic rationale but not an electrochemical one. For example, entropy profiles of lithium-ion cells at different temperatures require long relaxation periods to ensure that the cells are in thermodynamic equilibrium [104]. Investigation of faster methods to measure entropy coefficients for lithium-ion cells is an ongoing research avenue [104,105].

2.2.4 Electrochemical Impedance Spectroscopy (EIS): Localised Measurements at Low Temperatures

There are other techniques employed to obtain the cell characteristics such as impedance through AC based electrochemical impedance spectroscopy (EIS). EIS consists of sinusoidal AC current ($I\ (t)$), which is applied to the cells at different frequencies between 10 mHz to 10 kHz. The AC voltage response ($V\ (t)$) and the consequent phase shift ($\emptyset = \varphi_V - \varphi_I$) is measured to obtain the impedance response of the cell. The impedance ($Z\ (t)$) is calculated as follows:

$$I\ (t) = |I_0|\sin(\omega t + \varphi_{\mathrm{I}}) \tag{27}$$

$$V\ (t) = |V_0|\sin(\omega t + \varphi_{\mathrm{V}}) \tag{28}$$

$$\omega = 2\pi f \tag{29}$$

$$Z\ (t) = \frac{|V_0|\sin(\omega t+\varphi_{\mathrm{V}})}{|I_0|\sin(\omega t+\varphi_I)}$$

Or,

$$Z\ (t) = |Z_0|\sin(\omega t + \varphi_V - \varphi_I)$$

Or,

$$Z\ (t) = |Z_0|\sin(\omega t + \emptyset) \tag{30}$$

As shown in Figure 21, the cell's complex impedance can be interpreted to infer internal electrochemical processes. Note, impedance response obtained from EIS is usually represented using a Nyquist plot. Section 1 represents the high frequency inductive component of the impedance due to the metallic connections in the cell and wires. Section 2 represents the Ohmic resistance of the cell associated with current collectors, electrolyte and separator. Section 3 depicts the formation of SEI layer on the surface of the anode over the course of the cycle life of the cell. Section 4 depicts the double layer capacitance and charge-transfer resistance at the electrode/electrolyte interface. Section 5 represents diffusion processes within the electrodes' active material and within the electrolyte at low frequencies.

EIS has been widely used as a technique to investigate the effect of temperature on lithium-ion cells starting with Zhang *et al.* [106,107]. They found that charge transfer resistance (R_{CT}) was most sensitive to change in temperature. That is, as temperature decreased by 10 °C, the 2nd semi-circle (representing R_{CT}) in Figure 21 (Section 4) became larger (by 2-3 times) and occurred at a lower frequency than at room temperature [93,108,109]. In particular, at lower ambient temperature, slower charge transfer kinetics becomes the rate determining step for charge/discharge operation of lithium-ion cells [41]. Furthermore, Raijmakers *et al.* used the frequency at which the imaginary part of the impedance was zero, to successfully estimate the internal temperature of lithium-ion cells in equilibrium conditions and stated that this 'intercept' frequency increased as ambient temperature decreased [110,111]. However, this technique is largely unverified for *in operando* usage as errors arising from high operating currents and interference from other electrical components make on-board vehicular implementation challenging [112].

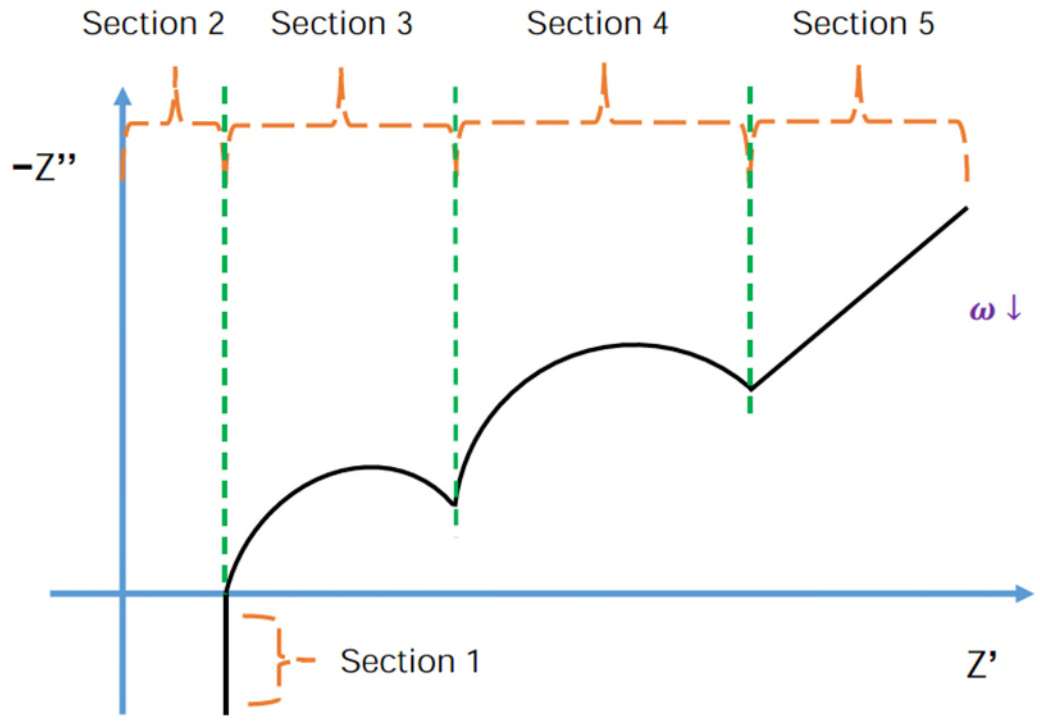

Figure 21. Schematic representation of an ideal EIS spectrum on a Nyquist plot for Lithium-ion Cells

EIS represents electrochemical phenomena more accurately than PPC as it involves negligible charge/discharge processes (low magnitude AC perturbation of about C/20

peak), but each experiment requires significant time [93]. A single EIS measurement takes more than 8 minutes when measuring down to 10 mHz frequency [100]. The cell SOC and operating temperature may change significantly during EIS measurements; these changes influence the measurement accuracy and make the method impractical at moderate and high current-rates, particularly *in operando* [113].

As introduced in Section 2.2.3, a single lithium-ion cell is made up of multiple layers which cause non-uniform temperature and SOC distribution internally [65,114]. In particular, cell characteristics deviate from lumped behaviour due to non-homogeneities as demonstrated by Troxler *et al.* [114]. Recently, Osswald *et al.* showed that for a particular AC signal applied on modified cylindrical cells, the resultant voltage perturbation decreases as distance from the current carrying tabs increases [115]. As shown in Figure 22, this gradient in voltage response became more prominent at 10 °C compared to at 25 °C due to slower chemical kinetics. Thus, for EIS measurements at even lower temperatures (for example, −20 °C), internal non-uniformities within a cell could lead to localised measurement and obscure critical information regarding its electrochemical behaviour.

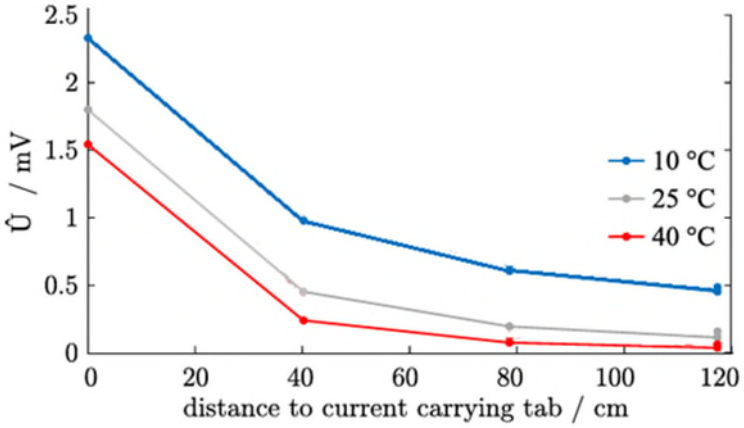

Figure 22. Amplitude of Voltage Response (at 167 mHz) at Different Temperatures for 50 mA AC Current Excitation (adapted from [115])

2.2.5 Open Circuit Voltage (OCV) and pseudo-OCV Measurements at Low Temperatures

Battery testing such as OCV versus SOC characterisation is also conducted to help parameterise battery models. The OCV versus SOC relationship is either obtained

from very low C-rate (≤0.2C) charge/discharge curves (known as pseudo-OCV), or, from rest voltage methods (known as galvanometric intermittent titration technique (GITT) by charging/discharge the cells at small SOC increments (≤10%) [86,116,117].

In the limited literature related to OCV characterisation experiments at low ambient temperatures, it has been argued that the dependence of OCV on ambient temperature and current rates is minimal compared to dependence of OCV on SOC and can thus be ignored in terms of ECM parameterisation [58]. However, pseudo-OCV tests which are used in place of GITT tests to reduce experimentation time, could be affected by increased cell overpotentials at low temperatures. This is because, as temperature decreases, for a particular C-rate employed for the pseudo-OCV test, the induced overpotential will increase, particularly due to kinetic contributions [117]. This will cause deviation from open circuit behaviour due to addition of polarisation related overpotentials [118,119]. Thus, for a particular SOC, the corresponding pseudo-OCV would be lower as temperature reduces [120]. This is shown in Figure 23, where the pseudo-OCV (0.04C discharge) measurements for 1.1 Ah lithium-ion cells are presented at different temperatures. In this case, it is likely that at low temperatures, the pseudo-OCV curve would diverge from the OCV value obtained using GITT. This issue could be compounded if higher C-rates are utilised, possibly leading to localised measurements and subsequently, affecting model accuracy [121].

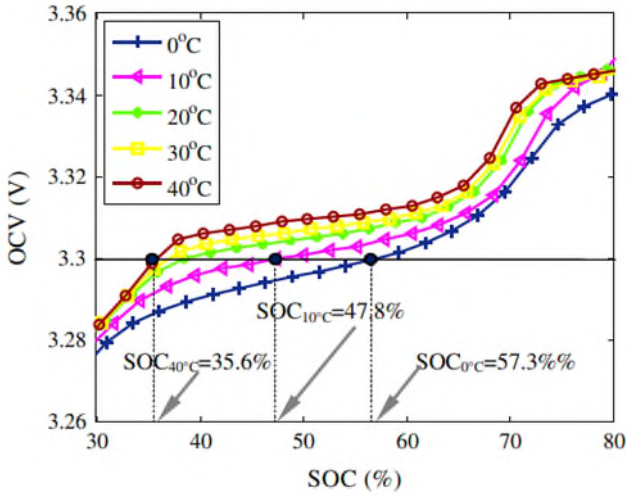

Figure 23. Pseudo-OCV Measurements at Different Temperatures shown between 30 to 80% SOC (Other SOC data unavailable) [120]

2.2.6 Gaps in Knowledge: Identified Concerns with Battery Characterisation at Low Temperatures

Results from galvanostatic battery experiments, at different ambient temperatures and C-rates, are employed to directly model the usable charge/discharge capacity of lithium-ion cells under different operating scenarios [60]. In these model parameterisation experiments, it is assumed that the test conditions are isothermal. However, at low ambient temperatures, due to higher cell internal resistances (R_{int}), ($Q_{gen} = I^2 \times R_{int}$), cells heat up more [80]. This effect is compounded if the operating current is high.

Grandjean *et al.* recently argued that cell heat generation is a performance enhancement feature for lithium-ion cells operating at low ambient temperatures [81]. As shown in Figure 14, they conducted galvanostatic discharge cycle experiments at −10 °C ambient temperature. Towards the end of discharge at 5C, the cell surface temperature was approximately 30 °C; a nearly 40 °C temperature rise due to internal heat generation. On the other hand, if the cells were not allowed to heat up, the cell voltage would have decreased at a faster rate and likely resulted in a lower capacity discharged. This implies that while the starting cell temperature may be close to the ambient temperature; at the end of a discharge cycle, the cell temperature can be considerably higher than the ambient temperature, particularly for high load currents. This is advantageous for operation in real-world applications but should be avoided for parameterisation experiments.

There is substantial literature on lithium-ion cells models, where researchers have claimed that model parameters have been obtained from battery experiments conducted under isothermal conditions [7,33,58,122,123]. On closer examination of the literature, claimed isothermal conditions are often found to be non-isothermal. For experiments conducted in air-based thermal chambers, under load, as a lithium-ion cell self-heats, its operating temperature increases and is widely reported in literature as such [58,81]. For example, Jaguemont *et al.* obtained discharge capacities for their cells at −20, −10, 0 and 25 °C ambient temperatures [58]. For 1C discharge at −20 °C, the final cell temperature was −5.6 °C and for 1C discharge at −10 °C, the final cell temperature was 0.9 °C. This means that the discharge characteristics were

representative of a test temperature much higher than either the −20 or −10 °C starting ambient temperature. In fact, the final cell temperature for the test at −20 °C is 4.4 °C higher than the starting ambient temperature of the next set point, −10 °C.

Conventionally, battery cycling is conducted in commercially available climatic test chambers. A climatic chamber allows control of operating temperature and humidity conditions during the test. Particularly, temperature control is achieved by forced convection of air within the chamber (Figure 24). Recently, Ardani *et al.* have argued that using thermal chambers that employ forced air convection may not be sufficient to maintain isothermal test conditions to conduct model parameterisation experiments [99]. Using an electrochemical model, they showed that non-isothermal test conditions could lead to inaccuracies in parameterising cell physiochemical parameters such as cathode diffusion coefficient. In particular, they showed that the model parameters estimated were more in line with a higher ambient temperature if only forced air convection was employed. For example, while the ambient temperature was 15 °C, the battery parameters estimated were more like those for 19 °C ambient temperature. In their study, Ardani *et al.* employed Peltier elements to control cell surface temperature during pulse discharge. However, their investigation did not consider the more extreme case of a continuous discharge at an ambient temperature (for example, 1C discharge).

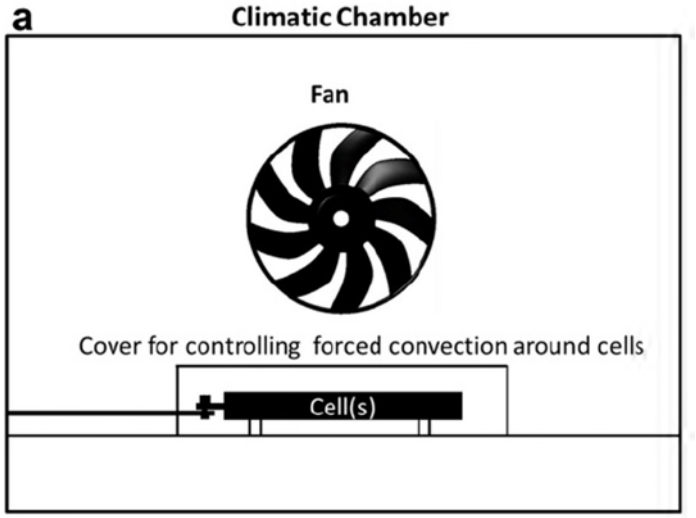

Figure 24. Schematic Representation of Climatic Test Chamber with Cooling Fan [124]

To reiterate, while beneficial for real-world usage, drive cycle testing, and model validation, heat generation during charge/discharge is an issue for a parameterisation experiment where repeatability is key. There is a clear disconnect between the requirement for parameterisation of cells at a fixed temperature, and the current experimental practise, which is deficient. This has not been extensively investigated and therefore there is a current gap in knowledge regarding the effect of this non-isothermal parameterisation and its significance.

In literature, active thermal management of lithium-ion cells (such as those employing oil baths) has largely been investigated from the perspective of the performance characteristics of the heating/cooling system [125,126]. Bolsinger *et al.* investigated the effect of different cooling configurations for cylindrical cells and argued that tab (or terminal) cooling is better than surface cooling. Similarly, other researchers compared the pros and cons of choosing between air cooling and liquid cooling [69,125,127]. They found that while air cooling is cheaper than liquid cooling, it demonstrates poor thermal performance of the battery pack being cooled. The comparisons were made on the basis of cost, complexity, efficiency, and direct versus indirect cooling.

Air has poor thermal properties compared to other materials (such as mineral/silicone oils) (Table 3), and so the cooling capability may be insufficient to counter the rapid internal heat generation seen for high load currents and/or low ambient temperatures. The thermal conductivity of air is 0.0242 W/mK, whereas that of commercially available mineral/silicone oils are in the range of 0.13-0.15 W/mK [125,127].

Similarly, the specific heat capacity also compares poorly, 1006 J/kgK for air compared to 1300-1900 J/kgK for cooling liquids [127]. This means that for a similar cooling area and coolant mass, the cooling capability of air is substantially lower than that of a direct liquid cooling system [128]. This may not allow for isothermal test conditions essential to obtaining accurate cell performance characteristics [128]. Compared to conductive cooling with Peltier elements [99], an immersed oil bath allows simultaneous cooling of all cell surfaces (including the tabs) and is independent of cell format or size. This will allow expansion of isothermal testing independent of cell format or size.

Table 3. Comparison of Typical Physical Properties of Different Coolants [127]

Physical Property	Air	Mineral Oil	Silicon Oil	Water/Glycol
Specific Heat Capacity (J/kgK)	1006	1900	1370	1069
Thermal Conductivity (W/mK)	0.0242	0.13	0.15	0.3892

2.2.6.1 Key Identified Concern: Isothermal Test Conditions during Battery Characterisation for Model Parameterisation

Isothermal test conditions are particularly important for low temperature parameterisation where the effects of rapid internal heat generation are much larger than at room temperature. This is an important limitation because by allowing the cells' operating temperature to diverge from the ambient (or test) temperature, the effect of temperature and current on the usable capacity can become convoluted. If the capacity performance is being assessed at a particular temperature, the cell itself should be anchored to that temperature for the duration of the parameterisation test. This is because cell internal resistances and in turn, overpotentials are a function of both operating current and operating temperature [89]. To draw out the effect of one, the other should be fixed for a particular experiment.

Furthermore, the implications of erroneous parameterisation and validation data on battery models will be discussed in Section 2.3.4. Before that, the state-of-the-art modelling techniques for battery models are reviewed in Sections 2.3.1-2.3.3.

2.3 Battery Modelling: Issues at Low Temperature

A battery management system (BMS) supervises the on-board battery pack in an electric vehicle [129]. The BMS ensures that the pack is within a safe operating area and controls its electrical and thermal performances [57,130]. It also informs the driver regarding the remaining driving range of the vehicle [57]. A BMS utilises both measured parameters (such as voltage and temperature) and inferred parameters (such as SOC and SOE) to maintain optimal battery pack performance and estimate other parameters, such as remaining driving range. These inferred parameters, also known

as battery states, are estimated by underlying battery models. The reliability of these battery states depends on the accuracy of the model.

2.3.1 Definition of State of Charge

The success of range estimation largely depends on the accuracy of the underlying battery state estimators such as SOC (state-of-charge) and SOH (state-of-health) [89]. SOC is used analogous to the fuel gauge in a conventional vehicle [57]. From a thermodynamic perspective, it is defined as [60]:

$$SOC = \frac{Remaining\ Exchageable\ Li^{+}}{Total\ Exchangeable\ Li^{+}} = \frac{Residual\ Capacity\ at\ Low\ C{-}rate}{Maximum\ Capacity\ at\ Low\ C{-}rate} = f(OCV) \quad (31)$$

From a thermodynamic perspective alone, SOC is related to the lithium concentration in the electrodes under open circuit conditions [116,131]. However, in terms of estimating the remaining driving range from SOC, the above definition can be misleading as the SOC relationship with open circuit voltage (OCV) is defined at equilibrium and does not account for the effect of operating conditions such as temperature, C-rate or for operation-induced overpotentials. The terminal voltage not only depends on the OCV of the cell but also on the operating current and the cell internal resistance. This means that if either the operating current or the cell internal resistance, or both, are high enough, the cell can reach its minimum cut off voltage. This could cause the discharge cycle to prematurely stop, leading to diminished capacity/energy being discharged and hence, lower actual driving range.

In contrast to Equation 31, under dynamic operating conditions, what is of more interest to the BMS is the accessible or usable battery capacity for a particular load profile and operating temperature [40]. As defined in the USABC test manual, SOC is based on the ratio of the remaining capacity and the usable capacity at a particular operating condition (in terms of operating current and temperature) [60,132]. In essence, as introduced in Figure 13, for a particular load current and operating temperature, SOC should be an indicator of remaining driving range if demand from the vehicle is maintained and minimum cut-off voltage is fixed [131,132]. At lower ambient temperatures (≤10 °C), Singer *et al.* explain the diminished battery performance as reversible capacity fading due to higher activation energies at the

electrodes and additional overpotentials induced due to slower chemical kinetics [40]. Nikolian *et al.* defined this method of inferring the SOC as the extended coulomb counting (ECC) method [59]. They defined SOC to account for the capacity usable for a particular ambient temperature and load current as:

$$SOC(t) = SOC(0) - \frac{\int_0^t Idt}{C_{DYN}} \times \frac{100}{3600} \quad (32)$$

Here, C_{DYN} is a lookup table outputting capacity values obtained from galvanostatic discharge experiments at different ambient temperatures and C-rates.

This algorithm is the least complex and closest to the conventional definition of SOC. It has some disadvantages as it is an open-loop approach and hence, is inherently inaccurate without the initial SOC [118]. Also, being entirely dependent on the current measurements, signal noise will adversely impact the accuracy of the algorithm [133].

A model-based approach allows a closed-loop approach to SOC estimation [134]. Any errors through the Coulomb Counting method can be minimised by comparing the measured terminal voltage to the output voltage estimated from the model [86]. Hence, accuracy in output voltage estimation becomes critical for ensuring accuracy in SOC estimation. To ensure accuracy in output voltage estimation, two aspects are very important: (a) collating a robust dataset for parameterising model parameters and, (b) validating the model for real-world applications.

The two most common approaches to model cells are electrochemical models and electrical equivalent cell models (ECMs). Electrochemical models, pioneered by Newman *et al.* solve a set of partial differential equations to solve the underlying electrochemical reactions happening within a cell [89,135]. These equations were detailed in Section 2.1.2.2. However, they require significant computational power and time, and a large parameterisation data set [77]. This is due to the large number of unknown parameters within the partial differential equations, particularly because these equations have to be separately solved for the positive electrode, separator and the negative electrode [136]. Being complex, with limited practical application, electrochemical models are not suited to online vehicle applications [137].

ECMs on the other hand, can be deployed online due to their simpler lumped parameter approach that is computationally inexpensive [123,136,138]. Hence, ECMs can be used as part of a battery management system (BMS) in automotive vehicles such as in a PHEV/BEV. These ECMs approximate the electrochemical processes inside the cell in the form of resistors and capacitors to estimate the voltage response under varying load conditions (current, temperature, SOC).

2.3.2 Parameterisation Methods for Equivalent Circuit Models

To parameterise an ECM, the three most important characteristics are open-circuit voltage, capacity characteristics to obtain SOC and impedance behaviour [110]. In an ECM, the OCV is represented as an ideal voltage source, generally variable with SOC, to which overpotential ($\eta = I \times R_{int}$) is added to obtain the terminal cell voltage:

$$V_{terminal} = OCV - I \times R_{int} \quad (33)$$

The nominal capacity of the cell is obtained from the manufacturers' data sheet, or through galvanostatic charge/discharge experiments that capture the effect of operating conditions such as temperature or C-rate. These capacity values are used to parameterise C_{DYN} in Equation 32 to obtain SOC. Depending on the model structure, cell internal resistances are conventionally represented as a resistor connected in series to a resistor-capacitor pair connected in parallel. This resistor-capacitor pair connected in parallel is termed as an RC network. This ECM itself is termed as a 1st order ECM. If further 'n' RC networks are connected in series, then the ECM is termed as an nth order ECM. Typical 1st and 2nd order ECMs are illustrated in Figure 25.

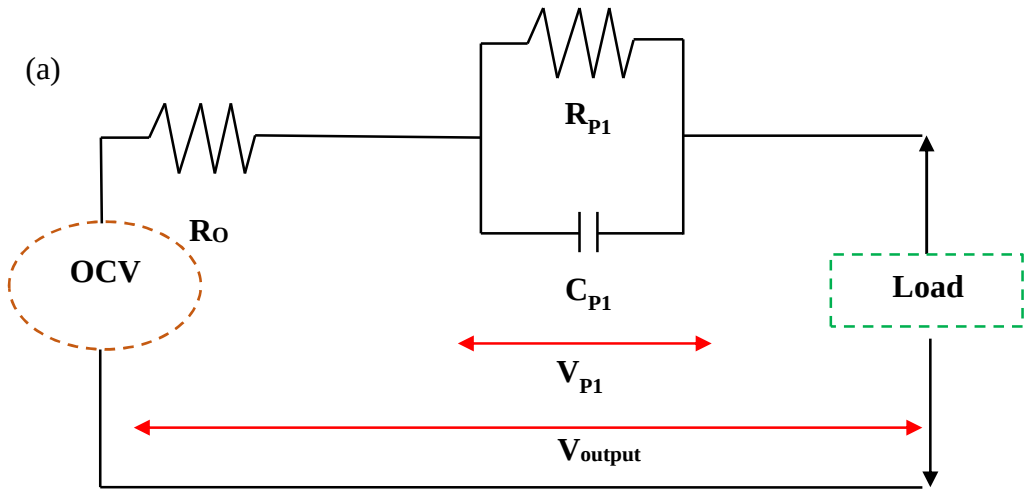

(b)

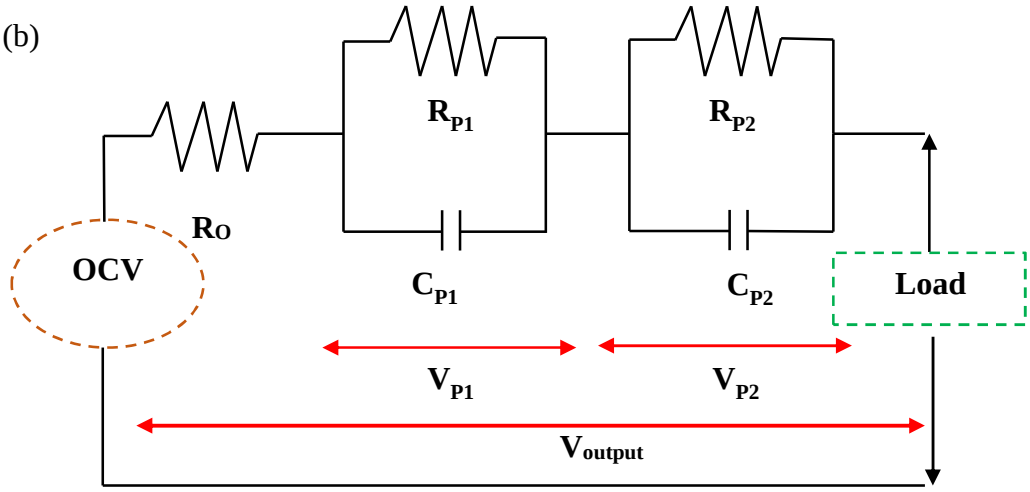

Figure 25. 'Thevenin' ECM Structures for a Lithium-ion Cell: (a) 1st and (b) 2nd Order

For a 2nd order ECM (i.e. having 2 RC networks), the voltage response for a particular current input is given below:

$$V_{output} = OCV - \left(I_{input} \times R_O\right) - V_{P1} - V_{P2} \tag{34}$$

$$\frac{dV_{P1}}{dt} = \frac{I_{input}}{C_{P1}} - \frac{V_{P1}}{R_{P1} \times C_{P1}} \tag{35}$$

The time constant, τ_{P1} for the first RC network is defined as follows:

$$\tau_{P1} = R_{P1} \times C_{P1} \tag{36}$$

$$\frac{dV_{P2}}{dt} = \frac{I_{input}}{C_{P2}} - \frac{V_{P2}}{R_{P2} \times C_{P2}} \tag{37}$$

$$\tau_{P2} = R_{P2} \times C_{P2} \tag{38}$$

Since Equations 34 and 37 are linear differential equations,

$$V_{P1} = I_{input} \times R_{P1}\left(1 - e^{-t/\tau_{P1}}\right) \tag{39}$$

$$V_{P2} = I_{input} \times R_{P2}\left(1 - e^{-t/\tau_{P2}}\right) \tag{40}$$

Thus, Equation 33 becomes,

$$V_{output} = OCV - I_{input}\left(R_O + R_{P1}\left(1 - e^{-t/\tau_{P1}}\right) + R_{P2}\left(1 - e^{-t/\tau_{P2}}\right)\right) \quad (41)$$

For an n[th] order ECM, the voltage response can generally be mathematically represented as:

$$V_{output}(t) = OCV - I_{input}(t) * \left(R_O + R_{P1}\left(1 - e^{-t/\tau_{P1}}\right) + R_{P2}\left(1 - e^{-t/\tau_{P2}}\right) + \cdots + R_{Pn}\left(1 - e^{-t/\tau_{Pn}}\right)\right) \quad (42)$$

As briefly discussed in Section 2.2.3, the voltage response to current pulses obtained from pulse power characterisation experiments can be utilised to obtain model parameters [93]. As shown in Figure 17, the overpotential (from the voltage response) can be utilised for the particular current magnitude to estimate the cell internal resistances. However, without using fitting algorithms, the possible capacitive behaviour seen for the non-linear overpotential (ΔV_1) cannot be calculated [101]. These model parameters of an ECM (based on the estimation data set) can then be estimated via a non-linear least squares algorithm (for example, Matlab® lsqcurvefit). The fitting is conducted by comparing the modelled voltage calculated from Equation 41 and the experimental voltage. The model parameters (R_O, R_{Pn} and τ_{Pn}) can then be iteratively changed based on tolerances set in the algorithm so as to minimise the error between the modelled voltage and the experimental voltage [81]. Depending on the test matrix employed for the pulse power characterisation experiments, model parameters can be obtained for different SOCs, temperatures and currents. Further functions can be utilised to reduce the number of iterations required for the non-linear least squares algorithm. This is generally the Jacobian matrix for the voltage response (or output) that allows linearisation of Equation 41. A Jacobian matrix (J) is comprised of all 1[st]-order partial derivatives of V_{output} with respect to R_O, R_{Pn} and τ_{Pn}:

$$\boldsymbol{J} = \begin{pmatrix} -I_{input}(0) & \cdots & 0 & 0 \\ \vdots & \cdots & \vdots & \vdots \\ -I_{input}(t) & \cdots & -I_{input}(t)\left(1 - e^{-t/\tau_{Pn}}\right) & \frac{-I_{input}(t) * R_{Pn} * \Delta t * e^{-t/\tau_{Pn}}}{\tau_{Pn}^2} \end{pmatrix} \quad (43)$$

In terms of parameter implementation techniques, either polynomial functions, correction factors or lookup tables can be used to represent the model parameters as part of an ECM [55]. To improve ECM accuracy and real-world applicability further, there are dedicated subsystems that can represent other cell characteristics such as hysteresis [139] and dynamic effect of cell heat generation (via thermal models) [58].

2.3.2.1 Thermal Feedback Model

Low ambient temperatures lead to greater coupling of electrochemical and thermal processes within a cell [66]. In this case, the accuracy in output voltage estimation will also depend more on the accuracy of the cell temperature measurements or heat generation estimations [74]. Also, depending upon the load profile, there will be a discrepancy between the cell surface temperature (measured using thermocouples attached to a few discrete points on the cell surface) and actual cell electrical performance characteristics [140]. For example, for a cylindrical cell, even at 25 °C ambient temperature, the temperature difference between the jelly-roll and the surface at the end of constant current continuous discharge duty cycles can be up to 18 °C for 5C discharge current, and at least 3 °C for 1C discharge current [15]. This difference is expected to be higher for lower ambient temperatures [141]. Thus, depending on how the temperature of the cell is considered to parameterise the ECM, the accuracy in output voltage estimation will be affected [58].

The general equation for local heat generation rate proposed by Bernardi *et al.* [142]:

$$Q_{gen} = I_{input} \times \left(OCV - V - T_{cell}\frac{dV}{dT}\right) \quad (44)$$

Li *et al.* suggested that reversible heating from entropic contributions can be ignored at low temperatures (such as at −20 °C) as contributions from Ohmic and polarisation resistances increase much more rapidly as temperature decreases from room temperature [65]. Thus, if reversible heat generation is ignored, the cell heat generation rate is presented as follows [74]:

$$Q_{gen} = I_{input} \times (OCV - V) \quad (45a)$$

Or,

$$Q_{gen} = I_{input}^2 \times (R_O + R_{Pn}) \quad (45b)$$

In literature, various thermal models have been considered, which take into account conductive and convective heat losses to estimate the internal temperature of the cell [74]. This 'true' cell temperature is then used to dynamically update the ECM parameters. Based on Equation 45, it can be inferred that heat generation within a lithium-ion cell is estimated based on the cumulative overpotential as well as the overall current. But, this is in contrast to Equations 39 and 40, where it is emphasised that depending on the time elapsed and the capacitance of a particular RC pair within an ECM, the currents would be different. This in turn implies that estimating the heat generated from different impedance elements separately might be prudent. However, this method (in Equation 46) has not been widely adopted in literature apart from [58].

$$Q_{gen} = I_{input}^2 \times R_O + I_{Pn}^2 \times R_{Pn} \quad (46)$$

Given that accurate estimation of heat generation within a lithium-ion cell is critical to accurate model estimation and a robust vehicular thermal management system [112,143]; the discrepancy between Equations 45b and 46 has not been explored in literature before and is identified as an existing gap in knowledge. The effect of an alternate method to capture battery heat generation and its effect on temperature estimation and model performance requires further investigation. This investigation is especially important at low temperatures, where the response of cells is substantially different to that at 25 ℃ [93].

2.3.3 Validation Methods for Equivalent Circuit Models

Equivalent circuit models (ECMs) are conventionally validated by comparing, for a duty cycle, the accuracy of the output voltage estimated by the model with cell voltage response obtained from the actual experiments [144]. This accuracy is generally reported on the basis of the 'Goodness-of-Fit' between the voltage estimated from the model and the voltage obtained experimentally. The Goodness-of-Fit usually describes how well the output voltage from the ECM fits the experimental voltage measured for a particular duty cycle, at specific operating conditions. Conventionally, the normalised root mean square error (RMSE) is employed as the metric for

comparing model accuracy. This value is either reported in millivolts (by battery modellers) or r-squared value (by statistical modellers) [101]. The lower the RMSE in millivolts or the higher the r-squared value, the more accurate the ECM. An illustrative example for ECM validation is given in Figure 26 [7].

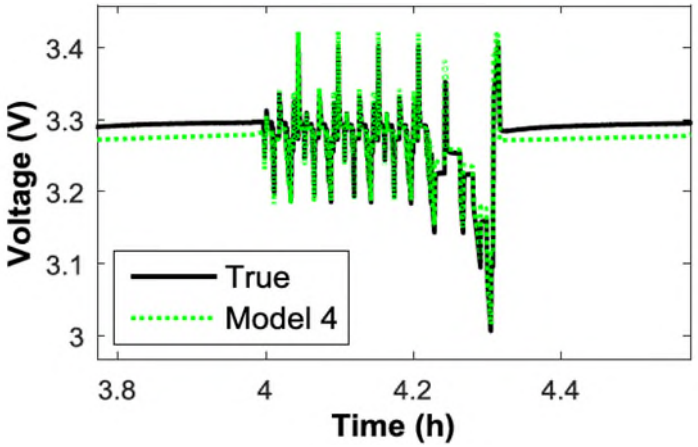

Figure 26. Illustrative Example of Validation for a 2nd order ECM with One-state Hysteresis for LFP cell against 1 New European Drive Cycle (NEDC) at 25 °C Ambient Temperature [7]

In early development of ECMs for lithium-ion cells, Liaw *et al.* used voltage data obtained from 0.04C and 1C continuous discharge duty cycles to validate their ECM [145]. This has been used by subsequent researchers to test the accuracy of the ECM developed. It is also used to decide the structure of the ECM in terms of number of RC networks via an iterative process [123]. Similarly, hybrid pulse tests that were used to obtain the parameterisation dataset for the ECMs were also employed to check the model accuracy. However, since these datasets were implicit in the ECM, validating the model against these datasets would render the validation process incomplete [123]. Hence, it was necessary to validate ECMs against new or unseen datasets.

When developing ECMs to be deployed in automotive systems, it is imperative that an ECM is validated against unseen duty cycles that depict real world drive cycles [7]. Thus, the research community utilised real-world drive cycles such as the Urban Dynamometer Driving Schedule (UDDS) and the New European Drive Cycle (NEDC) to dynamically excite the cells under investigation with variable current amplitudes and durations [7,123]. These drive cycles are widely used in the evaluation of ECM accuracy and SOC estimation of battery management systems. The NEDC was

developed in the 1970s from a theoretical driving profile and consists of four portions of urban driving style characterised by low speeds followed by a higher speed section [6,146].

In literature, either 1st or 2nd order ECM with hysteresis corrections have been considered as the best compromise between model accuracy and model complexity for the majority of lithium-ion cells [147,148]. Conclusions were made on the basis that beyond a certain accuracy, there were diminishingly small improvements for increasing model complexity. For example, He *et al.* and Hu *et al.* compared the model accuracy for various types of ECMs, including 0th, 1st and 2nd order models with/without hysteresis, for lithium-ion cells with NMC and LFP cathodes [123,147]. They compared the model accuracy on the basis of results obtained for the UDDS at different ambient temperatures between 45 and 10 °C, but no lower. The root mean squared error in voltage estimation was 5-15 mV. Similarly, Nejad *et al.* employed self-designed pulse tests and the NEDC legislative drive cycle, but extended the ambient temperature range down to 5 °C [7]. The self-designed pulse test was a sequence of charge/discharge pulses of varying magnitudes and durations and was used to parameterise the models.

It is widely accepted that the accuracy in output voltage estimation for ECMs for lithium-ion cells generally decreases with ambient temperature [7,58,144]. For example, in their modelling of cylindrical lithium-ion cells, Nejad *et al.* found that the RMSE in output voltage estimation for validation against the parameterisation data increased from 2 mV at 25 °C ambient temperature to about 8 mV at 5 °C ambient temperature. They ascribed the reduced accuracy of ECMs at low ambient temperatures to the inherent electrochemical processes within a lithium-ion cell being significantly slower. Thus, it becomes more difficult to model the underlying cell dynamics due to more distinct non-linear behaviour, leading to a larger modelling and SOC error [149].

In literature there is limited evidence of comparing ECM validation accuracy at ambient temperatures less than 5 °C, particularly in terms of optimal number of RC networks [59]. In [59], Nikolian *et al.* generated ECMs for lithium-ion cells between −5 and 45 °C for NMC, LFP and LTO chemistries. In all three chemistries, the

simulations performed at the lowest temperature (−5 ℃) had higher modelling error compared to at 25 ℃ when validated against the 'Worldwide harmonised Light duty Test Cycle' (WLTC). For example, for the 20 Ah lithium-ion cells with NMC cathode/graphite anode, the total root-mean-squared-error (RMSE) in voltage estimation increased from ~2% at 25 ℃ to ~4.5% at −5 ℃ (Figure 27). Nikolian *et al.* reasoned that this is related to the voltage behaviour of the cells at these temperatures being affected by the lower capacity value of the cell, and a greater degree of non-linearity combined with slow dynamics inside the cell. However, there remains much work to be done to understand the effect of temperature on model accuracy.

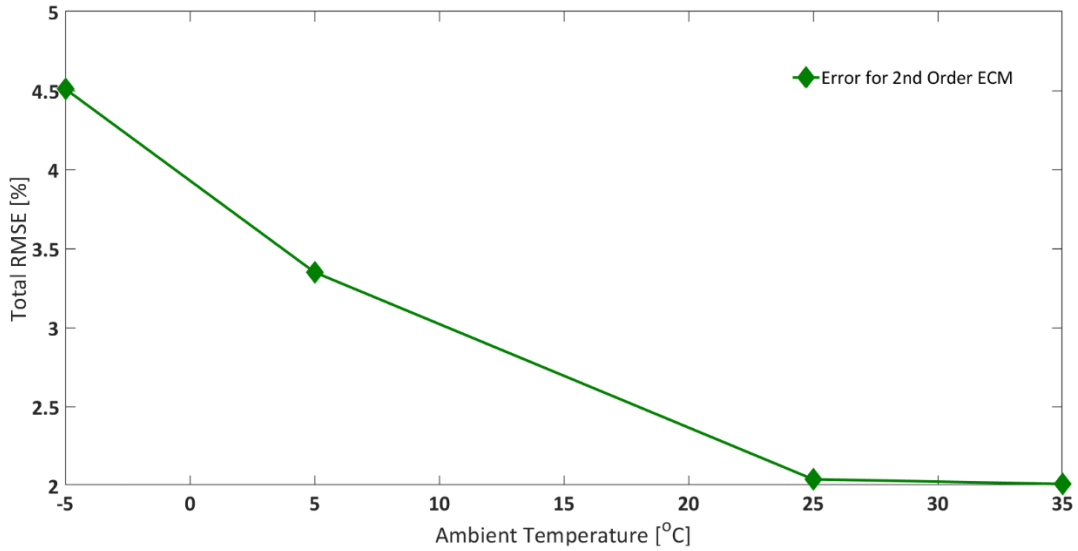

Figure 27. Effect of Ambient Temperature on Total RMSE in Voltage estimated from 2nd Order 'Thevenin' ECM for WLTC Drive Cycle (Adapted from [59])

2.3.4. Gaps in Knowledge: Identified Concerns with Characterisation for Battery Modelling at Low Temperatures

2.3.4.1 Issue with ECM Validation

As discussed in Section 2.2.2, scaled-down current profiles, derived from legislative drive cycles (NEDC, FTP75, etc.) have been used to obtain validation data for ECMs [7]. These profiles employ an arbitrary reference voltage (usually the nominal cell voltage presented in the manufacturers' datasheet) to ensure consistency in capacity throughput across varying operating conditions for a particular duty cycle [32,49]. As

shown in Figure 16, this method of scaling down vehicle level speed versus time profile to cell level current versus time profile (assuming a reference voltage) is known as testing via **current control** (IC). On the other hand, scaling down to a cell level power profile (considering dynamically changing cell voltage) is termed as **power control** (PC). The use of current control is prevalent in literature for a number of different types of investigations, such as validation of SOC/SOE algorithms or thermal models [56,91,150]. The use of power control (PC) to validate ECMs is important at lower temperatures where a combination of low operating voltages and higher operating currents are prevalent. This will ensure consistency in energy throughput across operating conditions which is comparable with real-world applications. Furthermore, based on the operating currents in PC, the heat generation rates will also be different from those calculated from IC. Furthermore, different operating currents, SOCs and temperatures will lead to different output voltage estimates. Although, in limited literature, power control is chosen over current control, either to investigate low temperature performance of the energy storage system (ESS) [83] or to quantify battery degradation [88], comparison between current control and power control approaches to obtaining data for ECM validation has not been explored in literature.

2.3.4.2 Issue with ECM Parameterisation

In operation, cells naturally heat up due to internal resistances. However, if battery testing for model parameterisation is conducted in a far-from-isothermal setup, the effect of current and temperature on discharge capacity can become convoluted, particularly at low temperatures. This is illustrated in Figure 28 for a typical SOC estimation algorithm based on extended coulomb counting.

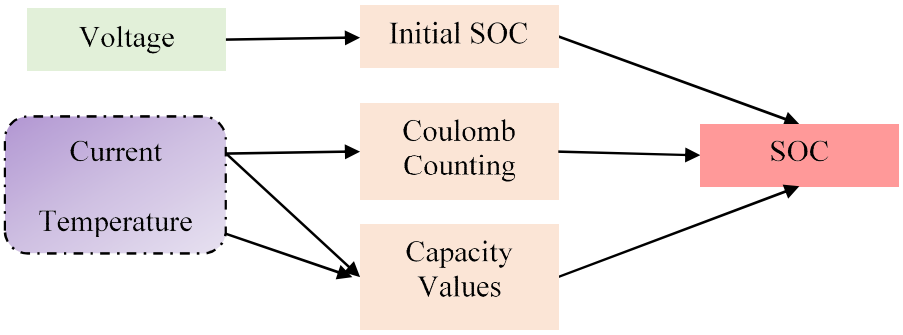

Figure 28. Typical Literature SOC Estimation Algorithm based on Coulomb Counting

It is possible that traditional (air) thermal control methods potentially lead to overestimation of battery SOC and thus, remaining driving range by inaccurately tracking usable capacity/energy characteristics. Research is required to develop a methodology to conduct close-to-isothermal experiments to prove whether this is the case. This will potentially improve tracking of usable capacity as a function of temperature and current (Figure 29). This would allow better correlation of usable battery capacity/energy with remaining driving range. A similar assessment can be conducted for SOE evolution as well.

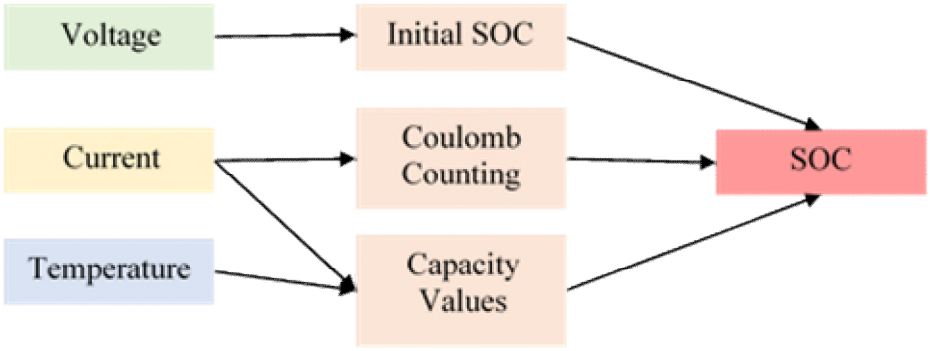

Figure 29. Proposed SOC Estimation Algorithm based on Coulomb Counting

Furthermore, if reversible heat generation is ignored, the total cell heat generation rate is presented as in Equation 45. As discussed in Chapter 2, at lower ambient temperatures, potential gradients occur due to slower charge transfer whereas, concentration gradients occur due to slower mass transport. This has physical basis in the characteristic times of the different internal cell processes. Thus, depending on the time elapsed and the current flowing through these resistors (R_p, R_{p1} and R_{p2}), the heat generated from each impedance element in the ECM would be different. The above suggests that 'separation of currents' should be considered as part of the thermal feedback subsystem of an ECM to ensure practical implementation.

2.4 Summary of Gaps in Knowledge and Research Question

In this chapter, literature related to lithium-ion battery characterisation and modelling for low operating temperatures was reviewed. A literature review on lithium-ion battery fundamentals, battery testing techniques and battery modelling (ECM) techniques contextualising low temperatures was undertaken. Based on existing

literature, the following knowledge gaps were identified in the methodology of experimental data generation for parameterising and validating ECMs operating at low temperatures:

1. Experiments to parameterise ECM for low temperature automotive applications (Section 2.2.6.1):

Battery characterisation is assumed to be isothermal for the duration of a particular experiment. Due to high cell internal resistances, the battery operating temperature changes substantially over the course of a duty cycle, particularly for large load currents. There is limited literature investigating how thermal boundary conditions during testing is an issue affecting battery testing for model development and how discrepancies due to far-from-isothermal testing can be resolved. This knowledge gap can be addressed by designing a novel experimental methodology aimed at providing close-to-isothermal control (by using immersed oil-based experimental setup) to better separate electrical and thermal phenomena while testing lithium-ion batteries at low ambient temperatures.

2. Experiments to validate ECM for applications operating at low temperatures (Section 2.3.4.1):

Current control is traditionally employed to obtain validation data from legislative drive cycles. This potentially leads to under-testing of lithium-ion cells at lower temperatures by underestimating the energy throughput and heat generation rates. There exists no literature contrasting the limitations of current control approach with the more realistic power control approach. This knowledge gap should be addressed by comparing both current control and power control and investigating their impact on battery performance characteristics. This will offer a standardised way forward in terms of model validation suitable for low temperature applications.

3. Improvements to parameterisation/validation methods on battery states evolution and model accuracy (Section 2.3.4.2):

Battery states and model accuracy are often compared on the basis of the modelling methods chosen or the algorithms employed. However, there is limited literature

comparing the effects of experimental parameterisation and validation methods and their origin on the model. For example, battery capacities at different temperatures and C-rates are used for SOC estimation algorithms, but the data itself is not evaluated to inspect for suitability. This knowledge gap should be addressed by quantifying the effect of choosing different parameterisation and validation methods on battery states' evolution and model accuracy.

In particular, the effect of close-to-isothermal parameterisation on battery states and model accuracy, and the effect of choosing separate currents (by inclusion of polarisation currents) for each impedance element to estimate heat generation rates on model accuracy and battery operating temperature should be investigated. This will evaluate the impact of choosing the dataset and overall, the benefits of a new experimental design and its propagation to the modelling stage.

To restate, the aim of this research is to propose a novel experimental methodology and alternative modelling approaches to improve the range estimation accuracy of EVs operating at low temperatures. Therefore, based on the gaps in research identified in this chapter, the research question is defined as, 'how to improve experimental evaluation methods and examine alternative approaches for parameterising and validating battery models for low temperature automotive applications?'

The research methodology adopted to answer the above research question is detailed in Chapter 3.

3. Research Methodology

In Chapter 2, the state-of-the-art related to low temperature performance evaluation and modelling methods for lithium-ion batteries was discussed. It was identified that gaps in knowledge exist related to how lithium-ion batteries are evaluated to parameterise and validate models at low temperatures. Based on these knowledge gaps, the research question for this thesis was identified, ‘how to improve experimental evaluation methods and examine alternative approaches for parameterising and validating battery models for low temperature automotive applications?’

This chapter outlines the methodology that has been adopted to logically answer this research question. Chapters 4-6 contain details of corresponding experimental setup, modelling methods, results and discussion.

3.1 Aim, Research Question and Objectives

The aim of this research is to propose a novel experimental methodology and alternative modelling approaches to improve the range estimation accuracy of EVs operating at low temperatures. Based on the gaps in knowledge, the research question identified was, ‘how to improve experimental evaluation methods and examine alternative approaches for parameterising and validating battery models for low temperature automotive applications?’ This will improve model performance and lead to better range estimation at low temperatures. To achieve this aim and to address the research question, the following research objectives were identified:

3.1.1 Objective I: Propose novel experimental methodology for improving the accuracy of parameterisation experiments at low temperatures

Capacity values at different temperatures and load currents are adopted by academic researchers and industry professionals to assess, or track, the usable performance of the battery. However, it was identified in Section 2.2.4 that these experiments are mostly performed within thermal chambers which maintain pre-set temperatures using

forced air convection. Although these setups claim to maintain isothermal test conditions, they rarely do so, as cell temperature deviates from the pre-set ambient temperature. In operation, cells naturally heat up. However, for model parameterisation, separation of electrical and thermal effects for a discharge cycle are imperative. Therefore, in this research, the following research tasks are proposed to improve the experimental method to correctly assess battery discharge capacity/energy:

1. Show that traditional (air-based) thermal control method leads to overestimation of capacity and energy performance at low temperatures and high discharge C-rates.
2. Design a novel experimental methodology to conduct close-to-isothermal experiments to track usable capacity.
3. Contrast performance characteristics obtained from traditional and the proposed thermal control methods to quantify benefits from close-to-isothermal experiments.

The outcomes of the above research tasks are discussed in Chapter 4.

3.1.2 Objective II: Using an equivalent circuit model, investigate the modelling performance of existing and improved low temperature parameterisation methods

Electrical equivalent circuit models (ECMs) are employed by researchers to model lithium-ion cell characteristics for current loads under different operating scenarios. An OCV versus SOC relationship is implemented to represent the lithium-ion cell in equilibrium conditions. The internal electrochemical processes are represented as ‘n’ number of resistors and capacitors, where ‘n’ depends on the complexity of the model chosen. Based on the time elapsed and the operating current, the current passing through these resistors and capacitors translates to an overpotential that is subtracted from the OCV to obtain the terminal voltage. This modelled voltage is then compared with the experimental voltage obtained for that operating current profile to evaluate the accuracy of the model.

To ensure accuracy in output voltage estimation, two aspects are very important: (a) collecting a robust dataset for parameterising model parameters and, (b) validating the model for real-world applications. To develop this model, the following research tasks are identified:

1. Assemble data obtained from galvanostatic discharge experiments, OCV versus SOC characterisation, and pulse power characterisation to parameterise the equivalent circuit models.
2. Use look-up tables and mathematical fitting to implement parameterisation data into an ECM developed in a commonly used battery modelling software, MATLAB/Simulink (Version: R2017b).

The justification regarding the experimental test matrix is given in Section 3.2. The modelling methods, including datasets to populate look-up tables and underlying mathematical equations are discussed in Chapter 5.

3.1.3 Objective III: Improve surface temperature and voltage error predictions through use of alternative modelling methods

It was identified in Section 2.3.4.1 that, using current control for drive cycle testing at cell level can be misleading particularly at low temperatures where the average operating voltage is lower than the nominal voltage. This results in variation in energy throughput for a particular drive cycle as operating conditions change. For example, if temperature and thus, operating voltages, are lower, the energy throughput is lower compared to that observed at a higher temperature.

It was highlighted in Section 2.3.4.2 that, using separate currents instead of a common Ohmic current for the various impedance elements considered as part of a thermal feedback could affect model performance, particularly at low temperatures, where there exists greater electro-thermal coupling of battery phenomena.

Therefore, the following research tasks are proposed to determine the best approaches to validating lithium-ion cells' performance against legislative drive cycles and to estimating model heat generation:

1. Using experimental data, contrast power control against current control on the basis of capacity and energy throughputs, and cell voltage evolution to investigate whether power control is the more realistic approach for testing lithium-ion cells for scaled-down realistic drive cycles.
2. Implement thermal feedback model to dynamically update ECM parameters (Compare between choosing common (Ohmic) current or separate polarisation currents for each impedance element).

The outcomes of the above research tasks are discussed in Chapter 5. The justification regarding the validation dataset and drive cycle choice is given in Section 3.2.

3.1.4 Objective IV: Quantify improvements to model performance and battery state estimation based on novel experimentally obtained model parameterisation data

The reliability of range estimation largely depends on the accuracy of the battery's underlying state estimators: state-of-charge and state-of-energy. This is affected by accuracy of the models embedded in the battery management system. The performance of these models fundamentally depends on experimentally obtained parameterisation and validation data (Section 2.3.4). To investigate the effect of improvements (Objectives I-III) undertaken, it is imperative that the effect on battery state evolution and model accuracy is quantified. This will allow direct correlation of quality of test data and model performance. The following research tasks are proposed to examine the effect of changes to battery evaluation methods for modelling parameterisation and validation for lithium-ion cells operating at low temperatures:

1. Quantify and contrast the effect of choosing between air-based parameterisation data and new isothermal parameterisation data on battery state (SOC and SOE) evolution.
2. Quantify the effect of choosing isothermal parameterisation data over air-based parameterisation data in terms of model accuracy and model order.
3. Quantify and contrast the effect of choosing separate current rather than common current for each ECM impedance element on model performance in terms of accuracy in surface temperature and terminal voltage estimates.

The outcomes of the above research tasks are discussed in Chapter 6.

3.2 Research Decisions

In this section, the justifications regarding the experimental test matrix chosen for developing both parameterisation and validation datasets are given. Furthermore, the justification regarding choosing the reference validation drive cycle is also given.

3.2.1 Experimental Test Matrix

In this thesis, low ambient temperature is defined as any temperature less than 10 °C. Thus, for parameterisation, the ambient temperatures chosen were −20, −10, 0 and 25 °C similar to other literature [40,58]. The upper limit of 25 °C was chosen as it is a reference ambient temperature widely used by researchers. The lower limit of −20 °C was chosen as it is representative of harsh winter conditions and is generally the lower operating limit for typical commercially available lithium-ion batteries.

For validation, the ambient temperatures were chosen as −15, −5, 5 and 25 °C. The validation temperatures were chosen as such as they are between the parameterisation temperatures above [151]. Here, the validation temperature points lie within the extremes of the parameterisation temperature points. Finally, 25 °C was chosen as a reference validation temperature.

The parameterisation SOC points chosen were 20%, 50% and 80% to represent real-world operating conditions for contemporary battery electric vehicles. The validation SOC set point chosen was 65% SOC to ensure that the SOC during the entire drive cycle lay above the 20% SOC cut-off. This is also based on the SOC set-points recommended in the latest IEC 62660-1 [103].

Correspondingly, C-rates higher than the nominal C-rate for the cell (which is C-rates higher than 0.5C) are considered as high currents, and C-rates lower than 0.3C are considered as low currents [60] for that particular cell. In this study, three parameterisation C-rates are considered, 0.25C, 1C and 3C. While 0.25C is representative of a low C-rate, 1C is the reference C-rate for the cell. 3C is considered

representative of a high C-rate as that is the highest current at which the cells were able to discharge at −20 ℃ ambient temperature.

To obtain pulse power data, more pulse currents, such as 0.5C, 2C, etc. were considered as they added to the fidelity of the model and did not require disproportionate experimental efforts. The full list of pulses at different temperatures and SOCs is given in Table 6 in Section 4.1.2.3. Note, for the continuous discharge capacity experiments, other C-rates (apart from 0.25C, 1C and 3C) were not considered due to the additional time required to charge the cell every time at 25 ℃. The pulse length chosen was 10 s in accordance with the latest IEC 62660-1 test standard [103]. Note, further details for the experimental methods chosen are given in Section 4.1.

3.2.2 Drive Cycle Choice

The New European Driving Cycle (NEDC), commonly chosen to validate ECMs, is a modal drive cycle part of the EU standards [7,34]. However, the NEDC has been criticised for being unrealistic as it lacks acceleration/deceleration dynamics as compared to transient drive cycles [152,153]. The US06, a supplemental drive cycle, was designed to address the lack of aggressive high-speed driving in the other drive cycles in US Environmental Protection Agency standards, mainly the FTP75. The US06 is one of the more aggressive drive-cycles with a top speed of 35.7 m/s and an average speed of 25.3 m/s (Figure 30).

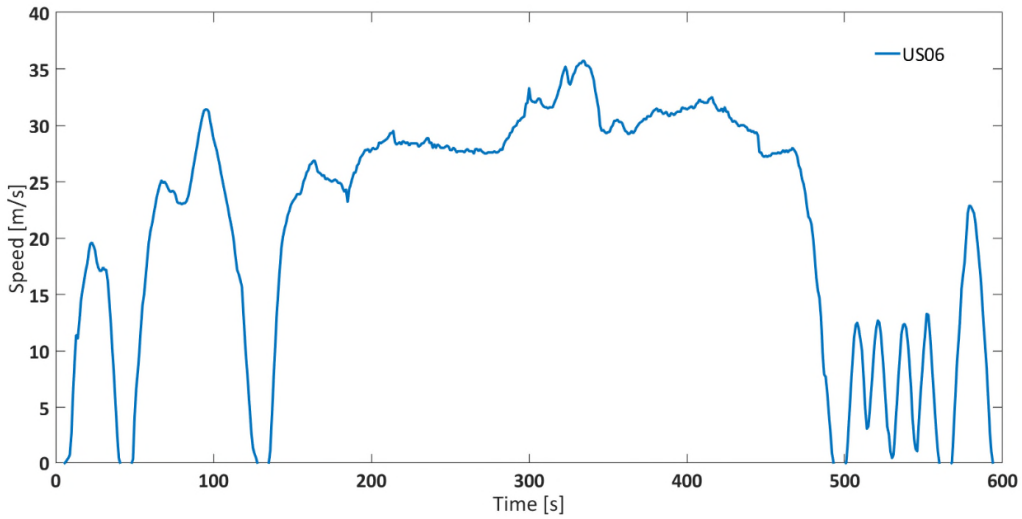

Figure 30. Vehicle Level Speed Time Profile for US06 Legislative Drive Cycle

The US06 features frequent load changes with considerable acceleration and deceleration rates. The maximum acceleration is 3.7 m/s^2 and the maximum deceleration is 3.1 m/s^2. Hence, it is an ideal candidate to analyse the impact of high current at lower ambient temperatures for real-world driving conditions [32,49,83]. The total duration was 600 s. Further, the amount of acceleration and braking events in the US06 is the highest amongst all highway driving cycles [49]. The NEDC, has maximum acceleration and deceleration rates of 1.1 m/s^2 and 1.4 m/s^2, respectively. However, the US06 has maximum acceleration and deceleration rates of 3.7 m/s^2 and 3.1 m/s^2, respectively. Hence, if the cells can provide sufficient power for the US06, they would be able to deliver over other urban/rural driving conditions as well [83].

To obtain validation data for the models developed as part of this research the US06 drive cycle was employed. To ensure that the drive cycle caused the cells to discharge below 50%, to prevent discharge below 20% and to cover both SOC parameterisation spaces (80 to 50% and 50 to 20%), two back-to-back US06 drive cycles (2xUS06) were considered for model validation.

3.2.3 Modelling Framework

For all the ECMs developed in this thesis, the inputs are experimental current, experimental power and experimental surface temperature. The outputs are modelled terminal voltage and surface temperature. The details of the ECMs developed are presented in Chapter 5 and the validation methodology is given in Chapter 6. In this thesis, 1st and 2nd order ECMs were chosen for investigation at a modelling stage. These two model structures were chosen as their accuracy was the best found in literature and they were commonly employed in literature to investigate model performance [7,123,154]. Experimental parameterisation and validation data is obtained for 3 cell samples. Three cells were used to ensure statistical significance, as well as to account for cell-to-cell variations [155]. Before feeding into the different equivalent circuit models, the experimental values are averaged.

3.3 Chapter Summary

The aim of this thesis is to propose a novel experimental methodology and alternative modelling approaches to improve the range estimation accuracy of EVs at low ambient temperatures. In particular, the following research question is defined, ‘how to improve experimental evaluation methods and examine alternative approaches for parameterising and validating battery models for low temperature automotive applications?’

In this chapter, the research objectives to achieve this were defined, the flow of research undertaken was presented, and the various research decisions taken were detailed.

4. Development of An Experimental Method to Investigate Differences between Air and Oil Characterisation for Lithium-ion Cells at Low Temperatures

This chapter offers a novel methodology to conduct experiments under isothermal conditions that accurately quantifies usable capacity/energy performance as a function of temperature and current (Objective I). This is achieved by conducting experiments within an immersed oil bath with direct liquid cooling to allow isothermal control. Results will be compared with that obtained from traditional air-based thermal control methods. A key contribution of this chapter is to show that traditional air-based thermal control methods inaccurately assess usable capacity/energy characteristics, potentially leading to overestimation of remaining driving range. Using an oil-based method is expected to allow better correlation of usable battery capacity/energy with remaining driving range. The modelling validation will follow in Chapters 5 and 6.

The chapter is structured as follows. In Section 4.1, the experimental methods employed for this study are detailed including the experimental setup and test matrix chosen. In Section 4.2, the results are presented and discussed to support the hypothesis that close-to-isothermal parameterisation is important for accurate assessment of lithium-ion battery characteristics, particularly at low ambient temperatures. Finally, in Section 4.3, the key findings of this chapter are summarised.

4.1 Experimental Test Design

For this study, three 40 Ah lithium-ion pouch cells were procured from Xalt Energy. The cells contained a Nickel-Manganese-Cobalt (NMC) cathode and graphite anode (Table 4). The cells were chosen based on properties such as capacity, form factor and chemistry, making them comparable to cells used in popular passenger battery electric vehicles (BEVs) such as the Nissan Leaf [156]. The cells had a 3.7 V nominal voltage and a discharge temperature range between −20 to 60 °C. The composition of the electrolyte was not made available on request to the manufacturer. However,

generally, the electrolyte is expected to include 1.0–1.2 mol $LiPF_6$ combined with a blend of 2–3 organic solvents, such as ethylene carbonate (EC), dimethyl carbonate (DMC) and diethyl carbonate (DEC).

Table 4. Performance characteristics of 40 Ah lithium-ion pouch cell.

Characteristic	**Range/Value**
Supplier	XALT Energy
Chemistry	NMC/Graphite
Capacity, Ah (Nominally Rated at 0.5C)	40
Nominal Voltage, V	3.7
Energy, Wh (Nominally Rated at 0.5C)	148
Weight, kg	0.97
Specific Energy, Wh/kg	153
Volumetric Energy Density, Wh/L	350
Direct Current Resistance (10 s at 50% SOC), mΩ	1.35
Max C-rate Continuous at 25 ℃ (Charge)	3C
Max C-rate Continuous at 25 ℃ (Discharge)	8C
Max C-rate Pulse at 25 ℃ (Discharge) (10 s)	10C
Peak Power, kW	2.6
Specific Power, W/kg	2600
Volumetric Power Density, W/L	5900
Upper Voltage Limit, V	4.2
Lower Voltage Limit, V	2.7
Charge Temperature Range, °C	0 to 45
Discharge Temperature Range, °C	−20 to 60

As part of the oil-based active thermal management system (immersed oil bath with direct liquid cooling), a low-viscosity silicone oil (Kryo 95) with excellent dielectric properties was employed (Table 5).

Table 5. Properties of Kryo-95 silicone oil for low temperature applications.

Characteristic	**Range/Value**
Operating Temperature Range, °C	−95 to 60
Chemical Characterisation	Polydimethylsiloxane
Colour	Colourless
Kinematic Viscosity, mm^2/s (at 20 °C)	1.6
Density, kg/m^3 (at 20 °C)	855
Specific Heat Capacity, J/kgK	~1800
Pour Point, °C	≤ −111
Boiling Point, °C	≥ 190

The oil is insoluble in water and fluid properties such as specific heat capacity, kinematic viscosity and density were advertised to be consistent across operating temperature range (−20 to 60 °C) of the experiments. An oil-based thermal control setup was employed rather than water/glycol based because the specific heat capacity of Kryo-95 was higher compared to that of water (Table 3 and Table 5). Further, by using dielectric oil rather than a water/glycol mixture, any potential of an external short-circuit and related safety hazards were eliminated.

4.1.1 Experimental Setup

All experiments were conducted in an Espec Platinous J Series thermal chamber with spatial temperature accuracy of ±0.3 °C. The cells were cycled using a Maccor Series 4000 cell cycler and relevant cycling control software was employed. To ensure that there was no free air flow from outside the chamber into the chamber, any gaps (due to current carrying cables, etc.) were sealed using thermally-insulating putty. To measure the surface temperature of the cells, hermetically sealed T-type thermocouples were used with ±0.5 °C accuracy. At each experimental condition, measurements from three cells were used to ensure statistical significance, as well as to account for cell-to-cell variations [155].

A schematic of the immersed oil bath with a cooling system is given in Figure 31. A Lauda Pro unit (model number: RP 245 E) was employed as the chilling system, which uses a Pt-100 thermocouple placed inside the oil bath (close to the cells) to control the inlet coolant temperature (Figure 31e). The Lauda unit had a working temperature range of −45 to 200 °C and a maximum cooling capability of 2.5 kW across the temperature range. The cells were placed within the box (with an open lid) and the entire arrangement was placed inside the thermal chamber (Figure 31a–h). A cell cycler channel was connected to each cell using a standard 10mm diameter cable, and a T-type thermocouple was placed on the geometric centre of the cell surface (according to latest IEC 62660-1 standard) using a perspex block and cable tie. This setup was tested for thermal mass distribution and temperature homogeneity within the box. For direct liquid cooling with an immersed oil rig, the thermal gradients across the cell surface are expected to be miminal, given that the cells and oil bath (~20 ℓ) were controlled at the ambient temperature for 4 h before any charge/discharge

operation, and the cooling capability of the Lauda unit is 2.5 kW. Note that, for 'air cooling' experiments, the Lauda unit was switched-off and the oil bath was emptied and the box removed to allow free flow of air around the cells (Figure 32 a & b).

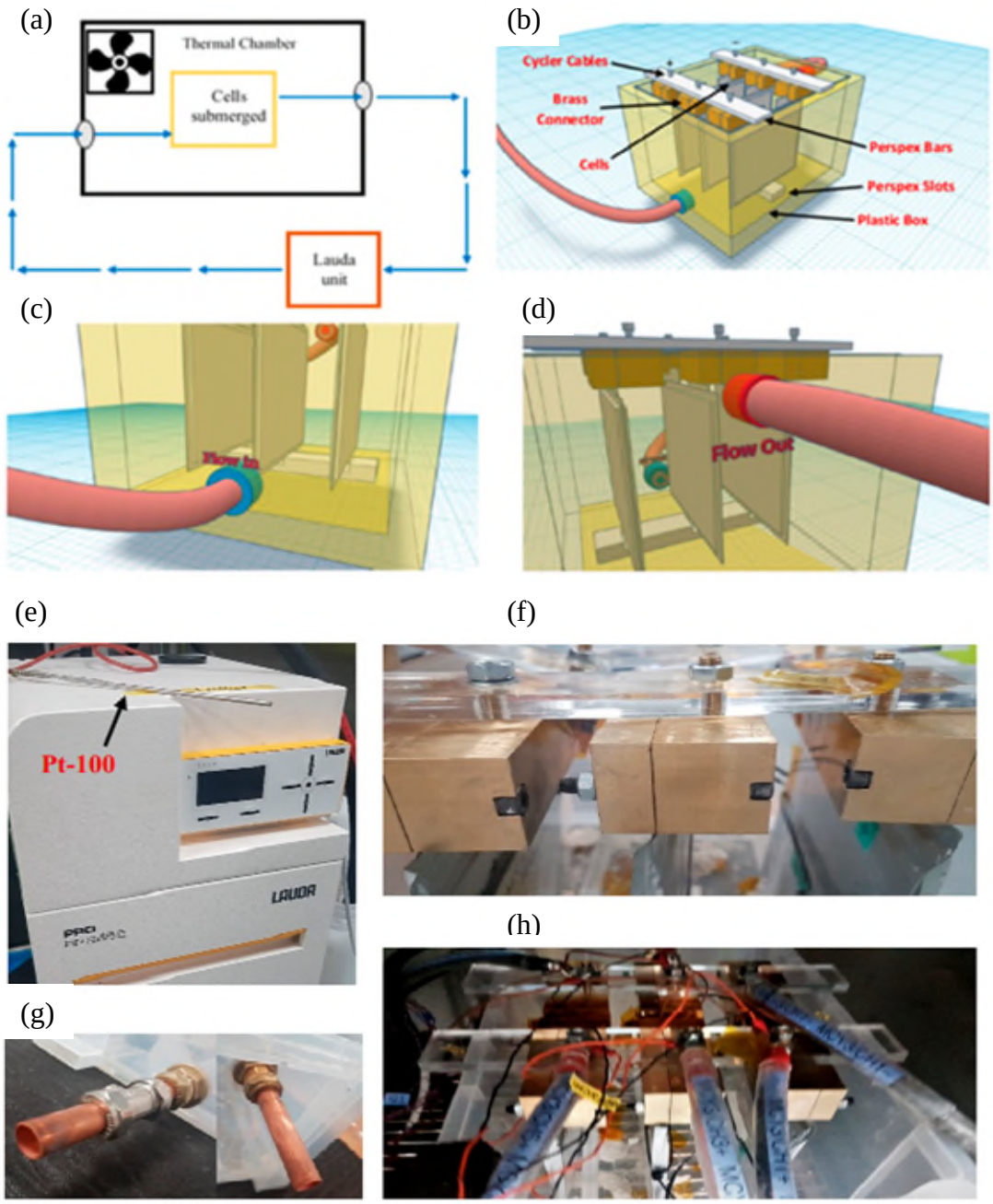

Figure 31. Oil-based Experimental Setup: (a) Schematic representation of oil based thermal control system, (b) Cooling configuration for oil based immersion bath with cells connected, (c & d) Coolant inlet and outlet for connections from thermal control unit, respectively, (e) Lauda Pro RP 245E used for this study and Pt-100 unit, (f) Cells connected in box using brass blocks and Perspex bars, (g) Pipework for box (left: inlet & right: outlet) and (h) Cells connected inside box within thermal chamber.

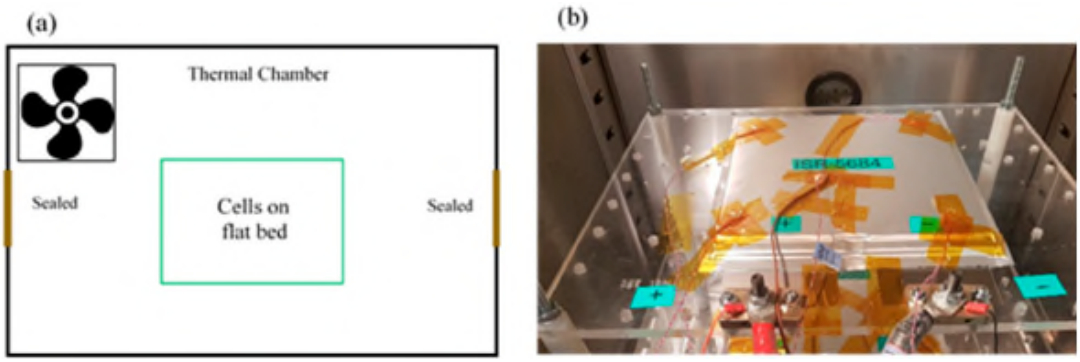

Figure 32. Air-based Experimental Setup: (a) Schematic representation of air based thermal control system, and (b) Traditional flat-bed test setup in forced air based thermal chamber.

4.1.2 Experimental Methods

4.1.2.1 Galvanostatic Cycling Performance

Galvanostatic discharge cycles were performed at different ambient temperatures for various discharge C-rates. As part of these galvanostatic tests, the ambient temperatures considered were −20, −10, 0 and 25 °C. The discharge C-rates considered were 0.25C, 1C and 3C. This suite of tests was performed for both ‘air-based’ and ‘oil-based’ cooling cases. Between each discharge test, the cells were charged at 25 °C ambient temperature using the Constant Current Constant Voltage (CCCV) protocol (0.5C charge current to 4.2 V, where the cells were held until current reduced to 0.05C). This was done to ensure that the cells were fully charged at the same level at the same temperature, 25 °C, before conducting low temperature discharge. This is important because the cells are not being tested for real-world usage, but are characterised in close-to-isothermal lab conditions to improve applicability of the subsequent models in the real world.

4.1.2.2 Open Circuit Voltage (OCV) vs State-of-Charge (SOC) Characterisation

To obtain the OCV-SOC relationship of the cells, the cells were charged using the CCCV protocol with a C-rate of 0.5C, to a maximum voltage of 4.2 V and a 0.05C cut-off. Then, the cells were discharged using 1C until 4% of the rated cell capacity (40 Ah) was discharged. Then, the cells were at rest for 4 h and the voltage recorded.

After this, the 4% discharge step and 4 h rest period regime was repeated until the cells reached the 2.7 V cut-off. A similar process was used to obtain the charge OCV-SOC relationship of the cells. The above technique (GITT) was employed to obtain OCV-SOC relationship at 25 ℃ only as this relationship has negligible dependence on temperature [157]. However, pseudo-OCV measurements were avoided as they can change particularly at low temperatures due to increased cell overpotentials making any direct comparison difficult (Section 2.2.5).

4.1.2.3 Pulse Power Characterisation

To map the power capability of the cells with respect to SOC, ambient temperature and current magnitude, the cells were subjected to 10 s charge/discharge current pulses of varying amplitudes (Table 6). The charge and discharge pulse amplitudes were chosen to ensure that at least 3 pulses were met at a particular SOC and ambient temperature.

Table 6. Test Matrix for Pulse Power Characterisation of Lithium-ion Pouch Cell

Ambient Temperature [°C]	SOC [%]	Charge Pulse C-rates (−)	Discharge Pulse C-rates (+)
−20, −10, 0 & 25	20, 50 & 80	0.25C, 0.5C, 0.75C, 1C, 1.5C & 2C	0.25C, 0.5C, 0.75C, 1C, 1.5C, 2.0C & 3C

Following on from Section 3.2.1, discharge pulses higher than 3C were avoided as the cells were unable to deliver higher currents for 10 s at any of the SOCs at the lower ambient temperatures. Charge pulses higher than 2C were avoided for the same reason. This is discussed further in Section 4.2.3 and then Section 5.1.3. The SOCs chosen for these tests were 20%, 50% and 80% as this is the usual SOC operating window for conventional BEVs and PHEVs [60]. Note, discharge current is positive.

The experimental flow followed in this research is detailed in Figure 33.

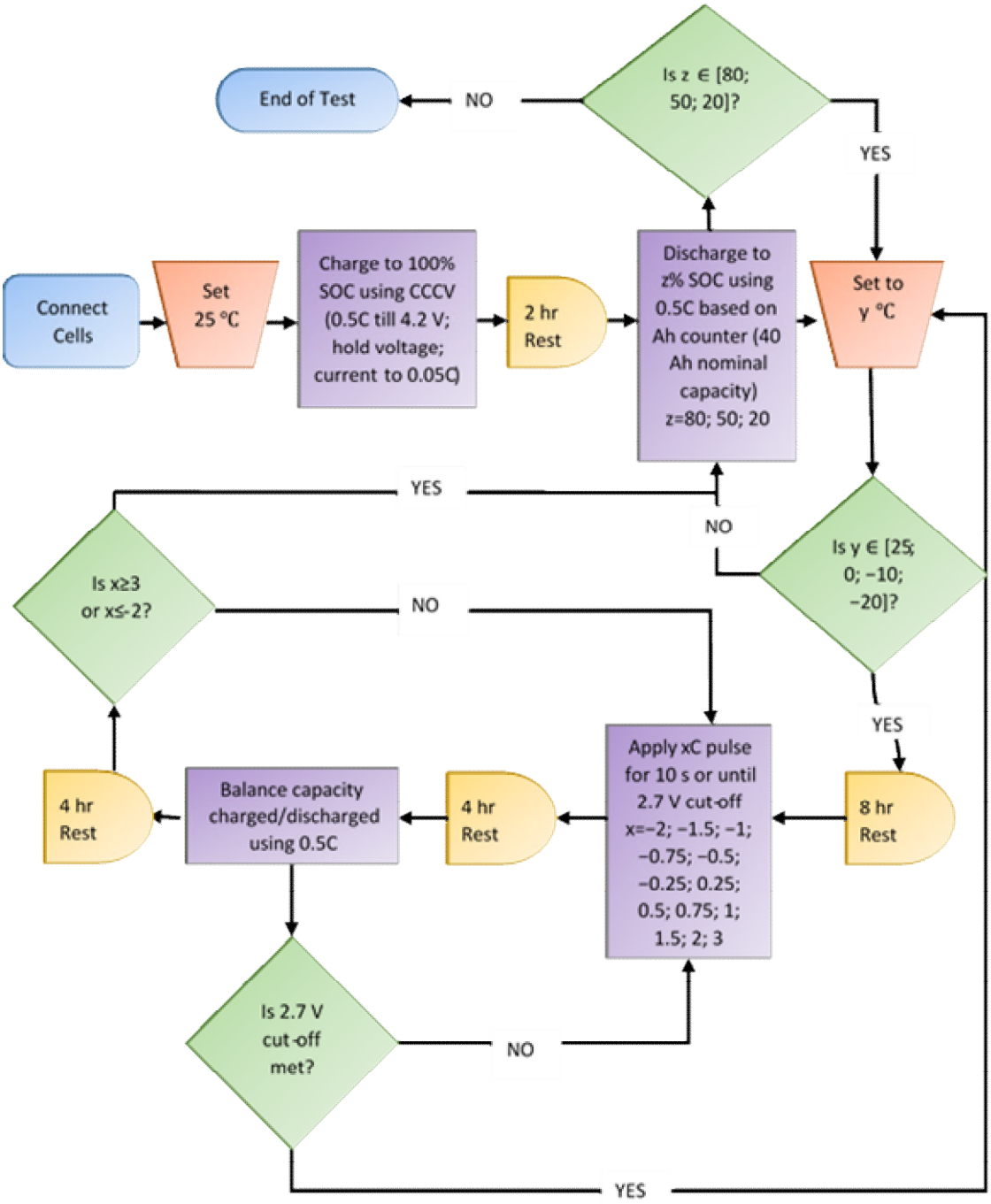

Figure 33. Flow chart for Pulse Power Characterisation at Different SOCs and Ambient Temperatures for Various 10 s Charge/Discharge Pulses

4.2 Results and Discussion

Table 7 presents the capacity test results for the air-based parameterisation condition. Capacity measured at a particular discharge rate decreased with temperature, and cell

surface temperature was higher at lower temperature, as expected [58,65,71]. At 25 °C both capacity and total energy discharged decreased with discharge rate. In contrast, capacity increased at lower temperatures, e.g. at −20 °C capacity increased by 0.9 % and 8.8 % at 1C and 3C, compared to 0.25C. This is directly linked to the temperature rise of the cell. For example, at −20 °C as discharge current increased from 0.25C to 3C, the temperature rise changed from 4.7 °C to 30.7 °C with respect to the ambient temperature. This implies that the capacity/energy performance cannot just be ascribed to the starting ambient temperature.

Although cell capacity takes into account the change in lithium concentration in the electrode's active material, it does not consider the energy used to change the concentration. The energy delivered is the energy that is transferred to an external load when the cell is being discharged. Thus, depending upon the cell voltage, the energy delivered can be different for a particular capacity (Ah) discharged. As shown in Table 5, this is the case at 0 °C ambient temperature, where discharge capacity increased as discharge current increased from 1C to 3C, but the discharge energy decreased. This implies that the effect of internal heat generation is not enough to affect the voltage as much as it affects the cell overpotential. That is, while the discharge duration is increased, the voltage at which this increase takes place is lower for 3C compared to 1C.

Table 7. Discharge characteristics for different C-rates at different ambient temperatures for 'air cooling' test cases

Ambient Temperature		**−20 °C**	**−10 °C**	**0 °C**	**25 °C**
Capacity [Ah]	0.25C	31.9±0.7	33.2±0.9	38.4±0.7	42.3±0.2
	1C	32.2±0.9	34.2±0.9	36.4±0.8	40.6±0.2
	3C	34.7±0.9	36.3±0.8	37.3±0.7	39.5±0.4
Energy [Wh]	0.25C	108.9±2.0	113.2±2.6	138.7±2.1	156.4±0.5
	1C	105.4±2.7	115.8±2.7	126.9±2.4	148.0±0.5
	3C	109.9±2.8	118.0±2.4	124.5±2.1	140.2±1.1
Surface Temperature Rise [°C]	0.25C	4.7±0.1	2.3±0.8	2.4±0.3	1.4±0.0
	1C	15.1±1.8	11.4±2.0	9.1±1.3	4.4±0.1
	3C	30.7±4.1	26.8±3.4	22.9±3.2	12.0±0.7

4.2.1 Comparison between Air and Oil based Thermal Control System for Low Temperatures and High Load Currents

Table 8 presents the capacity test results for the oil cooling method. Conducting experiments using an oil based thermal control system makes a substantial difference to the discharge capacity of the cell compared to air control in a thermal chamber.

Table 8. Discharge characteristics for different C-rates at different ambient temperatures for 'oil cooling' test cases

Oil Bath Temperature [°C]		**−20 °C**	**−10 °C**	**0 °C**	**25 °C**
Capacity [Ah]	0.25C	30.7 ± 0.9	31.9±0.9	38.2±0.6	41.7±0.3
	1C	24.6±0.8	31.4±0.9	34.1±0.8	40.3±0.5
	3C	13.3±0.4	24.8±0.9	30.5±0.9	39.2±0.2
Energy [Wh]	0.25C	102.6 ± 2.7	109.4±2.5	138.1±2.0	153.7±1.0
	1C	75.7±2.5	103.8±2.5	117.0±2.3	145.9±1.6
	3C	38.0±1.2	75.7±2.8	101.6±2.6	136.7±1.8
Surface Temperature Rise [°C]	0.25C	1.2 ± 0.5	1.6±0.4	1.8±0.3	0.8±0.1
	1C	5.7±0.1	4.4±0.4	2.8±0.3	1.7±0.5
	3C	10.1±0.4	8.0±0.4	3.3±0.9	2.4±0.1

Figure 34 shows 1C discharge curves at −20 °C for both air and oil cooled methods. The air cooling method produced 31.7% higher capacity (39.2% higher energy) than when employing active thermal management (oil cooled). This implies that battery heat generation is substantially affecting cell discharge behaviour at −20 °C ambient temperature. This is reflected in the voltage profiles as well, which is the cause for higher percentage of total energy. For the same discharge current, the voltage for the oil-based case decreased much faster than for the air-based cooling case. The counterintuitive increase in cell voltage observed for the air cooling case, which was also reported in previous research [82] is not seen for the oil cooling case, as it is likely related to the temperature increase of the cell.

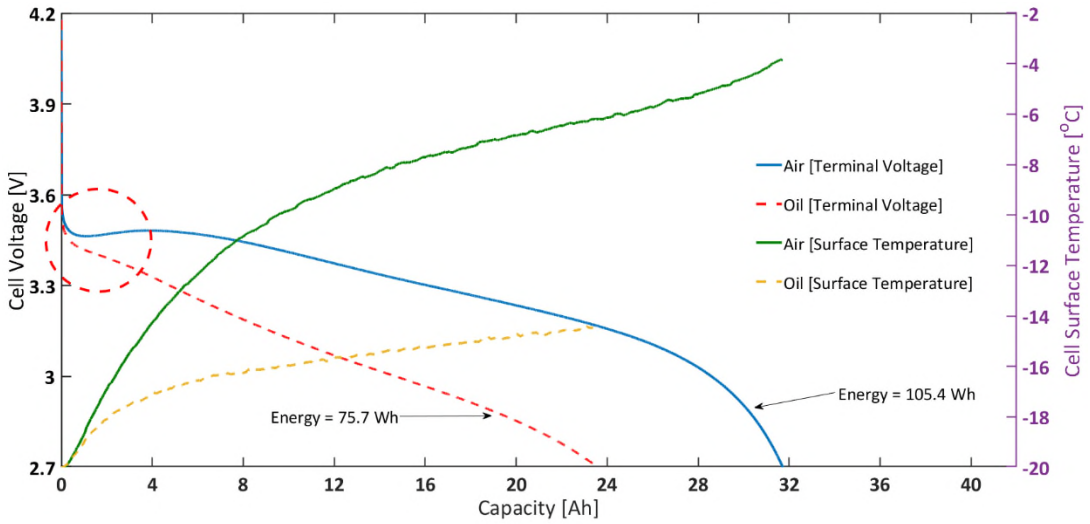

Figure 34. At −20 °C Ambient Temperature: Capacity vs Voltage for 1C constant current discharge (left) and cell surface temperature for the same test (right) (Note: results are reported in Figure for 1 cell, results for 3 cells with standard deviation reported in Table 7 and Table 8 above)

As also shown in Figure 34 for the same test, the final surface temperature for the 'air cooling' case is −3.9 °C, considerably higher than the −14.4 °C measured for the 'oil cooling' case. Similarly, the average surface temperature for the air-based case was −7.7 °C compared to −16 °C for the oil-based case. Note that, even for the oil cooling case, there is a temperature rise seen during the discharge cycle, indicating it is also not completely adiabatic. This is likely due to the limited cooling capability of the oil-based immersion rig; this is further restricted by the performance of the Lauda unit at −20 °C and below. This is possibly complicated by the decreased heat capacity, increased viscosity and decreased viscosity of Kryo-95 in such conditions; although the oil is rated for use till −95 °C. Therefore, the difference in capacity seen will be higher when the surface temperature is controlled exactly at the ambient temperature. The shape of temperature change, i.e., a sharp increase at the beginning and slower increase for remaining discharge duration is likely due to the change of resistance with temperature and SOC.

4.2.2 Implications of Open Circuit Voltage Behaviour

Based on Section 4.1.2.3, to investigate the effect of low ambient temperature induced cell overpotential, the OCV-SOC discharge relationship of the cells was included in the comparison. This experiment was conducted only at 25 ℃ as there is expected to be a minimal effect of ambient temperature on OCV-SOC relationship [58]. As shown in Figure 35, at a particular SOC, there is a distinction between the OCVs for charge and discharge. This difference is presented as the OCV hysteresis in Figure 35: inset.

Similar to [116], voltage hysteresis is defined as the difference between charge OCV and discharge OCV at a particular SOC. The hysteresis in a cell is due to the possibility of different thermodynamic equilibria at the same stoichiometric lithium content [116,158]. This means that depending upon whether the cell is charging or discharging, the electrodes could be at different potentials even though lithium content is identical and thus, the cell voltage will be different. For example, at 30% SOC, the charge OCV was 3.639 V, the discharge OCV was 3.614 V and the voltage hysteresis was approximately 25 mV. The OCV hysteresis evolution with SOC at 25 °C ambient temperature was comparable to other literature employing lithium-ion cells of similar chemistry and capacity [116,159].

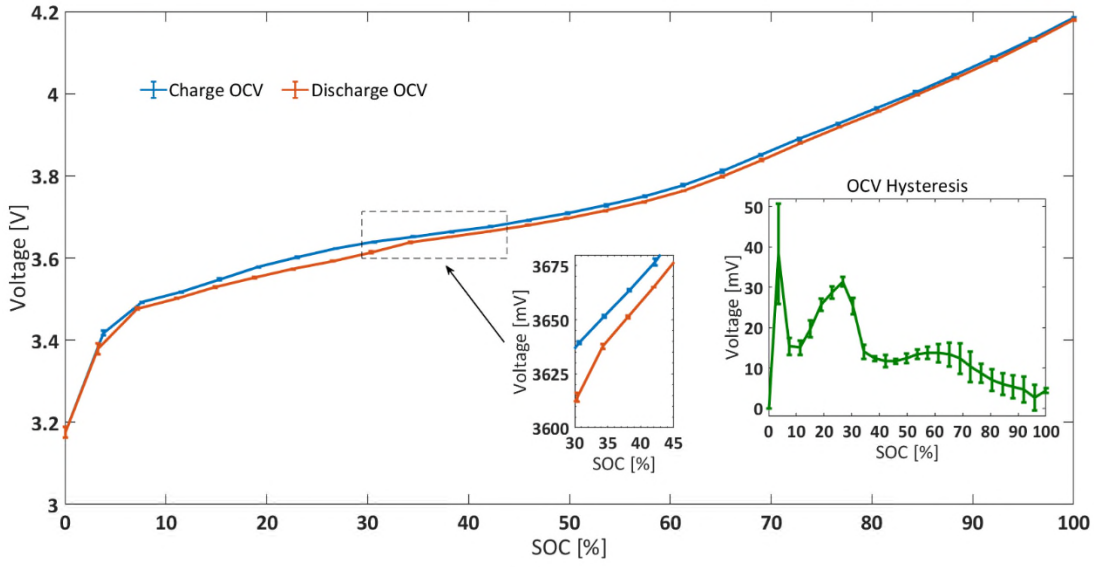

Figure 35. Experimental OCV versus SOC relationship at 25 °C Ambient Temperature at 4% SOC Step Change (Inset: Evolution of OCV Hysteresis versus SOC)

To validate the effect of overpotential for both cases (‘air cooling’ and ‘oil cooling’ parameterisation), after discharge at the low ambient temperature was terminated, the cells were brought up to 25 °C ambient temperature and then discharged with a nominal 0.10C constant discharge current. This is shown in Figure 36 and is termed as the ‘residual capacity’ [131]. To investigate the effect of low ambient temperature induced cell overpotential, the OCV-SOC discharge relationship of the cells was also included in the comparison. While the residual capacity for the air-based cooling case was 9.8 Ah, the corresponding value for the oil-based cooling case was 18.0 Ah. This aggregates to a total capacity discharged of 41.7 Ah and 41.8 Ah, respectively. Furthermore, the total capacity discharged for the OCV case was similar (41.7 Ah). This further shows that the air-based method includes more contributions from higher temperatures compared to the oil-based method.

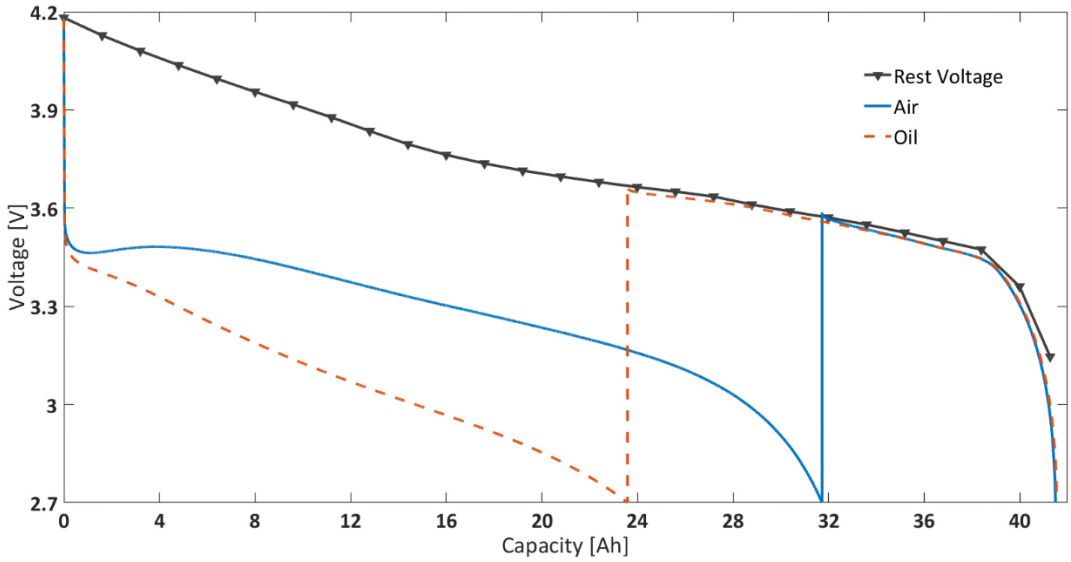

Figure 36. Comparison of Discharge Characteristics for 1C at −20 °C Ambient Temperature

4.2.3 Implications of Pulse Power Characterisation

DC resistance was measured using 1C discharge pulses of 10 sec at 20%, 50% and 80% SOC, at −20, −10, 0 and 25 °C. The 10 s DC resistances (DCR) are illustrated in Figure 37. From an average of 1.8 mΩ at 25 °C to 21.7 mΩ at −20 °C, DCR increased with decreasing ambient temperature because of higher overpotentials induced due to

charge transfer, lower ionic conductivity and sluggish diffusion in the electrode active material [58,93].

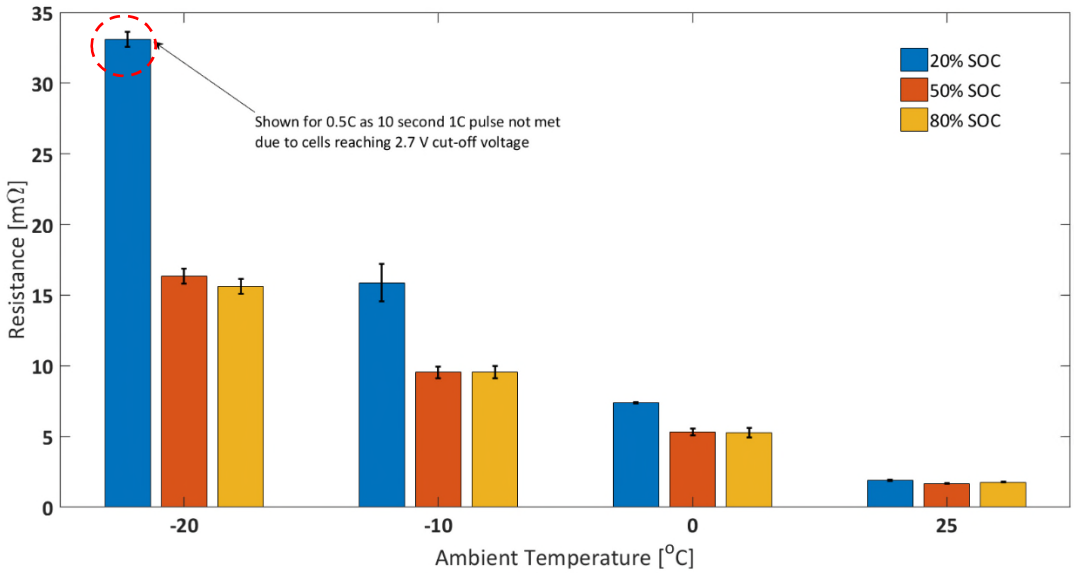

Figure 37. Effect of Temperature and SOC on DC Resistance for 1C Discharge Pulse

The DCR is also not expected to remain constant over the SOC range tested. In Figure 38, for 1C discharge pulse, it is shown that DCR remains largely independent of SOC at 25 °C. The mean SOC is around 1.8 mΩ and the standard deviation across SOCs as a percentage of the mean is 5.7%. However, at −20 °C, the mean SOC is 21.7 mΩ and the standard deviation across SOCs as a percentage of the mean increases to 45.6%.

Furthermore, as ambient temperature decreases, the DCR tends to increase as SOC decreases. This is because when SOC decreases, the cathode is becoming lithiated and the anode is becoming de-lithiated. This causes more pronounced potential and concentration gradients to be induced as active material in the anode is depleting whereas the cathode is becoming congested. As SOC decreases, electrode limitations become pronounced earlier, in particular as temperature decreases. This is demonstrated by DCR for discharge pulses at −20 °C for 20% SOC, where the 1C pulse is not met by the cells as they reach the 2.7 V minimum cut-off voltage (denoted by red circles in Figure 37 and Figure 38).

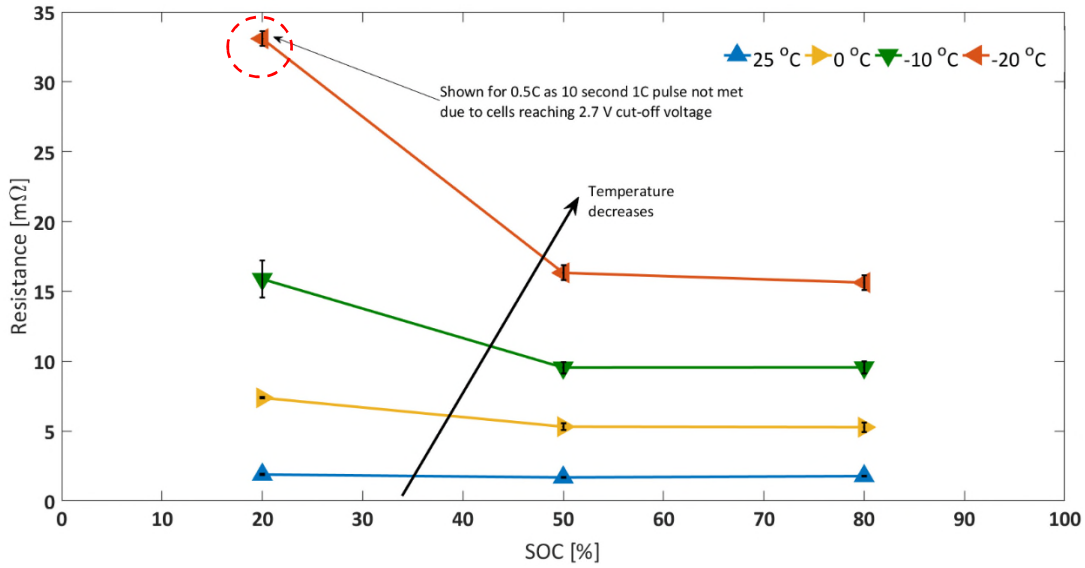

Figure 38. Effect of Decreasing SOC and Ambient Temperature on DCR for 1C Discharge Pulse

For a −20 °C ambient temperature, the DCR is 21.7 mΩ. For results discussed in Section 4.2.1, for both oil and air cases, the electrical characteristics for the constant current discharges are similar until internal heat generation takes effect and becomes dominant. At the end of discharge, when the load current was removed, it was seen that for the air test, the corresponding DCR was 7.8 mΩ (this is assuming cubic fit for resistance from Figure 39 at −3.9 °C). However, for the oil test, the corresponding value was 15.6 mΩ (fit at −14.4 °C). If the voltage rise is considered 0.1 s after the 40 A current load is removed, the instantaneous resistance was 1.1 mΩ for the air case. However, for the oil case it was higher (1.5 mΩ). In fact, the difference between the two thermal control methods and thus, the impact of battery internal heat generation is reflected in the rising cell voltage seen for discharge using air cooling (red circle in Figure 34). As temperature increases, DCR decreases, producing less heat, and slowing the temperature rise rate.

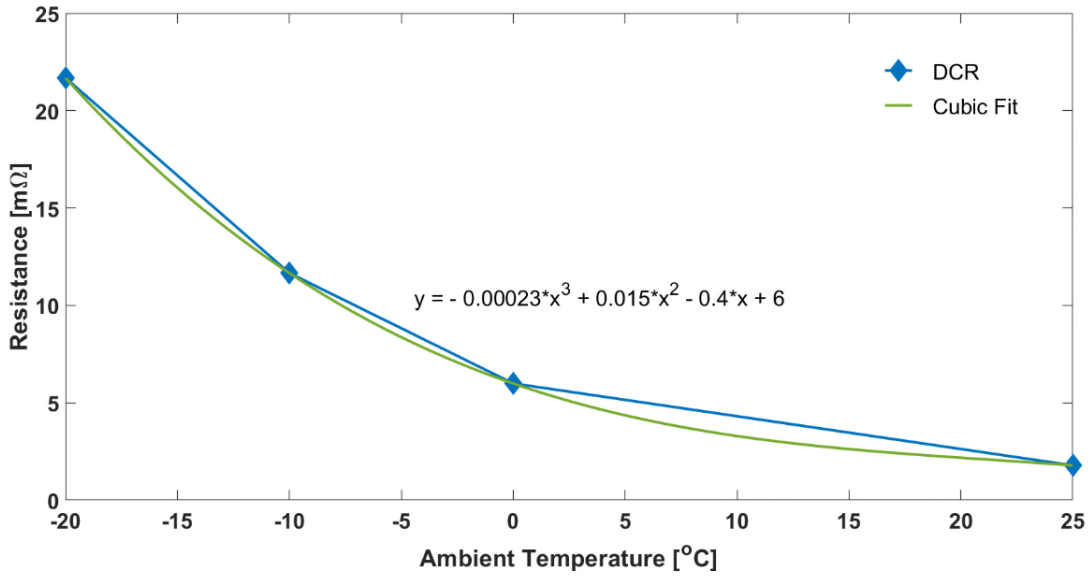

Figure 39. Effect of Temperature on DC Resistance for 1C Discharge Pulse

As introduced in Section 2.2.3, for a current pulse, cell internal resistance can be categorised into Ohmic resistance (based on voltage drop after 0.01 s) and polarisation resistance (based on voltage drop in the remainder of the 10 s pulse duration). For ease of understanding, this is illustrated in Figure 40. The voltage before the pulse is applied was 3703.5 mV, after 0.01 s it was 3576.5 mV and after 10 s it was 3317.1 mV. For this particular 1C discharge pulse, the Ohmic resistance or R_O is 3.2 mΩ. Correspondingly, the polarisation resistance or R_P is 6.1 mΩ after 5.00 s and 6.5 mΩ after 10.00 s. It is clear the R_P is time dependent; this is also reflected in the way the cell relaxes after the current load is removed. In literature, such voltage evolution is assumed to be exponential in nature, and the RC parameters are obtained through mathematical fitting; this will be discussed further in Chapter 5.

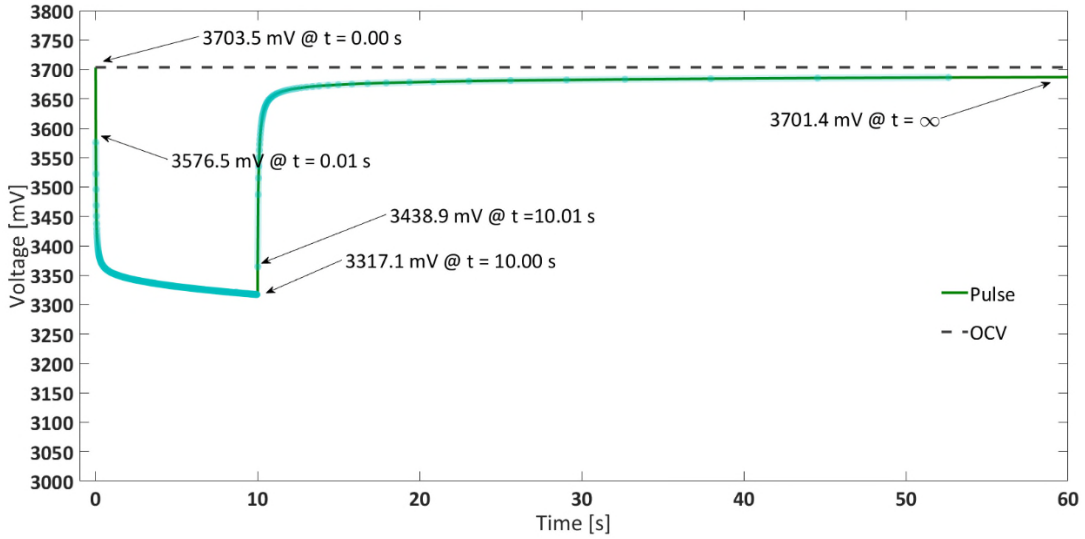

Figure 40. Voltage Response for 10 s 1C Discharge Pulse at −10 °C and 50% SOC

As illustrated in Figure 41, as ambient temperature decreases, the R_O, which represents the electrical aspect of the cell internal resistance, increases by 7.4 times between 25 and −20 °C. Electronic conductivity improves at lower temperature and ionic conductivity decreases at the same time. The temperature coefficient of resistance for the current collectors (assuming for copper/aluminium) is approximately, 0.0039 K^{-1} [115]. Thus, as temperature decreases from 25 to −20 °C, resistance decreases by ~18%. On the other hand, ionic conductivity decreases by up to 50% [41,72,74]. Therefore, R_O is affected by both of these phenomena. Also, R_O should be calculated from instantaneous drop; 0.01 sec might be too long and could include a portion of charge transfer resistance. In combination of these, R_O increases at lower temperature.

In contrast R_P ($R_P = DCR - R_O$) will only see an increase with lower temperature as charge transfer, ionic and solid state diffusion is limited at lower temperature [72]. As shown in Figure 41, R_P increased by more than 23 times as temperature decreased from 25 to −20 °C. From Figure 41, it is clear that, compared to the Ohmic resistance, the polarisation resistance (R_P) increases at a faster rate as ambient temperature decreases. This is probably due to cell physiochemical parameters, based on the Arrhenius equation (Equation 25), having an exponential relationship with temperature. The effect of polarisation resistances can also be understood from how the cell voltage relaxes after the current pulse is removed. As ambient temperature

decreases, it takes longer for the cells to reach their OCV after the current load is removed (Figure 41). This will be discussed further in Chapter 5.

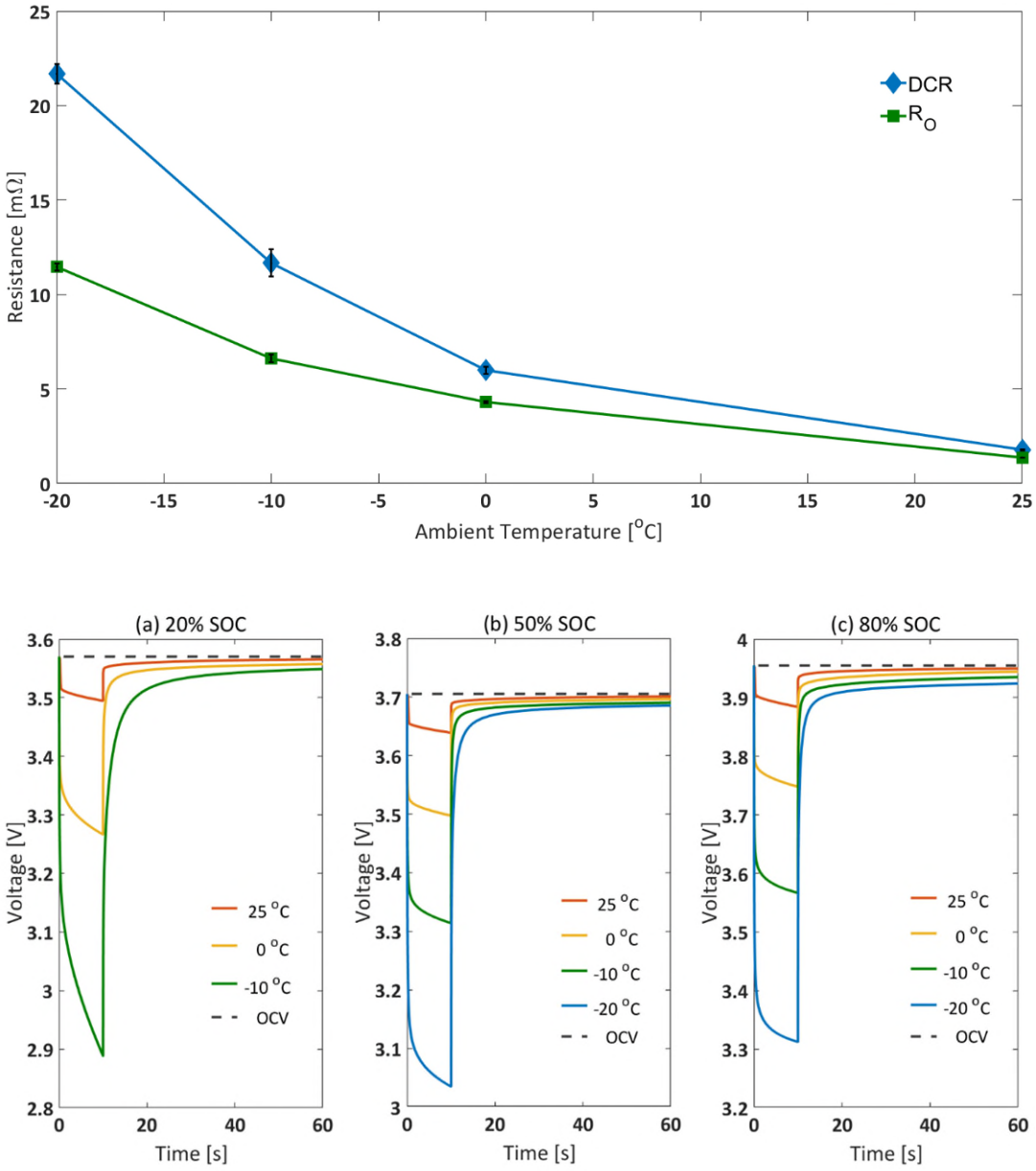

Figure 41. Effect of Ambient Temperature for 10s 1C Discharge Pulse: (top) Effect of Temperature on DCR and R_O and (bottom) Voltage Response at SOCs: (a) 20%, (b) 50% and (c) 80%

4.2.4 Discussion

In Figure 42 it is shown that the discrepancy between choosing air based and oil based thermal control system for parameterisation tends to become more prominent as ambient temperature decreases and/or discharge C-rate increases. For the air-based cooling case, higher discharge C-rate and lower ambient temperature means greater internal heat generation and higher cell temperatures. However, for the oil-based cooling cases, the surface temperature rise seen was suppressed to a considerably smaller value. This was reflected in the capacity characteristics for the oil cooling cases compared to the air cooling cases. For example, for 3C discharge at −10 °C, the capacity discharged for the air-based cooling case was higher by 9.5% than that discharged for 0.25C. However, for the oil-based cooling case, the capacity discharged for 3C was lower than that for 0.25C by 22.3%.

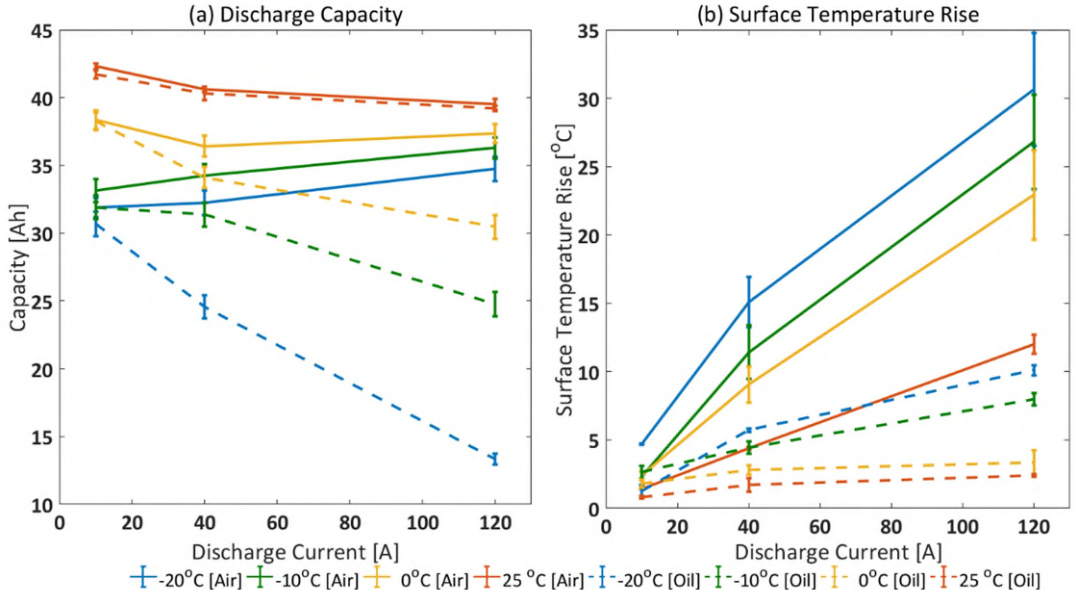

Figure 42. Discharge Characteristics at Different Ambient Temperatures for Various C-rates: (left) Capacity and (right) Surface Temperature Rise

Forced air convection (air-based thermal control) is employed as part of traditional parameterisation methods. However, this method overestimates usable capacity at low ambient temperatures, due to rapid degree of internal heating making corresponding models unreliable. This means that depending on the thermal control system, any conclusions regarding the effect of battery heat generation can be different. Therefore,

when reviewing models, the temperature rise for the capacity test used in parametrisation is important because the lower the temperature rise, the more reliable the data. Thus, it is recommended that active thermal management or 'oil cooling' is employed as part of standardised parameterisation methods. In contrast to Peltier element based thermo-electric cooling, isothermal testing with immersed oil setup is independent of cell format or size, allowing other researchers to replicate the work more easily.

In literature, it is argued that battery internal heat generation helps improve discharge performance of cells at low ambient temperatures. While internal heat generation is beneficial in terms of real-world performance, it adversely affects the cell characterisation data for battery modelling, where the performance of the cell is required to be maintained at the desired parameterisation temperature. For example, to obtain capacity values for different C-rates at an ambient temperature (for example − 20 °C), it is imperative that the cell operating temperature remains close to the ambient temperature throughout the experiment i.e. isothermal test conditions.

For the air-based cooling cases, for example at −20°C for 1C discharge, the final cell temperature was −4.9 °C. This means that the capacity value obtained would be for an effective temperature between −20 and −4.9 °C (average −7.7 °C) rather than at the chosen ambient temperature. In this section, it has been shown that by keeping the test conditions more isothermal (using oil cooling), the capacity values obtained are considerably lower than those seen in the air cooling cases. This issue has been shown to become more prominent as ambient temperature decreased and/or discharge C-rate increased. For example, at 25 °C ambient temperature and 0.25C discharge current, the air-based capacity was only higher by 0.5% than the oil-based capacity (Figure 43). This could be the reason isothermal test conditions have received relatively little attention. However, at −20 °C and for 3C discharge, the air-based capacity was 61.7% higher than the corresponding oil-based capacity. Finally, due to convolution of electrical and thermal phenomena, for 3C discharge, as ambient temperature decreases from 25 to −20 °C, the capacity reduction should be about 66% (oil-based cooling case), rather than just 12.1% (air-based cooling case). The modelling implications are demonstrated in Chapter 6.

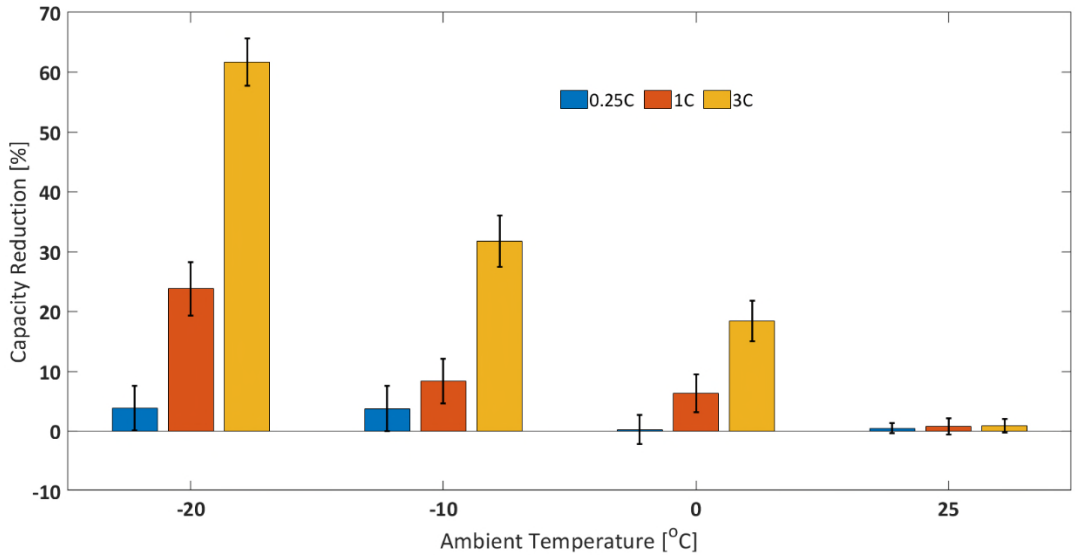

Figure 43. Percentage Reduction in Capacity for Oil Cooling Relative to Corresponding Capacity for Air Cooling at Different Ambient Temperatures and Discharge C-rates

4.3 Chapter Summary

In this chapter, **Objective I** of this thesis is addressed. The primary objective of this chapter was to investigate experimental methods for improving the accuracy of parameterisation experiments at low temperatures.

First, it was shown that conventional discharge capacity measurement methodology (using air-based thermal chambers) overestimates battery capacity at low ambient temperatures. This is mainly due to the coupling of electrical and thermal phenomena owing to rapid heat generation, particularly for large discharge C-rates. In the real-world, prompt temperature rise due to internal heat generation is beneficial for battery performance. However, this can be detrimental to battery model parameterisation where isothermal boundary conditions are critical for separating battery electrical and thermal behaviours. Therefore, battery state estimation models parameterised under far-from-isothermal conditions will likely lead to overestimation of remaining driving range for a battery electric vehicle operating in cold weather conditions.

This chapter presents a novel methodology to capture battery capacity at close-to isothermal conditions for battery model parameterisation. This is achieved by using

an immersed dielectric oil bath which is thermally controlled by a chilling unit allowing for close-to-isothermal test conditions. It is shown that capacity values obtained for oil-based cooling are substantially lower than that obtained for air-based cooling. This discrepancy is more pronounced as ambient temperature decreases and/or discharge C-rate increases. Similar results are observed for discharge energy measurements.

The difference between the two approaches is largely due to the difference in the cell temperature over the course of a duty cycle. By allowing for cell temperatures to rise in the air-based cooling test cases, cell internal resistances become suppressed (reducing cell overpotential), leading to benefits to discharge performance. However, this means that the capacity value obtained is based on a temperature that is substantially different to the starting ambient temperature. This is verified using resistance data at different temperatures and residual capacity experiments.

Battery models are reliant on the accuracy of their parameters and the experiments conducted to obtain them. In previous literature, the significance of ensuring isothermal operating conditions may have been overlooked as most battery testing is conducted at higher operating temperatures where the degree of internal heat generation and their impact on capacity are lower. Therefore, it is recommended that future model parameterisation experimental programmes should attempt to separate battery electrical and thermal behaviour by conducting model parameterisation in isothermal test conditions, especially for models applied at low temperatures.

In Chapter 6, the modelling implications of these findings are investigated.

5. Approaches to Determine the State-of-the-Art Lithium-ion Cell ECM for Low Temperature Applications

This chapter describes the development of a state-of-the-art equivalent circuit model for a lithium-ion cell which is parameterised at low ambient temperatures (Objective II of this thesis). The parameterisation experiments were discussed in Chapter 4. In this chapter, a state-of-the-art ECM is developed that utilises (a) impedance parameters updated based on input SOC, current and operating temperature, (b) SOC estimator based on oil/air parameterisation data and (c) operating/surface temperature estimates from heat generation rates calculated separately for each impedance element. The results of this chapter enable discussion of model validation results in Chapter 6.

The second objective of this chapter (Objective III of this thesis) is to demonstrate that the power control approach should be chosen over current control as the primary means to obtain data from scaled-down realistic drive cycles for model validation. This is particularly relevant at low temperatures where lower operating voltages are expected. A key contribution of this chapter is to validate that the use of a power control approach ensures equivalence in energy throughput and peak powers for a particular drive cycle, irrespective of the operating condition.

This chapter is structured as follows. In Section 5.1, the parameterisation methodology for the ECM including the various subsystems are discussed. In Section 5.2, the case for choosing power control for obtaining validation data for ECMs is made. It is shown that power control is more realistic. In Section 5.3, the key findings of the chapter are summarised.

5.1 Parameterisation of Equivalent Circuit Models at Low Temperatures

A schematic of the features of the ECM developed as part of this study is illustrated in Figure 44. Apart from the parameters in the SOC/SOE subsystems where both air

and oil-based experimental data are implemented, the other subsystems are parameterised using air-based experimental data. This was because negligible surface temperature rise was expected in these experiments. The inputs to the ECM are experimental current and surface temperature. The outputs are modelled terminal voltage, operating temperature, surface temperature, capacity, and energy throughputs, SOC and SOE. In the following sections, each of the subsystems along with their inputs and outputs, are described:

- Capacity, Energy, SOC and SOE (Section 5.1.1)
- OCV and OCV Hysteresis (Section 5.1.2)
- Overpotential and Output Voltage (Section 5.1.3)
- Thermal Feedback: Operating and Surface Temperatures (Section 5.1.4)
  - The alternate method considering polarisation currents for heat generation estimation is presented in Section 5.1.4 (Figure 44).

Note, the relevant MATLAB/Simulink models are illustrated in Appendix A. The corresponding scripts, functions, etc. are given in Appendix B.

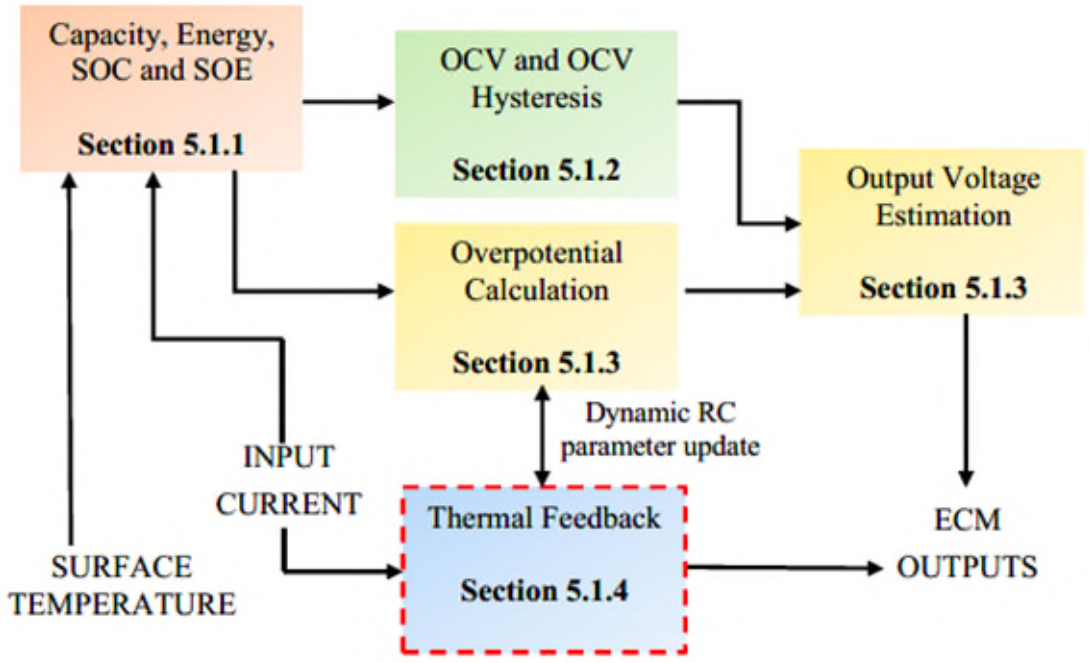

Figure 44. ECM Subsystems

5.1.1 Capacity, Energy, State-of-Charge and State-of-Energy

The capacity throughput is calculated on the basis of the input current as follows:

$$Capacity\ Throughput, Ah = \frac{\int_0^t Idt}{3600} \quad (47)$$

Here, I is the input current in Amperes and t is the time elapsed in the simulation in seconds.

The energy throughput is calculated based on the input power as follows:

$$Energy\ Throughput, Wh = \frac{\int_0^t Pdt}{3600} \quad (48)$$

Here, P is the power in Watts and t is the time elapsed in the simulation in seconds. The power is calculated using the input current and the experimental voltage obtained.

Essentially, the capacity and energy throughputs described above rely on experimental data and are a characteristic of the duty cycle rather than the model itself.

5.1.1.1 SOC Estimation

As discussed in Section 2.3.1, there can be multiple definitions of SOC depending on the application field, i.e. electrochemistry, modelling, systems engineering, etc. Based on recent literature [59], the SOC definition employed in this thesis is as follows: SOC is used analogous to the fuel gauge in a conventional vehicle [57]. From an application perspective, it is defined based on the capacity usable for a particular temperature and load current [59]:

$$SOC(t) = SOC(0) - \frac{\int_0^t Idt}{C_{DYN}} \times \frac{100}{3600} \quad (49)$$

Here, C_{DYN} (in Ah) is the capacity value obtained from galvanostatic discharge experiments at different ambient temperatures and C-rates. This is calculated by employing a two dimensional (2D) lookup table that uses current and temperature as inputs (Figure 45). The capacity values were obtained from galvanostatic discharge experiments at different ambient temperatures and C-rates; as shown in Chapter 4. The

data tables used to populate the corresponding look-up tables are given in Appendix C. The initial SOC is estimated from the OCV SOC relationship (to be discussed in Section 5.2.2). The coloumb counter operates as a simple integrator of current at each time step (0.1 s). The experimental surface temperature of the cell is chosen to ensure that the SOC estimation subsystem is independent of the rest of the ECM and thus, the C_{DYN} can be parameterised purely on the basis of experimental data from Chapter 4.

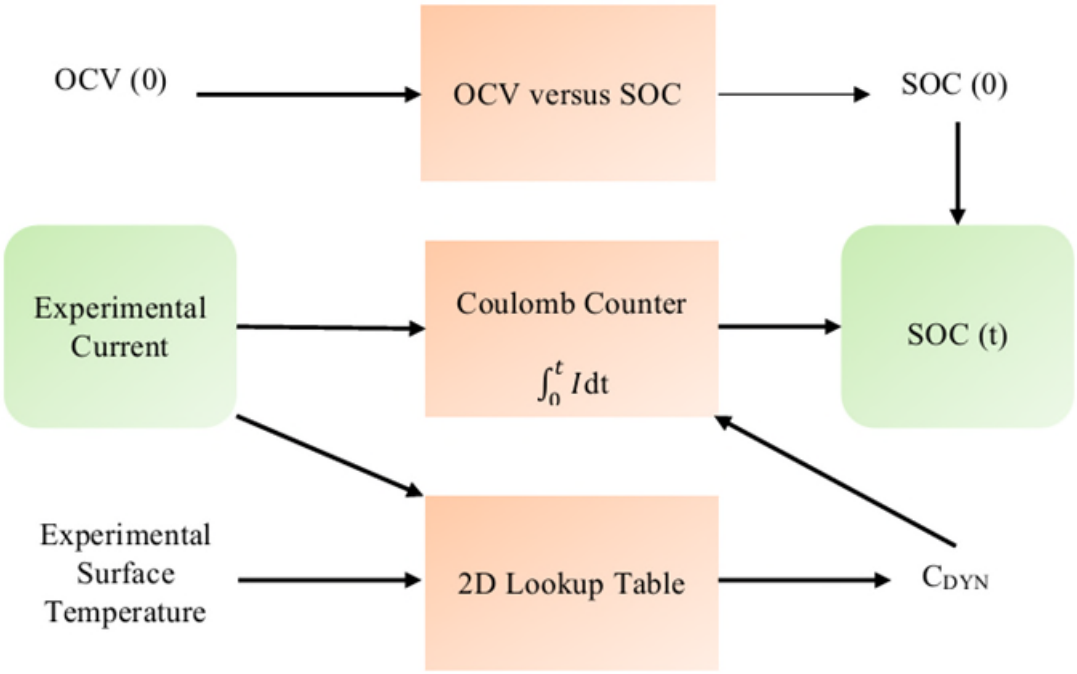

Figure 45. SOC Estimation Subsystem

5.1.1.2 SOE Estimation

Recently in literature, state-of-energy (SOE), instead of SOC, has been proposed as a metric to quantify the remaining available energy of lithium-ion cells and in turn, the remaining driving range of BEVs [56,57,86,87]. Analogous to SOC, SOE is defined as follows:

$$SOE(t) = SOE(0) - \frac{\int_0^t Pdt}{E_{DYN}} \times \frac{100}{3600} \quad (50)$$

Here, E_{DYN} (in Wh) is the energy value obtained from galvanostatic discharge experiments at different ambient temperatures and C-rates. This is calculated by employing a two dimensional (2D) lookup table that uses current and temperature as

inputs (Figure 46). The data tables used to populate the corresponding look-up tables are given in Appendix C. The energy values were obtained from galvanostatic discharge experiments at different ambient temperatures and C-rates. The initial SOE is estimated from the OCV SOE relationship (to be discussed in Section 5.1.2). The Watt counter operates as a simple integrator of power at each time step (0.1 s). Similar to the SOC subsystem, the experimental surface temperature of the cell is chosen to ensure that the SOE estimation subsystem is independent of the rest of the ECM and the E_{DYN} can be parameterised purely on the basis of experimental data.

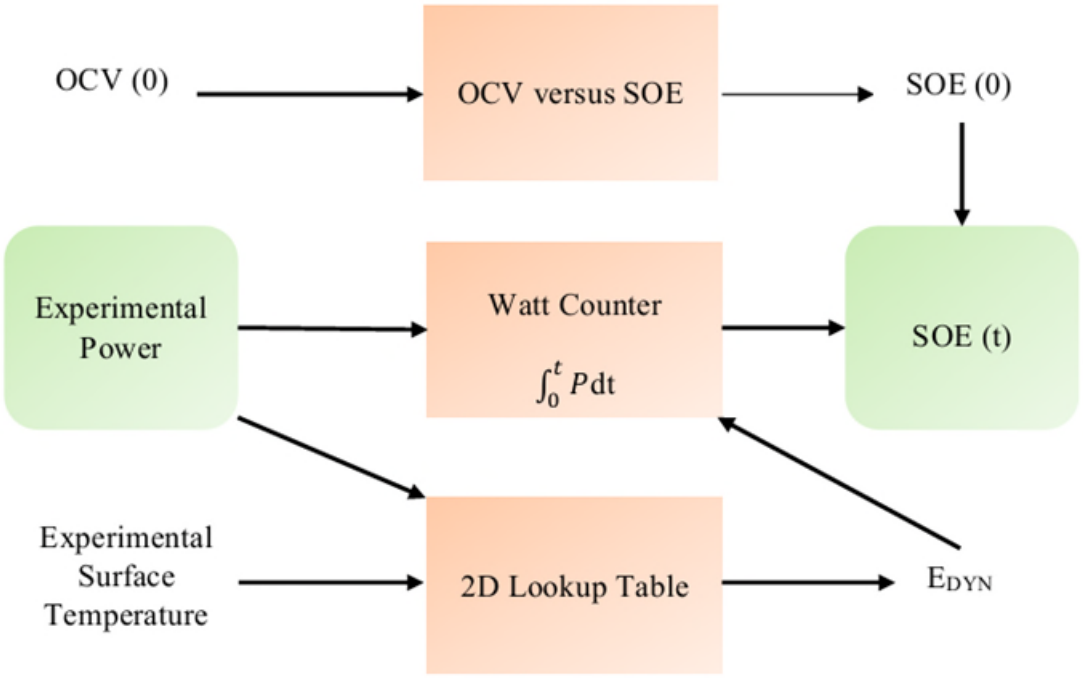

Figure 46. SOC Estimation Subsystem

Note, for the SOC and SOE estimation functions, capacity and energy values for both air based and oil based cases were employed. This enables comparison of the battery states, viz. SOC and SOE based on air-based and oil-based parameters in Chapter 6.

5.1.2 Open Circuit Voltage and Hysteresis

For the lithium-ion cells under test, the OCV versus SOC relationship including hysteresis was introduced in Section 4.2.2. To implement the OCV versus SOC relationship in an ECM, both charge and discharge OCV values were interpolated to

a 1% SOC step size. To implement OCV hysteresis as part of the ECM, the following relationship was defined:

1. At each SOC point, the average OCV ($\overline{OCV}$), used to estimate the OCV at an SOC value, was calculated for the corresponding discharge and charge OCV values:

$$\overline{OCV}(SOC) = \frac{OCV_{discharge}+OCV_{charge}}{2} \quad (51)$$

2. To define OCV as a function of SOC and to account for the transition between charge and discharge, the following rate transition model as detailed in [116] is employed:

$$OCV(SOC) = \overline{OCV}(SOC) + h(SOC) \quad (52)$$

Here, a hysteresis state variable, $h(SOC)$, is solved as per the following:

$$\frac{dh}{dSOC} = K(H(SOC) - h(SOC)) \quad (53)$$

Here, $H\ (SOC)$ is the absolute difference between $\overline{OCV}$ and $OCV_{discharge}$ (a converse method would work with OCV_{charge} as well) and K is the rate at which the hysteresis state, $h(SOC)$, achieves $H\ (SOC)$.

3. To implement in an ECM, $h(SOC)$ is calculated as a time dependent variable. In Equation 53, left side is multiplied by $\frac{dSOC}{dt}$ whereas the right side is multiplied by $\left|\frac{I}{C_{NOM}}\right|$ to obtain the following equation (Note, $\frac{dSOC}{dt} = \left|\frac{I}{C_{NOM}}\right|$):

$$\frac{dh}{dt} = K\left|\frac{I}{C_{NOM}}\right|(H(SOC) - h(SOC)) \quad (54)$$

$H\ (SOC)$ as a function is obtained from the OCV versus SOC experiments conducted. Similar to relevant literature [116], a transition rate of $K = 50$ was employed. Using this, the hysteresis state variable, $h\ (SOC)$ is calculated and implemented in the ECM (as illustrated in Figure 47):

$$h(SOC) = \int K\left|\frac{I}{C_{NOM}}\right|(H(SOC) - h(SOC))\,dt \quad (55)$$

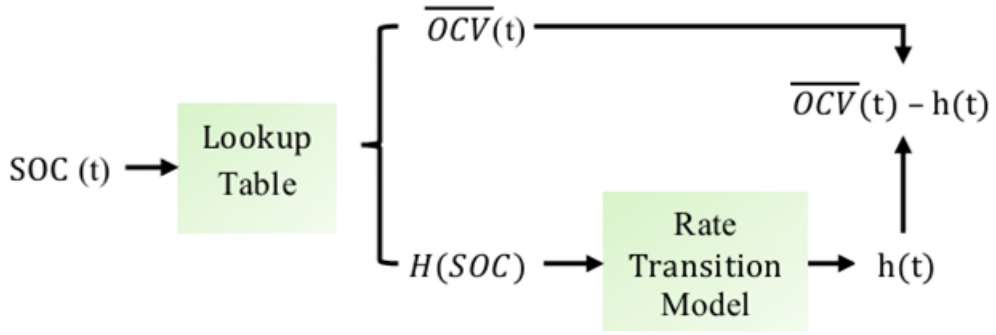

Figure 47. OCV and OCV Hysteresis Subsystem

The $\overline{OCV}$ versus SOC relationship is illustrated in Figure 48, along with the H versus SOC relationship. A similar $\overline{OCV}$ versus SOE relationship can be defined and is illustrated in Figure 49.

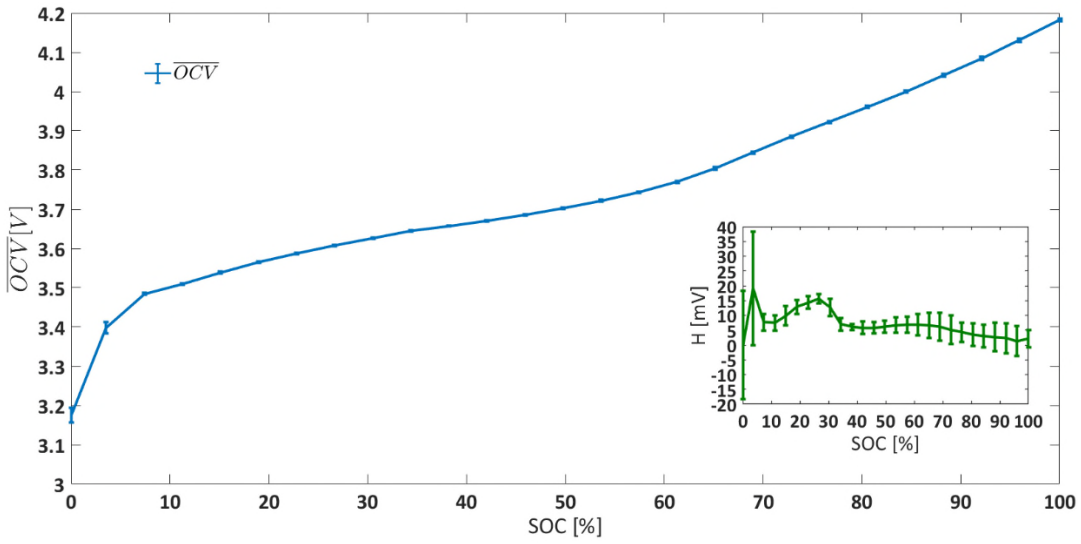

Figure 48. $\overline{OCV}$ versus SOC relationship at 25 °C Ambient Temperature (Inset: $H\ (SOC)$ versus SOC)

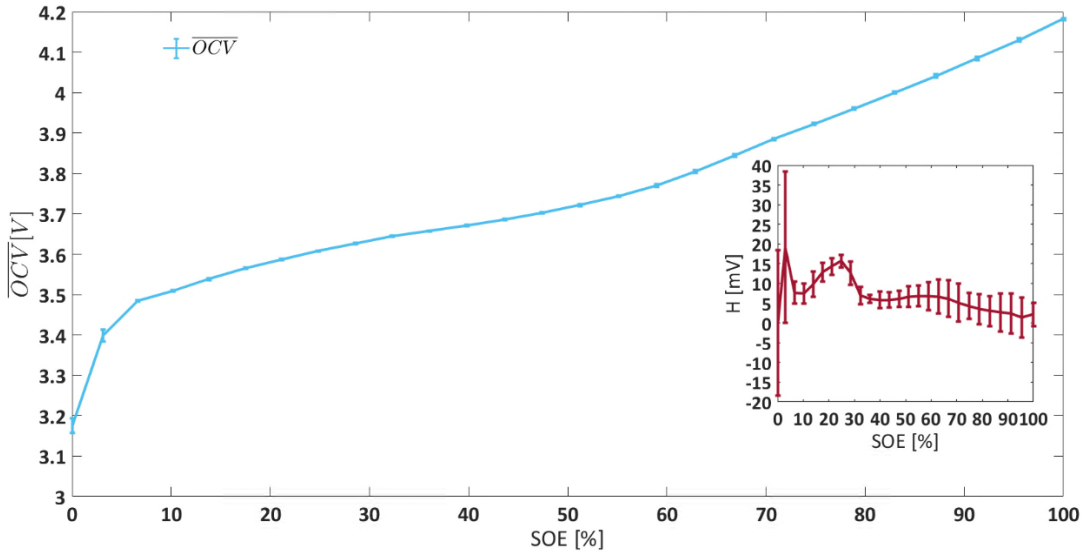

Figure 49. $\overline{OCV}$ versus SOE relationship at 25 °C Ambient Temperature (Inset: H (SOE) versus SOE)

5.1.3 Overpotential and Output Voltage

For a particular duty cycle, the model voltage output is essentially obtained, by solving the following equation at each time step:

$$V = OCV(SOC) - \eta \tag{56}$$

Here, η is the cell overpotential which is obtained by multiplying the input current with the overall resistance at each time step. The DCR response of the cells under investigation was discussed briefly in Chapter 4. The DCR response was experimentally obtained at different ambient temperatures and SOCs for 10 s charge/discharge pulses of varying magnitudes (Note, discharge is positive). The effect of decreasing ambient temperature is illustrated in Figure 50. At 25 °C, across all SOCs and charge/discharge pulses, the average DCR is 1.7 mΩ, but at −20 °C, the average DCR is 24.8 mΩ. This is due to cell electrochemical processes slowing down as well as physiochemical parameters such as ionic conductivity and solid-state diffusivity decreasing as ambient temperature decreased. This is manifested as an increase in DCR values. It was also observed that DCR tended to decrease as current magnitude increased, this is probably due to cell heating related suppression of cell internal resistances in the internal layers of the pouch cell [114].

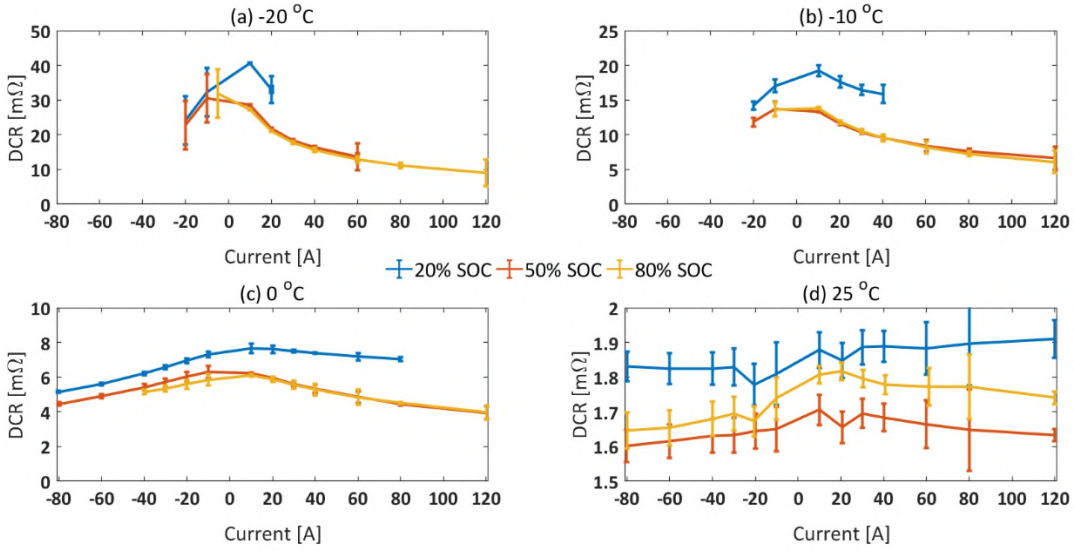

Figure 50. Effect of Temperature and SOC on Air-based Experimental DC Resistance for Varying Magnitudes of 10 s Charge/Discharge Pulses: (a) −20 °C, (b) −10 °C, (c) 0 °C and (d) 25 °C (Note, discharge is positive)

Similarly, for low operating currents (< 0.5C), only a portion of the electrodes' active material surface area will take part in the discharge operation. Thus, pulse power testing at lower current amplitude could lead to localised measurement, increasing the resistance. On the other hand, due to temperature difference between the core and the cell surface, the resistances of internal pouch cell layers would be lower compared to those closer to the cell surface. This would cause the hotter layers to have lower resistances, and thus carry more current, causing overall cell DCR to decrease. This is in agreement with recent work by Troxler *et al.* and Klein *et. al.* who stated that, based on the operating temperatures of the various layers within a pouch cell, there would be internal temperature and SOC gradients whose individual behaviours would affect the overall cell behaviour [98,114].

The heating effect was more pronounced at lower temperatures (Figure 50 & Figure 51). This is because for the same 120 A pulse current, the heating power at 25 °C would be approximately 25 W, whereas the heating power at −10 °C would be approximately 85 W. Using the mass and the heat capacity of the cell, this would lead to a theoretical temperature rise of approximately 0.7 °C. A similar temperature rise (~0.4 °C) is illustrated in Figure 51. It is also seen that as discharge pulse amplitude increases, the surface temperature rise becomes more prominent. However, the actual

temperature rise is marginally lower than the theoretical value probably due to convective heat losses at the cell surfaces and the accuracy of the t-type thermocouple (±0.5 °C). Thus, further inference cannot be drawn from these measurements.

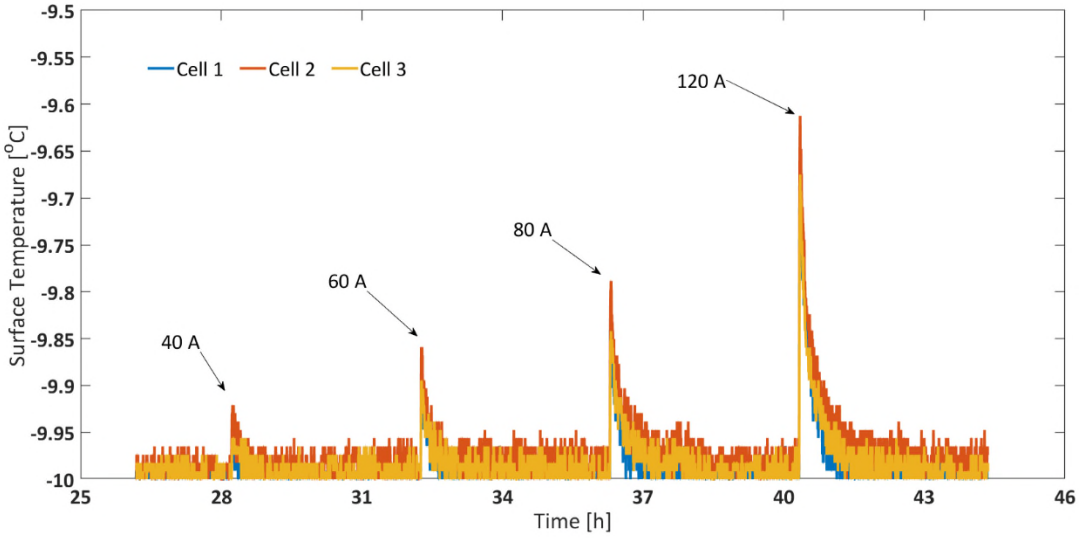

Figure 51. An Illustrative Example of Surface Temperature Rise for Pulses at −10 °C and 50% SOC [Thermocouple accuracy is ±0.5 °C]

5.1.3.1 Impedance Representation and Mathematical Fitting

As discussed in Chapter 2, cell internal resistances are conventionally represented as a resistor connected in series to a resistor-capacitor pair connected in parallel. This resistor-capacitor pair connected in parallel is termed as an RC network. If 'n' RC networks are connected in series, then the ECM is termed as an n^{th} order ECM. For an n^{th} order ECM, the voltage response can generally be mathematically represented as:

$$V_{output}(t) = OCV - I_{input}(t) * \left(R_O + R_{P1}\left(1 - e^{-t/\tau_{P1}}\right) + R_{P2}\left(1 - e^{-t/\tau_{P2}}\right) + \cdots + R_{Pn}\left(1 - e^{-t/\tau_{Pn}}\right)\right) \quad (57)$$

Using Equation 57 and the corresponding Jacobian matrix described in Equation 43 as the function handle, the model parameters can be estimated via a non-linear least squares algorithm [151] for each pulse at different SOCs and ambient temperatures (MATLAB scripts provided in Appendix B). For this study, the default optimisation options were chosen for the fitting. However, the lower bound for the model

parameters was set to 0 as neither resistance not time constants can be negative. The initial value for R_O is calculated from the voltage response after the first time interval (0.01 s in this study). The initial value for R_{Pn} is set at 1 mΩ, in the same order of magnitude as the rated DCR value for this particular cell. The τ_n values were set as 10^{n-1} s based on relevant characteristic times for charge transfer and diffusion processes [160]. The optimisation was stopped either when the maximum number of function evaluations (set at 1000) was undertaken or the terminal tolerance (10^{-5}) was achieved.

In the following sections, the model parameters obtained for 1st order and 2nd order ECMs are discussed in terms of their accuracy in estimating the corresponding experimental voltage profiles and in terms of their relationship with SOC and ambient temperature.

5.1.3.2 1st Order ECM

As discussed in Chapter 2, the impedance element in a 1st order ECM consists of a resistor connected in series (R_O) with an RC network (R_{P1} and τ_1). As shown in Figure 41 in Chapter 4, for a 1C discharge pulse, the voltage response depended on the SOC and the ambient temperature. However, just based on the DCR values it was difficult to comment on the detailed time characteristics of such a response. The time constant for an RC network is the time required to charge the capacitor from 0 V to 63.2% of the applied voltage. This essentially means that at the beginning of the discharge pulse, there is no current passing through the resistor (R_{P1}) because all of the current is used to charge the capacitor (C_1). However, as time elapses, more and more current passes through the resistor. At t=τ_1, 63.2% of the load current is flowing through the polarisation resistance. Conversely, as the load current is removed, the capacitor begins discharging at t=0. In which case, if the capacitor was fully charged, then at t=τ_1, the capacitor discharges by 63.2% of its initial voltage.

Table 9 shows the ECM parameters obtained from the fitting process. As ambient temperature decreases, the capacitance (C_1) decreases substantially. For example, it is 19388.5 F at 25 °C, and 117.5 F at −20 °C. This implies that the RC network becomes resistive faster (as capacitance decreases) when ambient temperature decreases. This

is probably due to internal electrochemical processes slowing down [50]. It should be noted that R_{P1} tended to decrease marginally (for both 50% and 80% SOC) as temperature decreased from 25 (1.42 mΩ at 50% SOC) to 0 ℃ (1.30 mΩ at 50% SOC). As shown in Table 9, the corresponding time constant also decreased substantially, so the effect of overpotential induced from the impedance element tended to increase as temperature decreased from 25 to 0 ℃. Similarly, at 25 ℃, R_{P1} value at 20% SOC is lower than at higher SOCs, however, the capacitance value was also lower. Thus, it was likely that the RC circuit would become resistive faster for lower SOC at 25 ℃. The change in R_O was more drastic than the change in R_{P1}. The average R_{P1} increased by ~3.8 times and the average R_O increased by ~5.7 times. This could be because, the measurement frequency for the experiments was 100 Hz. It is likely that at lower temperatures, the R_O also included charge transfer contributions, rather than just Ohmic resistance. However, these parameters are based on mathematical equations and although some inferences can be drawn from them, they can be misleading if used to explain electrochemical phenomena without validation.

Table 9. Effect of Ambient Temperatures/SOC on 1st Order ECM Parameters for 1C 10 s Discharge Pulse

Ambient Temperature [℃]		**−20**	**−10**	**0**	**25**
SOC [%]	**Parameter**				
20	R_O [mΩ]	N/A	8.1±0.34	4.69±0.11	1.43±0.07
	R_{P1} [mΩ]	N/A	7.88±1.25	2.58±0.41	1.25±0.10
	τ_1 [s]	N/A	3.36±0.36	2.5±0.11	20.6±3.12
	C_1 [F]	N/A	426.39±0.19	968.99±0.17	16480±0.17
50	R_O [mΩ]	9.69±0.37	5.82±0.14	4.23±0.20	1.33±0.07
	R_{P1} [mΩ]	6.39±0.15	3.49±0.18	1.03±0.06	1.49±0.38
	τ_1 [s]	0.87±0.08	0.65±0.12	2.45±0.49	34.81±1.71
	C_1 [F]	136.15±0.03	186.24±0.20	2378.64±0.21	23362.4±0.42
80	R_O [mΩ]	8.62±0.32	5.92±0.32	3.99±0.18	1.34±0.07
	R_{P1} [mΩ]	6.89±0.18	3.44±0.12	1.3±0.05	1.42±0.67
	τ_1 [s]	0.69±0.09	0.74±0.03	3.04±0.27	25.43±1.72
	C_1 [F]	100.14±0.09	215.11±0.05	2338.46±0.1	17908.5±0.84
Average	R_O [mΩ]	9.16±0.49	6.61±0.49	4.30±0.29	1.37±0.12
	R_{P1} [mΩ]	6.64±0.23	4.94±1.27	1.64±0.42	1.39±0.40
	τ_1 [s]	0.78±0.12	1.58±0.38	2.66±0.57	26.95±3.95
	C_1 [F]	117.46±0.09	319.83±0.28	1621.95±0.29	19388.5±0.95

To show that DC and AC based testing indicates similar trends as temperature decreased, the electrochemical impedance spectroscopy (EIS) technique was employed. EIS consists of sinusoidal AC current, which are applied to the cells at different frequencies between 10 mHz to 10 kHz. The AC voltage response and the consequent phase shift is measured to obtain the impedance response of the cell. In this study, this experiment was carried out at −20, −10, 0 and 25 ℃ ambient temperatures for 50% SOC. This is illustrated in Figure 52. As illustrated in Figure 52, as ambient temperature decreases, the magnitudes of both real and imaginary parts of impedance, Z' and Z'' increase. The frequency at which the local maxima for Z'' occurs, also decreases as ambient temperature decreases. Similarly, the local minima for Z'' occurs at a lower frequency as ambient temperature decreases. This implies that electrochemical processes are slowing down as ambient temperature decreases; this local minima is the frequency at which the cell operation transforms from charge transfer to mass transport. These results imply that charge transfer and diffusion related resistances will either be higher at low ambient temperatures compared to at room temperature, or, the corresponding capacitance values would be lower (Table 10), making the RC networks resistive faster. Note, the resistance and capacitance values are different for PPC and EIS data (as they are simply fitted parameters), but they both indicate increased resistances and slower electrochemical phenomena at low temperatures compared to at 25 ℃.

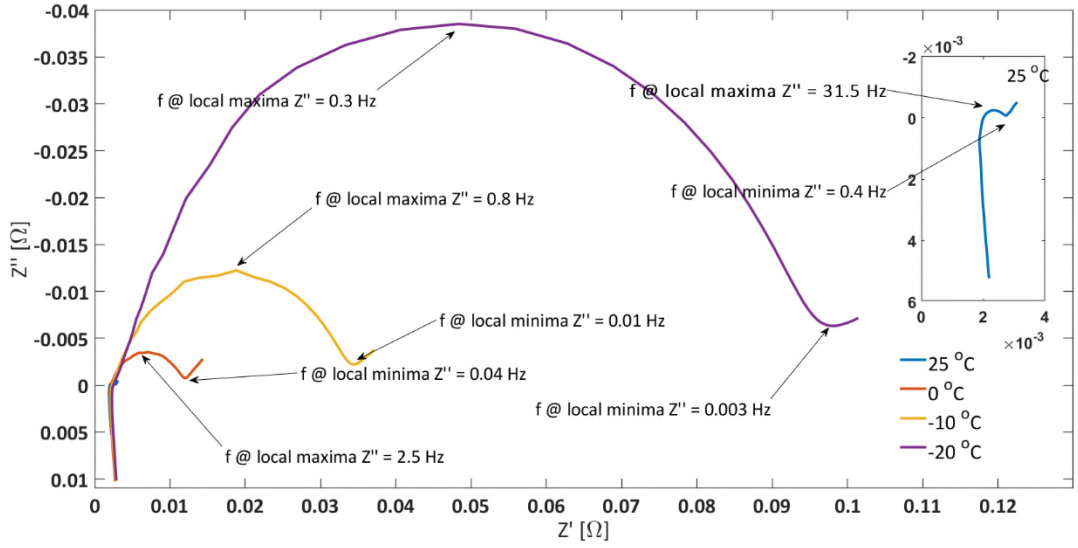

Figure 52. EIS Plot at 50% SOC for Different Ambient Temperatures (Inset: 25 ℃)

Table 10. Capacitance Values corresponding to EIS Data shown in Figure 52 for Different Ambient Temperatures

Temperature [℃]	**−20**	**−10**	**0**	**25**
Polarisation Resistance [mΩ]	95.3	32.1	9.8	0.02
Capacitance [F]	5.5	6.2	6.5	218.7

Conversely, the frequencies in Figure 52 also explain why, at lower temperatures, it takes longer for the cells to relax back to the OCV immediately after a current pulse is removed. This is because at lower ambient temperatures, when a current load is applied, greater potential gradients are induced at the electrode electrolyte interface as the charge transfer process is slower. This is largely due to slower chemical activity as well as slower ionic conductivity. Furthermore, it takes longer for the active material to diffuse from the bulk of the electrode to the surface, leading to greater concentration gradients. On the other hand, when the current load is removed, due to slower nature of the cell internal processes, it takes longer for the cell to go into equilibrium. In this case, as the polarisation resistance is higher, the corresponding overpotential is also higher at lower ambient temperature compared to room temperature.

In Figure 53, the standard deviation in R_O and R_{P1} across all the 10 s discharge current pulses successfully met by the cells at different ambient temperatures are illustrated. At 25 ℃, for the R_O, the mean was 1.36 mΩ and the standard deviation was 0.06 mΩ. Correspondingly, the standard deviation as a percentage of mean for all discharge pulses was 4.1% at 25 ℃. However, this value increased to 31.0% at −20 ℃. Similarly, for R_{P1} the corresponding standard deviation as a percentage of mean increased from 19.9% at 25 ℃ to 63.1% at −20 ℃. This means that the effect of current magnitude on cell pulse power capability and in turn the RC parameters becomes more prominent as ambient temperature decreases. Note, as introduced in Figure 50, any discharge pulses higher than 0.5C and 1.5C were not met for 10 s at 20% and 50% SOC at −20 ℃, respectively. Similarly, any discharge pulses higher than 1C and 2C were not met for 10 s at −10 and 0 ℃ for 20% SOC, respectively.

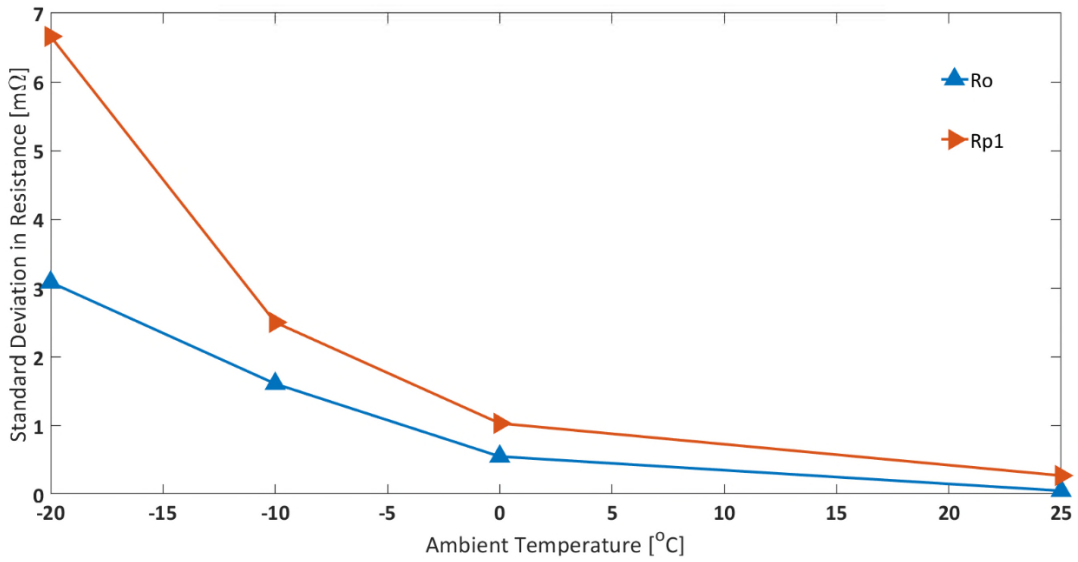

Figure 53. Using Standard Deviation of R_O and R_P for All 10 s Discharge Pulses at a Particular Ambient Temperature to Illustrate Effect of Pulse Current Amplitude at Different Ambient Temperatures

5.1.3.3 2nd Order ECM

As discussed in Chapter 2, the impedance elements in a 2nd order ECM consists of a resistor connected in series (R_O) with two RC networks (R_{P1} and τ_1, and R_{P2} and τ_2). Similar to the fitting results for the 1st order ECM, the resistances (R_O, R_{P1} and R_{P2}) increase as ambient temperature decreases (Table 11). However, the time constants tend to become more convoluted. This is because, as stated in Section 5.1.3.2, these parameters are based on mathematical equations and although some conclusions can be drawn from them, they can be misleading if relied on to explain electrochemical phenomena without validation.

As suggested in Section 3.2.3, the reason a 2nd order ECM is being explored in this study along with a 1st order ECM, is due to this model structure being commonly employed in literature to investigate model performance [7,123,154].

Table 11. Effect of Ambient Temperatures/SOC on 2nd Order ECM Parameters for 1C 10 s Discharge Pulse

Ambient Temperature [℃]		**−20**	**−10**	**0**	**25**
SOC [%]	**Parameter**				
20	R_O [mΩ]	N/A	3.7±0.09	2.1±0.12	1.4±0.07
	R_{P1} [mΩ]	N/A	6.0±0.81	3.3±0.47	0.4±0.03
	τ_1 [s]	N/A	0.2±0.02	0.1±0.01	4.8±0.68
	C_1 [F]	N/A	31.6±1.55	33.6±1.61	13250.0±10.55
	R_{P2} [mΩ]	N/A	7.1±1.36	2.2±0.06	3.0±0.61
	τ_2 [s]	N/A	5.4±0.35	5.0±0.90	144.9±6.60
	C_2 [F]	N/A	758.1±0.85	2238.7±0.91	48939.2±1.10
50	R_O [mΩ]	5.4±0.03	2.9±0.14	1.5±0.11	1.3±0.06
	R_{P1} [mΩ]	8.6±0.81	4.3±0.91	3.1±0.25	0.3±0.09
	τ_1 [s]	0.2±0.01	2.3±0.60	0.1±0.01	5.4±0.19
	C_1 [F]	22.1±1.69	541.0±1.07	15.9±1.77	19321.4±1.97
	R_{P2} [mΩ]	4.0±0.81	2.9±0.12	1.1±0.21	2.7±0.49
	τ_2 [s]	8.5±0.22	4.7±0.57	9.1±0.07	157.9±4.42
	C_2 [F]	2124.4±0.99	1615.9±1.74	8234.2±1.07	58932.8±1.12
80	R_O [mΩ]	5.7±0.03	3.4±0.07	2.2±0.02	1.3±0.05
	R_{P1} [mΩ]	8.5±1.85	6.7±0.10	1.7±0.07	0.4±0.05
	τ_1 [s]	0.2±0.02	23.3±0.63	0.1±0.02	4.9±0.95
	C_1 [F]	24.7±1.71	3500.8±1.28	63.2±1.73	13243.2±1.97
	R_{P2} [mΩ]	17.9±2.17	9.4±0.29	7.5±0.82	3.4±1.07
	τ_2 [s]	88.7±1.00	59.0±9.97	113.5±6.33	179.0±7.85
	C_2 [F]	4949.7±1.84	6312.3±1.91	15051.7±1.01	52029.1±1.13
Average	R_O [mΩ]	5.5±0.04	3.3±0.18	1.9±0.16	1.3±0.10
	R_{P1} [mΩ]	8.5±2.02	5.7±1.22	2.7±0.54	0.3±0.11
	τ_1 [s]	0.2±0.02	8.6±0.87	0.1±0.02	5.0±1.18
	C_1 [F]	23.4±2.40	1520.4±2.28	33.1±2.95	14794.1±10.91
	R_{P2} [mΩ]	11.0±2.32	6.5±1.39	3.6±0.85	3.0±1.33
	τ_2 [s]	48.6±1.02	23.0±9.97	42.5±6.39	160.6±11.17
	C_2 [F]	4430.3±2.09	3570.5±2.72	11748.6±1.73	53000.0±1.93

In Figure 54 it is shown that accuracy in voltage estimation increases as model order increases. For example, for the 1st order ECM (1RC), the average root-mean-squared error in voltage estimation (V_{RMSE}) at −10 ℃ is 10.67 mV but decreases to 5.08 mV for the 2nd order ECM (2RC). Furthermore, V_{RMSE} is shown to increase for both ECM structures as ambient temperature decreases. This implies that model accuracy suffers as ambient temperature decreases. Particularly, the decline is worse for the 1st order

ECM compared to the 2nd order ECM. Although not a lot of scientific inferences can be drawn from the mathematical ECM parameters obtained from curve fitting; it can be inferred that that there are two different underlying processes when it comes to cell behaviour as ambient temperatures decrease (see τ values for 2RC in Table 11). These processes are not adequately represented by the 1RC model. However, model parameters for both 1RC and 2RC models were deemed reliable as the standard deviation of each parameter across all iterations of the mathematical fitting operation was an order lower than the average value that was estimated for a current pulse at a particular SOC and/or temperature. For example, at −20 °C and at 50% SOC, for 0.5C discharge pulse, the R_O was 10.2 mΩ for 1RC parameterisation, whereas the standard deviation across the entire fitting operation for that pulse was 0.2 mΩ. Note, this standard deviation is for a single pulse illustrating how each impedance parameter varies across multiple iterations of the mathematical fitting function, whereas those reported earlier in this thesis (such as in Figure 53 is for estimated parameters across multiple pulses at different operating conditions).

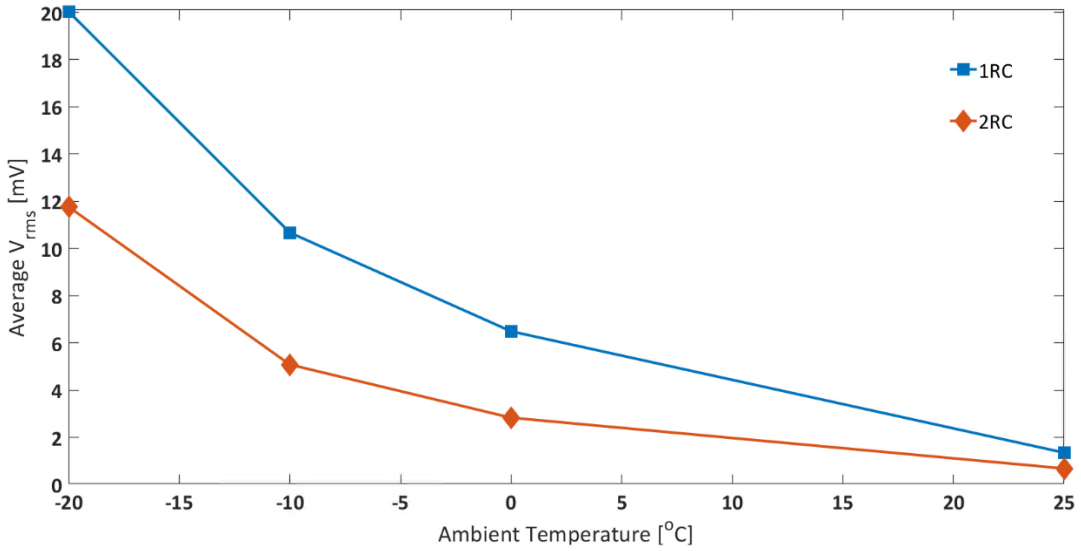

Figure 54. Comparison of Errors for Pulse Fitting: 1RC v/s 2RC

The inputs and outputs for the overpotential subsystem are illustrated in Figure 55 and Figure 56. The data tables used to populate the corresponding look-up tables are given in Appendix C. The RC parameters are updated based on the SOC, the input current and the operating temperature. Then, based on Equation 57, the overpotential is calculated.

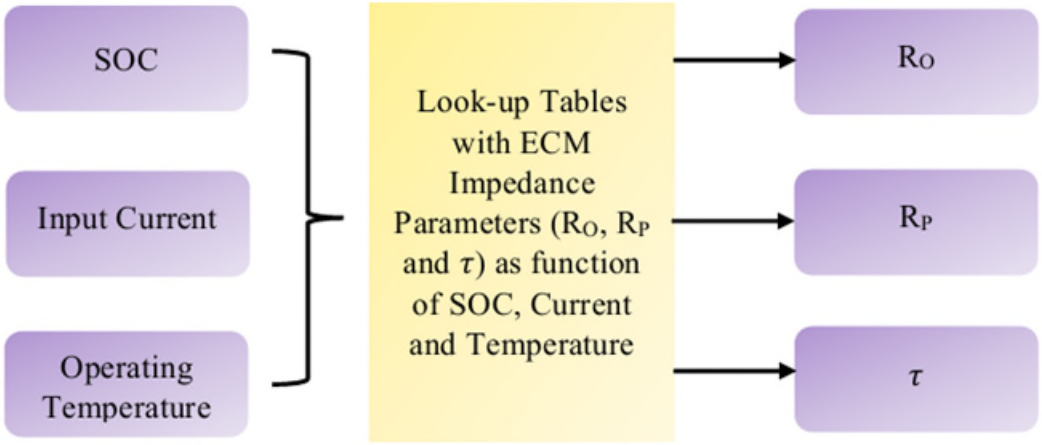

Figure 55. RC Parameters Subsystem

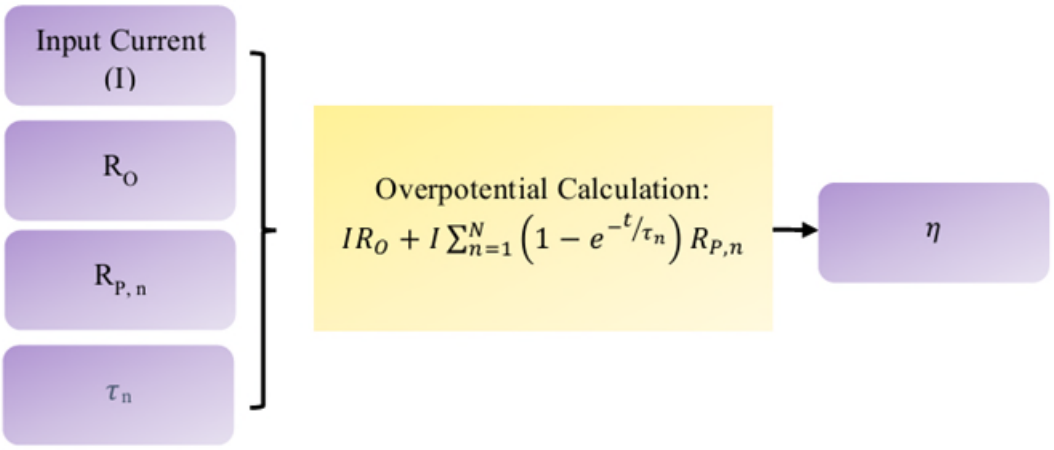

Figure 56. Overpotential Calculation Subsystem

The current passing through any RC network $(I_{P,n})$ i.e. the polarisation current is a function of the load current (I_{input}) and time as per below:

$$I_{P,n}(t) = I_{input}(t) * \left(1 - e^{-t/\tau_{Pn}}\right) \quad (58)$$

As Equation 58 is only applicable for constant currents, Equation 59 discretising Equation 58 was implemented in Matlab®/Simulink using a 'Discrete-Time Integrator' block:

$$I_{P,n}\,[k+1] = e^{\frac{-\Delta t}{\tau_{Pn}}} * I_{P,n}[k] + \left(1 - e^{\frac{-\Delta t}{\tau_{Pn}}}\right) * I_{input}[k] \quad (59)$$

The integration method employed was the default Forward Euler method:

$$y(n) \;=\; y(n-1) \;+\; K * [t(n) - t(n-1)] * u(n-1) \quad (60)$$

Here, $y\,(n)$ is the block output at step 'n', K is the initial gain (set to 1 here), $u\,(n-1)$ is the block input in the previous step and $t\,(n)$ – $t\,(n-1)$ is the sample time.

5.1.4 Thermal Feedback Subsystem

As part of the ECM, a 1st order thermal feedback model was employed that included convective heat losses at the cell surface (illustrated in Figure 57).

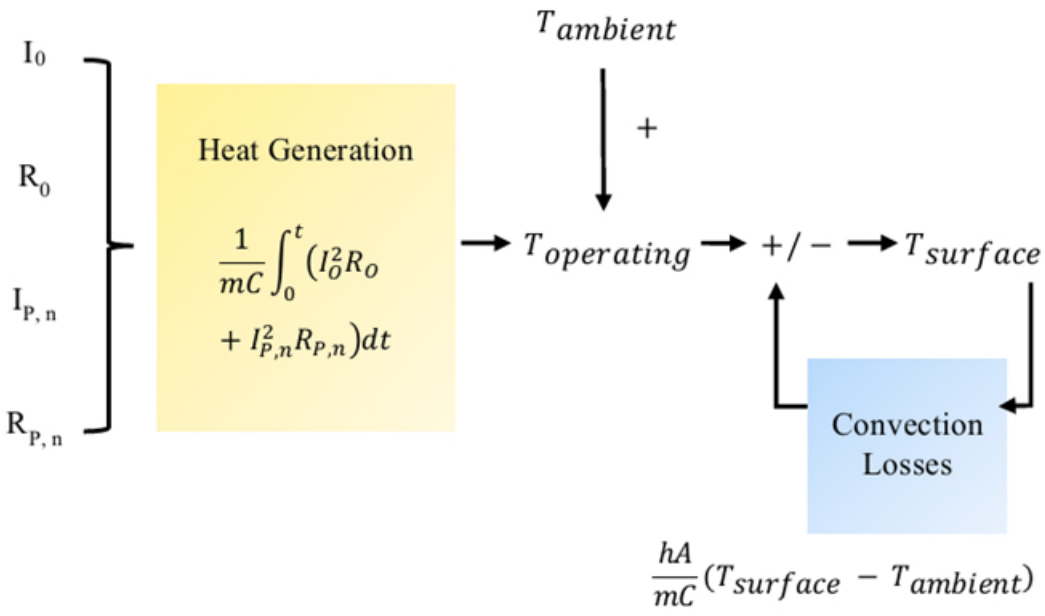

Figure 57. Thermal Feedback Subsystem

The following cell parameters were employed as part of this:

- Mass of cell, 'm': 0.97 kg (manufacturer's datasheet)
- Surface area of cell, 'A': 0.10125 m^2 (manufacturer's datasheet)
- Specific heat capacity of cell, 'C': 1243 J/kg/K [161]
- Convective heat transfer coefficient of cell operating in thermal chamber, '$h - value$': 20 $W/m^2/K$ (averaged from [65,124,162])

The inputs to this subsystem were the input current, the polarisation currents and the impedance parameters (depending upon the number of RC networks). The outputs of this subsystem were operating temperature and surface temperature. While operating temperature was calculated from the heat generated by the ECM for a particular duty cycle, the surface temperature calculation also included the convective heat losses (Figure 57). The following protocol was followed to obtain the operating temperature and surface temperature of the ECM at each time step:

1. At every time step heat generation was calculated as:

    a. For 1st Order ECM ('1RC') with one RC network:

$$Q_{gen} = I_{input}^2 \times R_{ohmic} + I_{p1}^2 \times R_{p1} \quad (61)$$

    b. For 2nd Order ECM ('2RC') with two RC networks:

$$Q_{gen} = I_{input}^2 \times R_{ohmic} + I_{p1}^2 \times R_{p1} + I_{p2}^2 \times R_{p2} \quad (62)$$

2. The change in operating temperature at every time step (ΔT) was calculated as:

$$\Delta T = \frac{Q_{gen}}{m \times C} \quad (63)$$

3. The operating temperature of cell was calculated as:

$$T_{operating} = T_{\infty} + \int_0^t \Delta T \quad (64)$$

where, T_{∞} is the ambient temperature for the duty cycle.

4. The surface temperature of cell was calculated as:

$$T_{surface} = T_{operating} - T_{loss} \quad (65)$$

5. T_{loss} was calculated as [163]:

$$T_{loss} = \frac{h-value \times A}{m \times C} \int_0^t \left(T_{surface} - T_{\infty}\right) dt \quad (66)$$

As shown in Equations 61 and 62, the heat generation value (Q_{gen}) can be separated into two components depending on the number of RC networks - heat generated from

the Ohmic resistances and heat generated from polarisation resistances. However, in literature, if reversible heat generation is ignored, the total cell heat generation rate is presented as in Equation 45. As discussed in Chapter 2, at lower ambient temperatures, potential gradients occur due to slower charge transfer whereas, concentration gradients occur due to slower mass transport. Furthermore, this has physical basis in the characteristic times of the different internal cell processes. Thus, depending on the time elapsed and the current flowing through these resistors (R_{Pn}), the heat generated from each impedance element in the ECM would be different. The above suggests that 'separation of currents' should be considered as part of the thermal feedback subsystem of an ECM to ensure practical implementation. This hypothesis will be examined in Chapter 6.

5.2 Drive Cycle Experiments: Obtaining ECM Validation Data using Power Control Approach

In this section, a short comparison between current control and power control approaches to battery testing is conducted. This comparison has been undertaken to support **objective III** of this research work. The comparison has been undertaken using reference legislative drive cycles. At the end of this chapter, it will be confirmed that only the power control approach should be chosen for drive cycle testing, particularly at low temperatures or low operating voltages.

5.2.1 Backward Facing Model

The vehicle level duty cycle was scaled down for the cells used for this study. As illustrated in Figure 58 (Figure 16 reproduced for ease of understanding), the scaling of the duty cycle was achieved using a backward facing model, where the legislative speed versus time profile was converted to a vehicle level power versus time profile [164,165]. The conversion was carried out for a typical passenger BEV with a kerb weight of approximately 1600 kg [149]. Other parameters were: Coefficient of Drag, C_D = 0.28, Density of Air, ρ = 1.225 kg/m^3, Frontal Area of Vehicle, A_f = 2.744 m^2, Gravitational Acceleration, g = 9.81 m/s^2, Friction Coefficient, f_r = 0.01 [146,166]. The gear-box ratio (G) was 7.94. The motor efficiency was assumed to be 0.9 at ambient temperatures [44,165], and 100% regenerative-braking efficiency (RE) was

assumed. Since the study is focused at low ambient temperatures, a 5 kW load for cabin-heating was added at every time step [167]. It was assumed that the vehicle battery pack consisted of 48 modules and each module consisted of four cells arranged in a SP2S2P architecture [34]. The nominal voltage of a single cell was 3.7 V, and nominal voltage of the battery pack was 355.2 V. The power demand per second of a single cell was calculated. The ideal energy available from the battery pack at the nominal pack voltage was 28.4 kWh, which is comparable to a real BEV [168].

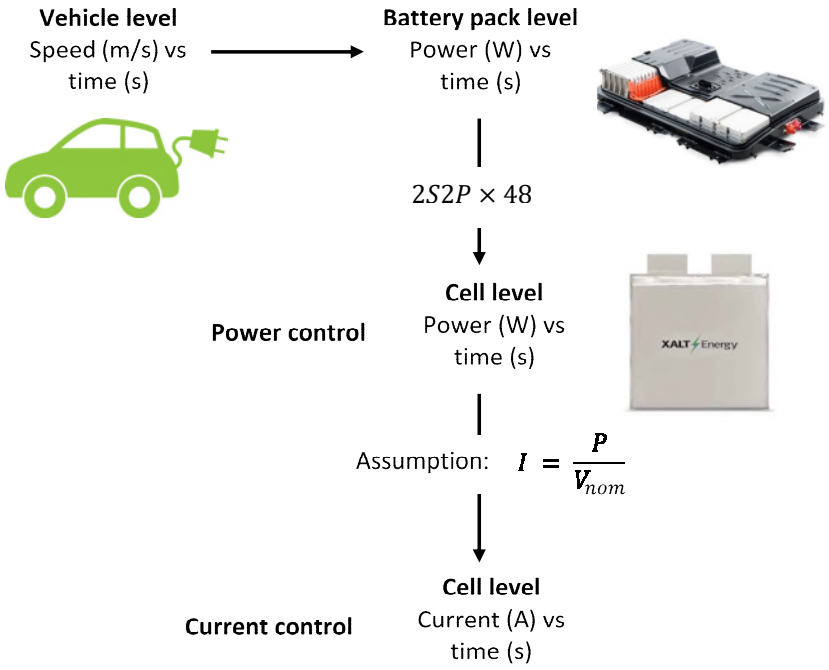

Figure 58. Backward Facing Model to obtain Cell-level Profile from Vehicle-level Speed Profile: Contrast between Power Control and Current Control (Images for EV, battery pack and cell obtained from Internet)

As discussed in Chapter 3, to compare the effect of choosing different control methods (power and current), the US06 drive cycles were considered. The cells were cycled for two back-to-back 600 s long US06 drive cycles (2xUS06) for equivalence. The starting SOC chosen was 65%. As justified in Chapter 3, the ambient temperatures chosen were −15, −5, 5 and 25 °C. Fully charged cells were first discharged to 65% SOC using 0.5C operating current at 25 °C ambient temperature. Then, the cells were cooled down to the test temperature and rested for 4 hours before employing the drive cycle.

Note, the drive cycle experiments were conducted in a standard thermal chamber with forced air convection (air-based method). This is because these drive cycles are representative of real-world load currents/voltages and operating conditions where battery internal heating would be beneficial to battery performance. This is in contrast to the SOC parameterisation experiments that were conducted for both air-based and oil-based methods. The equipment used for these experiments is identical to those used in Chapter 4. In the following section, it is shown that discrepancy between power control and current control approaches increases as temperature decreases and/or drive cycle demand increases. In particular, power and energy demands are underestimated in the current control approach compared to the actual drive cycle demand.

5.2.2 Results and Discussion

In Figure 59, the experimental current profiles for both power control and current control approaches are illustrated for the 2xUS06 at −15 ℃ and 65% starting SOC. The experimental current profile for the power control approach is based on the actual power requirement for the drive cycle.

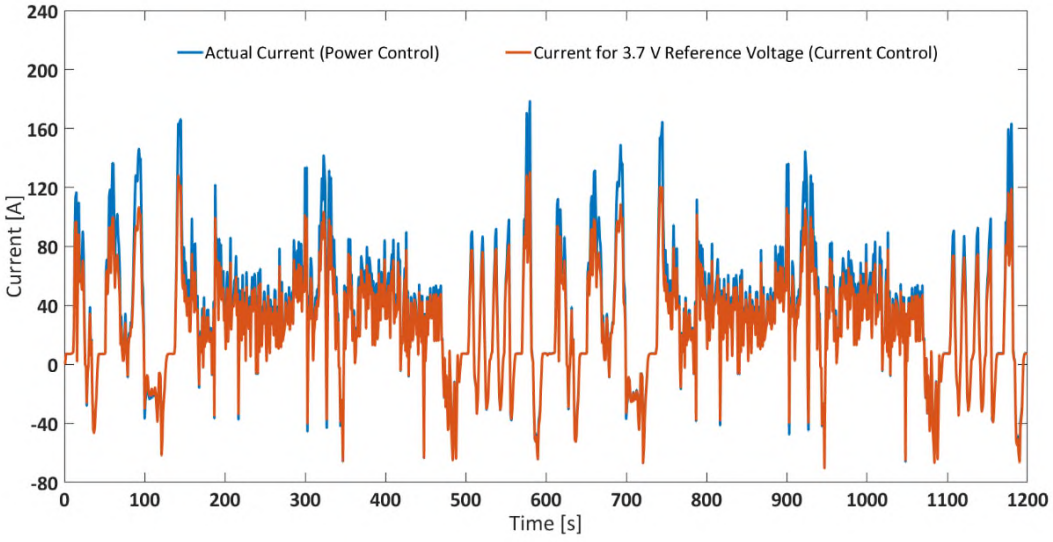

Figure 59. Comparison between Experimental Current and Current for 3.7 V Voltage for 2xUS06 at −15 °C Ambient Temperature and 65% Starting SOC

In Figure 59, it is shown that the current values for the power control (or actual) approach are higher than the theoretical current values for the current control (calculated for the 3.7 V reference voltage) approach. This is reflected in the 10.9 Ah

capacity discharged in the actual experiment compared to the theoretical 9.1 Ah calculated for current control approach.

As shown in Figure 60, the capacity discharged increases as ambient temperature decreases for the 2xUS06; as ambient temperature decreased from 25 to −15 °C, the capacity discharged from the cells increased by 13.2%. This is because as ambient temperatures decrease, cell internal resistances increase, resulting in a lower operating voltage. To meet the power demand of the drive cycle, which is independent of the ambient temperature, the current values have to increase, leading to increased capacity discharged.

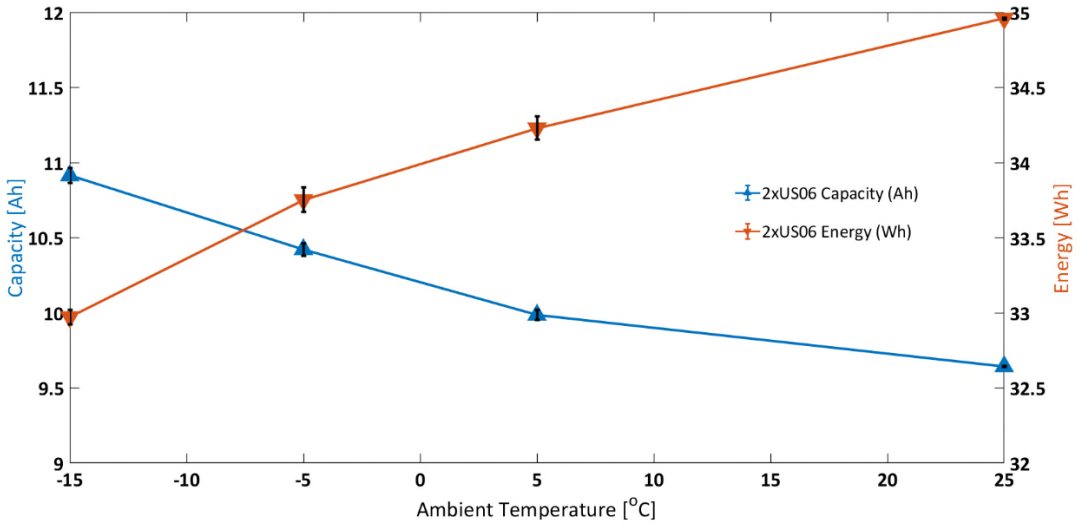

Figure 60. Effect of Starting Ambient Temperature on Capacity (left) and Energy (right) Discharged for 2xUS06 for 65% Starting SOC

Furthermore, as shown in Figure 60, between 25 and −15 °C, as ambient temperature decreased, the energy discharged decreased by 5.7%. This is because at this temperature, the cells reached the 2.7 V minimum cut-off voltage at several points during the drive cycle (red circles) and the current had to be reduced (compared to the actual demand for the drive cycle) to prevent over-discharge related damage to the cells. At 25 °C ambient temperature, the peak power required in both the 1st and 2nd US06 driving phases was ~614 ±3 W, and the corresponding peak currents were ~176 A and ~181 A, respectively. The corresponding cell voltages at those points in the drive cycle were 3.46 V and 3.41 V, respectively. However, at −15 °C, the cells hit the minimum cut-off voltage of 2.7 V and were only able to deliver ~155 A and ~165 A

peak currents, respectively and thus, the cells were unable to deliver the required power levels. This is illustrated in Figure 61c.

There is a clear inconsistency between reference voltage based current profiles and actual (or real-world) power profiles particularly at low temperatures. Therefore, in this thesis only power control with a dynamically changing voltage will be considered for obtaining validation experimental data.

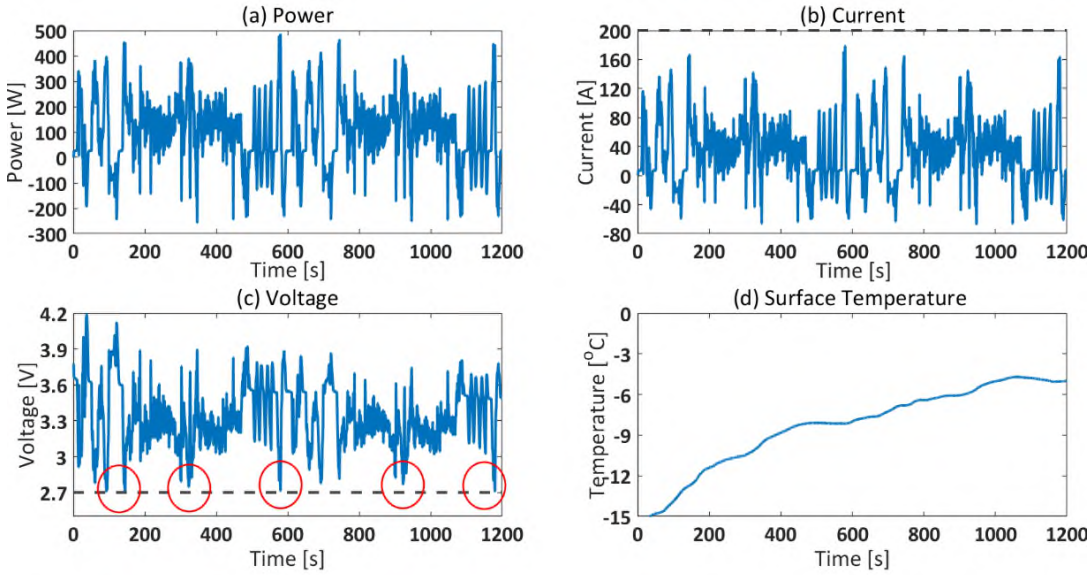

Figure 61. Experimental Characteristics of 2xUS06 for 65% Starting SOC and −15 °C Starting Ambient Temperature: (a) Power, (b) Current, (c) Voltage and (d) Surface Temperature

5.3 Chapter Summary

In this chapter, **Objectives II and III** of this thesis are addressed.

In this chapter, the alternative approaches to modelling lithium-ion batteries at low temperatures were investigated. Initially, the various subsystems that comprise of a typical equivalent circuit model were discussed including SOC/SOE estimation, overpotential calculation and output voltage estimation, and thermal feedback subsystem. As part of the thermal feedback subsystem, it was hypothesised that instead of a common current for estimating the heat generated in the model, it may be better

to use separate polarisation currents for each RC network. This alternative approach to estimating heat generation will be examined further in Chapter 6.

To implement the cell impedance in the ECM, two model structures were considered, 1RC and 2RC. The independent variables considered were temperature, SOC and charge/discharge current. To parameterise the ECM, as well as to implement the different subsystems, underlying mathematical equations and flow charts were detailed and illustrated. The MATLAB/Simulink subsystems are further illustrated in Appendix A, the background MATLAB scripts are given in Appendix B and key look-up tables are presented in Appendix C. This enables model validation to be discussed in Chapter 6.

Performance testing of lithium-ion cells under different operating conditions is a key stage in battery pack design process of an electric vehicle. It was found in this chapter that it is crucial that power control rather than current control is employed as the primary approach to obtain validation data for cell models. This is because power control is representative of real-world driving scenarios in terms of energy and power demands. A power control approach would account for real-time cell voltage response, depending on the operating state of the battery.

In Chapter 6, the ECMs generated in this chapter, along with the power control based validation data, will be utilised to validate the following: (a) oil-based parameters lead to better estimation of battery states such as SOC and SOE and (b) Battery states parameterised using oil-based parameters and heat generation rates calculated using separate currents for each impedance element can improve model accuracy and applicability.

6. Effect of Close-to-Isothermal Parameterisation on Battery State Estimation and ECM Performance

The primary objective of this chapter is to examine the effect of improvements to battery model parameterisation methods and how that has positive effect on battery state estimation and how that affects model accuracy (Objective IV of this thesis**)**.

First, the effect of choosing oil-based parameters over air-based parameters to estimate battery SOC and SOE is investigated. Then, the benefits of choosing oil-based SOC estimates, rather than air-based SOC estimates, on accuracy in output voltage estimation for 1st and 2nd order ECMs is quantified to further contrast the effect of the two parameterisation datasets. Following from Section 5.1.4, it is examined whether employing separate currents for each impedance element (by considering polarisation currents) is better than using a common (Ohmic) current to calculate the heat generation from the cell. This is investigated by comparing effect on model accuracy in terms of output voltage estimated as well as surface temperature estimated.

A key contribution of this chapter is demonstrating that better isothermal control while conducting battery model parameterisation experiments leads to improved battery state estimation. Improved battery state estimation in turn leads to improved model accuracy. These findings will establish a better methodology for parameterising models for low temperature performance investigations, thus improving range estimation in cold weather conditions. A further contribution from this chapter is that using separate currents (allowing for inclusion of polarisation currents) rather than only the common Ohmic current as part of the thermal feedback subsystem leads to improved estimation of modelled surface temperature and output voltage.

The chapter is structured as follows. In Section 6.1, the validation methodology is discussed along with key metrics chosen. In Section 6.2, the comparison between air-based and oil-based parameterisation datasets on SOC and SOE evolution is undertaken. In Section 6.3, the effect of heat generation estimates on surface temperature estimation and on model accuracy is investigated. In Section 6.4, the key findings of the chapter are given. Note, the validation datasets chosen for these

investigations are cell level power control based back-to-back US06 (2xUS06) drive cycles obtained using an air-based thermal chamber at different ambient temperatures.

6.1 Validation Methods

To validate the effect of parameterisation data on battery states (SOC and SOE), the definitions of SOC and SOE as given in Equations 49 and 50 are used; they are repeated here for convenience:

$$SOC(t) = SOC(0) - \frac{\int_0^t Idt}{C_{DYN}} \times \frac{100}{3600} \tag{67}$$

$$SOE(t) = SOE(0) - \frac{\int_0^t Pdt}{E_{DYN}} \times \frac{100}{3600} \tag{68}$$

To validate the effect of parameterisation and validation methods on model accuracy, the accuracy in output voltage estimation (V_{RMSE}) is considered:

$$V_{RMSE} = \sqrt{\frac{\sum_{t=0}^{t_{total}} |(V_{MODEL}(t) - V_{EXP}(t))|^2}{N}} \tag{69}$$

Here, t_{total} is the total time with change in time being 0.1 s (size of each time step). V_{MODEL} is the modelled voltage at each time step and V_{EXP} is the experimentally obtained voltage of the cell at each time step for the 2xUS06 drive cycle discussed in Section 5.2. The starting ambient temperatures chosen were −15, −5, 5 and 25 ℃ and the starting SOC was 65%.

To validate the effect of thermal feedback subsystem of model accuracy and surface temperature estimation, the accuracy in surface temperature estimation (T_{RMSE}) is considered:

$$T_{RMSE} = \sqrt{\frac{\sum_{t=0}^{t_{total}} |(T_{MODEL}(t) - T_{EXP}(t))|^2}{N}} \tag{70}$$

T_{MODEL} is the modelled surface temperature at each time step and T_{EXP} is the experimentally obtained voltage of the cell at each time step for the 2xUS06 drive cycle discussed in Section 5.2. The method to estimate the surface temperature was discussed in Section 5.1.4.

6.2 Battery State Estimation: Effect of Close-to-Isothermal Parameterisation

In this section, the effect of choosing 'air' and 'oil' based parameters on battery state estimators will be discussed. The state estimators considered are SOC and SOE. As discussed in Section 5.1.1, the inputs to the SOC/SOE algorithm were experimental current/power (current for SOC and power for SOE) and experimentally measured surface temperature obtained for the power control based 2xUS06 drive cycle at different ambient temperatures for 65% starting SOC. The outputs of the subsystem are SOC and SOE. Fully charged cells were first discharged to 65% SOC using 0.5C operating current at 25 °C ambient temperature. Then, the cells were cooled down to the test temperature and rested for at least 4 h before being used for the drive cycle tests.

Note, the drive cycle experiments were conducted in a standard thermal chamber with air-based cooling (Espec Platinous J Series). This was done to replicate real-world operating conditions and thus allowing the cells to rise in temperature as they would in a real application due to internal heat generation.

6.2.1 SOC Estimation

To compare the effect of choosing different thermal control parameterisation methods (air-based and oil-based), the ambient temperatures chosen were −15, −5, and 5 °C. As an example, the power, current, voltage and surface temperature profiles for the 2xUS06 drive cycle at −15 °C are given in Figure 62.

The inputs considered for the SOC estimation model are experimentally obtained current and surface temperature (as per Figure 62 b & d). For the 2xUS06 cycling at −15 °C starting ambient temperature, the experimental capacity and energy discharged were 11.3 Ah and 33.9 Wh, respectively. The surface temperature at the end of the drive cycle was −4.8 °C. Thus, the surface temperature rose by 10.2 °C over the course of the 2xUS06 drive cycle.

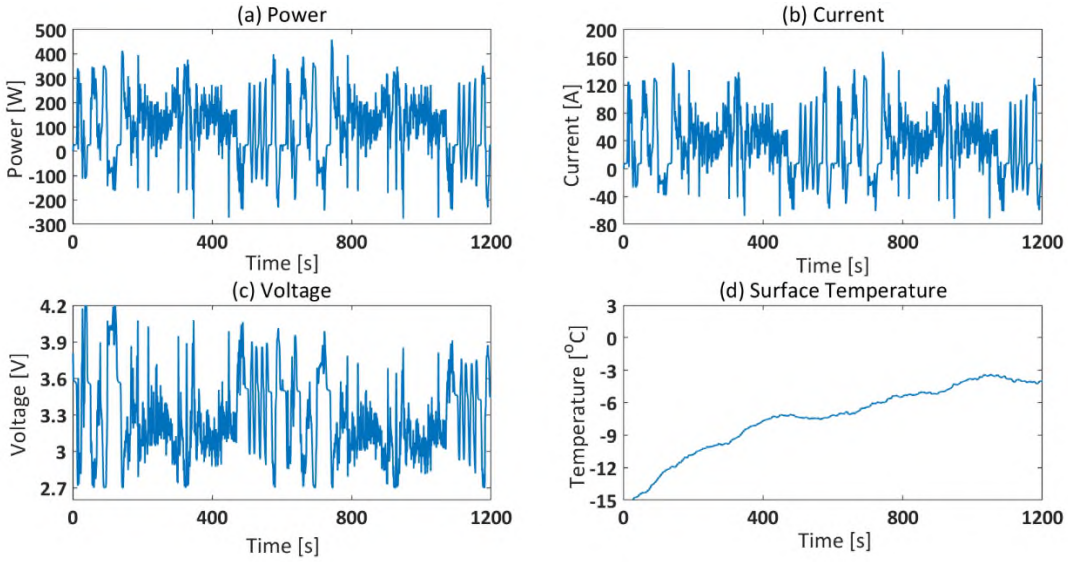

Figure 62. Experimental characteristics of the power control based 2xUS06 for 65% starting SOC and −15 °C starting ambient temperature: (a) power, (b) current, (c) voltage and (d) surface temperature

As illustrated in Figure 63, from the SOC estimation model, at the end of the drive cycle, the SOC estimated for the air case was 33.4% and that for the oil case was 23.9%. The absolute difference in SOC between the two approaches is 9.5% and there is an overestimation in the air case compared to the oil case. If a 100 mile remaining driving range is assumed for 100% SOC, the remaining driving range would therefore be 8.4 miles lower for the oil approach compared to air approach.

To obtain the approximate real SOC of the cells under operation, the following steps were followed:

1. Calculate the mean power of the drive cycle (2xUS06), i.e. 140 W in this case.
2. Following the 2xUS06 cycle:
    a. Immediately further discharge the cell using constant power of 140 W.
    b. Set the cell voltage limit as 2.7 V.
    c. Stop discharge as power delivery from cells reduces by 50% to 70 W.
3. Essentially, to calculate the real SOC, after the drive cycle, the cell was discharged to 0% SOC using the mean power of the drive cycle. Then, using Equation 71, the approximate real SOC at the end of the drive cycle was back-calculated:

$$real\ SOC, \% = \frac{Ah\ during\ constant\ power\ discharge\ phase}{Discharge\ capacity\ from\ OCV\ characterisation} \times \frac{100}{3600} \qquad (71)$$

Note, the constant power discharge phase is terminated at 50% of mean power. This metric is comparable to other literature where power reduction is employed as an end-of-test condition for performance assessment of automotive lithium-ion batteries [35,83,150]. This is illustrated in Figure 64. Thus, assuming a 41.7 Ah capacity from the OCV experiments in Section 4.2, the approximate real SOC at the end of 2xUS06 was calculated to be 19.8% using Equation 71 above (Figure 63).

Assuming the 19.8% end SOC value as the reference end SOC for the 2xUS06 drive cycle at −15 ℃ ambient temperature, the thesis finds that the oil-based parameters, at 23.9% end SOC estimated, are closer to the reference value (Figure 63). The 5.1% absolute SOC difference in the oil-based case is substantially lower than the 13.5% absolute SOC error estimated from the air-based parameters where a 33.4% end SOC is estimated. Therefore, employing an 'air' parameterised dataset will lead to a more inaccurate assessment of usable capacity and cause models to overestimate remaining driving range compared to those parameterised using oil-based thermal control, using data from the cell closer to the predefined parameterisation temperature.

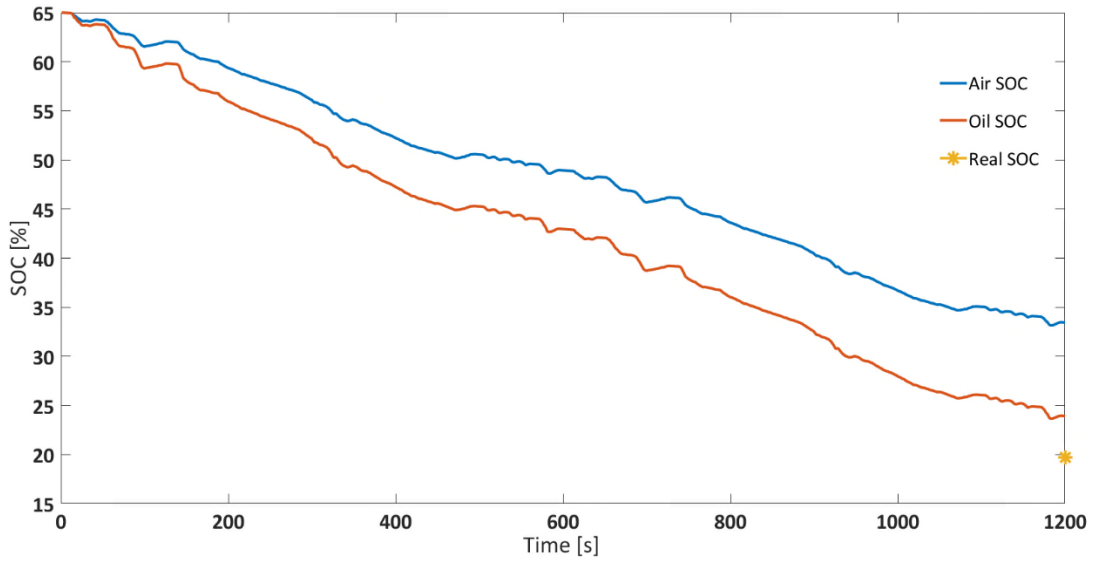

Figure 63. Comparison between air and oil parameterised SOC profiles for 2 back-to-back US06 cycles (2xUS06) at 65% starting SOC and −15 °C ambient temperature.

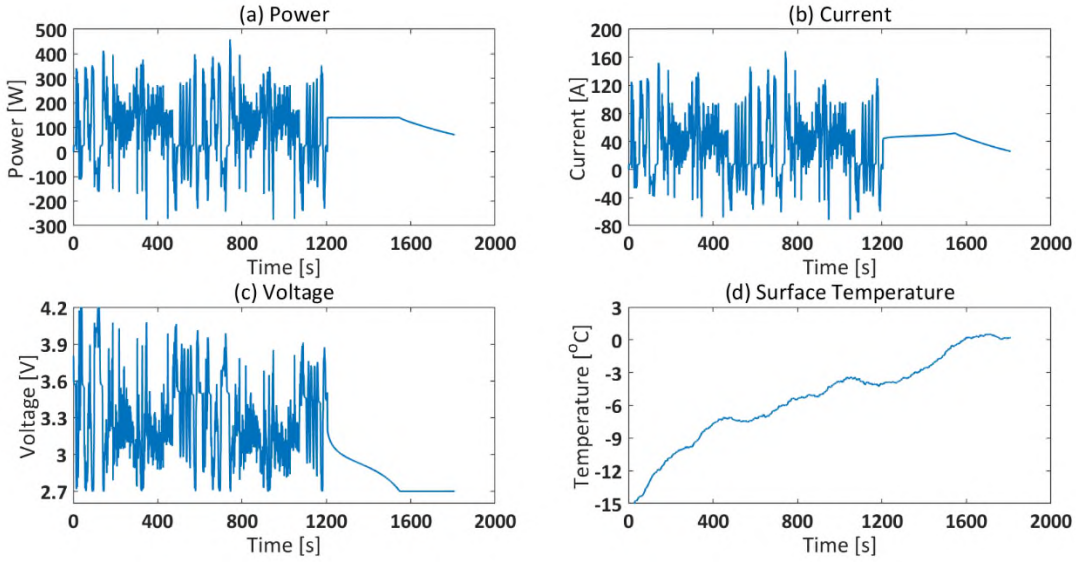

Figure 64. Experimental characteristics of 2xUS06 for 65% starting SOC and −15 °C starting temperature: (a) power, (b) current, (c) voltage and (d) surface temperature (Includes post drive cycle discharge at 140 W until power drops below 70 W)

These experiments were repeated for −5, 5 and 25 °C. The remaining SOCs estimated for these starting ambient temperatures are shown in Figure 65. It is shown that for the 2xUS06, the remaining SOC values parameterised for air and oil cases converge at higher ambient temperatures. The absolute difference in the remaining SOC values for air compared to oil decreases from 9.5% (at −15 °C ambient temperature) to 0.1% at 25 °C ambient temperature. This shows reduced impact of differences in surface temperature control during parameterisation at higher temperatures. This is due to the cell internal resistances being lower at higher temperature, leading to lower heat generation rates. This is likely why the significance of ensuring isothermal operating conditions may have been overlooked until now. This is because most battery testing is conducted at higher operating conditions where the degree of internal heat generation is lower. This follows from Chapter 4, where it is shown that while at −20 °C the air-based capacity for 1C discharge was 31.7% higher than oil-based capacity, at 25 °C this difference was negligible. It should be noted that the experimental remaining SOC for 25 °C starting temperature was higher than the SOCs predicted by both the air and oil based estimators. This is because parameterisation data at temperatures higher than 25 °C was not measured, which was the surface temperature range during the extended 140 W discharge period.

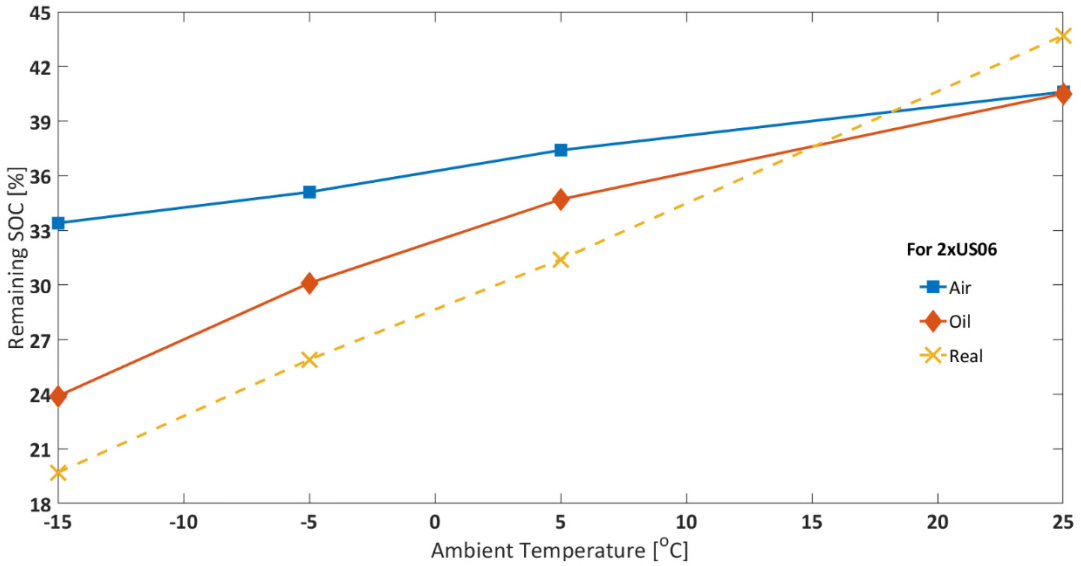

Figure 65. Comparison of Remaining SOCs: Effect of Using Air and Oil thermal control Parameters at Different Starting Ambient Temperatures (for 65% Starting SOC) for 2 back-to-back US06 Cycles (2xUS06)

Correspondingly, the experimental surface temperature rise also reduces as ambient temperature increases. Note, the surface temperature data reported are experimentally obtained, therefore, there is no distinction between air-based and oil-based values. As shown in Figure 66, the experimental surface temperature rise for −15 ℃ and 25 ℃ starting ambient temperatures are 10.2 °C and 1.2°C, respectively. Note, the cell core temperature will be higher due to poor through-plane thermal conductivity of lithium-ion cells [140], which can be estimated through an appropriate thermal model. In the ECM discussed in the following sections, operating temperature estimated from the thermal model is utilised to parameterise the model impedance parameters as they represent cell internal processes. Furthermore, if temperature is measured at the core, a better thermal control can be effected [104]. This could be more appropriate, allowing better separation of thermal and electrical phenomena by maintaining exact isothermal conditions during the experiment.

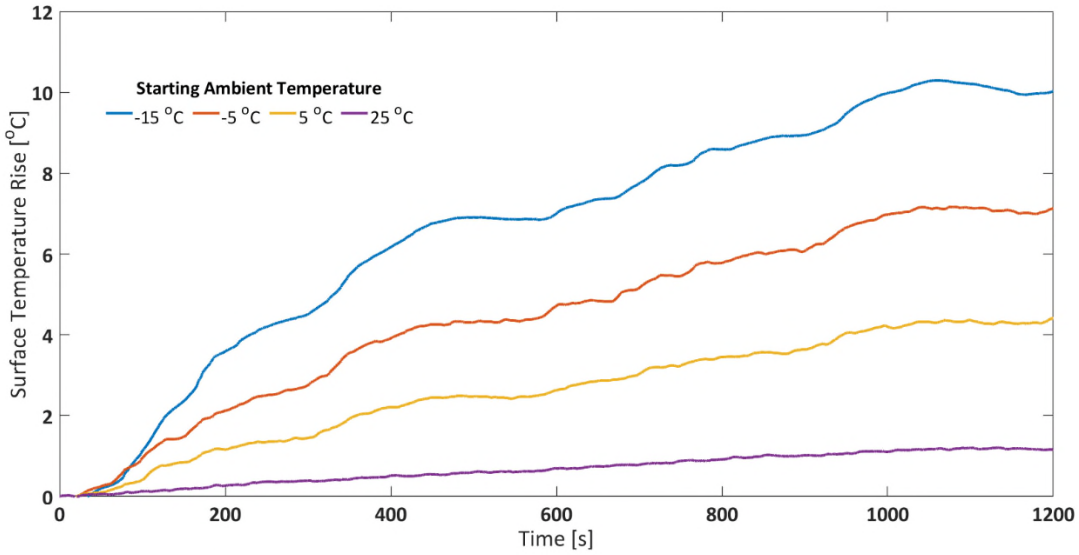

Figure 66. Experimental Surface Temperature Rise for Experimental 2xUS06 for Different Starting Ambient Temperatures and 65% Starting SOC

For a particular drive cycle, the greater the surface temperature rise, the larger is the discrepancy between choosing air and oil based parameters to estimate the SOC (Table 12). For example, at 25 ℃, the surface temperature rise experimentally recorded for the 2xUS06 is only 1.2 ℃, so there is negligible difference between using air or oil based parameters for SOC estimation. However, at −15 ℃, the air based remaining SOC estimated is higher by 9.5% (absolute SOC difference) than the oil based remaining SOC. Correspondingly, the surface temperature rise is 10.2 ℃. This suggests that due to higher degree of internal heat generation at low temperatures, the SOC is likely to be overestimated if using air-based parameters because of mixing of electrical and thermal phenomena. Therefore, it is recommended that parameters collected from isothermal or close to isothermal test setup are used, such as the oil-based setup presented here. This will ensure that the capacity values used to populate the look-up tables are obtained accurately. This will ensure better estimation of SOC evolution and in turn, improve range prediction accuracy.

Table 12. Comparison between Remaining SOC Estimated from Air and Oil based Parameters and Surface Temperature Rise Obtained from Experiments

Ambient Temperature [°C]	Remaining SOC (Air) [%]	Remaining SOC (Oil) [%]	Absolute SOC Difference [%]	Actual Surface Temperature Rise [°C]
−15	33.4	23.9	9.5	10.2
−5	35.1	30.2	4.9	7.1
5	37.4	34.7	2.7	4.4
25	40.6	40.5	0.1	1.2

6.2.2 SOE Estimation

Using the experimental data obtained for the 2xUS06 cycling at −15 °C starting ambient temperature, the end SOE estimated from the model for the air case was 36.4% and that for the oil case was 20.1% (Figure 67). The absolute difference in SOE between the two approaches is 16.3%. Assuming a 100 mile remaining driving range for 100% SOE, the remaining driving range would therefore be 16.3 miles lower for the oil-based approach compared to the air-based approach.

Similar to the validation for SOC, assuming a 148 Wh capacity from the OCV characterisation in Chapter 4, the approximate real SOE was 15.8% (obtained from experiment). Therefore, employing an air parameterised dataset will lead to inaccurate assessment of usable energy as well and cause models to overestimate remaining driving range compared to those parameterised using oil cooling, using data from the cell closer to the desired parameterisation temperature.

Note, for both SOC and SOE there is still a slight overestimation for the model compared to the real values. This is because despite a sophisticated oil based thermal control system employed, there exists a marginal temperature rise within the cell internal layers which can only be validated or controlled by placing a temperature sensor at the cell core [169]. This is because, for the results reported in this thesis, the cooling effect of the Lauda unit is controlled by the Pt-100 placed on the cell surface rather than at the cell core.

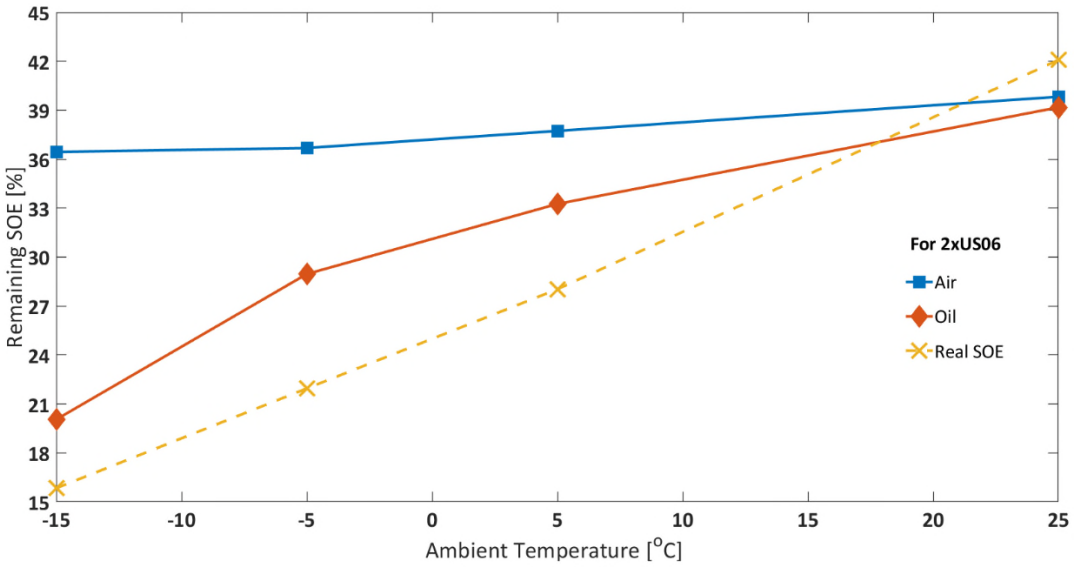

Figure 67. Comparison of Remaining SOEs: Effect of Using Air and Oil Parameters at Different Starting Ambient Temperatures (for 65% Starting SOC) for 2 back-to-back US06 Cycles (2xUS06)

Comparing Figure 65 and Figure 67, for the air cases, it should also be noted that as ambient temperature decreases, the SOE values tend to be higher than the SOC values (Table 12 and Table 13). For example, at −15 °C, for the air parameterisation case, while the remaining SOC is 33.4%, the remaining SOE is 36.4%. This trend is in contrast to that observed for the oil parameterisation cases. At −15 °C, for the oil case, while the remaining SOC is 23.9%, the remaining SOE is 20.1%. This is probably because of the higher degree of heat generation observed for the air based parameterisation data as the ambient temperature decreases (Section 4.2.1). This results in cell voltage being affected to the extent that it prolongs discharge. This is contrary to the assumption in literature that as ambient temperature decreases, the operating cell voltages would be lower and hence, the SOE should be lower than SOC [86]. Since temperature rise is minimal for the oil-based parameterisation data, the operating voltages for the parameterisation experiments are lower. This further affirms the hypothesis that isothermal control of battery model parameter experiments is required to adequately separate electrical and thermal phenomena, especially at lower operating temperatures.

Table 13. Comparison between Remaining SOE Estimated from Air and Oil based Parameters and Surface Temperature Rise Obtained from Experiments

Ambient Temperature [°C]	Remaining SOE (Air) [%]	Remaining SOE (Oil) [%]	Absolute SOE Difference [%]	Surface Temperature Rise [°C]
−15	36.4	20.1	16.3	10.2
−5	36.6	29.0	7.6	7.1
5	37.7	33.2	4.5	4.4
25	39.8	39.2	0.6	1.2

Overall, the results have demonstrated that maintaining isothermal test conditions during model parameterisation experiments have a direct effect on battery state calculation. However, the latest testing standards, such as the IEC 62660-1 and UNECE 38.3, only specify the ambient temperature. This is because most standards are defined to emulate testing for real-world performance of lithium-ion cells. However, for modelling purposes, particularly to parameterise models, there do not exist any testing standards. Most researchers and OEMs rely on engineering best practices to obtain repeatable data [60]. However, the effect of thermal boundary conditions during a charge/discharge process especially at low temperatures has been largely ignored. It is recommended that future testing standards should include adherence to isothermal test conditions and a maximum tolerance level away from isothermal conditions. This should allow for improvement to the quality of model parameterisation data and in turn battery state estimates relying on them.

6.2.3 Effect on Model Accuracy

In this section, it is investigated whether using oil-based SOC estimates instead of air-based SOC estimates leads to ECM performance improvements in terms of improving model accuracy in output voltage estimation. Furthermore, the effect of temperature and model order on the accuracy in output voltage estimation (V_{RMSE}) is discussed. In this section, both 1st order and 2nd order ECMs (1RC and 2RC, respectively) are considered. The validation duty cycle considered is the same as above i.e. 2xUS06 at different ambient temperatures for 65% starting SOC.

First, using the 1st order ECM (1RC), for the 2xUS06 drive cycle, the accuracy in output voltage estimation (quantified as a root-mean-squared error, V_{RMSE}) is compared at different temperatures (Figure 68). Initially, this is done for air-based SOC estimates which are used to parameterise the impedance parameters as per Section 5.1.3. It is shown below that model accuracy decreases as ambient temperature increases. For example, from 18.8 mV V_{RMSE} at 25 °C ambient temperature, the V_{RMSE} at −15 °C ambient temperature was 134.2 mV. This is in line with literature that model accuracy decreases as temperature decreases due to greater coupling of electrical and thermal phenomena [7,59,66]. It is also due to increased internal SOC and thermal gradients within the cell that cause non-uniform cell behaviour at low temperatures [65]. Lastly, in Section 5.1.3.3, it was shown that even for parameterisation datasets, model accuracy decreased as ambient temperature decreased (Figure 54).

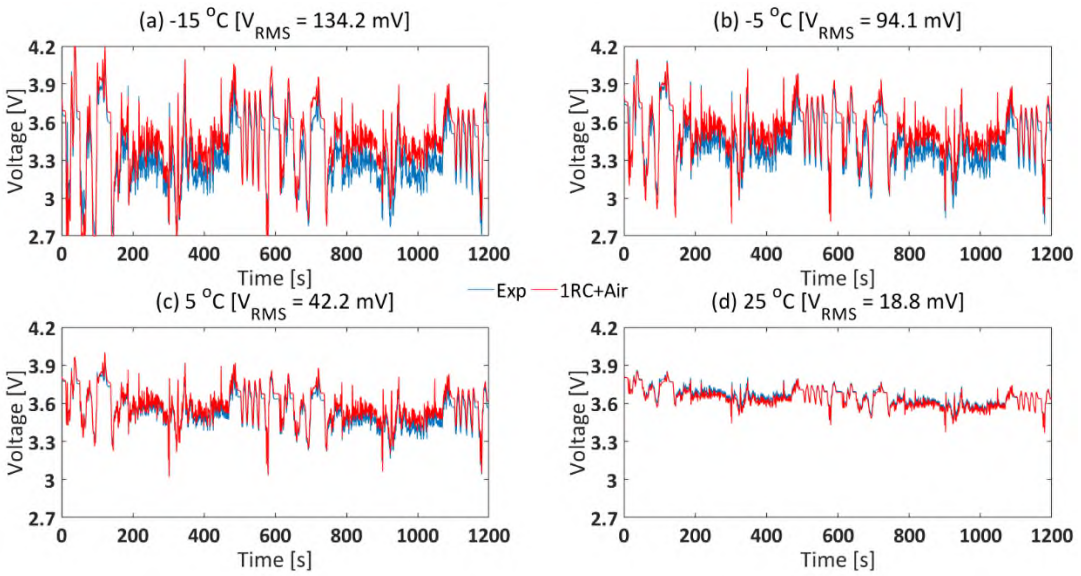

Figure 68. Output Voltage Estimation from **1RC and Air** based SOC ECM and Experimental Voltage Profiles for 2xUS06 for 65% Starting SOC at different Ambient Temperatures: (a) −15 °C, (b) −5 °C, (c) 5 °C and (d) 25 °C

Similarly, for the 1RC ECM with oil-based SOC estimates, as ambient temperature decreased from 25 °C to −15 °C, the V_{RMSE} increased from 19.0 mV to 101.4 mV (Figure 69). Furthermore, it should be noted that model accuracy for both (1RC+air) and (1RC+oil) was similar at 25 °C in terms of V_{RMSE}. However, as ambient temperature decreased, the (1RC+oil) model became more accurate than the

(1RC+air) model in terms of V_{RMSE}. For example, at 25 °C, while the difference between the two models is 0.2 mV, at −15 °C, the (1RC+oil) model has a 32.8 mV lower V_{RMSE} compared to the (1RC+air) model for the same experimental validation dataset. This suggests that using oil-based SOC rather than air-based SOC improves model accuracy in terms of output voltage estimation. This is probably because the oil-based SOC decreases faster compared to the air-based SOC, which allows higher internal resistances associated with lower SOC operation or with non-uniform cell behaviour to be captured more accurately (Figure 63).

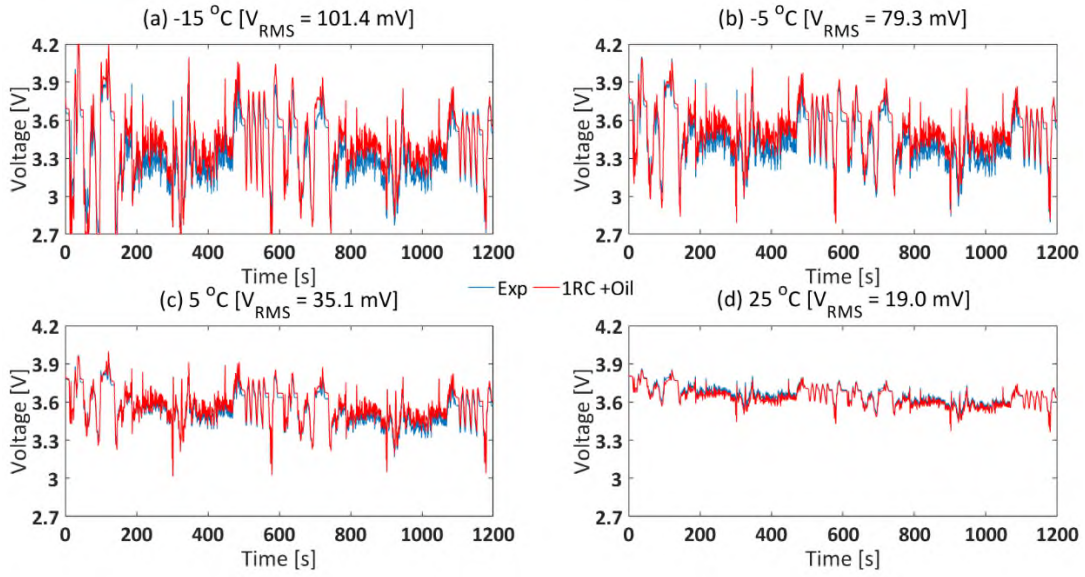

Figure 69. Output Voltage Estimation from **1RC and Oil** based SOC ECM and Experimental Voltage Profiles for 2xUS06 for 65% Starting SOC at different Ambient Temperatures: (a) −15 °C, (b) −5 °C, (c) 5 °C and (d) 25 °C

At −15 °C ambient temperature, although for the oil-based SOC case, the V_{RMSE} was 101.4 mV overall, the V_{RMSE} for the 1st US06 was 109.4 mV and that for the 2nd US06 was 92.6 mV (Figure 70 a & b). This is in contrast to the air-based SOC case, where the V_{RMSE} was higher - 134.2 mV overall for the 2xUS06, and that for the 1st and 2nd US06 cycles were 127.6 mV and 140.5 mV, respectively. As shown in Figure 70c, at the end of the 1st and 2nd US06 cycles at −15 °C starting temperature, the end SOCs for the air parameters were 48.9% and 33.4%, respectively. Whereas for the oil case, the end SOCs were lower at 42.9% and 23.9%, respectively (Figure 70d). This further

implies that the oil-based SOC captures the real cell behaviour better compared to the air-based SOC, resulting in lower modelling errors as the duty cycle progresses.

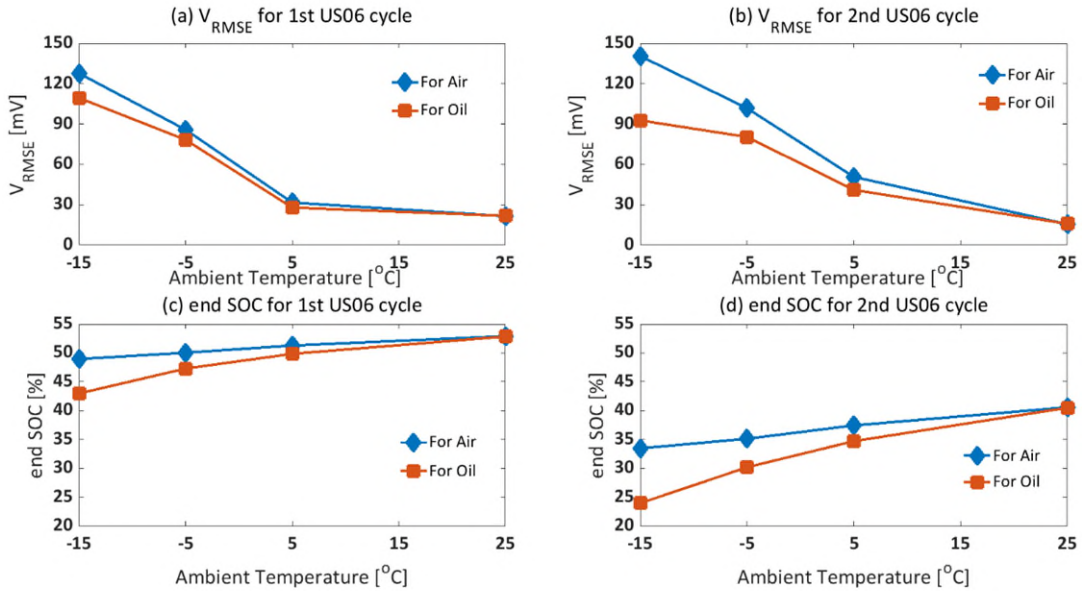

Figure 70. Correlation between Accuracy in Output Voltage Estimation (V_{RMSE}) and SOC Evolution at Different Starting Ambient Temperatures for 1st Order ECM: Investigating the Effect of Air and Oil Based SOC Estimation

In Figure 71, the results contrasting the effect of air-based and oil-based SOC estimation on estimated voltage errors for both 1st and 2nd order ECMs are presented. As discussed above and as shown in Figure 71a, at lower temperatures, using oil-based SOC leads to improved accuracy in output voltage estimation. Similar conclusions can be made for the 2RC ECM (Figure 71b). This figure suggests that as ambient temperature decreases, a greater degree of non-uniformities are caused within the cell, probably due to mass transport limitations. This results in effectively a lower usable capacity that is better captured by the oil-based SOC compared to the air-based SOC. Note that the improvement in model error is lesser for the 2nd order ECM compared to the 1st order ECM. This could be because the 2nd RC network impedance values are captured similarly for both air and oil-based cases.

The findings in this section support that usable capacity values obtained from close-to-isothermal testing are employed for parameterising/modelling lithium-ion cells, particularly for low temperature applications. The improvements compared to

traditional (air-based) parameterisation are two-fold: battery state variables (SOC/SOE) are tracked better and model performance improves in terms of accuracy in output voltage estimation.

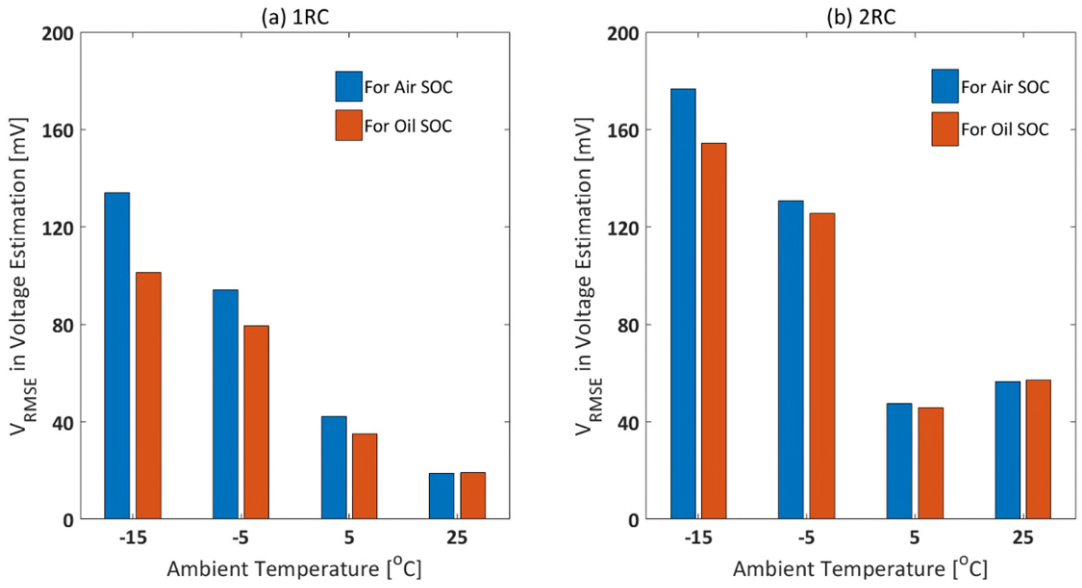

Figure 71. Comparison between Accuracy in Output Voltage Estimation at Different Temperatures for both 1st and 2nd Order ECMs (1RC and 2RC): Effect of Air and Oil Based SOC Estimation

6.3 Effect of Thermal Feedback Subsystem on ECM Performance

As discussed in Section 5.1.4, separate currents depending on the model structure (R_0, R_{Pn} and τ_n) were employed to estimate the heat generated from each resistive element of the ECM. This is because the polarisation currents in each RC network are time dependent and depend not just on the load current but also on the corresponding time constant (or capacitance value). This is in contrast to traditional ECMs which employ a common current (usually the Ohmic current) to estimate heat generation. Further, the 'separate currents' approach was used for the results reported in Section 6.2.3. The following section illustrated the advantages of this approach over the traditional 'common current approach'. Here, a 1st order ECM is used to investigate the difference between the 'separate currents' and 'common current' approaches as it has a single polarisation element. In this section, only oil-based, rather than air-based, SOC

estimates are used for validation as they led to better ECM accuracy. As an example, in Figure 72, the polarisation current and the total load current (Ohmic current) are illustrated for the 2xUS06 at −15 ℃. Note, the polarisation current and the corresponding heat generation calculations/equations were detailed in Section 5.1.4.

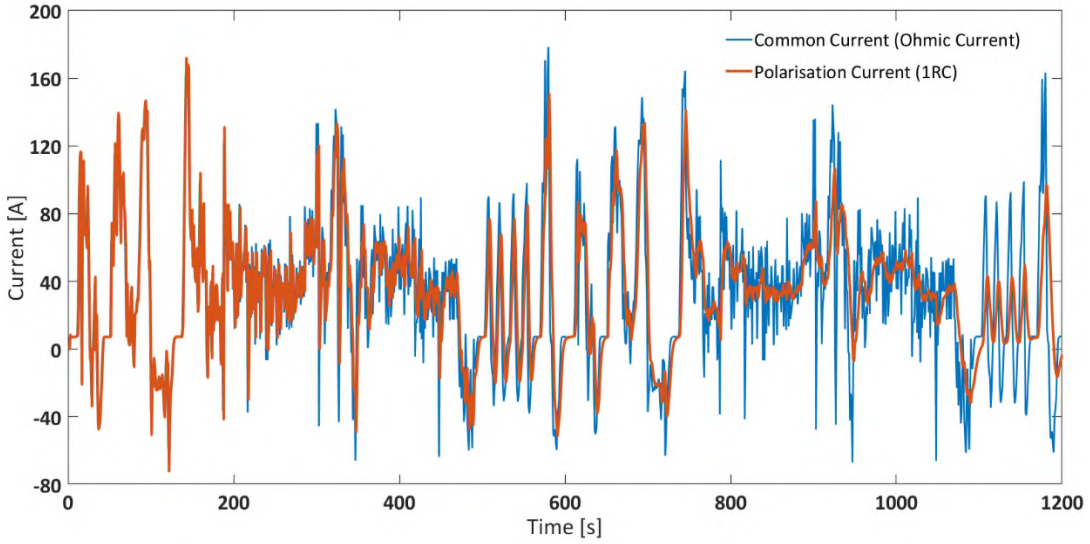

Figure 72. Total Load Current Profile and Polarisation Load Current Profile for 2xUS06 for 65% Starting SOC at −15 ℃ Ambient Temperature using 1RC ECM

In Figure 73a, the heat generation rates in the RC element for both ‘common current’ and ‘separate currents’ approaches are illustrated for the 2xUS06 at −15 ℃ using a 1RC ECM. The waste energy passing (in Wh) through the RC network is 2.49 Wh for the ‘common current’ approach compared to 2.15 Wh for the ‘separate currents’ approach (Figure 73b). Therefore, for this drive cycle, the heat generated by the RC element is overestimated in the ‘common current’ approach by 15.8% compared to in the ‘separate currents’ approach. This is because instead of using the load current, the polarisation current (calculated based on Equation 58) is used.

Similarly, the total waste heat (in Wh) is also higher for the ‘common current’ approach compared to the ‘separate currents’ approach (higher by 4.3%) (Figure 73c). Following which, the operating temperature rise for both approaches is also different with final operating temperature for the ‘common current’ approach being 0.9 ℃ higher than for the ‘separate currents’ approach. This suggests that heat generation rates are overestimated in the ‘common current’ due to inaccurate consideration of the

heat generated by the different impedance element. To show that the 'separate currents' approach is more accurate than the 'common current' approach as part of the thermal feedback subsystem in the ECMs considered, the accuracy in modelling the surface temperature rise compared to the experimental values should be considered. Furthermore, the effect of the difference in operating temperature estimates on the ECM should be quantified in terms of modelling accuracy in output voltage estimation. The surface temperature was estimated based on the subsystem described in Figure 57 (Section 5.1.4).

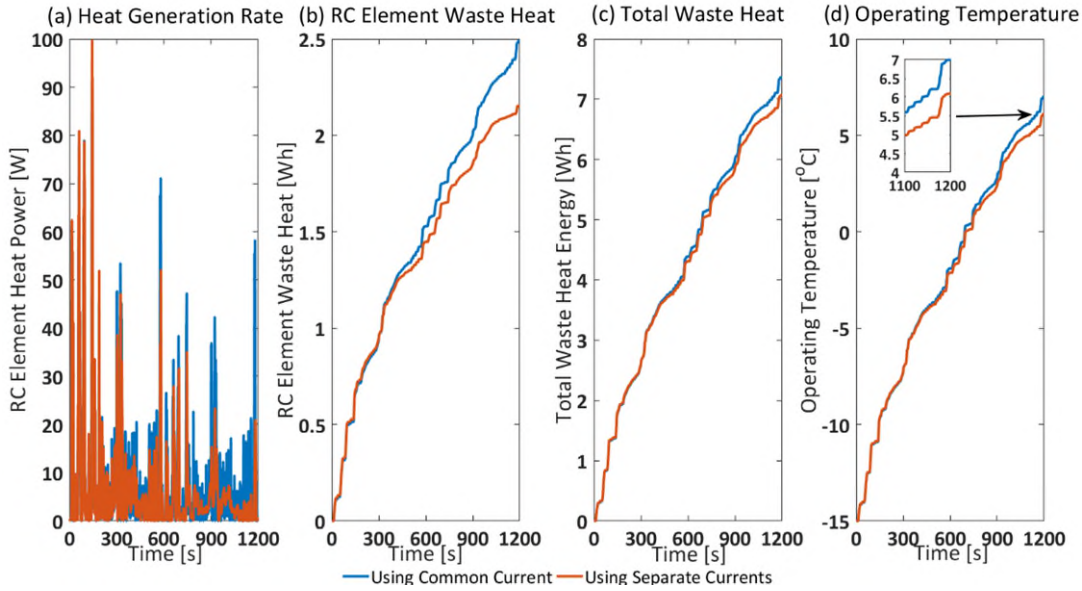

Figure 73. (a) Heat Generation Rate in RC Element, (b) Waste Heat Generated in RC Element, (c) Total Waste Heat Generated by Model and (d) Operating Temperature Evolution for Common Current and Separate Current Approaches using 1RC ECM for 2xUS06 for 65% Starting SOC at −15 °C Ambient Temperature

As illustrated in Figure 74, it was found that for −15 °C starting temperature, the T_{RMSE} for the 'separate currents' approach was 1.4 °C; lower than the T_{RMSE} for the 'common current' approach (2.5 °C). This supports the hypothesis that using a 'separate currents' approach may be advantageous in terms of accurately capturing the thermal behaviour of a cell, particularly at low temperatures. Further, the surface temperature at the end of the drive cycle for the 'common current' approach was −2.2 °C (estimating a temperature rise of 12.8 °C). However, the surface temperature at the end for the 'separate currents' approach was −7.4 °C. The actual surface temperature

was measured to be −4.8 °C. These results further support the suggestion above that heat generation rates are over-predicted if a 'common current' is employed. Finally, as shown in Figure 75a-b, for both 1RC and 2RC ECMs types, choosing 'separate currents' leads to improved accuracy in capturing the surface temperature evolution of the cell for the 2xUS06 validation drive cycle at different ambient temperatures.

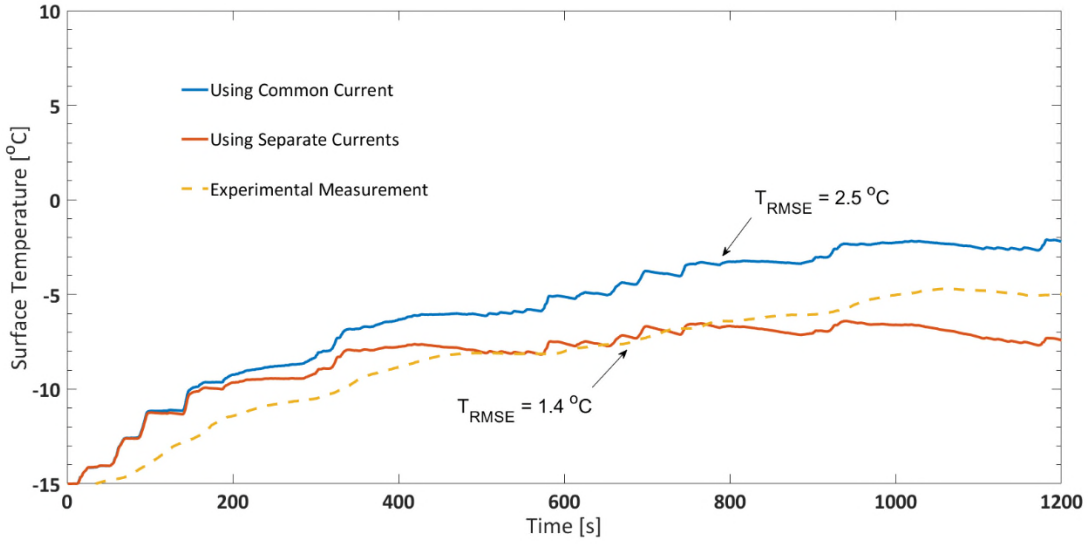

Figure 74. Surface Temperature Estimation for Common Current and Separate Current Approaches c.f. Experimentally Measured Surface Temperature for 1RC ECM for 2xUS06 for 65% Starting SOC at −15 °C Ambient Temperature

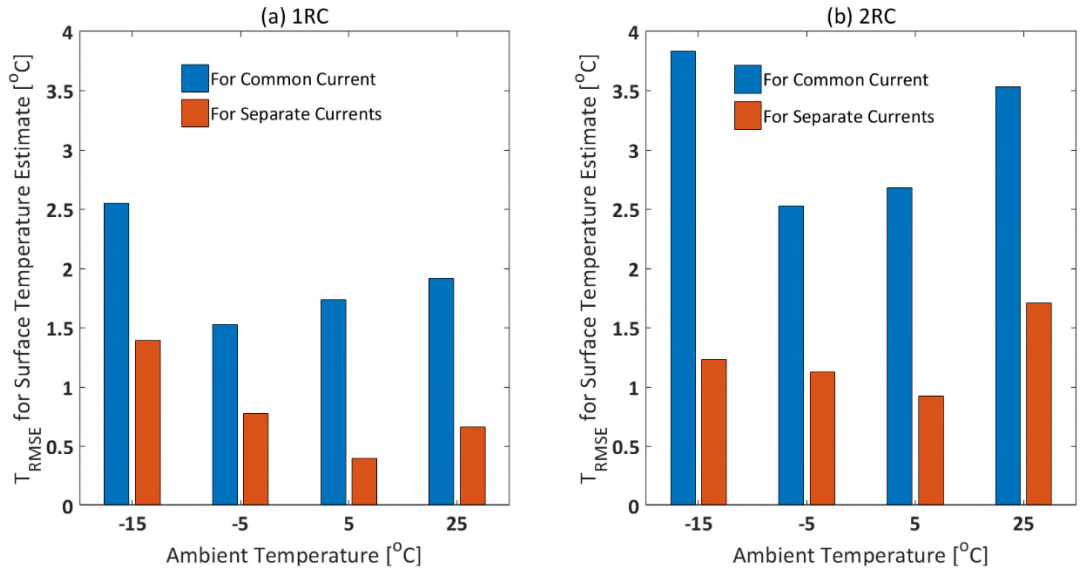

Figure 75. Comparison between Accuracy in Surface Temperature Estimation at Different Ambient Temperatures for both 1st and 2nd Order ECMs (1RC and 2RC): Effect of Choosing Separate Currents or Common Current for Thermal Feedback

To confirm that the 'separate currents' approach is better, the accuracy in output voltage estimation (in terms of V_{RMSE}) was compared. Within an ECM, in an RC network circuit, the capacitor acts as a high pass filter. This is validated by conducting a Fast Fourier transformation (FFT) of the drive cycle power profile at the different validation ambient temperatures. The FFT was conducted by using the MATLAB 'fft' function directly. So, when the branch current (polarisation current) was accounted for, higher frequency currents did not pass through the polarisation resistor (Figure 76). In which case, the polarisation resistor is heated up by a lower frequency current. The higher the frequency content of the duty cycle (more transient), the more the polarisation current is important and therefore would be more accurate than considering just an Ohmic current. This is probably the reason why, even at 25 ℃ ambient temperature, as the time constants are longer indicating greater capacitive effect, the surface temperature estimation is more accurate for the separate currents approach compared to the common current approach (Figure 76d).

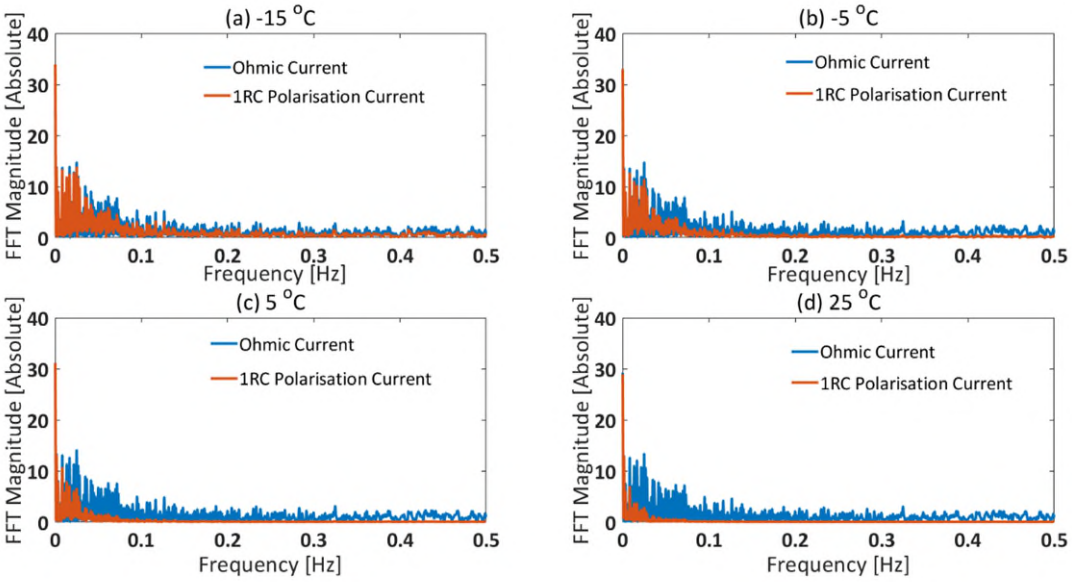

Figure 76. FFT of 2xUS06 Drive Cycle Power Profile at Different Starting Ambient Temperatures for 1st Order ECM: (a) −15 ℃, (b) −5 ℃, (c) 5 ℃ and (d) 25 ℃

As the RC parameters are updated based on the operating temperature, this could have a direct effect on model accuracy (in terms of output voltage estimation). As illustrated in Figure 77a, although there is a marginal increase in model accuracy for the 1RC ECM, a greater degree of improvement is seen if separate currents are used instead of

common current for the 2RC ECM type (Figure 77b). For example, at −15 °C, if a common current approach is chosen, the V_{RMSE} is 209.9 mV. However, if a separate currents approach is chosen, the V_{RMSE} decreases to 154.4 mV. This supports the hypothesis that the method to estimate heat generated in an ECM has a direct effect on its accuracy in terms of output voltage estimation. The effect on output voltage estimation is not as pronounced as on surface temperature estimation. However, accurate surface temperature estimates are critical to model reliability.

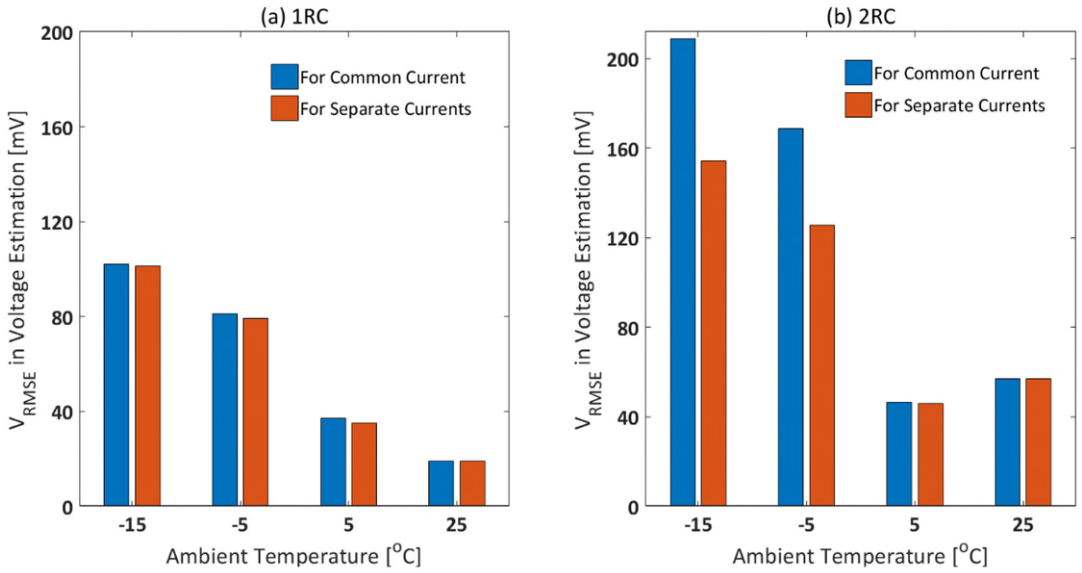

Figure 77. Comparison between Accuracy in Output Voltage Estimation at Different Ambient Temperatures for (a) 1st and (b) 2nd Order ECMs (1RC and 2RC): Effect of Choosing Separate Currents or Common Current for Thermal Feedback

6.4 Summary

In this chapter, **Objective IV** of this thesis is addressed.

The primary objective of this chapter was to examine the effect of experimental parameterisation data on subsequent battery models. In particular, the benefits of choosing oil-based parameters over air-based parameters on battery state evolution were examined. The findings in this chapter support that usable capacity values obtained from close-to-isothermal testing are employed for parameterising/modelling lithium-ion cells, particularly for low temperature applications. This is because maintaining isothermal test conditions during model parameterisation experiments

have a direct effect on battery state calculation. It was shown that, battery SOC/SOE estimates parameterised using oil-based datasets were shown to be closer to real-world battery performance. Furthermore, using 1st and 2nd order ECMs, it was shown that using oil-based SOC rather than air-based SOC improved model accuracy in terms of output voltage estimation. Thus, it is imperative that at least at a model parameterisation stage, electrical and thermal effects on battery performance are adequately separated.

The significance of ensuring isothermal operating conditions has been overlooked as most battery testing and modelling validation is conducted at higher operating temperatures where the degree of internal heat generation and their impact on usable capacity are lower. In this chapter, it was shown that difference between battery states (SOC and SOE) estimated from air and oil based datasets increased as ambient temperature decreased; with oil-based SOC/SOE being substantially lower. Thus, the improvements from close-to-isothermal (oil-based) parametrisation compared to traditional (air-based) parameterisation are two-fold: battery state variables (SOC/SOE) are tracked better and model performance improves in terms of accuracy in output voltage estimation.

It has been shown for the first time in this study that the 'separate currents' method of calculating heat generated within an ECM positively affects the accuracy of an ECM in terms of modelled surface temperature estimation and output voltage estimation. The effect of thermal feedback on model accuracy validates greater coupling of electrical and thermal phenomena, particularly at lower ambient temperatures. Furthermore, it supports the argument that modelling assumptions that are acceptable at higher operating temperatures (say, 25 °C) may become detrimental to model performance at lower operating temperatures.

The above findings can potentially help standardise the approach for a model-based design process (in particular, methods to experimentally obtain model parameterisation data), leading to improved performance estimation of lithium-ion cells in real applications. This will ultimately improve the reliability of battery range predictions for electric vehicles, particularly in cold weather conditions.

7. Discussion and Future Work

Discrepancy in estimated range is accepted as the norm in conventional IC engine based vehicles. For example, in terms of real-world usage, the reduction can be up to 22% compared to the range advertised (at 18 ℃, based on WLTC) by the manufacturer [170]. Similarly, for EVs, this discrepancy is also known to customers [171]. However, the issue with estimated range becomes more prominent at low temperatures [43,172]. At low temperatures, for EVs, the discrepancy between advertised range and actual range increases by a large margin. This creates an issue in regions which have low temperatures such as Norway, Sweden and large parts of North America. For example, before a road test for the Nissan Leaf at about −15 ℃, the initial estimated range was 126 miles (compared to 151 miles claimed) [54]. However, after an actual 64 mile journey, the estimated range decreased by 116 miles. This indicates an initially overestimated range by almost 45%. Clearly, the estimated driving range displayed at the beginning of the journey was inaccurate. This thesis provides insight into the fundamental cause of such discrepancies and proposes novel methods to reduce them.

The primary objective of this chapter is to bring together the contributions from the results chapters and highlight novelty and significance in the context of the gaps highlighted in the literature review (Section 7.1). Future avenues of research are also proposed in this chapter and ongoing research work is outlined (Section 7.2).

7.1 Discussion

Countries like Norway and Sweden, and large parts of continental Europe and North America, are characterised by seasonally extreme cold weather down to −20 °C [5,34]. In these conditions, a lithium-ion battery's capacity, maximum output power and charge acceptance capability are reduced. These manifest as reductions in driving range and performance of EVs at low ambient temperatures [42]. These reductions are worsened by increased energy/power demands due to higher cabin heating requirements in cold weather conditions [44,45]. For instance, the real-world range of the latest Chevy Bolt was ~184 miles at −2 ℃ [42,43]. This is a substantial reduction (29.8% less) from the 263 mile range advertised as per the WLTC (at 18 ℃). Low temperatures also lead to large inaccuracies in range estimation of EVs [54,173],

unlike at higher temperatures (between 18 to 25 ℃), where the range estimates are close to the actual distances driven [171]. For example, for a road test conducted at around −15 ℃, a Tesla Model 3 showed a predicted range of 293 miles [54]. However, after a 64 mile journey, the remaining range decreased by 104 miles. This suggests that the range displayed initially was overestimated by 38.4%. The range estimation inaccuracy, in particular at low temperatures, is largely due to the increased errors in estimating the underlying battery states such as SOC or SOE [7,122]. Nejad *et al*. stated that, at low temperatures, existing battery models fail to capture the slower dynamics of internal electrochemical processes of the on-board battery pack [7]. This indicates that battery model parameters or the underlying parameterisation data could be the source of modelling error. This in turn implies that the battery model parameters should be captured accurately from experiments at low temperatures to ensure applicability in real-world cold weather conditions [59,99].

7.1.1 Advantages of Close-to-Isothermal Model Parameterisation and Battery State Estimation

The environmental requirements for battery testing can be different, based on whether the data is used to assess battery performance or to parameterise battery models. For instance, rapid heat generation is critical to improving battery performance at low temperatures [82]. This is confirmed by results in Section 4.2, Table 7, showing that at −20 ℃ ambient temperature, as discharge C-rate increased from 0.25C to 3C, the capacity discharged increased from 31.9 Ah to 34.7 Ah. This is largely related to suppression of internal cell resistances as the internal layers of the cell get hotter as discharge progresses [97]. This was demonstrated in Section 4.2.1, Figure 34, where for −20 ℃ ambient temperature, at the end of 1C discharge cycle, the cell surface temperature was −3.9 ℃, deviating by 16.1 ℃ from the starting ambient temperature. This leads to inhibited cell overpotentials, leading to sustained discharge and apparent benefits to cell discharge performance. This rapid heat generation is beneficial to battery performance in the real-world by allowing the cells to reach more favourable operating temperatures more quickly. This is probably the reason why previously battery modellers used experimental data which were not obtained at isothermal conditions as they assumed that the data represented real-world conditions. But the

issue is different in state-of-the-art battery models as fundamental parameters need to be quantified accurately first; then the variation coming from a secondary (such as thermal) effect should be introduced. That is, if a particular battery performance metric is being quantified as a function of two parameters, viz. current and temperature, then the two parameters should be independent of each other. Thus, for battery model parameterisation it is crucial that battery testing is conducted in isothermal environmental conditions, to separate electrical and thermal processes.

Usable capacity, obtained from galvanostatic battery experiments at different temperatures and C-rates, is employed to directly model battery performance and in turn EV range under different operating scenarios for automotive applications [60]. However, by allowing the battery temperature to deviate from the starting ambient temperature, the electrical and thermal effects become convoluted. For example, it is possible that if battery temperature was held constant at −20 °C, as reported in Section 4.2.1, Figure 34, the capacity discharged from the cells would have been lower than the 32.2 Ah obtained from air-based experiments. In Section 4.2, additional DCR measurements and residual capacity experiments confirm that data generated in air based experiments are representative of much higher temperatures, than that reported.

This lack of isothermal test conditions during battery model parameterisation experiments could be the reason for inaccuracies in EV range estimation, especially in winter conditions. Inaccurate quantification of usable capacity of lithium-ion batteries could also be the reason why BEVs run out of driving range even if the dashboard indicator suggests otherwise [52]. Furthermore, there is a vast literature on lithium-ion cell models, where researchers have claimed that model parameters have been obtained from battery experiments conducted under isothermal conditions, see for example [7,33,58,122,123]. On closer examination of the literature, claimed isothermal conditions are often found to be non-isothermal.

In fact, substantial literature attests to the rapid heat generation seen in lithium-ion batteries at low temperatures and how that is a potential performance enhancement strategy [65,82,174]. However, there is very little literature investigating whether claimed isothermal test conditions in literature are actually maintaining their thermal boundary conditions [99].

In recent work, using an electrochemical model, Ardani *et al.* concluded that by conducting experiments in environmental chambers based on forced air convection, internal cell properties such as diffusivity and conductivity are representative of higher temperatures rather than the pre-set lower ambient temperature [99]. For stepped discharge (10% SOC change with 30 minute intermittent rest periods) experiments, claimed to be conducted at 5 °C ambient temperature, they suggested that the physiochemical parameters obtained were actually more representative of 10 °C. Their research did not consider the more extreme case of continuous discharge which is critical to quantifying the usable capacity of a lithium-ion cell and hence estimating EV range, especially for lower temperatures.

There is no clear distinction between how battery experiments are conducted for performance characterisation and model parameterisation. Researchers assume that the environmental conditions are isothermal, but this is not the case. Very few researchers have investigated the effect of non-isothermal test conditions on battery model parameters [99]. In fact, no research has been undertaken to quantify the effect of isothermal model parameters on model performance and battery state estimation. In this thesis, this gap in knowledge is identified, confirmed using state-of-the-art experiments and then addressed by proposing a novel immersed oil-based isothermal experimental setup.

In the present study, to try and separate battery electrical and thermal phenomena, a novel immersed oil bath based cooling system was proposed (Section 4.1.1, Figure 31). The experimental setup was not intended for examining the thermal management system but to allow for battery testing under isothermal environmental conditions. To the best of the author's knowledge, this is the first time in literature that an isothermal experimental setup to measure usable capacity/energy has been proposed. In this work, it was evidenced that, compared to traditional air-based model parameterisation, isothermal model parameterisation using immersed oil bath could lead to improved BMS range estimation accuracy of EVs operating at low temperatures.

Using immersed oil cooling, it was reported in Chapter 4 that at the same starting ambient temperature, the capacity and energy discharged for a particular C-rate is lower than that recorded for air cooling. These results demonstrate the importance of

battery temperature on its electrical characteristics. It was shown that as starting ambient temperature decreased and/or discharge C-rate increased, the capacity discharged for the air cooling case was higher than that for the oil cooling case. Battery models and particularly, state estimation algorithms have utilised non-isothermal capacity/energy values for parameterisation. By allowing battery temperature to deviate from the pre-set ambient temperature, the parameters obtained become unreliable and the experiment itself inconsistent. This is because different thermal chambers will have different heat transfer properties depending on the model (such as Espec [82] or Neware [175]) and their heating/cooling capabilities. However, isothermal testing will ensure that primarily the true electrical characteristics of the lithium-ion cells are extracted as any thermal behaviour is eliminated. This will make battery testing more accurate, and allow better repeatability; similar to how a calorimeter is employed to measure the true heat generation during a battery charge/discharge operation [176].

Recently, it has been suggested that energy (in Wh), rather than capacity (in Ah), should be employed as the primary parameter for estimating remaining driving range (RDR) [56,87]. It was shown in Chapter 4 that the effect of isothermal operating conditions is more prominent on discharged energy rather than on discharged capacity. This is because the operating voltages for the oil cases are lower than that for the air cases. Hence, the power delivery capability of the cell is reduced if the oil-based approach is employed rather than the air-based approach. Thus, using a traditional air-based approach would also lead to overestimated battery power capability by underestimating battery resistance. This could also explain why commercial EVs suddenly lose power despite the battery being at a high enough SOC [83]. In Section 5.1.3, Figures 50-51, due to increased heat generation, the DC resistance of the cells is shown to decrease as the magnitude of the current pulse increases. Thus, even for pulse power characterisation, isothermal test conditions are crucial to ensuring that battery power capability is quantified accurately. Otherwise, it is possible that the DC resistances obtained for different SOCs and temperatures, are only characterised for a few hotter layers within a lithium-ion cell and do not represent the entire cell [97,115].

Accurate assessment of usable capacity/energy characteristics is particularly important for range estimation algorithms which consist of look-up tables with current and

temperature as inputs [177]. In look-up tables, capacity is a function of current and temperature. These should both be independent of each other as to elicit the effect of one variable on battery capacity, the other should be kept constant. However, by allowing cell temperatures to change substantially, the result is a convoluted effect of temperature and current on the discharged capacity/energy. Despite this, in the latest testing standards, such as the IEC 62660-1 and UNECE 38.3, only the ambient temperature is specified [60,103]. This is because most standards are defined to emulate testing for real-world performance of lithium-ion cells. However, for modelling purposes, particularly to parameterise models, there do not exist any testing standards. It is recommended that future testing standards should include adherence to isothermal test conditions and a maximum tolerance level away from isothermal conditions. This should allow for improvement to the quality of model parameterisation data and in turn battery state estimates relying on them.

To validate the importance of isothermal model parameterisation experiments at a modelling stage, scaled-down cell level versions of realistic driving scenarios were considered. Using two back-to-back US06 drive cycles (2xUS06) it was shown that SOC/SOE estimated using oil parameters was closer to how the actual cells behaved compared to estimates using air parameters. For example, employing an immersed oil-cooled experimental setup it was found that battery state estimation reduced absolute SOC error from 13.5% to 5.1% at −15 °C. It was also shown that greater the surface temperature rise for a particular drive cycle, the larger is the discrepancy between choosing air and oil based parameters to estimate battery states. This is illustrated in Section 6.2.1, Table 12. This suggests that if the battery temperature deviates substantially during the parameterisation experiments, it leads to overestimation of battery states and subsequently, inaccurate assessment of vehicular remaining driving range. This is consistent with findings of Ardani *et al.* who reported that solid-phase diffusivity and ionic conductivity values are overestimated at low temperatures [99]. Therefore, it is recommended that parameters collected from close-to-isothermal or better isothermal test setup, such as the oil-based setup proposed, should be considered for parameterising battery state estimation algorithms.

Artificial reduction in capacity has also been previously employed by limited researchers as a tool to improve model performance at low temperatures [40,59,138].

Nikolian *et al.* utilised 'optimised capacity' to estimate SOC at 5 °C for WLTC drive cycles [59]. This 'optimised capacity' was a mathematical value which led to minimisation of the modelled voltage error. They showed that the 'optimised capacity' was lower than that obtained for nominal 0.2C discharge; which led to improvement in model accuracy. They attributed this to slower electrochemical dynamics. However, this could also be due to overestimation of battery capacity from using a thermal chamber (manufactured by CTS, series C-40/350 L) to conduct the experiments.

In this study, it was shown that oil-based capacity values rather than air-based capacity values lead to improved accuracy in voltage estimation for both 1st and 2nd order ECMs, particularly at low temperatures. This could be because lower capacity values better capture cell internal non-uniformities that arise due to low temperature induced potential and concentration gradients. This argument is supported by the observation that for the 2xUS06 validation cycle, the improvements to V_{RMSE} due to using oil-based SOC over air-based SOC were higher for the 2nd US06 phase (Figure 70). At the same time, the oil-based SOC decreased at a much faster rate compared to the air-based SOC. This feature could be similar to the reversible capacity fade concept suggested by Singer *et al.* [40]. They found that even for pseudo-OCV tests, the cell capacities are reduced at low temperatures. This reversible capacity fade could also be due to SOC and temperature gradients within the layers of the cell (with internal layers being hotter), potentially causing localised measurements, even for low C-rates.

Thus, it is recommended that for model parameterisation oil-based capacity values, obtained under close-to-isothermal conditions, should be used rather than air-based capacity values. The improvements are two-fold: battery state variables (SOC/SOE) are tracked better and model performance improves in terms of accuracy in output voltage estimation.

7.1.2 Model Prediction Improvements through Consideration of Polarisation Currents for Thermal Feedback

A battery thermal management system is critical to ensuring optimal battery performance and maintaining safe operation [69,75]. Within this, it is important that the heat generated inside a battery pack (and cells) is estimated accurately. To achieve

this in real-time, the accuracy of the thermal feedback subsystem is critical to ECM performance as it helps update the electrical parameters dynamically as battery temperature changes [74]. This is particularly important at low temperatures, where a greater coupling between electrical and thermal battery phenomena exists [58]. However, it is known that accuracy of thermal models in predicting cell temperature evolution decreases as temperature decreases [91]. For example, Hosseinzadeh *et al*. showed that for a WLTC cycle, the peak error in estimating the temperature profile increased from 5.3% at 25 ℃ to 12.1% at 5 ℃ [91]. Thus, further research is required into how cell behaviour is modelled thermally at lower temperatures.

The majority of thermal models in literature make certain assumptions such as ignoring reversible heat generation [178] by arguing that the larger irreversible heat component decreases its influence particularly at higher C-rates [179]. In literature, if reversible heat generation is ignored, the total cell heat generation rate (Q_{gen}) is calculated as in Equation 45b. Equation 45b is reproduced here for convenience:

$$Q_{gen} = I_{input}^2 \times (R_O + R_{Pn}) \tag{45b}$$

Here, it is assumed that that the heat generated by the various impedance elements is dependent on the Ohmic current (which is the input current) and the various resistances (Ohmic and polarisation). However, as shown in Equation 46, the heat generation rate (Q_{gen}) should be separated into two components depending on the number of RC networks (heat generated from the Ohmic resistances and heat generated from polarisation resistances). Equation 46 is reproduced here for convenience:

$$Q_{gen} = I_{input}^2 \times R_O + I_{Pn}^2 \times R_{Pn} \tag{46}$$

To calculate heat generated from the polarisation resistances, the time dependent current (polarisation current) flowing through the RC circuits should be considered separately. This has physical basis in the characteristic times of the different internal cell processes such as diffusion and charge transfer. Thus, depending on the time elapsed and the current flowing through the RC networks, the heat generated from each impedance element in the ECM would be different and could potentially affect model performance.

It has been shown for the first time in this study that the 'separate currents' method of calculating heat generated within an ECM (by including polarisation currents in thermal feedback subsystem) directly affects the accuracy of an ECM in terms of modelled surface temperature estimation and output voltage estimation. As discussed in Chapter 6, Section 6.3, using separate currents method leads to improved accuracy in estimating cell surface temperature evolution for both 1st and 2nd order ECMs. Similarly, the accuracy in output voltage estimation is also improved; albeit to a lesser extent. For example, for the 2xUS06 drive cycle at −15 °C, the root-mean-squared error in surface temperature estimate decreased from 3.8 °C to 1.2 °C if separate currents method was used instead of common current method. Correspondingly, the root-mean-squared error in terminal voltage also decreased from 209.9 mV to 154.4 mV. This effect of thermal feedback on model accuracy validates greater coupling of electrical and thermal phenomena, particularly at lower ambient temperatures. This further suggests that there is a more intricate coupling of electrical and thermal behaviour as ambient temperature decreases, particularly due to the temporal and spatial temperature gradients within the cell. These localised effects and deviations from average behaviour arise from the edge and geometrical aspects of the cell [141].

Osswald *et al.* stated that, particularly at low temperature, there exist gradients in current distribution within a cell, which is frequency (and thus, time) dependent [115]. Within an ECM, in an RC network, the capacitor acts as a high pass filter (as shown in Section 6.3, Figure 76). So, when the branch current (polarisation current) is accounted for, higher frequency currents do not pass through the polarisation resistor. In which case, the polarisation resistor is heated up by a lower frequency current. The higher the frequency content of the duty cycle (more transient), the greater the increase in accuracy that would arise from considering polarisation currents rather than considering just an Ohmic current. Thus, based on the method of calculating heat generation within an ECM, the surface temperature estimates are different, that also lead to improved accuracy in output voltage estimation.

A key objective of the IEC 62660-1 standard is to obtain the essential characteristics of lithium-ion cells to be used for the propulsion of electric road vehicles (BEVs/HEVs) [180]. This implies that if a lithium-ion cell is to be used as a part of an automotive battery, the duty cycles used for characterising these cells should be

representative of the real-world. However, as discussed in Chapter 2, Section 2.2.2, most battery testing for legislative drive cycles is conducted using current control as the default approach. While this approach ensures that consistency in capacity throughput is maintained across all operating scenarios, energy throughput is not maintained. For example, in a battery cycle life test conducted by Keil *et al.* current control is employed to cycle the cells until end-of-life [49]. This means that if actual cell level energy/power demands were accounted for (using power control), the cycle life may be lower, leading to misleading real-world decisions.

In this thesis, it was shown that if current control approach to testing lithium-ion cells for model validation is employed, the resulting capacity throughput and peak currents are unrealistic and inadequate in terms of capturing the real-world energy/power demands seen for the same drive cycle. Conversely, if power control is used, allowing current to change based on the voltage response, consistency in energy throughput and peak power values are ensured, across all driving scenarios. Thus, it is recommended that power control approach to testing lithium-ion cells is chosen over current control to ensure suitability for model validation, and to inform ageing characterisation methods, consequently improving real-world applicability.

7.1.3 Research Impact

Today's market leading electric vehicles, driven on typical UK motorways, have real-world range estimation inaccuracy of up to 27%, at around 10 °C outside temperature [52]. In this work, by employing an immersed oil-cooled experimental setup, which can create close-to isothermal conditions, it has been shown that battery state estimation can be improved by reducing absolute SOC error from 13.5% to 5.1% (reducing absolute SOE error from 20.6% to 4.3%) at −15 °C. These findings provide a way forward towards improving range estimation in cold weather conditions for automotive applications.

Learnings from this research have also helped inform experimental rig design for WMG's various research projects [**J4, J5 and C3**: See 'List of Publications'], such as the Faraday Degradation study which now uses immersed oil bath for maintaining an isothermal test environment. Even outside WMG, other industrial partners have

replicated similar setups, particularly to obtain experimental data at low temperatures for modelling purposes. The journal articles published as part of this research meaningfully show that battery evaluation methods, particularly at low temperatures, can be improved to produce more accurate battery parameters, especially for state estimation. In particular, advances from this research positively impact how usable capacity is evaluated, especially at low temperatures. This will potentially lead to increased adherence to rigid environmental conditions for global testing standards for lithium-ion batteries (such as IEC 62660-1 and UN ECE 38.3) and battery modelling research community.

Building on the success of land transport EVs, aerospace electrification is fast emerging [181]. Although inaccuracies in range estimation would rarely have caused catastrophic failure in road transport EVs, in electric aircraft they could. For example, following an aborted landing, inaccurate range estimation could be the difference between an aircraft undertaking a safe holding pattern or an unsafe future landing. Therefore, with burgeoning aircraft electrification, accurate range estimation has never been more important.

Similarly, in an automotive context, a modelling error of 5-10% is acceptable, but these errors have a more severe impact in aerospace applications. A range estimation error of 10% means that the size of the battery pack (and weight) has to increase by 10%; this in turn will reduce the range. In the aerospace sector, the range estimation error is required to be minimal. This is only possible by most accurately capturing fundamental battery parameters under different operating conditions (low temperatures, extreme currents, etc.). The research presented in this thesis addressed this for low temperature by meaningfully separating battery electrical and thermal phenomena for model parameterisation experiments.

7.2 Future Work

In this study, every effort has been made to improve experimental methods for battery model parameterisation and validation for low temperature applications. The work in this thesis, also opens up other research avenues that can be explored.

In the following section, recommendations regarding future research and related ongoing work are outlined.

1. Isothermal Parameterisation using Smart Thermal Sensing

In the experimental work in this thesis, a single hermetically sealed t-type thermocouple has been positioned at the geometric centre of the cell surface in accordance with IEC 62660-1 testing standard. There will exist a temperature inhomogeneity across the surface where testing is conducted using air cooling. However, for the oil cooling there should exist minimal in-plane thermal gradients due to high thermal conductivity for pouch cells in that direction, large thermal mass of the oil bath and high transfer capability of the cooling system. In this study, additional thermocouples were also avoided because, inside the oil bath, attaching thermocouples is very difficult and was only possible using Perspex and cable ties. This created impressions on the cell surface and adding more Perspex would have also compromised the area available for heat transfer. Thus, further work is required to investigate how improvements can be made to the experimental test setup.

Lithium-ion cells display substantial thermal gradients in the through-plane direction [140,182]. This is supported by the difference in cell operating temperature and surface temperature reported in this thesis (Chapter 6, Section 6.3). Thus, control of the oil bath temperature through measurements provided from the cell core would be crucial to maintaining isothermal test conditions. Further, there is burgeoning literature where *in situ* measurements of cell thermal characteristics are conducted by placing temperature sensors in the cell core or between the layers of a pouch cell [104,183,184]. This allows monitoring of the temperature characteristics of the cells during both charge and discharge operations.

For future replication, to improve the experimental setup used in this study, instrumentation of the lithium-ion cells internally using negative temperature coefficient (NTC) thermistor elements is suggested (Figure 78). This will allow better thermal control by using temperatures measured inside the cell rather than outside (on the surface) as with the Pt-100 discussed in Chapter 4, Section 4.1.2. Techniques for internal cell instrumentation have only matured recently, hence could not have been applied as part of the work presented in this thesis. However, it is likely that using

internal thermal control using thermistors would allow for idealised isothermal test conditions producing a more accurate usable capacity value.

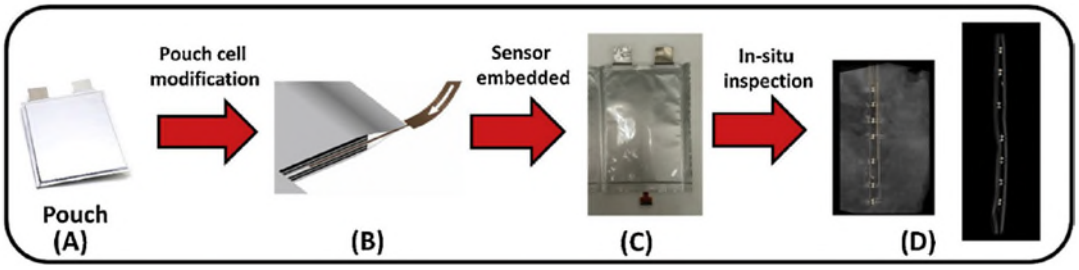

Figure 78. Smart Pouch Cell Construction using NTC Thermistor Elements having Kapton tape substrate and electrolyte resistant conformal coating [184]

2. Immersion oil cooling using dielectric fluids is a promising technique to reduce thermal gradients within a real-world battery pack due to the large thermal mass of the cooling system [127]. In future work, effect of this thermal management system can be investigated at module level, particularly to investigate thermal performance for motorsport applications and cycling life for passenger car applications. This can be contrasted against traditional battery modules that employ either air cooling or indirect liquid cooling using water/glycol. This comparison will be particularly relevant for rapid heating/cooling and fast charging scenarios.
3. It was established in this thesis that separate currents should be considered while calculating individually the heat generated from each impedance element in an ECM. It was shown that this leads to improved model performance. This should be explored further by a combination of electrochemical-thermal modelling and thermal impedance spectroscopy. This will allow researchers to explore the time/frequency dependent heat generation in a lithium-ion cell better, especially at low temperatures.

4. The research presented in this thesis, although performed on cells with NMC cathode and graphite anode, is transferable to other battery chemistries and format. However, validation exercises for other cell chemistries/format were not undertaken since the key contribution is related to the isothermal model parameterisation. The lithium-ion cell employed in this thesis was a high-

power cell. Extending this research to high-energy cells may lead to interesting conclusions. This is because high-power cells tend to have lower internal resistances than high-energy cells. Also, the ratio of active material and current collector mass changes, leading to different specific heat capacity for high-energy cells compared to high-power cells.

5. Finally, it is proposed in this thesis, that isothermal parameterisation leads to improved range accuracy for electric vehicles in the real-world. This should be validated: (a) through BMS implementation in a prototype EV, and (b) by contrasting against legacy data from EV fleets operating in winter conditions.

8. Conclusions

This chapter summarises the significant findings from the work and highlights their contributions to the knowledge.

Very little research has earlier been undertaken into the validity of battery parameterisation experiments, particularly for low temperatures. This thesis proposes novel dielectric oil-based thermal control experimental setup for isothermal battery testing for model parameterisation; which is a substantial improvement over the state-of-the-art air-based thermal chambers wherein cell temperature deviates from the predefined chamber temperature.

For the first time, it was demonstrated that using oil-based rather than air-based thermal control, battery usable capacity and energy characteristics were substantially lower, especially at low temperatures and/or high C-rates. An immersed oil-based method allowed for close-to-isothermal tracking of battery usable capacity, by eliminating the effect of rapid heat generation at low temperatures and high C-rates. This novel method therefore will lead to more accurate capacity/energy parameterisation for models used for range estimation in future electric vehicles.

It was also established that model parameterisation data obtained from oil-based rather than air-based experiments leads to far more accurate estimation of battery states i.e. SOC and SOE comparable to actual or measured values. Employing the proposed methodology, the absolute SOC error for scaled-down legislative drive cycles can be reduced (compared to state-of-the-art) from 13.5% to 5.1% (20.6% to 4.3% absolute SOE error) at −15°C starting ambient temperature. This can translate to improved BEV range estimation under cold weather conditions.

It was demonstrated that use of oil-based SOC leads to improved accuracy in terminal voltage estimation due its faster decrease compared to the air-based SOC. Greater improvements to accuracy in terminal voltage estimation were also observed during the 2nd phase of the 2xUS06 drive cycle. Thus, the oil-based SOC captures the real cell behaviour better compared to the air-based one, resulting in lower modelling errors particularly as the drive cycle progresses. The differences between air and oil based

SOC and SOE estimations became more pronounced as cell surface temperature deviated more from the starting ambient temperature for a particular drive cycle. The difference between the two approaches was also observed to increase with decreasing starting ambient temperature for the drive cycle.

A new method for estimating heat generation within an ECM thermal feedback subsystem has also been presented. For the first time, it is demonstrated that by including polarisation current in a thermal feedback subsystem in place of only the common (Ohmic) current leads to more accurate modelled surface temperature and terminal voltage estimates. The effect of thermal feedback on model performance demonstrates greater coupling between electrical and thermal phenomena, particularly at lower temperatures. This validates that assumptions acceptable at room temperatures for modelling lithium-ion batteries do not hold true at lower temperatures.

Lastly, the thesis demonstrates that it is better to employ power control as the sole approach to obtain validation data for cell models. This is because the power control approach updates the current based on the instantaneous operating voltage and ensures consistency in energy/power delivery across all driving conditions.

These findings will ensure increased adherence to rigid environmental test conditions in the battery research community and inform global battery testing standards. Overall, the key contributions are:

- Novel oil-based experimental test methodology, which generates close-to-isothermal test conditions, leads to more reliable and repeatable method to accurately assess usable capacity/energy of lithium-ion batteries, especially at low temperatures.
- A model parameterised using datasets obtained from oil-based experiments compared to traditional air-based experiments, leads to more accurate estimation of battery states and terminal voltage, particularly at low temperatures.
- Inclusion of polarisation currents for heat generation estimates as part of thermal feedback subsystem improves model performance by better capturing battery temperature evolution.

- Use of power control approach for experimentally characterising batteries for model validation is recommended because it ensures consistency in energy throughput and power, especially at low temperatures and low operating voltages.

Advances from this research can improve range estimation accuracy for BEVs operating under cold weather conditions, paving the way for increased market uptake of electrified transportation.

References

[1] Climate Change Act 2008 CONTENTS, n.d. https://www.legislation.gov.uk/ukpga/2008/27/pdfs/ukpga_20080027_en.pdf (accessed August 30, 2018).

[2] A. Emadi, K. Rajashekara, S.S. Williamson, S.M. Lukic, Topological overview of hybrid electric and fuel cell vehicular power system architectures and configurations, IEEE Trans. Veh. Technol. 54 (2005) 763–770. doi:10.1109/TVT.2005.847445.

[3] J. Neubauer, E. Wood, The impact of range anxiety and home, workplace, and public charging infrastructure on simulated battery electric vehicle lifetime utility, J. Power Sources. 257 (2014) 12–20. doi:10.1016/j.jpowsour.2014.01.075.

[4] M.H. Nehrir, C. Wang, K. Strunz, H. Aki, R. Ramakumar, J. Bing, Z. Miao, Z. Salameh, A review of hybrid renewable/alternative energy systems for electric power generation: Configurations, control, and applications, IEEE Trans. Sustain. Energy. 2 (2011) 392–403. doi:10.1109/TSTE.2011.2157540.

[5] S.A.H. Zahabi, L. Miranda-Moreno, P. Barla, B. Vincent, Fuel economy of hybrid-electric versus conventional gasoline vehicles in real-world conditions: A case study of cold cities in Quebec, Canada, Transp. Res. Part D Transp. Environ. 32 (2014) 184–192. doi:10.1016/j.trd.2014.07.007.

[6] S.F. Tie, C.W. Tan, A review of energy sources and energy management system in electric vehicles, Renew. Sustain. Energy Rev. 20 (2013) 82–102. doi:10.1016/j.rser.2012.11.077.

[7] S. Nejad, D.T. Gladwin, D.A. Stone, A systematic review of lumped-parameter equivalent circuit models for real-time estimation of lithium-ion battery states, J. Power Sources. 316 (2016) 183–196. doi:10.1016/j.jpowsour.2016.03.042.

[8] UK becomes first major economy to pass net zero emissions law - GOV.UK,

(n.d.). https://www.gov.uk/government/news/uk-becomes-first-major-economy-to-pass-net-zero-emissions-law (accessed July 16, 2020).

[9] Fast Facts on Transportation Greenhouse Gas Emissions | Green Vehicle Guide | US EPA, (n.d.). https://www.epa.gov/greenvehicles/fast-facts-transportation-greenhouse-gas-emissions (accessed June 28, 2020).

[10] Greenhouse gas emissions from transport in Europe — European Environment Agency, (n.d.). https://www.eea.europa.eu/data-and-maps/indicators/transport-emissions-of-greenhouse-gases/transport-emissions-of-greenhouse-gases-12 (accessed June 28, 2020).

[11] Factcheck: How electric vehicles help to tackle climate change, (n.d.). https://www.carbonbrief.org/factcheck-how-electric-vehicles-help-to-tackle-climate-change (accessed June 28, 2020).

[12] H. Li, K. Hosoi, K. Amine, D. Howell, S. Passerini, H. Zeisel, D. Bresser, Perspectives of automotive battery R&D in China, Germany, Japan, and the USA, J. Power Sources. 382 (2018) 176–178. doi:10.1016/j.jpowsour.2018.02.039.

[13] Lithium and cobalt: A tale of two commodities | McKinsey, (n.d.). https://www.mckinsey.com/industries/metals-and-mining/our-insights/lithium-and-cobalt-a-tale-of-two-commodities (accessed February 2, 2020).

[14] World’s first fully electric commercial aircraft takes flight in Canada | World news | The Guardian, (n.d.). https://www.theguardian.com/world/2019/dec/11/worlds-first-fully-electric-commercial-aircraft-takes-flight-in-canada (accessed February 11, 2020).

[15] Green Flyway: Norway, Sweden Create Airspace For Electric Plane Tests, (n.d.). https://www.forbes.com/sites/davidnikel/2020/01/30/green-flyway-norway-sweden-create-airspace-for-electric-plane-tests/#28ea997541b9 (accessed February 11, 2020).

[16] Electric aviation ready for take-off in Norway by 2030, report says | The Independent Barents Observer, (n.d.). https://thebarentsobserver.com/en/travel/2020/03/electric-aviation-should-be-ready-take-norway-2030 (accessed July 19, 2020).

[17] Widespread EV Adoption Will Require Infrastructure, Education, (n.d.). https://www.govtech.com/fs/data/Widespread-EV-Adoption-Will-Require-Infrastructure-Education.html (accessed June 28, 2020).

[18] Automotive Batteries 101 - Everything you ever wanted to know about batteries for electric vehicles < News | Northern Automotive Alliance : Northern Automotive Alliance, (n.d.). http://northernautoalliance.com/news/automotive-batteries-101-everything-ever-wanted-know-batteries-electric-vehicles/ (accessed June 28, 2020).

[19] H. Hao, Z. Mu, S. Jiang, Z. Liu, F. Zhao, GHG Emissions from the production of lithium-ion batteries for electric vehicles in China, Sustain. 9 (2017). doi:10.3390/su9040504.

[20] P.G. Pereirinha, M. González, I. Carrilero, D. Anseán, J. Alonso, J.C. Viera, Main Trends and Challenges in Road Transportation Electrification, in: Transp. Res. Procedia, Elsevier B.V., 2018: pp. 235–242. doi:10.1016/j.trpro.2018.10.096.

[21] M. Ehsani, G. Yimin, J.M. Miller, Hybrid Electric Vehicles: Architecture and Motor Drives, Proc. IEEE. 95 (2007) 719–728. doi:10.1109/jproc.2007.892492.

[22] C.C. Chan, The state of the art of electric, hybrid, and fuel cell vehicles, Proc. IEEE. 95 (2007) 704–718. doi:10.1109/JPROC.2007.892489.

[23] S.M. Lukic, J. Cao, R.C. Bansal, F. Rodriguez, A. Emadi, Energy storage systems for automotive applications, IEEE Trans. Ind. Electron. 55 (2008) 2258–2267. doi:10.1109/TIE.2008.918390.

[24] E. Karden, S. Ploumen, B. Fricke, T. Miller, K. Snyder, Energy storage

devices for future hybrid electric vehicles, J. Power Sources. 168 (2007) 2–11. doi:10.1016/j.jpowsour.2006.10.090.

[25] P. Miller, Automotive Lithium-ion Batteries, Johnson Matthey Technol. Rev. 59 (2015) 4–13. doi:10.1595/205651315X685445.

[26] Cenex, Oxford Brookes University, Assessing the viability of EVs in daily life, Ultra Low Carbon Veh. Demonstr. Program. 96 (2013) 3S-4S. doi:10.1037/e530172011-002.

[27] G. Nielson, A. Emadi, Hybrid Energy Storage Systems for High Performance Hybrid Electric Vehicles, Veh. Power Propuls. Conf. (VPPC), 2011 IEEE. (2011) 1–6. doi:10.1109/vppc.2011.6043052.

[28] The Different Types of Hybrid Cars | HowStuffWorks, (n.d.). https://auto.howstuffworks.com/different-types-of-hybrid-cars1.htm (accessed July 14, 2020).

[29] B.V. Padma Rajan, Plug in Hybrid Electric Vehicle Energy Management System for Real World Driving, PhD Thesis, University of Warwick, 2014. http://wrap.warwick.ac.uk/67891/1/WRAP_THESIS_Rajan_2014.pdf.

[30] J. Liu, H. Peng, Modeling and control of a power-split hybrid vehicle, IEEE Trans. Control Syst. Technol. 16 (2008) 1242–1251. doi:10.1109/TCST.2008.919447.

[31] S. Roberts, E. Kendrick, The re-emergence of sodium ion batteries: testing, processing, and manufacturability, Nanotechnol. Sci. Appl. (2018) 23–33. doi:10.2147/NSA.S146365.

[32] P. Keil, A. Jossen, Improving the low-temperature performance of electric vehicles by hybrid energy storage systems, 2014 IEEE Veh. Power Propuls. Conf. VPPC 2014. (2014). doi:10.1109/VPPC.2014.7007087.

[33] N. Watrin, R. Roche, H. Ostermann, B. Blunier, A. Miraoui, Multiphysical lithium-based battery model for use in state-of-charge determination, IEEE Trans. Veh. Technol. 61 (2012) 3420–3429. doi:10.1109/TVT.2012.2205169.

[34] Y. Tripathy, A. McGordon, J. Low, J. Marco, Low Temperature Performance of Lithium-ion Batteries for Different Drive Cycles, in: Electr. Veh. Symp. (EVS 29), Montréal, Québec, 19-21 Jun 2016, 2016: pp. 1–12.

[35] C. Pastor-Fernández, T. Bruen, W.D. Widanage, M.A. Gama-Valdez, J. Marco, A Study of Cell-to-Cell Interactions and Degradation in Parallel Strings: Implications for the Battery Management System, J. Power Sources. 329 (2016) 574–585. doi:10.1016/j.jpowsour.2016.07.121.

[36] A. Barai, T.R. Ashwin, C. Iraklis, A. McGordon, P. Jennings, Scale-up of lithium-ion battery model parameters from cell level to module level – identification of current issues, Energy Procedia. 138 (2017) 223–228. doi:10.1016/J.EGYPRO.2017.10.154.

[37] B. Nykvist, M. Nilsson, Rapidly falling costs of battery packs for electric vehicles, Nat. Clim. Chang. 5 (2015) 329–332. doi:10.1038/nclimate2564.

[38] C. Pastor-Fernández, K. Uddin, G.H. Chouchelamane, W.D. Widanage, J. Marco, A Comparison between Electrochemical Impedance Spectroscopy and Incremental Capacity-Differential Voltage as Li-ion Diagnostic Techniques to Identify and Quantify the Effects of Degradation Modes within Battery Management Systems, J. Power Sources. 360 (2017) 301–318. doi:10.1016/j.jpowsour.2017.03.042.

[39] X. Feng, M. Ouyang, X. Liu, L. Lu, Y. Xia, X. He, Thermal runaway mechanism of lithium ion battery for electric vehicles: A review, Energy Storage Mater. 10 (2018) 246–267. doi:10.1016/j.ensm.2017.05.013.

[40] J.P.J.P. Singer, K.P.K.P. Birke, Kinetic study of low temperature capacity fading in Li-ion cells, J. Energy Storage. 13 (2017) 129–136. doi:10.1016/j.est.2017.07.002.

[41] G. Zhu, K. Wen, W. Lv, X. Zhou, Y. Liang, F. Yang, Z. Chen, M. Zou, J. Li, Y. Zhang, W. He, Materials insights into low-temperature performances of lithium-ion batteries, J. Power Sources. 300 (2015) 29–40.

doi:10.1016/j.jpowsour.2015.09.056.

[42] J. Rizalino, M.D. Reyes, A. Member, R. V Parsons, R. Hoemsen, Winter Happens : The Effect of Ambient Temperature on the Travel Range of Electric Vehicles, IEEE Trans. Veh. Technol. 65 (2016) 4016–4022.

[43] Biggest Winter Range Test Ever Reveals Best EVs For Cold Weather, (n.d.). https://insideevs.com/news/404632/winter-range-test-best-evs-cold-weather/ (accessed March 28, 2020).

[44] J. Jeffs, A. McGordon, A. Picarelli, S. Robinson, Y. Tripathy, W. Widanage, Complex Heat Pump Operational Mode Identification and Comparison for Use in Electric Vehicles, Energies. 11 (2018) 2000. doi:10.3390/en11082000.

[45] Z. Zhang, W. Li, C. Zhang, J. Chen, Climate control loads prediction of electric vehicles, Appl. Therm. Eng. 110 (2017) 1183–1188. doi:10.1016/j.applthermaleng.2016.08.186.

[46] J. Neubauer, E. Wood, Thru-life impacts of driver aggression , climate , cabin thermal management , and battery thermal management on battery electric vehicle utility, 259 (2014) 262–275.

[47] T. Yuksel, J.J. Michalek, Effects of regional temperature on electric vehicle efficiency, range, and emissions in the united states, Environ. Sci. Technol. 49 (2015) 3974–3980. doi:10.1021/es505621s.

[48] J. Lindgren, P.D. Lund, Effect of extreme temperatures on battery charging and performance of electric vehicles, J. Power Sources. 328 (2016) 37–45. doi:10.1016/j.jpowsour.2016.07.038.

[49] P. Keil, A. Jossen, Aging of Lithium-Ion Batteries in Electric Vehicles : Impact of Regenerative Braking, EVS28 Int. Electr. Veh. Symp. Exhib. (2015) 1–11. doi:10.13140/RG.2.1.3485.2320.

[50] J. Jiang, H. Ruan, B. Sun, W. Zhang, W. Gao, L.Y. Wang, L. Zhang, A reduced low-temperature electro-thermal coupled model for lithium-ion batteries, Appl. Energy. 177 (2016) 804–816.

doi:10.1016/J.APENERGY.2016.05.153.

[51] J. Remmlinger, S. Tippmann, M. Buchholz, K. Dietmayer, Low-temperature charging of lithium-ion cells Part II: Model reduction and application, J. Power Sources. 254 (2014) 268–276. doi:10.1016/j.jpowsour.2013.12.101.

[52] We drove these electric cars until they DIED! - YouTube, (n.d.). https://www.youtube.com/watch?v=ZH7V2tU3iFc (accessed April 8, 2020).

[53] B. Varga, A. Sagoian, F. Mariasiu, Prediction of Electric Vehicle Range: A Comprehensive Review of Current Issues and Challenges, Energies. 12 (2019) 946. doi:10.3390/en12050946.

[54] Electric Car for a Cold Climate | Driving Range - Consumer Reports, (n.d.). https://www.consumerreports.org/hybrids-evs/buying-an-electric-car-for-a-cold-climate-double-down-on-range/ (accessed June 20, 2020).

[55] A. Fotouhi, D.J. Auger, K. Propp, S. Longo, M. Wild, A review on electric vehicle battery modelling: From Lithium-ion toward Lithium-Sulphur, Renew. Sustain. Energy Rev. 56 (2016) 1008–1021. doi:10.1016/j.rser.2015.12.009.

[56] Y. Wang, C. Zhang, Z. Chen, An adaptive remaining energy prediction approach for lithium-ion batteries in electric vehicles, J. Power Sources. 305 (2016) 80–88. doi:10.1016/j.jpowsour.2015.11.087.

[57] A. Barai, K. Uddin, W.D. Widanalage, A. McGordon, P. Jennings, The effect of average cycling current on total energy of lithium-ion batteries for electric vehicles, J. Power Sources. 303 (2016) 81–85. doi:10.1016/j.jpowsour.2015.10.095.

[58] J. Jaguemont, L. Boulon, Y. Dube, Characterization and Modeling of a Hybrid-Electric-Vehicle Lithium-Ion Battery Pack at Low Temperatures, IEEE Trans. Veh. Technol. 65 (2016) 1–14. doi:10.1109/TVT.2015.2391053.

[59] A. Nikolian, J. Jaguemont, J. de Hoog, S. Goutam, N. Omar, P. Van Den Bossche, J. Van Mierlo, Complete cell-level lithium-ion electrical ECM

model for different chemistries (NMC, LFP, LTO) and temperatures (−5 °C to 45 °C) – Optimized modelling techniques, Int. J. Electr. Power Energy Syst. 98 (2018) 133–146. doi:10.1016/j.ijepes.2017.11.031.

[60] A. Barai, K. Uddin, M. Dubarry, L. Somerville, A. McGordon, P. Jennings, I. Bloom, A comparison of methodologies for the non-invasive characterisation of commercial Li-ion cells, Prog. Energy Combust. Sci. 72 (2019) 1–31. doi:10.1016/J.PECS.2019.01.001.

[61] B.D. McCloskey, Expanding the Ragone Plot: Pushing the Limits of Energy Storage, J. Phys. Chem. Lett. 6 (2015) 3592–3593. doi:10.1021/acs.jpclett.5b01813.

[62] Z.P. Cano, D. Banham, S. Ye, A. Hintennach, J. Lu, M. Fowler, Z. Chen, Batteries and fuel cells for emerging electric vehicle markets, Nat. Energy. 3 (2018). doi:10.1038/s41560-018-0108-1.

[63] Y. Ding, Z.P. Cano, A. Yu, J. Lu, · Zhongwei Chen, Automotive Li-Ion Batteries: Current Status and Future Perspectives, Electrochem. Energy Rev. 2 (2019) 1–28. doi:10.1007/s41918-018-0022-z.

[64] G. Benveniste, H. Rallo, L. Canals Casals, A. Merino, B. Amante, Comparison of the state of Lithium-Sulphur and lithium-ion batteries applied to electromobility, J. Environ. Manage. 226 (2018) 1–12. doi:10.1016/j.jenvman.2018.08.008.

[65] Y. Ji, Y. Zhang, C.-Y. Wang, Li-Ion Cell Operation at Low Temperatures, J. Electrochem. Soc. 160 (2013) A636–A649. doi:10.1149/2.047304jes.

[66] J. Jaguemont, L. Boulon, Y. Dube, D. Poudrier, Low temperature discharge cycle tests for a lithium ion cell, 2014 IEEE Veh. Power Propuls. Conf. VPPC 2014. (2014). doi:10.1109/VPPC.2014.7007097.

[67] A. Senyshyn, M.J. Muhlbauer, O. Dolotko, H. Ehrenberg, Low-temperature performance of Li-ion batteries: The behavior of lithiated graphite, J. Power Sources. 282 (2015) 235–240. doi:10.1016/j.jpowsour.2015.02.008.

[68] The Three Laws of Batteries (and a Bonus Zeroth Law) – Gigaom, (n.d.). https://gigaom.com/2011/03/18/the-three-laws-of-batteries-and-a-bonus-zeroth-law/ (accessed April 17, 2020).

[69] H. Liu, Z. Wei, W. He, J. Zhao, Thermal issues about Li-ion batteries and recent progress in battery thermal management systems: A review, Energy Convers. Manag. 150 (2017) 304–330. doi:10.1016/j.enconman.2017.08.016.

[70] A. Barai, Improvement of Consistency , Accuracy and Interpretation of Characterisation Test Techniques for Li-ion Battery cells for Automotive Application, PhD Thesis, University of Warwick, 2015. http://wrap.warwick.ac.uk/77676/1/WRAP_THESIS_Barai_2015.pdf.

[71] J. Jaguemont, L. Boulon, P. Venet, Y. Dube, A. Sari, Lithium-Ion Battery Aging Experiments at Subzero Temperatures and Model Development for Capacity Fade Estimation, IEEE Trans. Veh. Technol. 65 (2016) 4328–4343. doi:10.1109/TVT.2015.2473841.

[72] J. Li, C.F. Yuan, Z.H. Guo, Z.A. Zhang, Y.Q. Lai, J. Liu, Limiting factors for low-temperature performance of electrolytes in LiFePO 4/Li and graphite/Li half cells, Electrochim. Acta. 59 (2012) 69–74. doi:10.1016/j.electacta.2011.10.041.

[73] J.B. Goodenough, K.-S. Park, The Li-Ion Rechargeable Battery: A Perspective, J. Am. Chem. Soc. 135 (2013) 1167–1176. doi:10.1021/ja3091438.

[74] J. Jaguemont, L. Boulon, Y. Dube, A comprehensive review of lithium-ion batteries used in hybrid and electric vehicles at cold temperatures, Appl. Energy. 164 (2016) 99–114. doi:10.1016/j.apenergy.2015.11.034.

[75] Q. Wang, B. Jiang, B. Li, Y. Yan, A critical review of thermal management models and solutions of lithium-ion batteries for the development of pure electric vehicles, Renew. Sustain. Energy Rev. 64 (2016) 106–128. doi:10.1016/j.rser.2016.05.033.

[76] K.A. Smith, Electrochemical Control of Lithium-Ion Batteries, IEEE Control Syst. Mag. 30 (2010) 18–25. doi:10.1109/MCS.2010.935882.

[77] K. Smith, C.-Y. Wang, Power and thermal characterization of a lithium-ion battery pack for hybrid-electric vehicles, J. Power Sources. 160 (2006) 662–673. doi:10.1016/j.jpowsour.2006.01.038.

[78] I. V. Thorat, D.E. Stephenson, N.A. Zacharias, K. Zaghib, J.N. Harb, D.R. Wheeler, Quantifying tortuosity in porous Li-ion battery materials, J. Power Sources. 188 (2009) 592–600. doi:10.1016/j.jpowsour.2008.12.032.

[79] J. Yi, U.S. Kim, C.B. Shin, T. Han, S. Park, Modeling the temperature dependence of the discharge behavior of a lithium-ion battery in low environmental temperature, J. Power Sources. 244 (2013) 143–148. doi:10.1016/j.jpowsour.2013.02.085.

[80] Y. Ji, C.Y. Wang, Heating strategies for Li-ion batteries operated from subzero temperatures, Electrochim. Acta. 107 (2013) 664–674. doi:10.1016/j.electacta.2013.03.147.

[81] T. Grandjean, A. McGordon, P. Jennings, Structural Identifiability of Equivalent Circuit Models for Li-Ion Batteries, Energies. 10 (2017) 90. doi:10.3390/en10010090.

[82] T. Grandjean, A. Barai, E. Hosseinzadeh, Y. Guo, A. McGordon, J. Marco, Large format lithium ion pouch cell full thermal characterisation for improved electric vehicle thermal management, J. Power Sources. 359 (2017) 215–225. doi:10.1016/j.jpowsour.2017.05.016.

[83] P. Keil, M. Englberger, A. Jossen, Hybrid Energy Storage Systems for Electric Vehicles: An Experimental Analysis of Performance Improvements at Subzero Temperatures, IEEE Trans. Veh. Technol. 65 (2016) 998–1006. doi:10.1109/tvt.2015.2486040.

[84] A. Barré, B. Deguilhem, S. Grolleau, M. Gérard, F. Suard, D. Riu, A review on lithium-ion battery ageing mechanisms and estimations for automotive

applications, J. Power Sources. 241 (2013) 680–689. doi:10.1016/j.jpowsour.2013.05.040 Review.

[85] J. Vetter, P. Novák, M.R. Wagner, C. Veit, K.C. Möller, J.O. Besenhard, M. Winter, M. Wohlfahrt-Mehrens, C. Vogler, A. Hammouche, Ageing mechanisms in lithium-ion batteries, J. Power Sources. 147 (2005) 269–281. doi:10.1016/j.jpowsour.2005.01.006.

[86] X. Liu, J. Wu, C. Zhang, Z. Chen, A method for state of energy estimation of lithium-ion batteries at dynamic currents and temperatures, J. Power Sources. 270 (2014) 151–157. doi:10.1016/j.jpowsour.2014.07.107.

[87] K. Li, K.J. Tseng, An Equivalent Circuit Model for State of Energy Estimation of Lithium-ion Battery, in: IEEE Conf. Ind. Electron. Appl. ICIEA, 2016: pp. 3422–3430.

[88] Y. Zhang, C.Y. Wang, X. Tang, Cycling degradation of an automotive LiFePO4 lithium-ion battery, J. Power Sources. 196 (2011) 1513–1520. doi:10.1016/j.jpowsour.2010.08.070.

[89] M.T. Von Srbik, M. Marinescu, R.F. Martinez-Botas, G.J. Offer, A physically meaningful equivalent circuit network model of a lithium-ion battery accounting for local electrochemical and thermal behaviour, variable double layer capacitance and degradation, J. Power Sources. 325 (2016) 171–184. doi:10.1016/j.jpowsour.2016.05.051.

[90] A. Tourani, P. White, P. Ivey, Analysis of electric and thermal behaviour of lithium-ion cells in realistic driving cycles, J. Power Sources. 268 (2014) 301–314. doi:10.1016/J.JPOWSOUR.2014.06.010.

[91] E. Hosseinzadeh, R. Genieser, D. Worwood, A. Barai, J. Marco, P. Jennings, A systematic approach for electrochemical-thermal modelling of a large format lithium-ion battery for electric vehicle application, J. Power Sources. 382 (2018) 77–94. doi:10.1016/J.JPOWSOUR.2018.02.027.

[92] Y. Tripathy, A. McGordon, J. Low, J. Marco, Internal temperature prediction

of Lithium-ion cell using differential voltage technique, in: 2017 IEEE Transp. Electrif. Conf. Expo, IEEE, 2017: pp. 464–467. doi:10.1109/ITEC.2017.7993315.

[93] W. Waag, S. Käbitz, D.U. Sauer, Experimental investigation of the lithium-ion battery impedance characteristic at various conditions and aging states and its influence on the application, Appl. Energy. 102 (2013) 885–897. doi:10.1016/j.apenergy.2012.09.030.

[94] F. Zheng, J. Jiang, B. Sun, W. Zhang, M. Pecht, Temperature dependent power capability estimation of lithium-ion batteries for hybrid electric vehicles, Energy. 113 (2016) 64–75. doi:10.1016/j.energy.2016.06.010.

[95] J. Zhu, M. Knapp, M.S.D. Darma, Q. Fang, X. Wang, H. Dai, X. Wei, H. Ehrenberg, An improved electro-thermal battery model complemented by current dependent parameters for vehicular low temperature application, Appl. Energy. 248 (2019) 149–161. doi:10.1016/j.apenergy.2019.04.066.

[96] J. Wu, T. Li, H. Zhang, Y. Lei, G. Zhou, Research on modeling and SOC estimation of lithium iron phosphate battery at low temperature, in: Energy Procedia, Elsevier Ltd, 2018: pp. 556–561. doi:10.1016/j.egypro.2018.09.210.

[97] Y. Troxler, B. Wu, M. Marinescu, V. Yufit, Y. Patel, A.J. Marquis, N.P. Brandon, G.J. Offer, The effect of thermal gradients on the performance of lithium-ion batteries, J. Power Sources. 247 (2014) 1018–1025. doi:10.1016/j.jpowsour.2013.06.084.

[98] M. Klein, S. Tong, J.W. Park, In-plane nonuniform temperature effects on the performance of a large-format lithium-ion pouch cell, Appl. Energy. 165 (2016) 639–647. doi:10.1016/j.apenergy.2015.11.090.

[99] M.I. Ardani, Y. Patel, A. Siddiq, G.J. Offer, R.F. Martinez-Botas, Combined experimental and numerical evaluation of the differences between convective and conductive thermal control on the performance of a lithium ion cell, Energy. 144 (2018) 81–97. doi:10.1016/j.energy.2017.12.032.

[100] A. Barai, K. Uddin, W.D. Widanage, A. McGordon, P. Jennings, A study of the influence of measurement timescale on internal resistance characterisation methodologies for lithium-ion cells, Sci. Rep. 8 (2018) 1–13. doi:10.1038/s41598-017-18424-5.

[101] W.D. Widanage, A. Barai, G.H. Chouchelamane, K. Uddin, A. McGordon, J. Marco, P. Jennings, Design and use of multisine signals for Li-ion battery equivalent circuit modelling. Part 1: Signal design, J. Power Sources. 324 (2016) 70–78. doi:10.1016/j.jpowsour.2016.05.015.

[102] A. Barai, G.H. Chouchelamane, Y. Guo, A. McGordon, P. Jennings, A study on the impact of lithium-ion cell relaxation on electrochemical impedance spectroscopy, J. Power Sources. 280 (2015) 74–80. doi:10.1016/j.jpowsour.2015.01.097.

[103] IEC 62660-1:2018 | IEC Webstore, (n.d.). https://webstore.iec.ch/publication/28965 (accessed January 29, 2020).

[104] P.J. Osswald, M. Del Rosario, J. Garche, A. Jossen, H.E. Hoster, Fast and Accurate Measurement of Entropy Profiles of Commercial Lithium-Ion Cells, (2015). doi:10.1016/j.electacta.2015.01.191.

[105] Y. Zhao, X.-F. Zhang, Y. Patel, T. Zhang, W.-M. Liu, M. Chen, G.J. Offer, Y. Yan, Potentiometric Measurement of Entropy Change for Lithium Batteries Potentiometric measurement of entropy change for lithium batteries †, Artic. Phys. Chem. Chem. Phys. (2017). doi:10.1039/C6CP08505A.

[106] S.S. Zhang, K. Xu, T.R. Jow, The low temperature performance of Li-ion batteries, J. Power Sources. 115 (2003) 137–140. doi:10.1016/S0378-7753(02)00618-3.

[107] S.S. Zhang, K. Xu, T.R. Jow, Electrochemical impedance study on the low temperature of Li-ion batteries, Electrochim. Acta. 49 (2004) 1057–1061. doi:10.1016/j.electacta.2003.10.016.

[108] D. Andre, M. Meiler, K. Steiner, C. Wimmer, T. Soczka-Guth, D.U. Sauer,

Characterization of high-power lithium-ion batteries by electrochemical impedance spectroscopy. I. Experimental investigation, J. Power Sources. 196 (2011) 5334–5341. doi:10.1016/j.jpowsour.2010.12.102.

[109] S. Gantenbein, M. Weiss, E. Ivers-Tiffée, Impedance based time-domain modeling of lithium-ion batteries: Part I, J. Power Sources. 379 (2018) 317–327. doi:10.1016/j.jpowsour.2018.01.043.

[110] L.H.J. Raijmakers, D.L. Danilov, J.P.M. Van Lammeren, M.J.G. Lammers, P.H.L. Notten, Sensorless battery temperature measurements based on electrochemical impedance spectroscopy, J. Power Sources. 247 (2014) 539–544. doi:10.1016/j.jpowsour.2013.09.005.

[111] L.H.J. Raijmakers, D.L. Danilov, J.P.M. Van Lammeren, T.J.G. Lammers, H.J. Bergveld, P.H.L. Notten, Non-Zero Intercept Frequency : An Accurate Method to Determine the Integral Temperature of Li-Ion Batteries, 63 (2016) 3168–3178.

[112] L.H.J. Raijmakers, D.L. Danilov, R.A. Eichel, P.H.L. Notten, A review on various temperature-indication methods for Li-ion batteries, Appl. Energy. 240 (2019) 918–945. doi:10.1016/j.apenergy.2019.02.078.

[113] W. Waag, C. Fleischer, D.U. Sauer, Adaptive on-line prediction of the available power of lithium-ion batteries, J. Power Sources. 242 (2013) 548–559. doi:10.1016/j.jpowsour.2013.05.111.

[114] M. Marinescu, B. Wu, M. Von Srbik, V. Yufit, G.J. Offer, The effect of thermal gradients on the performance of battery packs in automotive applications, in: IET Hybrid Electr. Veh. Conf. 2013 (HEVC 2013), Institution of Engineering and Technology, London, 2013: pp. 1–5. doi:10.1049/cp.2013.1886.

[115] P.J. Osswald, S. V. Erhard, A. Noel, P. Keil, F.M. Kindermann, H. Hoster, A. Jossen, Current density distribution in cylindrical Li-Ion cells during impedance measurements, J. Power Sources. 314 (2016) 93–101. doi:10.1016/j.jpowsour.2016.02.070.

[116] A. Barai, W.D. Widanage, J. Marco, A. McGordon, P. Jennings, A study of the open circuit voltage characterization technique and hysteresis assessment of lithium-ion cells, J. Power Sources. 295 (2015) 99–107. doi:10.1016/j.jpowsour.2015.06.140.

[117] M. Petzl, M.A. Danzer, Advancements in OCV measurement and analysis for lithium-ion batteries, IEEE Trans. Energy Convers. 28 (2013) 675–681. doi:10.1109/TEC.2013.2259490.

[118] W. Waag, C. Fleischer, D. Uwe, Critical review of the methods for monitoring of lithium-ion batteries in electric and hybrid vehicles, J. Power Sources. 258 (2014).

[119] M. Dubarry, G. Baure, Perspective on Commercial Li-ion Battery Testing, Best Practices for Simple and Effective Protocols, Electronics. 9 (2020) 152. doi:10.3390/electronics9010152.

[120] Y. Xing, W. He, M. Pecht, K.L. Tsui, State of charge estimation of lithium-ion batteries using the open-circuit voltage at various ambient temperatures, Appl. Energy. 113 (2014) 106–115. doi:10.1016/j.apenergy.2013.07.008.

[121] S. V. Erhard, P.J. Osswald, P. Keil, E. Höffer, M. Haug, A. Noel, J. Wilhelm, B. Rieger, K. Schmidt, S. Kosch, F.M. Kindermann, F. Spingler, H. Kloust, T. Thoennessen, A. Rheinfeld, A. Jossen, Simulation and Measurement of the Current Density Distribution in Lithium-Ion Batteries by a Multi-Tab Cell Approach, J. Electrochem. Soc. 164 (2017) A6324–A6333. doi:10.1149/2.0551701jes.

[122] L.I. Silva, J. Jaguemont, C.H. De Angelo, Modeling an Electric Vehicle Lithium-Ion Battery Pack Considering Low Temperature, (2016). doi:10.1109/VPPC.2016.7791727.

[123] X. Hu, S. Li, H. Peng, A comparative study of equivalent circuit models for Li-ion batteries, J. Power Sources. 198 (2012) 359–367. doi:10.1016/j.jpowsour.2011.10.013.

[124] S. Chacko, Y.M. Chung, Thermal modelling of Li-ion polymer battery for electric vehicle drive cycles, J. Power Sources. 213 (2012) 296–303. doi:10.1016/j.jpowsour.2012.04.015.

[125] D. Chen, J. Jiang, G.-H.H. Kim, C. Yang, A. Pesaran, Comparison of different cooling methods for lithium ion battery cells, Appl. Therm. Eng. 94 (2016) 846–854. doi:10.1016/j.applthermaleng.2015.10.015.

[126] C. Bolsinger, K.P. Birke, Effect of different cooling configurations on thermal gradients inside cylindrical battery cells, J. Energy Storage. 21 (2019) 222–230. doi:10.1016/J.EST.2018.11.030.

[127] Y. Deng, C. Feng, J. E, H. Zhu, J. Chen, M. Wen, H. Yin, Effects of different coolants and cooling strategies on the cooling performance of the power lithium ion battery system: A review, Appl. Therm. Eng. 142 (2018) 10–29. doi:10.1016/J.APPLTHERMALENG.2018.06.043.

[128] W. Wu, S. Wang, W. Wu, K. Chen, S. Hong, Y. Lai, A critical review of battery thermal performance and liquid based battery thermal management, Energy Convers. Manag. (2019) 262–281. doi:10.1016/j.enconman.2018.12.051.

[129] C. Antaloae, J. Marco, F. Assadian, A Novel Method for the Parameterization of a Li-Ion Cell Model for EV / HEV Control Applications, IEEE Trans. Sustain. Energy. 61 (2012) 3881–3892.

[130] K.W.E. Cheng, B.P. Divakar, H. Wu, K. Ding, H.F. Ho, Battery-management system (BMS) and SOC development for electrical vehicles, IEEE Trans. Veh. Technol. 60 (2011) 76–88. doi:10.1109/TVT.2010.2089647.

[131] M. Dubarry, V. Svoboda, R. Hwu, B.Y. Liaw, Capacity loss in rechargeable lithium cells during cycle life testing: The importance of determining state-of-charge, J. Power Sources. 174 (2007) 1121–1125. doi:10.1016/j.jpowsour.2007.06.185.

[132] Z. Li, J. Huang, B.Y. Liaw, J. Zhang, On state-of-charge determination for

lithium-ion batteries, J. Power Sources. 348 (2017) 281–301. doi:10.1016/j.jpowsour.2017.03.001.

[133] Y. Tripathy, A. McGordon, J. Marco, M. Gama-Valdez, State-of-Charge estimation algorithms and their implications on cells in parallel, in: 2014 IEEE Int. Electr. Veh. Conf. IEVC 2014, 2014. doi:10.1109/IEVC.2014.7056168.

[134] F. Yang, Y. Xing, D. Wang, K.-L. Tsui, A comparative study of three model-based algorithms for estimating state-of-charge of lithium-ion batteries under a new combined dynamic loading profile, Appl. Energy. 164 (2016) 387–399. doi:10.1016/j.apenergy.2015.11.072.

[135] M. Doyle, Modeling of Galvanostatic Charge and Discharge of the Lithium/Polymer/Insertion Cell, J. Electrochem. Soc. 140 (1993) 1526. doi:10.1149/1.2221597.

[136] A. Seaman, T.S. Dao, J. McPhee, A survey of mathematics-based equivalent-circuit and electrochemical battery models for hybrid and electric vehicle simulation, J. Power Sources. 256 (2014) 410–423. doi:10.1016/j.jpowsour.2014.01.057 Review.

[137] X. Lai, Y. Zheng, T. Sun, A comparative study of different equivalent circuit models for estimating state-of-charge of lithium-ion batteries, Electrochim. Acta. 259 (2018) 566–577. doi:10.1016/j.electacta.2017.10.153.

[138] T. Huria, M. Ceraolo, J. Gazzarri, R. Jackey, High Fidelity Electrical Model with Thermal Dependence for Characterization and Simulation of High Power Lithium Battery Cells, in: 2012 IEEE Int. Electr. Veh. Conf., Greenville, SC, 2012: pp. 1–8. doi:10.1109/IEVC.2012.6183271.

[139] H. Zhang, M.Y. Chow, Comprehensive dynamic battery modeling for PHEV applications, IEEE PES Gen. Meet. PES 2010. (2010) 1–6. doi:10.1109/PES.2010.5590108.

[140] C. Veth, D. Dragicevic, C. Merten, Thermal characterizations of a large-

format lithium ion cell focused on high current discharges, J. Power Sources. 267 (2014) 760–769. doi:10.1016/j.jpowsour.2014.05.139.

[141] M.S.K. Mutyala, J. Zhao, J. Li, H. Pan, C. Yuan, X. Li, In-situ temperature measurement in lithium ion battery by transferable flexible thin film thermocouples, J. Power Sources. 260 (2014) 43–49. doi:10.1016/j.jpowsour.2014.03.004.

[142] D. Bernardi, E. Pawlikowski, J. Newman, A General Energy Balance for Battery Systems, J. Electrochem. Soc. 132 (1985) 5. doi:10.1149/1.2113792.

[143] G. Xia, L. Cao, G. Bi, A review on battery thermal management in electric vehicle application, J. Power Sources. 367 (2017) 90–105. doi:10.1016/j.jpowsour.2017.09.046.

[144] D. Andre, M. Meiler, K. Steiner, H. Walz, T. Soczka-Guth, D.U. Sauer, Characterization of high-power lithium-ion batteries by electrochemical impedance spectroscopy. II: Modelling, J. Power Sources. 196 (2011) 5349–5356. doi:10.1016/j.jpowsour.2010.07.071.

[145] B.Y. Liaw, G. Nagasubramanian, R.G. Jungst, D.H. Doughty, Modeling of lithium ion cells - A simple equivalent-circuit model approach, Solid State Ionics. 175 (2004) 835–839. doi:10.1016/j.ssi.2004.09.049.

[146] C. Fiori, K. Ahn, H.A. Rakha, Power-based electric vehicle energy consumption model: Model development and validation, Appl. Energy. 168 (2016) 257–268. doi:10.1016/j.apenergy.2016.01.097.

[147] H. He, R. Xiong, J. Fan, Evaluation of lithium-ion battery equivalent circuit models for state of charge estimation by an experimental approach, Energies. 4 (2011) 582–598. doi:10.3390/en4040582.

[148] H. He, R. Xiong, H. Guo, S. Li, Comparison study on the battery models used for the energy management of batteries in electric vehicles, Energy Convers. Manag. 64 (2012) 113–21. doi:10.1016/j.enconman.2012.04.014.

[149] Y. Tripathy, A. McGordon, C.T.J. Low, A New Consideration for Validating

Battery Performance at Low Ambient Temperatures, Energies 2018, Vol. 11, Page 2439. 11 (2018) 2439. doi:10.3390/EN11092439.

[150] D. Andre, C. Appel, T. Soczka-Guth, D.U. Sauer, Advanced mathematical methods of SOC and SOH estimation for lithium-ion batteries, J. Power Sources. 224 (2013) 20–27. doi:10.1016/j.jpowsour.2012.10.001.

[151] W.D. Widanage, A. Barai, G.H. Chouchelamane, K. Uddin, A. McGordon, J. Marco, P. Jennings, Design and use of multisine signals for Li-ion battery equivalent circuit modelling. Part 2: Model estimation, J. Power Sources. 324 (2016) 61–69. doi:10.1016/j.jpowsour.2016.05.014.

[152] A.F. Pacheco, M.E.S. Martins, H. Zhao, New European Drive Cycle (NEDC) simulation of a passenger car with a HCCI engine: Emissions and fuel consumption results, Fuel. 111 (2013) 733–739. doi:10.1016/j.fuel.2013.03.060.

[153] B. Degraeuwe, M. Weiss, Does the New European Driving Cycle (NEDC) really fail to capture the NO X emissions of diesel cars in Europe?, 222 (2016) 234–241. doi:10.1016/j.envpol.2016.12.050.

[154] A. Nikolian, Y. Firouz, R. Gopalakrishnan, J.-M. Timmermans, N. Omar, P. van den Bossche, J. van Mierlo, Lithium Ion Batteries—Development of Advanced Electrical Equivalent Circuit Models for Nickel Manganese Cobalt Lithium-Ion, Energies. 9 (2016) 360. doi:10.3390/en9050360.

[155] A. Barai, K. Uddin, J. Chevalier, G.H. Chouchelamane, A. McGordon, J. Low, P. Jennings, Transportation Safety of Lithium Iron Phosphate Batteries - A Feasibility Study of Storing at Very Low States of Charge, Sci. Rep. 7 (2017) 1–10. doi:10.1038/s41598-017-05438-2.

[156] Nissan LEAF Charger | Pod Point, (n.d.). https://pod-point.com/landing-pages/nissan-leaf-charging (accessed January 17, 2019).

[157] A. Barai, W. Dhammika Widanage, A. McGordon, P. Jennings, The influence of temperature and charge-discharge rate on open circuit voltage hysteresis of

an LFP Li-ion battery, in: 2016 IEEE Transp. Electrif. Conf. Expo, ITEC 2016, Institute of Electrical and Electronics Engineers Inc., 2016. doi:10.1109/ITEC.2016.7520299.

[158] M.A. Roscher, O. Bohlen, J. Vetter, OCV Hysteresis in Li-Ion Batteries including Two-Phase Transition Materials, Int. J. Electrochem. 2011 (2011) 1–6. doi:10.4061/2011/984320.

[159] F. Baronti, N. Femia, R. Saletti, W. Zamboni, Comparing open-circuit voltage hysteresis models for lithium-iron-phosphate batteries, IECON Proc. (Industrial Electron. Conf. (2014) 5635–5640. doi:10.1109/IECON.2014.7049363.

[160] Y. Merla, B. Wu, V. Yufit, R.F. Martinez-Botas, G.J. Offer, An easy-to-parameterise physics-informed battery model and its application towards lithium-ion battery cell design, diagnosis, and degradation, J. Power Sources. 384 (2018) 66–79. doi:10.1016/j.jpowsour.2018.02.065.

[161] B. Wu, Z. Li, J. Zhang, Thermal Design for the Pouch-Type Large-Format Lithium-Ion Batteries: I. Thermo-Electrical Modeling and Origins of Temperature Non-Uniformity, J. Electrochem. Soc. 162 (2014) A181–A191. doi:10.1149/2.0831501jes.

[162] D. Worwood, Q. Kellner, E. Hosseinzadeh, D. Mullen, D. Greenwood, J. Marco, R. McGlen, K. Lynn, Thermal analysis of fin cooling large format automotive lithium-ion pouch cells, in: IEEE Veh. Power Propuls. Conf. Belfort, Fr. 11-14 Dec 2017., 2017. doi:10.1109/VPPC.2017.8330874.

[163] D. Worwood, E. Hosseinzadeh, Q. Kellner, J. Marco, D. Greenwood, R. McGlen, W.D. Widanage, A. Barai, P.A. Jennings, Thermal analysis of a lithium-ion pouch cell under aggressive automotive duty cycles with minimal cooling, IET Hybrid Electr. Veh. Conf. London, UK, 2-3 Nov 2016. (2016) 2–3.

[164] S.A. Birrell, A. McGordon, P.A. Jennings, Defining the accuracy of real-world range estimations of an electric vehicle, in: 17th Int. IEEE Conf. Intell.

Transp. Syst., IEEE, 2014: pp. 2590–2595. doi:10.1109/ITSC.2014.6958105.

[165] Z. Gao, T. LaClair, S. Ou, S. Huff, G. Wu, P. Hao, K. Boriboonsomsin, M. Barth, Evaluation of electric vehicle component performance over eco-driving cycles, Energy. 172 (2019) 823–839. doi:10.1016/j.energy.2019.02.017.

[166] R.T. Doucette, M.D. Mcculloch, Modeling the CO 2 emissions from battery electric vehicles given the power generation mixes of different countries, Energy Policy. 39 (2010) 803–811. doi:10.1016/j.enpol.2010.10.054.

[167] K. Kambly, T.H. Bradley, Geographical and temporal differences in electric vehicle range due to cabin conditioning energy consumption, J. Power Sources. 275 (2015) 468–475. doi:10.1016/j.jpowsour.2014.10.142.

[168] D. Myall, D. Ivanov, W. Larason, M. Nixon, H. Moller, Accelerated Reported Battery Capacity Loss in 30 kWh Variants of the Nissan Leaf, Preprints. 2018 (2018) 2018030122. doi:10.20944/preprints201803.0122.v1.

[169] E. Vergori, Y. Yu, Monitoring of Li-ion cells with distributed fibre optic sensors, in: Procedia Struct. Integr., Elsevier B.V., 2019: pp. 233–239. doi:10.1016/j.prostr.2020.02.020.

[170] True MPG: which cars beat their official figures – and which are farthest away? | What Car?, (n.d.). https://www.whatcar.com/news/true-mpg-which-cars-beat-their-official-figures-–-and-which-are-farthest-away/n21535#11 (accessed June 20, 2020).

[171] Real-World Range Test Of 12 Electric Cars: Results Compared To EPA, (n.d.). https://insideevs.com/news/407807/eletric-car-real-world-range-tested/ (accessed June 20, 2020).

[172] Electric Vehicles Out in the Cold - MIT Technology Review, (n.d.). https://www.technologyreview.com/s/522496/electric-vehicles-out-in-the-cold/ (accessed July 6, 2017).

[173] Tesla, Jaguar and Nissan EVs lose power in freezing temps, (n.d.). https://www.cnbc.com/2019/02/05/tesla-jaguar-and-nissan-evs-lose-power-in-

freezing-temps-.html (accessed June 21, 2020).

[174] H. Wu, X. Zhang, C. Wang, R. Cao, C. Yang, Experimental study on aerogel passive thermal control method for cylindrical lithium-ion batteries at low temperature, Appl. Therm. Eng. 169 (2020). doi:10.1016/j.applthermaleng.2020.114946.

[175] Y. Wang, C. Zhang, Z. Chen, A method for joint estimation of state-of-charge and available energy of LiFePO4 batteries, Appl. Energy. 135 (2014) 81–87. doi:10.1016/j.apenergy.2014.08.081.

[176] J.G. Quintiere, On methods to measure the energetics of a lithium ion battery in thermal runaway, Fire Saf. J. 111 (2020). doi:10.1016/j.firesaf.2019.102911.

[177] C. Truchot, M. Dubarry, B.Y. Liaw, State-of-charge estimation and uncertainty for lithium-ion battery strings, Appl. Energy. 119 (2014) 218–227. doi:10.1016/j.apenergy.2013.12.046.

[178] D. Worwood, Q. Kellner, M. Wojtala, W.D. Widanage, R. McGlen, D. Greenwood, J. Marco, A new approach to the internal thermal management of cylindrical battery cells for automotive applications, J. Power Sources. 346 (2017) 151–166. doi:10.1016/j.jpowsour.2017.02.023.

[179] A. Eddahech, O. Briat, J.M. Vinassa, Thermal characterization of a high-power lithium-ion battery: Potentiometric and calorimetric measurement of entropy changes, Energy. 61 (2013) 432–439. doi:10.1016/j.energy.2013.09.028.

[180] IEC 62660-1:2010 | IEC Webstore | battery, energy efficiency, energy storage, smart city, transportation, mobility, (n.d.). https://webstore.iec.ch/publication/7331#additionalinfo (accessed August 3, 2018).

[181] A.W. Schäfer, S.R.H. Barrett, K. Doyme, L.M. Dray, A.R. Gnadt, R. Self, A. O'sullivan, A.P. Synodinos, A.J. Torija, Technological, economic and

environmental prospects of all-electric aircraft, Nat. ENeRGy |. 4 (n.d.). doi:10.1038/s41560-018-0294-x.

[182] T. Waldmann, M. Wohlfahrt-Mehrens, In-Operando Measurement of Temperature Gradients in Cylindrical Lithium-Ion Cells during High-Current Discharge, ECS Electrochem. Lett. 4 (2015) A1–A3. doi:10.1149/2.0031501eel.

[183] E. McTurk, T. Amietszajew, J. Fleming, R. Bhagat, Thermo-electrochemical instrumentation of cylindrical Li-ion cells, J. Power Sources. 379 (2018) 309–316. doi:10.1016/j.jpowsour.2018.01.060.

[184] J. Fleming, T. Amietszajew, J. Charmet, A.J. Roberts, D. Greenwood, R. Bhagat, The design and impact of in-situ and operando thermal sensing for smart energy storage, J. Energy Storage. 22 (2019) 36–43. doi:10.1016/j.est.2019.01.026.

Appendix A. MATLAB/Simulink ECMs: Graphical Representation and Implementation

In this thesis, MATLAB/Simulink software R2017b edition was employed to build the equivalent circuit models (ECMs) used in this research. In the following section, the corresponding Simulink representations of the models described in Chapter 5 are presented. Two ECM structures were discussed in Chapter 5. First, the 1st order ECM (1RC) with a R-RC (a resistor in series with a single RC network) configuration for its impedance element. An RC network is a resistor connected in parallel with a capacitor. Second, the 2nd order ECM (2RC) with a R-RC-RC (a resistor in series with two RC networks) configuration for its impedance element.

In Figure A-1, the inputs and ouputs to a 1st order ECM are given. The inputs are experimentally measured cell current, voltage and surface temperature. The outputs are SOC, modelled terminal voltage, estimated OCV, modelled surface temperature, modelled operating temperature and finally, SOE. For the 1RC ECM, discharge current is positive.

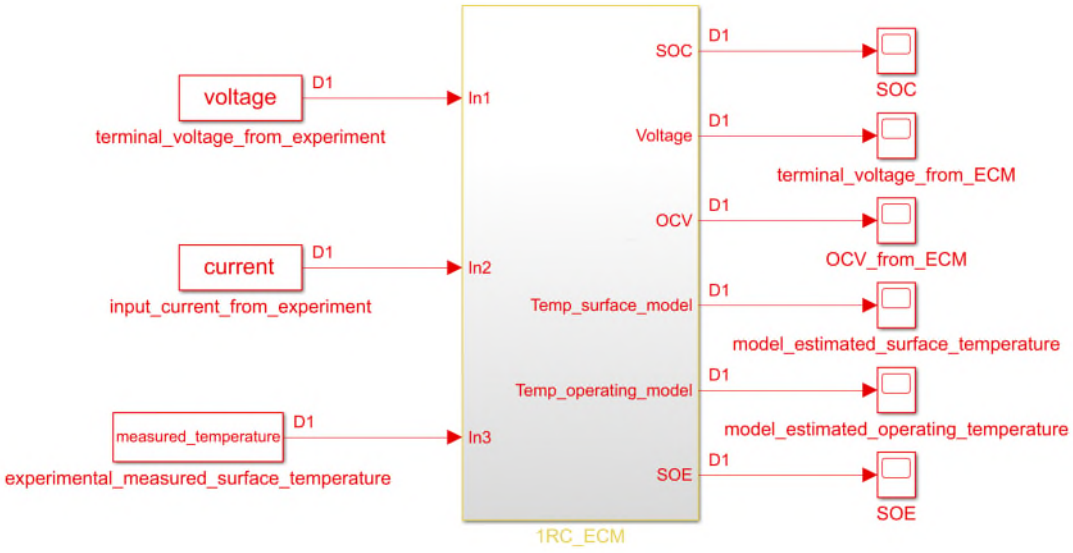

Figure A-1. Overview of MATLAB/Simulink Model for 1st Order (1RC) ECM

In Figure A-2, the overall Simulink graphical representation of the various subsystems of the 1RC ECM are presented.

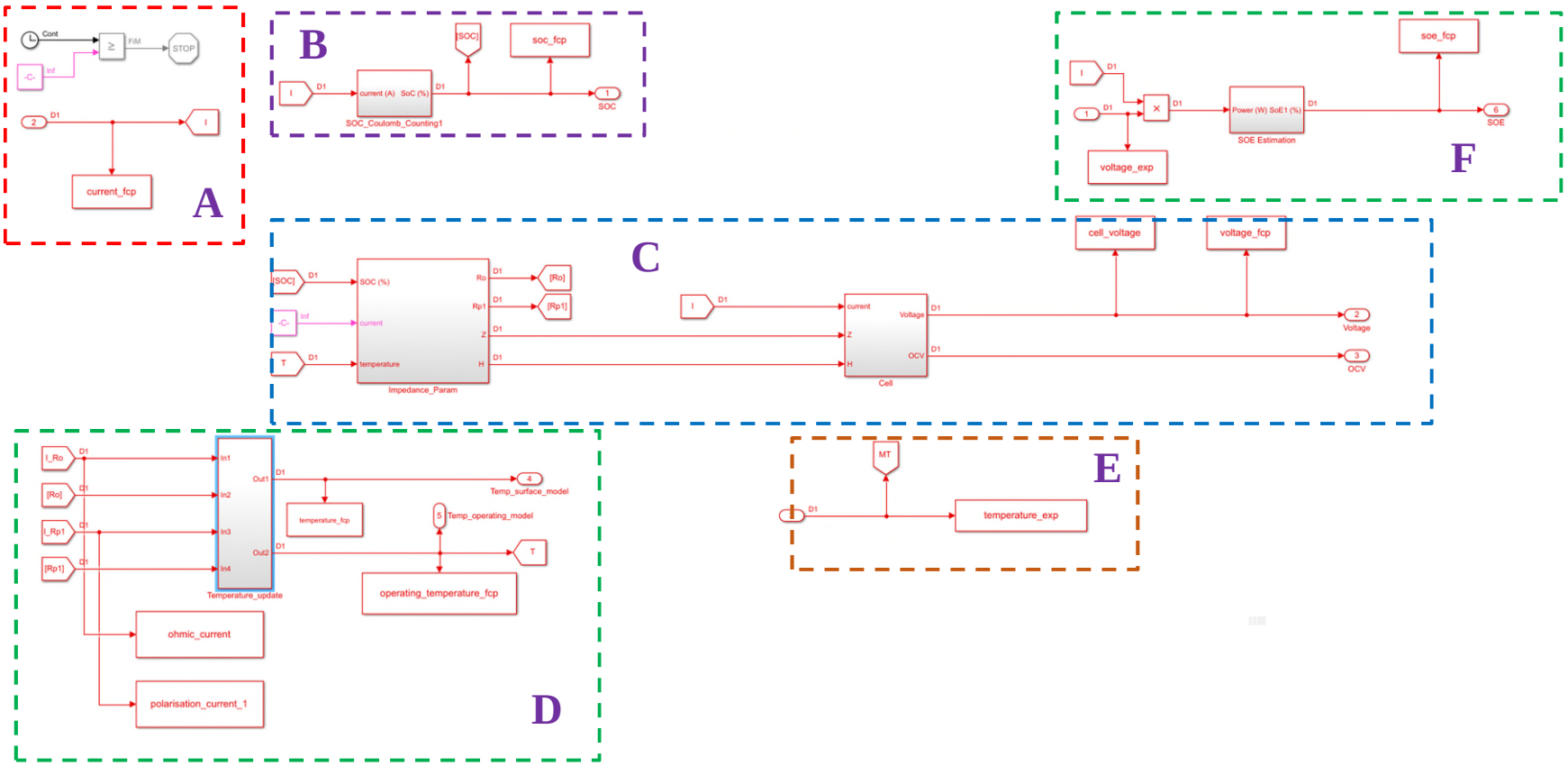

Figure A-2. Various Subsystems as part of 1RC ECM using MATLAB/Simulink: (a) Input Current and Simulation Time, (b) SOC Estimation, (c) Impedance and Terminal Voltage, (d) Thermal Feedback and (e) Surface Temperature Output

In Figure A-3, the SOC estimation subsystem developed in Simulink is presented. The inputs are measured current and measured surface temperature. The output is the SOC calibrated between 0 and 100. Note, the capacity values are parameterised based on input current and temperature and differ for air and oil based capacity datasets.

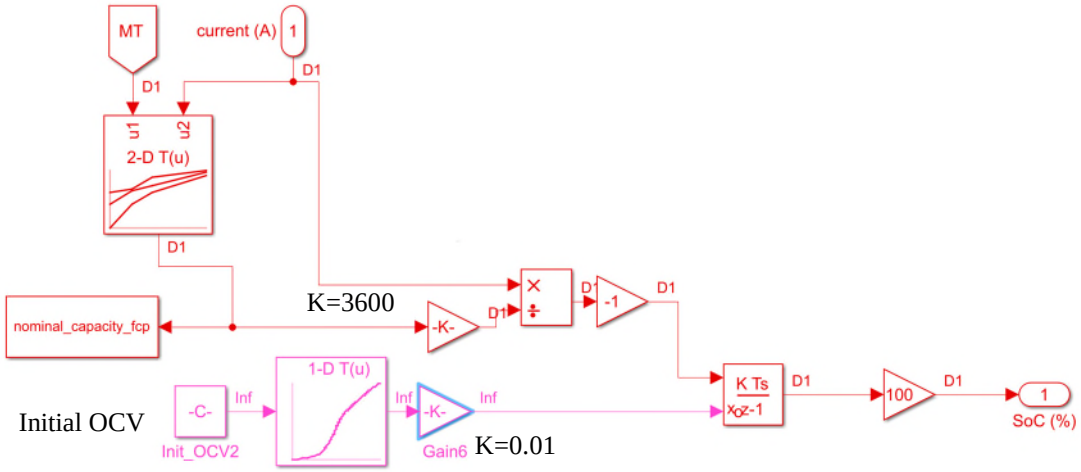

Figure A-3. SOC Estimation Subsystem for 1st order (1RC) ECM with Current Input and Measured Temperature Inputs

In Figure A-4, the thermal feedback subsystem designed for the 1RC ECM is given. The inputs are the Ohmic and Polarisation currents along with the corresponding resistances. The outputs are estimated operating temperature and estimated cell surface temperature. The cell heat transfer properties were detailed in Section 5.1.4.

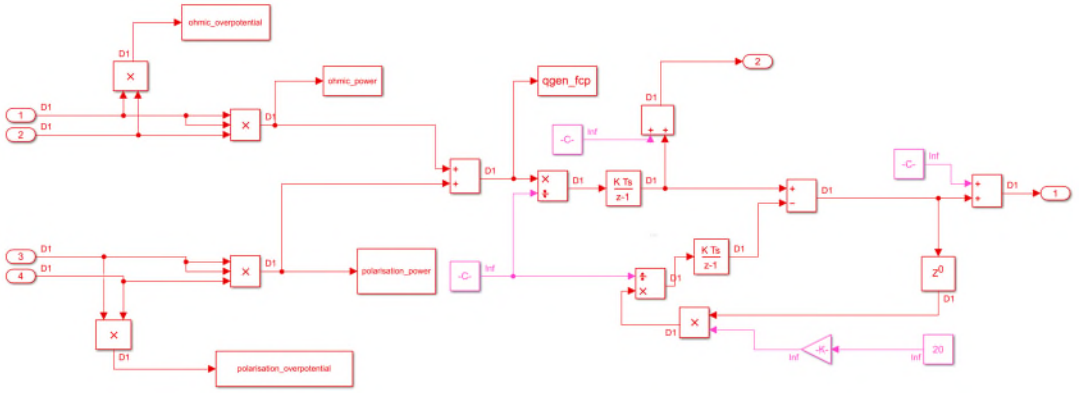

Figure A-4. Thermal Feedback Subsystem for 1st order (1RC) ECM

In Figure A-5, the impedance parameterisation for the 1RC ECM is presented. The inputs are estimated SOC, estimated operating temperature and drive cycle current. Note, the drive cycle current is the mean drive cycle current including both charge and discharge. Furthermore, the OCV and the H (SOC) as a function of estimated SOC and current sign are parameterised. The resistance values (R_O and R_{P1}) and τ_1 values are calculated using 3-D look-up tables. The 'n-D' look-up table Simulink blocks are used in their default configuration.

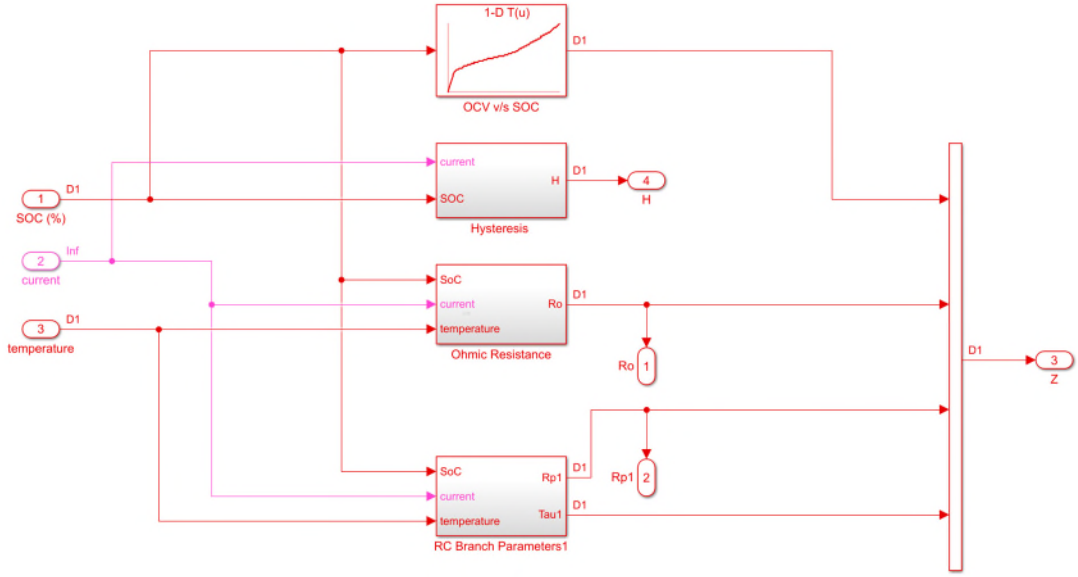

Figure A-5. Hysteresis and RC Parameters from Lookup Tables for 1st order (1RC) ECM

In Figure A-6, the overpotential and terminal voltage calculation subsystems for the 1RC ECM are presented.

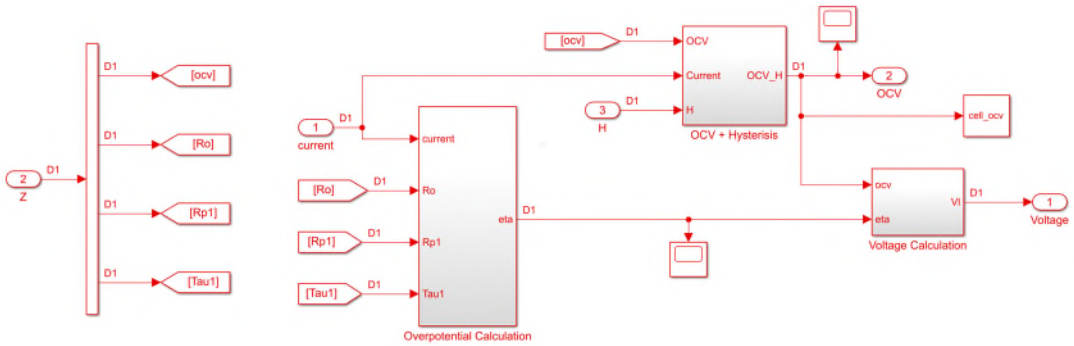

Figure A-6. Overpotential and Terminal Voltage Estimation for 1st order (1RC) ECM: (a) Overpotential Calculation, (b) OCV & Hysteresis and (c) Terminal Voltage

In Figure A-7, the Simulink implementation of cell overpotential calculation for the 1RC ECM is presented. The inputs are the parameterised impedance values and the experimental drive cycle current. As described in Section 5.1.3.2, the total overpotential arising from Ohmic overpotential and polarisation overpotential is calculated. The polarisation current implemented using a discrete time integrator Simulink block (in default setting) is saturated between −80 A (maximum charge current) and 200 A (maximum discharge current). The key outputs of the subsystem are total overpotential and polarisation current.

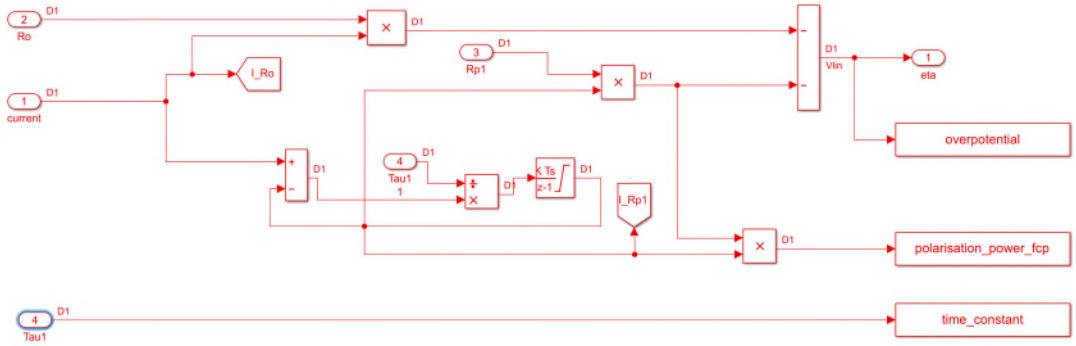

Figure A-7. Polarisation Currents and Cell Overpotential Calculation for 1st order (1RC) ECM

In Figure A-8, the implementation of voltage hysteresis to calculate model OCV is presented. The inputs are experimental current and H (SOC) and the output is modelled OCV.

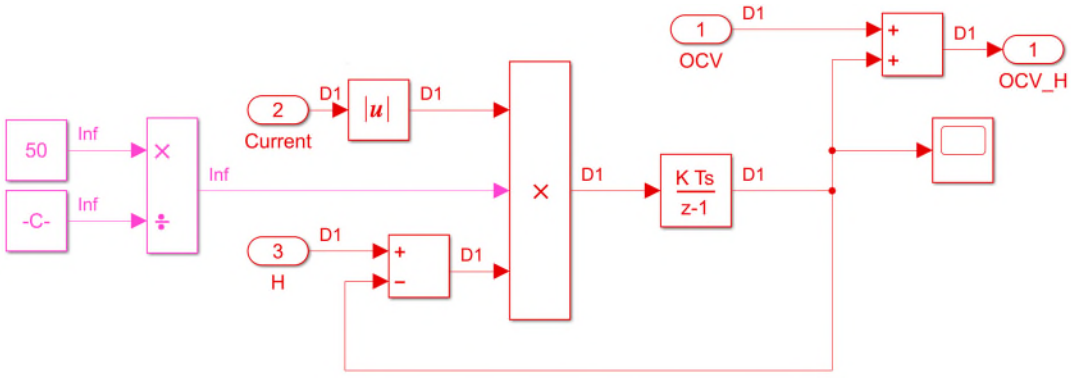

Figure A-8. Implementation of Hysteresis to OCV for 1st order (1RC) ECM

In Figure A-9, the terminal voltage calculation in the 1RC ECM is graphically presented. The inputs are OCV and cell total overpotential ('eta') at each time step. The output is modelled terminal voltage at each time step.

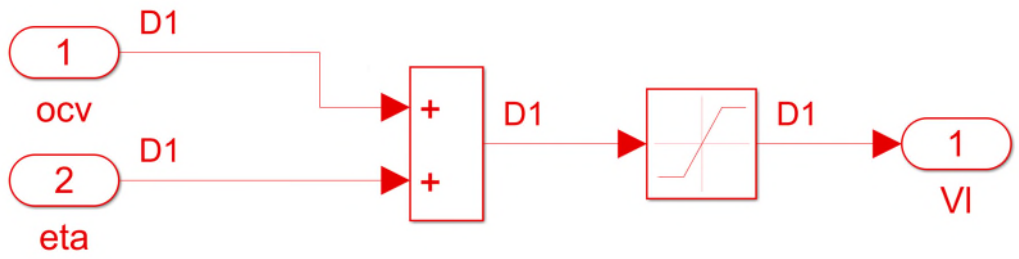

Figure A-9. Using OCV and Overpotential (eta) to Calculate 1st order (1RC) ECM

In Figure A-10, the SOE estimation subsystem implemented in Simulink is presented. The inputs are measured power ($P = V \times I$) and measured surface temperature. The energy values are parameterised based on these inputs and the output is SOE saturated between 0 and 100. Note, the energy values are parameterised based on measured input current and surface temperature and differ for air and oil based capacity datasets.

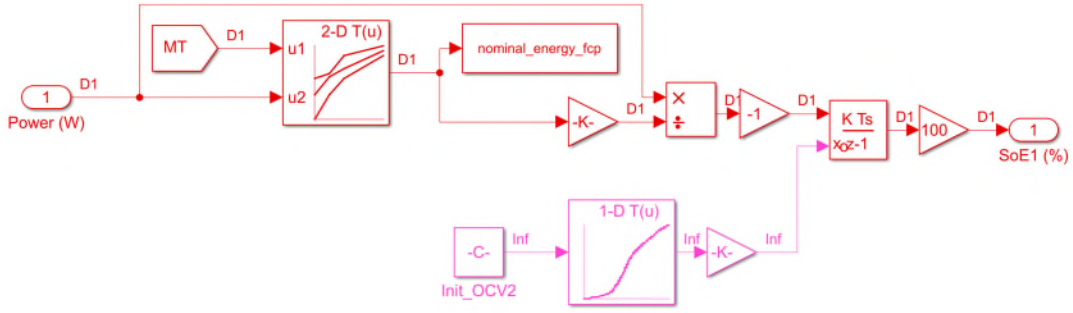

Figure A-10. SOE Estimation Subsystem with Current Input and Measured Temperature Inputs for 1st order (1RC) ECM

In Figure A-11, the Simulink model for the 2nd order ECM (2RC) is outlined. The inputs are experimentally measured cell current, voltage and surface temperature. The outputs are SOC, modelled terminal voltage, estimated OCV, modelled surface

temperature, modelled operating temperature and finally, SOE. For the 2RC ECM, discharge current is positive.

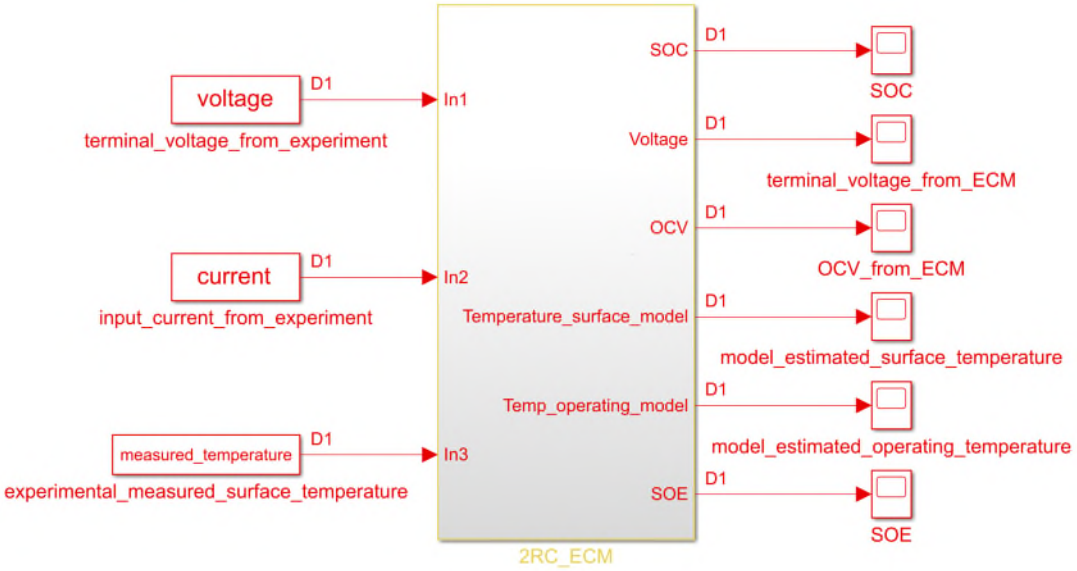

Figure A-11. Overview of MATLAB/Simulink Model for 2nd Order (2RC) ECM

In Figure A-12, the overall Simulink graphical representation of the various subsystems of the 1RC ECM are presented.

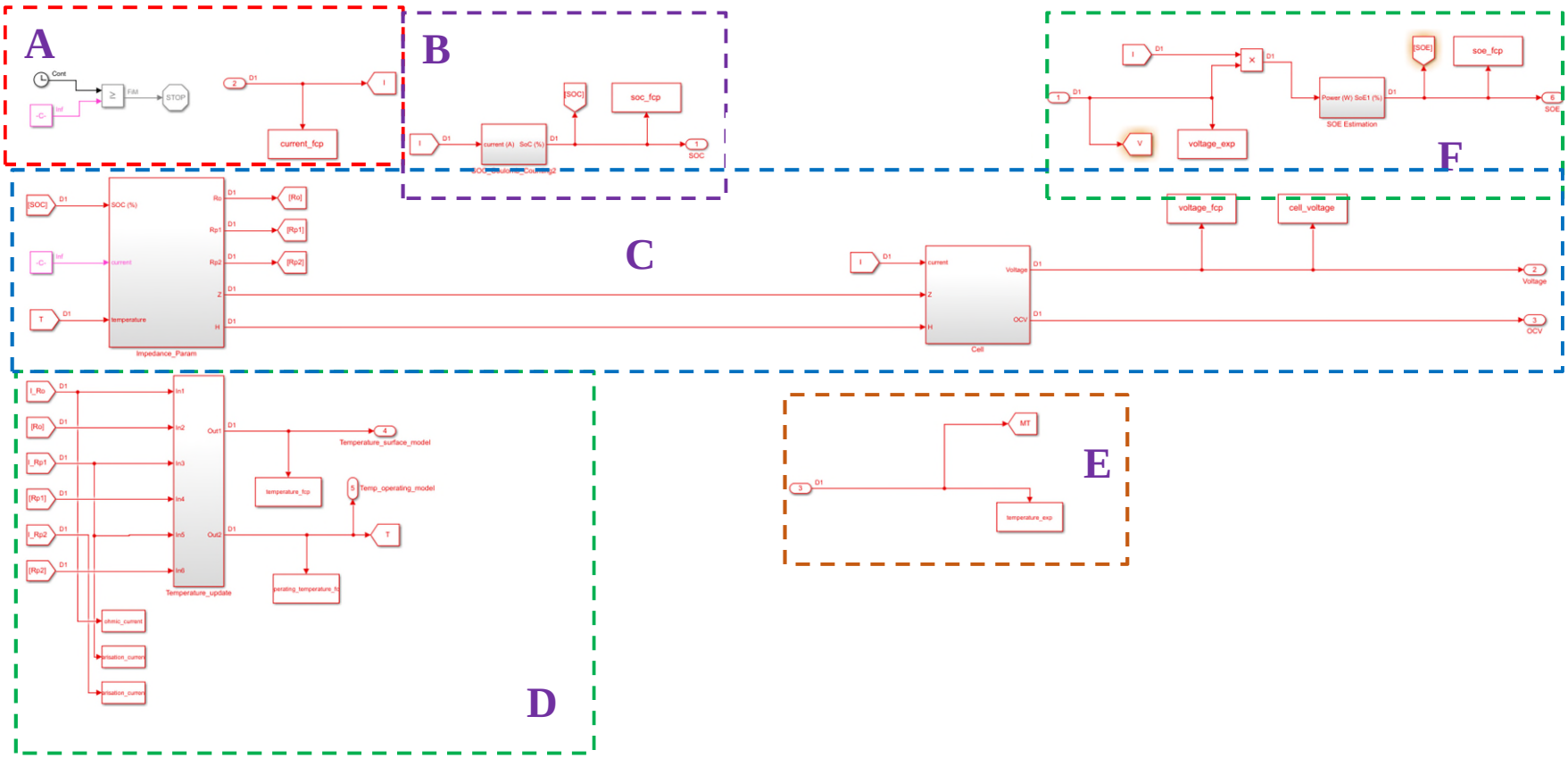

Figure A-12. Various Subsystems as part of 2RC ECM using MATLAB/Simulink: (a) Input Current and Simulation Time, (b) SOC Estimation, (c) Impedance and Terminal Voltage, (d) Thermal Feedback and (e) Surface Temperature Output

In Figure A-13, the SOC estimation subsystem developed in Simulink for the 2RC ECM is presented. The inputs are measured current and measured surface temperature. The output is the SOC calibrated between 0 and 100. Note, the capacity values are parameterised based on measured input current and surface temperature and differ for air and oil based capacity datasets.

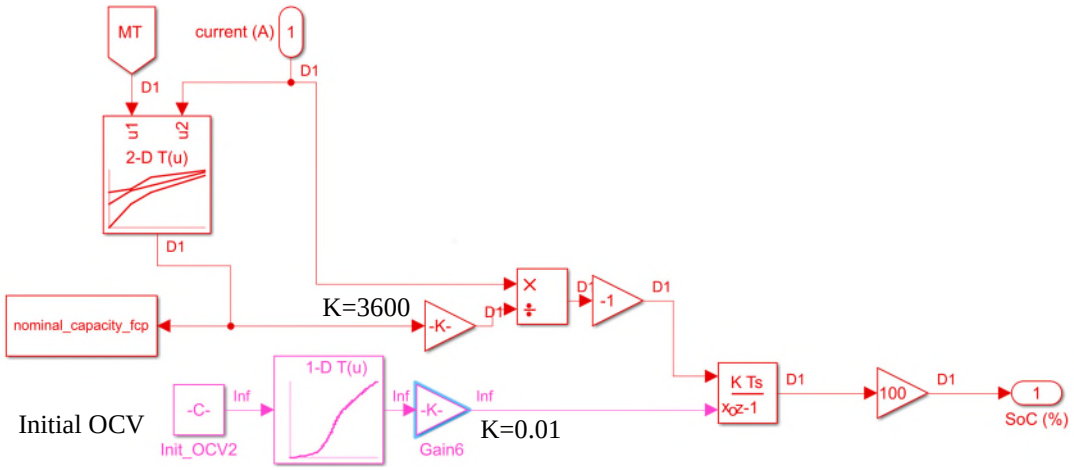

Figure A-13. SOC Estimation Subsystem for 2nd order (2RC) ECM with Current Input and Measured Temperature Inputs

Similar to the 1RC ECM, in Figure A-14, the thermal feedback subsystem designed for the 2RC ECM is given. The inputs are the Ohmic and Polarisation currents along with the corresponding resistances. The outputs are estimated operating temperature and estimated cell surface temperature. The cell heat transfer properties were detailed in Section 5.1.4.

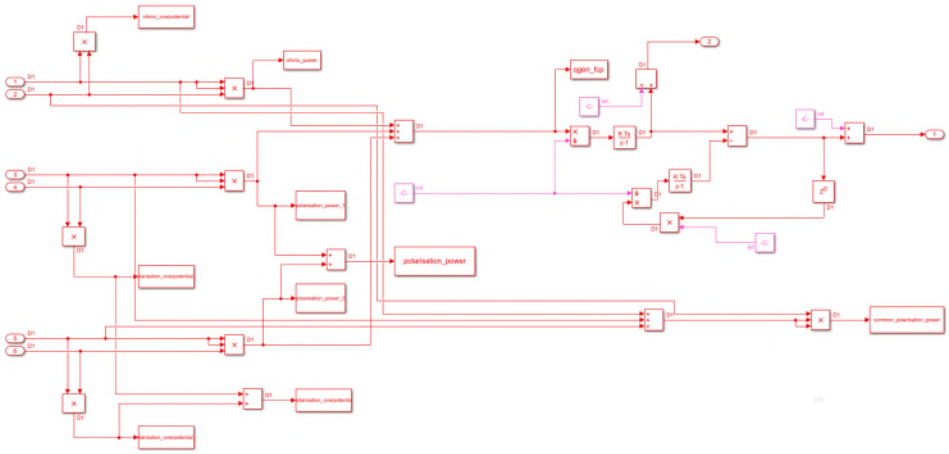

Figure A-14. Thermal Feedback Subsystem for 2nd order (2RC) ECM

In Figure A-15, the impedance parameterisation for the 2RC ECM is presented. The inputs are estimated SOC, estimated operating temperature and drive cycle current. Note, the drive cycle current is the mean drive cycle current including both charge and discharge. Furthermore, the OCV and the H (SOC) as a function of estimated SOC and current sign are parameterised. The resistance values (R_O, R_{P1} and R_{P1}) and, τ_1 and τ_2 values, were calculated using 3-D look-up tables. The 'n-D' look-up table Simulink blocks are used in their default configuration.

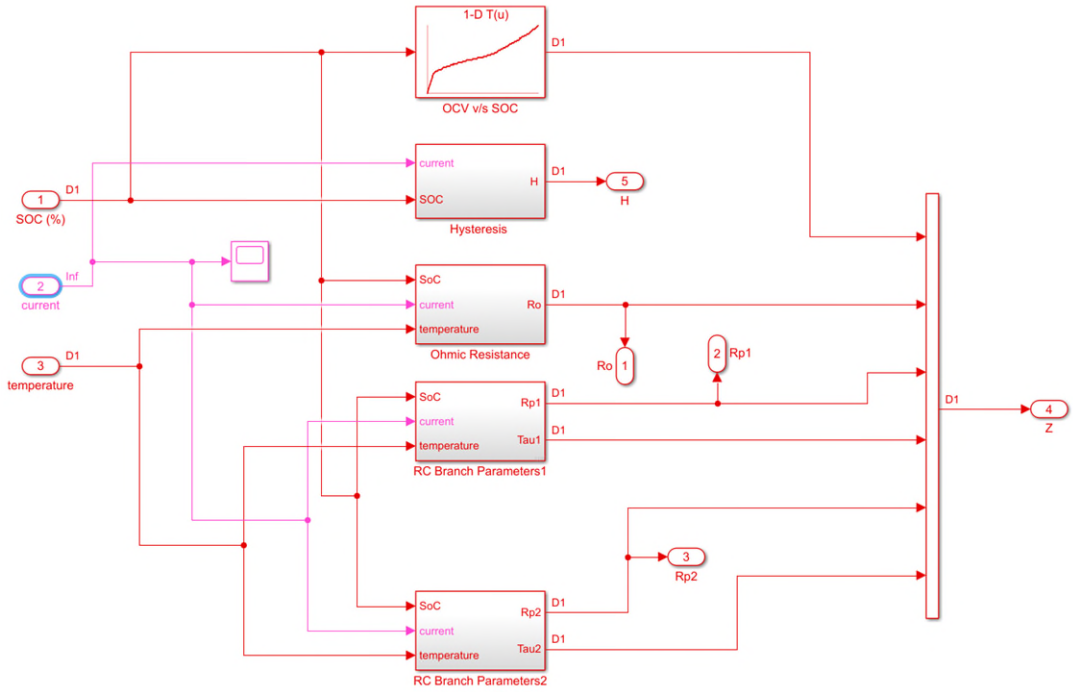

Figure A-15. Hysteresis and RC Parameters from Lookup Tables for 2nd order (2RC) ECM

In Figure A-16, the overpotential and terminal voltage subsystem for the 1RC ECM is presented.

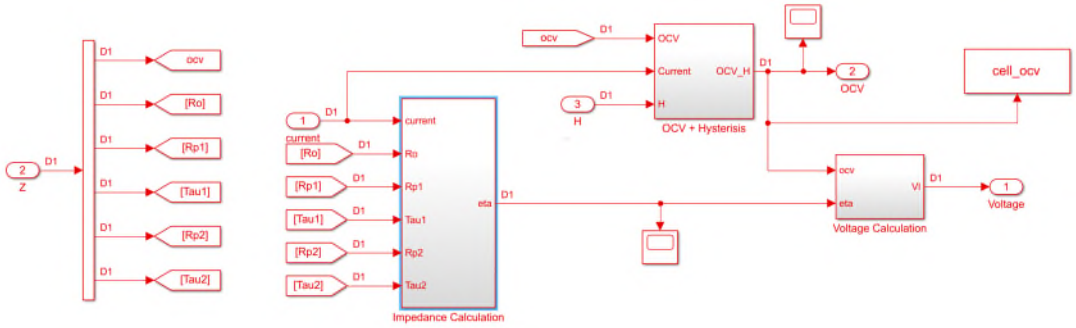

Figure A-16. Overpotential and Terminal Voltage Estimation for 2nd order (2RC) ECM: (a) Overpotential Calculation, (b) OCV & Hysteresis and (c) Terminal Voltage

In Figure A-17, the Simulink implementation of cell overpotential calculation for the 2RC ECM is presented. The inputs are the parameterised impedance values and the experimental current. As described in Section 5.1.3.2, the total overpotential arising from Ohmic overpotential and polarisation overpotential is calculated. The polarisation current implemented using a discrete time integrator Simulink block (in default setting) is saturated between −80 A (maximum charge current) and 200 A (maximum discharge current). The key outputs of the subsystem are total overpotential and the polarisation currents for the 2RC networks.

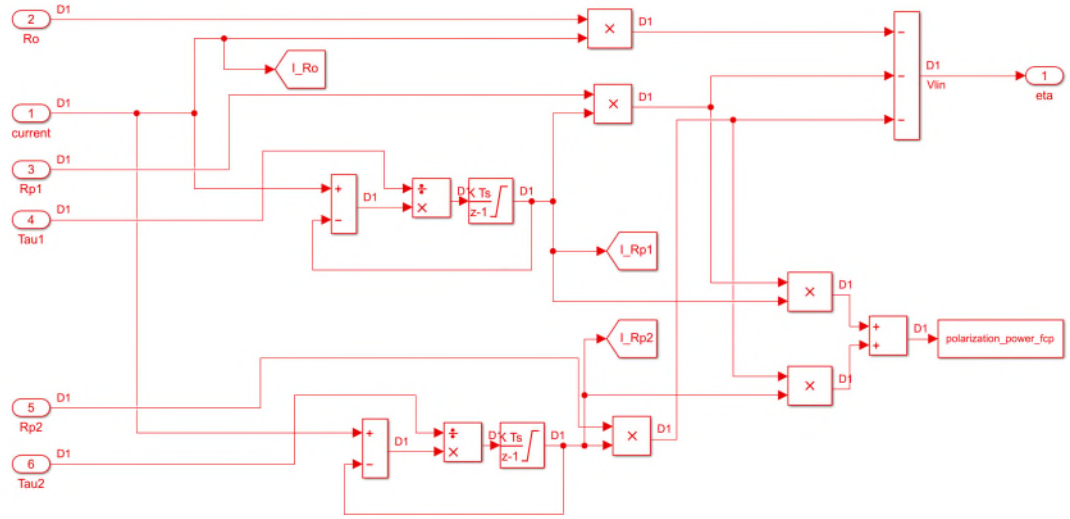

Figure A-17. Polarisation Currents and Cell Overpotential Calculation for 2nd order (2RC) ECM

In Figure A-18, the implementation of voltage hysteresis to calculate model OCV is presented. The inputs are experimental current and $H\,(SOC)$ and the output is modelled OCV.

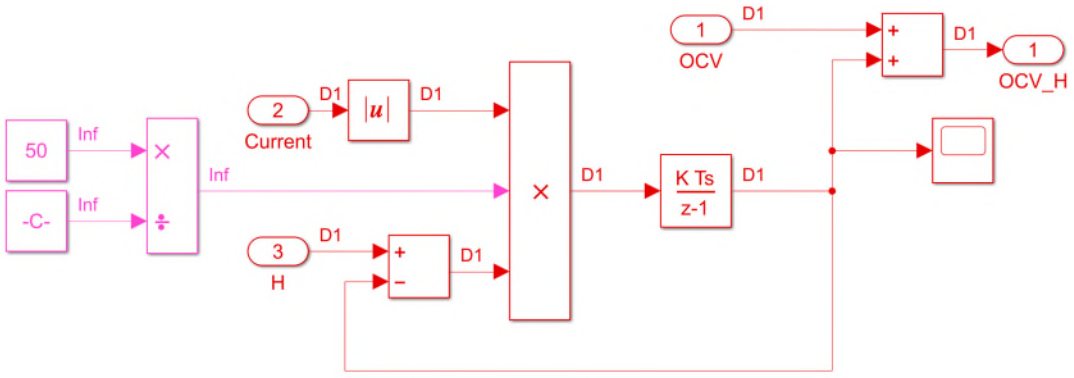

Figure A-18. Implementation of Hysteresis to OCV for 2nd order (2RC) ECM

In Figure A-19, the terminal voltage calculation in the 1RC ECM is graphically presented. The inputs are OCV and cell total overpotential ('eta') at each time step. The output is modelled terminal voltage at each time step.

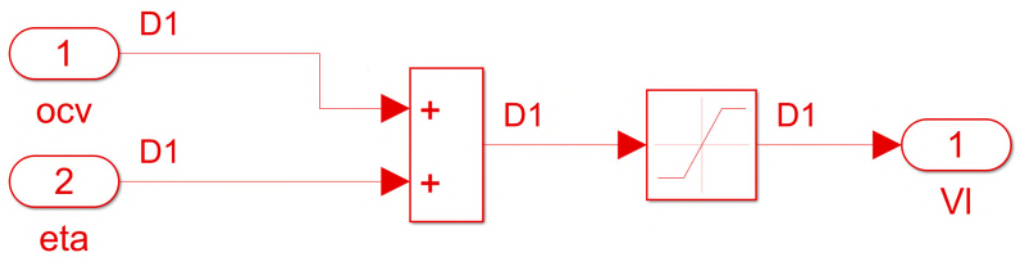

Figure A-19. Using OCV and Overpotential (eta) to Calculate 2nd order (2RC) ECM

In Figure A-20, the SOE estimation subsystem implemented in Simulink is presented. The inputs are measured power ($P = V \times I$) and measured surface temperature. The energy values are parameterised based on these inputs and the output is SOE saturated between 0 and 100. Note, the energy values are parameterised based on measured input current and surface temperature and differ for air and oil based capacity datasets.

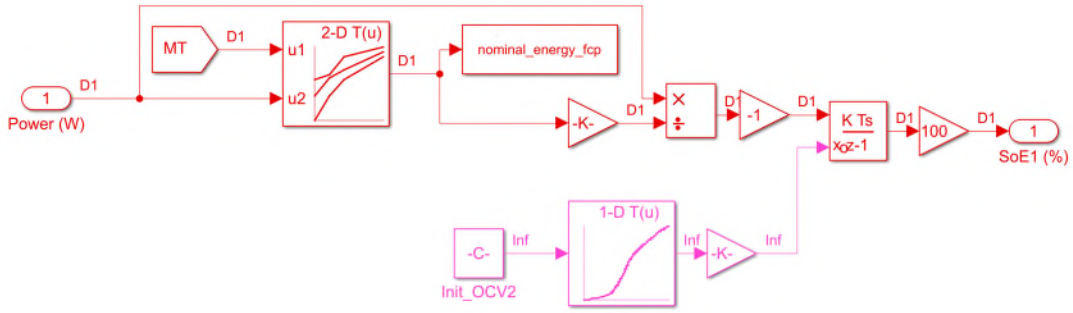

Figure A-20. SOE Estimation Subsystem with Current Input and Measured Temperature Inputs for 2nd order (2RC) ECM

Appendix B. MATLAB/Simulink ECMs: Code Employed to Develop and Simulate ECMs

1. For comparing air and oil based SOC estimation and for investigating their effect on model performance, the following MATLAB script was employed:

```
soc=65;
temperature='minus15';

load(['C:\PhD\Model\Validation_Data_New_Processed\2xUS06_',
temperature,'degC_master.mat'],'real_data','real_soc','real_soe');

order='2';
op_t=-15;

compare_US06
clearvars -except data1 soc temperature order op_t real_soc real_soe

warning off

% Initialise power profile for into current-based ECM

data1(1,4)=0;

test1=data1;

test=test1;

time=test(:,4);

current(:,1)=time;

current(:,2)=-test(:,1);

rc_current_discharge=mean(current(current(:,2)>0,2));
rc_current_charge=mean(current(current(:,2)>0,2));

rc_current=mean(current(:,2));

% rc_current_discharge=rc_current;

current_sign(:,1)=time;
current_sign(:,2)=0;

voltage(:,1)=time;
```

```
39 voltage(:,2)=test(:,2);
40
41 measured_temperature(:,1)=time;
42 measured_temperature(:,2)=test(:,3)+op_t;
43
44 load('C:\PhD\Model\Parameters_MATLAB\param_master_pulse_values.mat')
45
46 pulse_set=pulse_new;
47
48 load('C:\PhD\Model\Parameters_MATLAB\hysteresis.mat')
49
load(['C:\PhD\Model\Parameters_MATLAB\param_master_charge_and_discharge
_',
order,'_air_new.mat'])
50
51 init_ocv=voltage(1,2);
52
53 % Run current-based ECM for power profile
54
55 current(:,1)=time;
56 current(:,2)=-test(:,1);
57
58
sim(['C:\PhD\Model\ECM\Submission\Take_1_Current_Profile_',order,'RC_fi
nal.
slx']);
59
60 vrms(1,1)=1000*rms(voltage_exp-voltage_fcp);
61 vpeak(1,1)=1000*max(abs(voltage_exp-voltage_fcp));
62 trms(1,1)=rms(temperature_exp-temperature_fcp);
63
64 soc_air=soc_fcp-soc_fcp(1,1)+65;
65 soe_air=soe_fcp-soe_fcp(1,1)+65;
66
67 air_soc=soc_air(end);
68 air_soe=soe_air(end);
69
70 nominal_capacity(1,1)=mean(nominal_capacity_fcp);
71
72 nominal_energy(1,1)=mean(nominal_energy_fcp);
73
74 voltage_fcp1=voltage_fcp;
75
76 operating_temperature_fcp1=operating_temperature_fcp;
77
78 surface_temperature_fcp1=temperature_fcp;
79
80 polarisation_current_fcp1=polarisation_current_1;
```

```
81
82 polarisation_heat_fcp1=polarisation_power;
83
84 total_heat_fcp1=qgen_fcp;
85
86
87  clearvars  -except  air_soc  air_soe  real_soc  real_soe  pulse_set
total_heat_fcp1
polarisation_heat_common_fcp1                    polarisation_heat_fcp1
polarisation_current_fcp1
surface_temperature_fcp1    soc_star_air    soe_star_air    tm    vpeak
operating_temperature_fcp1
voltage_fcp1 soc temperature order op_t nominal_capacity nominal_energy
current time
rc_current_discharge rc_current_charge voltage vrms trms soc_air soe_air
temperature_fcp      temperature_exp      voltage_fcp      current_fcp
operating_temperature_fcp
measured_temperature
88
89 load('C:\PhD\Model\Parameters_MATLAB\hysteresis.mat')
90
load(['C:\PhD\Model\Parameters_MATLAB\param_master_charge_and_discharge
_',
order,'_oil_new.mat'])
91
92 init_ocv=voltage(1,2);
93
94 % Run current-based ECM for power profile
95
96
sim(['C:\PhD\Model\ECM\Submission\Take_1_Current_Profile_',order,'RC_fi
nal.
slx']);
97
98 vrms(1,2)=1000*rms(voltage_exp-voltage_fcp);
99 vpeak(1,2)=1000*max(abs(voltage_exp-voltage_fcp));
100 trms(1,2)=rms(temperature_exp-temperature_fcp);
101
102  rms  =  1000*sqrt(movmean((voltage_exp-voltage_fcp).*(voltage_exp-
voltage_fcp),
100));
103
104 soc_oil=soc_fcp(:,1)-soc_fcp(1,1)+65;
105 soe_oil=soe_fcp(:,1)-soe_fcp(1,1)+65;
106
107 oil_soc=soc_oil(end);
108 oil_soe=soe_oil(end);
109
```

```
110 nominal_capacity(1,2)=mean(nominal_capacity_fcp);
111
112 nominal_energy(1,2)=mean(nominal_energy_fcp);
113
114 voltage_fcp2=voltage_fcp;
115
116 operating_temperature_fcp2=operating_temperature_fcp;
117
118 surface_temperature_fcp2=temperature_fcp;
119
120 polarisation_current_fcp2=polarisation_current_1;
121
122 polarisation_heat_fcp2=polarisation_power;
123 total_heat_fcp2=qgen_fcp;
124
125 clearvars -except air_soc air_soe oil_soc oil_soe real_soc real_soe
vpeak
polarisation_heat_common_fcp1              polarisation_heat_common_fcp2
total_heat_fcp1
total_heat_fcp2 polarisation_heat_fcp1 polarisation_heat_fcp2
polarisation_current_fcp1                      polarisation_current_fcp2
surface_temperature_fcp1
surface_temperature_fcp2    soc_star_air    soe_star_air    soc_star_oil
soe_star_oil tm
measured_temperature                           operating_temperature_fcp1
operating_temperature_fcp2 soc
temperature     order     op_t     current_fcp     rc_current_discharge
rc_current_charge vrms trms
soc_air   soc_oil   soe_air   soe_oil   nominal_capacity   nominal_energy
voltage_fcp2
voltage_fcp1 voltage_exp
```

2. For comparing the effect of choosing polarisation current as part of thermal feedback subsystem on surface temperature estimation and for investigating their effect on model performance, the following MATLAB script was employed:

```
1 soc=65;
2 temperature='25';
3
4 load(['C:\PhD\Model\Validation_Data_New_Processed\2xUS06_',
temperature,'degC_master.mat'],'real_data','real_soc','real_soe');
5
6 order='1';
7 op_t=25;
8
```

```
9 compare_US06
10 clearvars -except data1 soc temperature order op_t real_soc real_soe
11
12 warning off
13
14 % Initialise power profile for into current-based ECM
15
16 data1(1,4)=0;
17
18 test1=data1;
19
20 test=test1;
21
22 time=test(:,4);
23
24 current(:,1)=time;
25
26 current(:,2)=-test(:,1);
27
28 rc_current_discharge=mean(current(current(:,2)>0,2));
29 rc_current_charge=mean(current(current(:,2)>0,2));
30
31 rc_current=mean(current(:,2));
32
33 % rc_current_discharge=rc_current;
34
35 current_sign(:,1)=time;
36 current_sign(:,2)=0;
37
38 voltage(:,1)=time;
39 voltage(:,2)=test(:,2);
40
41 measured_temperature(:,1)=time;
42 measured_temperature(:,2)=test(:,3)+op_t;
43
44 load('C:\PhD\Model\Parameters_MATLAB\param_master_pulse_values.mat')
45
46 pulse_set=pulse_new;
47
48 load('C:\PhD\Model\Parameters_MATLAB\hysteresis.mat')
49
load(['C:\PhD\Model\Parameters_MATLAB\param_master_charge_and_discharge
_',
order,'_oil_new.mat'])
50
51 init_ocv=voltage(1,2);
52
53 % Run current-based ECM for power profile
```

```
54
55 current(:,1)=time;
56 current(:,2)=-test(:,1);
57
58 sim(['C:\PhD\Model\ECM\Submission\Take_1_Current_Profile_',
order,'RC_final_common.slx']);
59
60 vrms(1,1)=1000*rms(voltage_exp-voltage_fcp);
61 vpeak(1,1)=1000*max(abs(voltage_exp-voltage_fcp));
62 trms(1,1)=rms(temperature_exp-temperature_fcp);
63
64 soc_air=soc_fcp-soc_fcp(1,1)+65;
65 soe_air=soe_fcp-soe_fcp(1,1)+65;
66
67 air_soc=soc_air(end);
68 air_soe=soe_air(end);
69
70 nominal_capacity(1,1)=mean(nominal_capacity_fcp);
71
72 nominal_energy(1,1)=mean(nominal_energy_fcp);
73
74 voltage_fcp1=voltage_fcp;
75
76 operating_temperature_fcp1=operating_temperature_fcp;
77
78 surface_temperature_fcp1=temperature_fcp;
79
80 polarisation_current_fcp1=polarisation_current_1;
81
82 polarisation_heat_fcp1=polarisation_power;
83
84 total_heat_fcp1=qgen_fcp;
85
86 total_heat_energy_fcp1=cumsum(qgen_fcp)/3600;
87
88
89 clearvars -except total_heat_energy_fcp1 air_soc air_soe real_soc
real_soe
pulse_set total_heat_fcp1 polarisation_heat_common_fcp1
polarisation_heat_fcp1
polarisation_current_fcp1 surface_temperature_fcp1 soc_star_air
soe_star_air tm vpeak
operating_temperature_fcp1 voltage_fcp1 soc temperature order op_t
nominal_capacity
nominal_energy current time rc_current_discharge rc_current_charge
voltage vrms trms
soc_air soe_air temperature_fcp temperature_exp voltage_fcp current_fcp
operating_temperature_fcp measured_temperature
```

```
90
91 load('C:\PhD\Model\Parameters_MATLAB\hysteresis.mat')
92
load(['C:\PhD\Model\Parameters_MATLAB\param_master_charge_and_discharge
_',
order,'_oil_new.mat'])
93
94 init_ocv=voltage(1,2);
95
96 % Run current-based ECM for power profile
97
98
sim(['C:\PhD\Model\ECM\Submission\Take_1_Current_Profile_',order,'RC_fi
nal.
slx']);
99
100 vrms(1,2)=1000*rms(voltage_exp-voltage_fcp);
101 vpeak(1,2)=1000*max(abs(voltage_exp-voltage_fcp));
102 trms(1,2)=rms(temperature_exp-temperature_fcp);
103
104  rms  =  1000*sqrt(movmean((voltage_exp-voltage_fcp).*(voltage_exp-
voltage_fcp),
100));
105
106 soc_oil=soc_fcp(:,1)-soc_fcp(1,1)+65;
107 soe_oil=soe_fcp(:,1)-soe_fcp(1,1)+65;
108
109 oil_soc=soc_oil(end);
110 oil_soe=soe_oil(end);
111
112 nominal_capacity(1,2)=mean(nominal_capacity_fcp);
113
114 nominal_energy(1,2)=mean(nominal_energy_fcp);
115
116 voltage_fcp2=voltage_fcp;
117
118 operating_temperature_fcp2=operating_temperature_fcp;
119
120 surface_temperature_fcp2=temperature_fcp;
121
122 polarisation_current_fcp2=polarisation_current_1;
123
124 polarisation_heat_fcp2=polarisation_power;
125
126 total_heat_fcp2=qgen_fcp;
127
128 total_heat_energy_fcp2=cumsum(qgen_fcp)/3600;
129
```

```
130 clearvars -except total_heat_energy_fcp1 total_heat_energy_fcp2
temperature_exp air_soc air_soe oil_soc oil_soe real_soc real_soe vpeak
polarisation_heat_common_fcp1              polarisation_heat_common_fcp2
total_heat_fcp1
total_heat_fcp2 polarisation_heat_fcp1 polarisation_heat_fcp2
polarisation_current_fcp1                      polarisation_current_fcp2
surface_temperature_fcp1
surface_temperature_fcp2    soc_star_air    soe_star_air    soc_star_oil
soe_star_oil tm
measured_temperature                          operating_temperature_fcp1
operating_temperature_fcp2 soc
temperature     order     op_t     current_fcp     rc_current_discharge
rc_current_charge   vrms   trms   soc_air   soc_oil   soe_air   soe_oil
nominal_capacity nominal_energy voltage_fcp2 voltage_fcp1 voltage_exp
```

3. The following MATLAB script was utilised to implement the fitted RC parameters into lookup-tables for both 1st and 2nd order ECMs (1RC and 2RC, respectively):

```
1 clearvars -except capacity energy_values hysteresis soe_ocv
2
3 ambient{1,1}='minus20';
4 ambient{2,1}='minus10';
5 ambient{3,1}='0';
6 ambient{4,1}='25';
7
8 soc{1,1}='20';
9 soc{2,1}='50';
10 soc{3,1}='80';
11
12 order=0;
13
14 master_Ro=zeros(3,18,4);
15
16 if order~=0
17
18 master_Rp1=zeros(3,18,4);
19 master_Tau1=zeros(3,18,4);
20
21 if order==2
22
23 master_Rp2=zeros(3,18,4);
24 master_Tau2=zeros(3,18,4);
25 end
26 end
27
```

```
28 for aa=1:4
29
30 for jj=1:3
31
32 load(['C:\PhD\Model\Xalt\MAT\PPC_',num2str(order),'RCx\',ambient{aa,
1},'degC_soc_',soc{jj,1},'.mat'])
33
34
35
36 nc=max(size(transpose(fliplr(RoCm))));
37
38 nd=max(size(transpose(RoDm)));
39
40 RoCm=fliplr(transpose(RoCm));
41
42 ErCm=fliplr(transpose(ErCm));
43
44 stdRoCm=fliplr(transpose(stdRoCm));
45
46 RoDm=transpose(RoDm);
47
48 ErDm=transpose(ErDm);
49
50 stdRoDm=transpose(stdRoDm);
51
52 PulseCm=fliplr(transpose(PulseCm));
53
54 PulseDm=transpose(PulseDm);
55
56 master_Ro(jj,9-nc:8+nd,aa)=[RoCm RoDm];
57
58 master_Er(jj,9-nc:8+nd,aa)=[ErCm ErDm];
59
60 master_stdRo(jj,9-nc:8+nd,aa)=[stdRoCm stdRoDm];
61
62 master_Pulse(jj,9-nc:8+nd,aa)=[PulseCm PulseDm];
63
64 if order ~= 0
65
66 RpCm=fliplr(transpose(RpCm));
67
68 stdRpCm=fliplr(transpose(stdRpCm));
69
70 RpDm=transpose(RpDm);
71
72 stdRpDm=transpose(stdRpDm);
73
74 TauCm=fliplr(transpose(TauCm));
```

```
75
76 stdTauCm=fliplr(transpose(stdTauCm));
77
78 TauDm=transpose(TauDm);
79 stdTauDm=transpose(stdTauDm);
80
81 master_Rp1(jj,9-nc:8+nd,aa)=[RpCm(1,:) RpDm(1,:)];
82
83 master_stdRp1(jj,9-nc:8+nd,aa)=[stdRpCm(1,:) stdRpDm(1,:)];
84
85 master_Tau1(jj,9-nc:8+nd,aa)=[TauCm(1,:) TauDm(1,:)];
86
87 master_stdTau1(jj,9-nc:8+nd,aa)=[stdTauCm(1,:) stdTauDm(1,:)];
88
89 if order==2
90
91 master_Rp2(jj,9-nc:8+nd,aa)=[RpCm(2,:) RpDm(2,:)];
92
93 master_stdRp2(jj,9-nc:8+nd,aa)=[stdRpCm(2,:) stdRpDm(2,:)];
94
95 master_Tau2(jj,9-nc:8+nd,aa)=[TauCm(2,:) TauDm(2,:)];
96
97 master_stdTau2(jj,9-nc:8+nd,aa)=[stdTauCm(2,:) stdTauDm(2,:)];
98
99 else
100
101 master_Rp2(jj,9-nc:8+nd,aa)=[RpCm(1,:) RpDm(1,:)];
102
103 master_stdRp2(jj,9-nc:8+nd,aa)=[stdRpCm(1,:) stdRpDm(1,:)];
104
105 master_Tau2(jj,9-nc:8+nd,aa)=[TauCm(1,:) TauDm(1,:)];
106
107 master_stdTau2(jj,9-nc:8+nd,aa)=[stdTauCm(1,:) stdTauDm(1,:)];
108
109 end
110
111 end
112
113 for index=1:18
114
115 if master_Ro(jj,index,aa)==0 && index<9
116
117 master_Ro(jj,index,aa)=master_Ro(jj,9-nc,aa);
118 master_Er(jj,index,aa)=master_Er(jj,9-nc,aa);
119 master_stdRo(jj,index,aa)=master_stdRo(jj,9-nc,aa);
120 master_Pulse(jj,index,aa)=master_Pulse(jj,9-nc,aa);
121
122 if order~=0
```

```
123 master_Rp1(jj,index,aa)=master_Rp1(jj,9-nc,aa);
124 master_Rp2(jj,index,aa)=master_Rp2(jj,9-nc,aa);
125 master_Tau1(jj,index,aa)=master_Tau1(jj,9-nc,aa);
126 master_Tau2(jj,index,aa)=master_Tau2(jj,9-nc,aa);
127
128 master_stdRp1(jj,index,aa)=master_stdRp1(jj,9-nc,aa);
129 master_stdRp2(jj,index,aa)=master_stdRp2(jj,9-nc,aa);
130 master_stdTau1(jj,index,aa)=master_stdTau1(jj,9-nc,aa);
131 master_stdTau2(jj,index,aa)=master_stdTau2(jj,9-nc,aa);
132
133 end
134
135 elseif master_Ro(jj,index,aa)==0 && index>8
136
137 master_Ro(jj,index,aa)=master_Ro(jj,8+nd,aa);
138 master_Er(jj,index,aa)=master_Er(jj,8+nd,aa);
139 master_stdRo(jj,index,aa)=master_stdRo(jj,8+nd,aa);
140 master_Pulse(jj,index,aa)=master_Pulse(jj,8+nd,aa);
141
142 if order~=0
143 master_Rp1(jj,index,aa)=master_Rp1(jj,8+nd,aa);
144 master_Rp2(jj,index,aa)=master_Rp2(jj,8+nd,aa);
145 master_Tau1(jj,index,aa)=master_Tau1(jj,8+nd,aa);
146 master_Tau2(jj,index,aa)=master_Tau2(jj,8+nd,aa);
147
148 master_stdRp1(jj,index,aa)=master_stdRp1(jj,8+nd,aa);
149 master_stdRp2(jj,index,aa)=master_stdRp2(jj,8+nd,aa);
150 master_stdTau1(jj,index,aa)=master_stdTau1(jj,8+nd,aa);
151 master_stdTau2(jj,index,aa)=master_stdTau2(jj,8+nd,aa);
152
153 end
154 end
155
156 end
157 end
158 end
159
160 clearvars -except master_Er order capacity energy_values hysteresis
soe_ocv
master_Ro  master_Rp1  master_Rp2  master_Tau1  master_Tau2  master_Pulse
master_stdRo
master_stdRp1 master_stdRp2 master_stdTau1 master_stdTau2
161
162 pulse=master_Pulse(:,[1 2 3 4 5 6 11 12 13 14 15 16 17],:);
163
164 Ro=master_Ro(:,[1 2 3 4 5 6 11 12 13 14 15 16 17],:);
165
166 Er=master_Er(:,[1 2 3 4 5 6 11 12 13 14 15 16 17],:);
```

```
167
168 stdRo=master_stdRo(:,[1 2 3 4 5 6 11 12 13 14 15 16 17],:);
169
170 Ro=1000*Ro;
171 stdRo=1000*stdRo;
172
173 if order~=0
174
175 Rp1=1000*master_Rp1(:,[1 2 3 4 5 6 11 12 13 14 15 16 17],:);
176
177 Tau1=master_Tau1(:,[1 2 3 4 5 6 11 12 13 14 15 16 17],:);
178
179 stdRp1=1000*master_stdRp1(:,[1 2 3 4 5 6 11 12 13 14 15 16 17],:);
180
181 stdTau1=master_stdTau1(:,[1 2 3 4 5 6 11 12 13 14 15 16 17],:);
182
183 if order==2
184
185 Rp2=1000*master_Rp2(:,[1 2 3 4 5 6 11 12 13 14 15 16 17],:);
186 Tau2=master_Tau2(:,[1 2 3 4 5 6 11 12 13 14 15 16 17],:);
187
188 stdRp2=1000*master_stdRp2(:,[1 2 3 4 5 6 11 12 13 14 15 16 17],:);
189 stdTau2=master_stdTau2(:,[1 2 3 4 5 6 11 12 13 14 15 16 17],:);
190
191 end
192
193 end
194
195 clearvars -except Er Ro Rp1 Tau1 Rp2 Tau2 pulse order stdRo stdRp1
stdTau1 stdRp2
stdTau2
196
197 pcRo=100*stdRo./Ro;
198
199 pcRp1=100*stdRp1./Rp1;
200
201 pcTau1=100*stdTau1./Tau1;
202
203 if order==2
204
205 pcRp2=100*stdRp2./Rp2;
206
207 pcTau2=100*stdTau2./Tau2;
208
209 end
210
211 data1.soc20.Pulse=(unique(pulse(1,:,1),'stable'));
212 data1.soc50.Pulse=(unique(pulse(2,:,1),'stable'));
```

```
213 data1.soc80.Pulse=(unique(pulse(3,:,1),'stable'));
214
215 data2.soc20.Pulse=(unique(pulse(1,:,2),'stable'));
216 data2.soc50.Pulse=(unique(pulse(2,:,2),'stable'));
217 data2.soc80.Pulse=(unique(pulse(3,:,2),'stable'));
218
219 data3.soc20.Pulse=(unique(pulse(1,:,3),'stable'));
220 data3.soc50.Pulse=(unique(pulse(2,:,3),'stable'));
221 data3.soc80.Pulse=(unique(pulse(3,:,3),'stable'));
222
223 data4.soc20.Pulse=(unique(pulse(1,:,4),'stable'));
224 data4.soc50.Pulse=(unique(pulse(2,:,4),'stable'));
225 data4.soc80.Pulse=(unique(pulse(3,:,4),'stable'));
226
227 data1.soc20.Ro=(unique(Ro(1,:,1),'stable'));
228 data1.soc50.Ro=(unique(Ro(2,:,1),'stable'));
229 data1.soc80.Ro=(unique(Ro(3,:,1),'stable'));
230
231 data2.soc20.Ro=(unique(Ro(1,:,2),'stable'));
232 data2.soc50.Ro=(unique(Ro(2,:,2),'stable'));
233 data2.soc80.Ro=(unique(Ro(3,:,2),'stable'));
234
235 data3.soc20.Ro=(unique(Ro(1,:,3),'stable'));
236 data3.soc50.Ro=(unique(Ro(2,:,3),'stable'));
237 data3.soc80.Ro=(unique(Ro(3,:,3),'stable'));
238
239 data4.soc20.Ro=(unique(Ro(1,:,4),'stable'));
240 data4.soc50.Ro=(unique(Ro(2,:,4),'stable'));
241 data4.soc80.Ro=(unique(Ro(3,:,4),'stable'));
242
243 data1.soc20.Er=(unique(Er(1,:,1),'stable'));
244 data1.soc50.Er=(unique(Er(2,:,1),'stable'));
245 data1.soc80.Er=(unique(Er(3,:,1),'stable'));
246
247 data2.soc20.Er=(unique(Er(1,:,2),'stable'));
248 data2.soc50.Er=(unique(Er(2,:,2),'stable'));
249 data2.soc80.Er=(unique(Er(3,:,2),'stable'));
250
251 data3.soc20.Er=(unique(Er(1,:,3),'stable'));
252 data3.soc50.Er=(unique(Er(2,:,3),'stable'));
253 data3.soc80.Er=(unique(Er(3,:,3),'stable'));
254
255 data4.soc20.Er=(unique(Er(1,:,4),'stable'));
256 data4.soc50.Er=(unique(Er(2,:,4),'stable'));
257 data4.soc80.Er=(unique(Er(3,:,4),'stable'));
258
259 if order~=0
260
```

```
261 data1.soc20.Rp1=(unique(Rp1(1,:,1),'stable'));
262 data1.soc50.Rp1=(unique(Rp1(2,:,1),'stable'));
263 data1.soc80.Rp1=(unique(Rp1(3,:,1),'stable'));
264
265 data2.soc20.Rp1=(unique(Rp1(1,:,2),'stable'));
266 data2.soc50.Rp1=(unique(Rp1(2,:,2),'stable'));
267 data2.soc80.Rp1=(unique(Rp1(3,:,2),'stable'));
268
269 data3.soc20.Rp1=(unique(Rp1(1,:,3),'stable'));
270 data3.soc50.Rp1=(unique(Rp1(2,:,3),'stable'));
271 data3.soc80.Rp1=(unique(Rp1(3,:,3),'stable'));
272
273 data4.soc20.Rp1=(unique(Rp1(1,:,4),'stable'));
274 data4.soc50.Rp1=(unique(Rp1(2,:,4),'stable'));
275 data4.soc80.Rp1=(unique(Rp1(3,:,4),'stable'));
276
277 data1.soc20.Tau1=(unique(Tau1(1,:,1),'stable'));
278 data1.soc50.Tau1=(unique(Tau1(2,:,1),'stable'));
279 data1.soc80.Tau1=(unique(Tau1(3,:,1),'stable'));
280
281 data2.soc20.Tau1=(unique(Tau1(1,:,2),'stable'));
282 data2.soc50.Tau1=(unique(Tau1(2,:,2),'stable'));
283 data2.soc80.Tau1=(unique(Tau1(3,:,2),'stable'));
284
285 data3.soc20.Tau1=(unique(Tau1(1,:,3),'stable'));
286 data3.soc50.Tau1=(unique(Tau1(2,:,3),'stable'));
287 data3.soc80.Tau1=(unique(Tau1(3,:,3),'stable'));
288
289 data4.soc20.Tau1=(unique(Tau1(1,:,4),'stable'));
290 data4.soc50.Tau1=(unique(Tau1(2,:,4),'stable'));
291 data4.soc80.Tau1=(unique(Tau1(3,:,4),'stable'));
292
293 if order==2
294
295 data1.soc20.Rp2=(unique(Rp2(1,:,1),'stable'));
296 data1.soc50.Rp2=(unique(Rp2(2,:,1),'stable'));
297 data1.soc80.Rp2=(unique(Rp2(3,:,1),'stable'));
298
299 data2.soc20.Rp2=(unique(Rp2(1,:,2),'stable'));
300 data2.soc50.Rp2=(unique(Rp2(2,:,2),'stable'));
301 data2.soc80.Rp2=(unique(Rp2(3,:,2),'stable'));
302
303 data3.soc20.Rp2=(unique(Rp2(1,:,3),'stable'));
304 data3.soc50.Rp2=(unique(Rp2(2,:,3),'stable'));
305 data3.soc80.Rp2=(unique(Rp2(3,:,3),'stable'));
306
307 data4.soc20.Rp2=(unique(Rp2(1,:,4),'stable'));
308 data4.soc50.Rp2=(unique(Rp2(2,:,4),'stable'));
```

```
data4.soc80.Rp2=(unique(Rp2(3,:,4),'stable'));

data1.soc20.Tau2=(unique(Tau2(1,:,1),'stable'));
data1.soc50.Tau2=(unique(Tau2(2,:,1),'stable'));
data1.soc80.Tau2=(unique(Tau2(3,:,1),'stable'));

data2.soc20.Tau2=(unique(Tau2(1,:,2),'stable'));
data2.soc50.Tau2=(unique(Tau2(2,:,2),'stable'));
data2.soc80.Tau2=(unique(Tau2(3,:,2),'stable'));

data3.soc20.Tau2=(unique(Tau2(1,:,3),'stable'));
data3.soc50.Tau2=(unique(Tau2(2,:,3),'stable'));
data3.soc80.Tau2=(unique(Tau2(3,:,3),'stable'));

data4.soc20.Tau2=(unique(Tau2(1,:,4),'stable'));
data4.soc50.Tau2=(unique(Tau2(2,:,4),'stable'));
data4.soc80.Tau2=(unique(Tau2(3,:,4),'stable'));

end

end
```

4. The following MATLAB script was utilised to combine the parameters obtained for the three lithium-ion cells used as part of the experiments:

```
clearvars

ambient{1,1}='minus20';
ambient{2,1}='minus10';
ambient{3,1}='0';
ambient{4,1}='25';

soc{1,1}='20';
soc{2,1}='50';
soc{3,1}='80';

cell{1,1}='1';
cell{2,1}='2';
cell{3,1}='3';

%choose ECM order

order=2;

%%%%%%%%%%%%%%%%%%%%%%%%%%%%%%%%
```

```
22
23 for aa=1:4
24
25 for jj=1:3
26
27 for kk=1:3
28
29 load(['C:\PhD\Model\Xalt\MAT\PPC_',num2str(order),'RC\',ambient{aa,
1},'degC_soc_',soc{jj,1},'_',cell{kk,1},'.mat'])
30
31 % if size(volVec,1)==size(vFit,1)
32 %
33 % vrms(1,kk)=1000*rms(vFit-volVec);
34 %
35 % end
36
37 c(1,kk)=size(PulseC,1);
38 d(1,kk)=size(PulseD,1);
39
40 numrows_c=min(c);
41 numrows_d=min(d);
42
43 end
44
45 for kk=1:3
46
47 load(['C:\PhD\Model\Xalt\MAT\PPC_',num2str(order),'RC\',ambient{aa,
1},'degC_soc_',soc{jj,1},'_',cell{kk,1},'.mat'])
48
49 if order==2
50
51 PulseCx(:,kk)=PulseC(1:numrows_c,:);
52 PulseDx(:,kk)=PulseD(1:numrows_d,:);
53 RoCx(:,kk)=RoC(1:numrows_c,:);
54 RoDx(:,kk)=RoD(1:numrows_d,:);
55 RpCx(:,2*kk-1:2*kk)=RpC(1:numrows_c,:);
56 RpDx(:,2*kk-1:2*kk)=RpD(1:numrows_d,:);
57 stdRoCx(:,kk)=stdRoC(1:numrows_c,:);
58 stdRoDx(:,kk)=stdRoD(1:numrows_d,:);
59 stdRpCx(:,2*kk-1:2*kk)=stdRpC(1:numrows_c,:);
60 stdRpDx(:,2*kk-1:2*kk)=stdRpD(1:numrows_d,:);
61 stdTauCx(:,2*kk-1:2*kk)=stdTauC(1:numrows_c,:);
62 stdTauDx(:,2*kk-1:2*kk)=stdTauD(1:numrows_d,:);
63 TauCx(:,2*kk-1:2*kk)=TauC(1:numrows_c,:);
64 TauDx(:,2*kk-1:2*kk)=TauD(1:numrows_d,:);
65
66 ErCx(:,kk)=RmsC(1:numrows_c,:);
67 ErDx(:,kk)=RmsD(1:numrows_d,:);
```

```
68
69 elseif order==1
70
71 PulseCx(:,kk)=PulseC(1:numrows_c,:);
72 PulseDx(:,kk)=PulseD(1:numrows_d,:);
73 RoCx(:,kk)=RoC(1:numrows_c,:);
74 RoDx(:,kk)=RoD(1:numrows_d,:);
75 RpCx(:,kk)=RpC(1:numrows_c,:);
76 RpDx(:,kk)=RpD(1:numrows_d,:);
77 stdRoCx(:,kk)=stdRoC(1:numrows_c,:);
78 stdRoDx(:,kk)=stdRoD(1:numrows_d,:);
79 stdRpCx(:,kk)=stdRpC(1:numrows_c,:);
80 stdRpDx(:,kk)=stdRpD(1:numrows_d,:);
81 stdTauCx(:,kk)=stdTauC(1:numrows_c,:);
82 stdTauDx(:,kk)=stdTauD(1:numrows_d,:);
83 TauCx(:,kk)=TauC(1:numrows_c,:);
84 TauDx(:,kk)=TauD(1:numrows_d,:);
85
86 ErCx(:,kk)=RmsC(1:numrows_c,:);
87 ErDx(:,kk)=RmsD(1:numrows_d,:);
88
89 else
90
91 PulseCx(:,kk)=PulseC(1:numrows_c,:);
92 PulseDx(:,kk)=PulseD(1:numrows_d,:);
93 RoCx(:,kk)=RoC(1:numrows_c,:);
94 RoDx(:,kk)=RoD(1:numrows_d,:);
95
96 end
97
98
99 clearvars -except vrms ambient soc cell aa jj kk PulseCx PulseDx RoCx
RoDx RpCx RpDx stdRoCx stdRoDx stdRpCx stdRpDx stdTauCx stdTauDx TauCx
TauDx ErCx ErDx
c d numrows_c numrows_d order
100 end
101
102 if order==2
103
104 for ss=1:numrows_c
105
106 if TauCx(ss,1)>TauCx(ss,2)
107
108 temp=TauCx(ss,1);
109 TauCx(ss,1)=TauCx(ss,2);
110 TauCx(ss,2)=temp;
111
112 temp=stdTauCx(ss,1);
```

```
113 stdTauCx(ss,1)=stdTauCx(ss,2);
114 stdTauCx(ss,2)=temp;
115
116 temp=RpCx(ss,1);
117 RpCx(ss,1)=RpCx(ss,2);
118 RpCx(ss,2)=temp;
119
120 temp=stdRpCx(ss,1);
121 stdRpCx(ss,1)=stdRpCx(ss,2);
122 stdRpCx(ss,2)=temp;
123
124 end
125
126 end
127
128 for ss=1:numrows_d
129
130 if TauDx(ss,1)>TauDx(ss,2)
131
132 temp=TauDx(ss,1);
133 TauDx(ss,1)=TauDx(ss,2);
134 TauDx(ss,2)=temp;
135
136 temp=stdTauDx(ss,1);
137 stdTauDx(ss,1)=stdTauDx(ss,2);
138 stdTauDx(ss,2)=temp;
139
140 temp=RpDx(ss,1);
141 RpDx(ss,1)=RpDx(ss,2);
142 RpDx(ss,2)=temp;
143
144 temp=stdRpDx(ss,1);
145 stdRpDx(ss,1)=stdRpDx(ss,2);
146 stdRpDx(ss,2)=temp;
147
148 end
149
150 end
151
152 end
153
154 if order==1
155
156 PulseCm=mean(PulseCx,2);
157 PulseDm=mean(PulseDx,2);
158
159 RoCm=mean(RoCx,2);
160 RoDm=mean(RoDx,2);
```

```
161
162 ErCm=mean(ErCx,2);
163 ErDm=mean(ErDx,2);
164
165 RpCm=mean(RpCx,2);
166 RpDm=mean(RpDx,2);
167
168 TauCm=mean(TauCx,2);
169 TauDm=mean(TauDx,2);
170
171 stdRoCm=mean(stdRoCx,2);
172 stdRoDm=mean(stdRoDx,2);
173
174 stdRpCm=mean(stdRpCx,2);
175 stdRpDm=mean(stdRpDx,2);
176
177 stdTauCm=mean(stdTauCx,2);
178 stdTauDm=mean(stdTauDx,2);
179
180 elseif order==2
181
182 PulseCm=mean(PulseCx,2);
183 PulseDm=mean(PulseDx,2);
184
185 RoCm=mean(RoCx,2);
186 RoDm=mean(RoDx,2);
187
188 ErCm=mean(ErCx,2);
189 ErDm=mean(ErDx,2);
190
191 RpCm=[mean(RpCx(:,1:2:end),2) mean(RpCx(:,2:2:end),2)];
192 RpDm=[mean(RpDx(:,1:2:end),2) mean(RpDx(:,2:2:end),2)];
193
194 TauCm=[mean(TauCx(:,1:2:end),2) mean(TauCx(:,2:2:end),2)];
195 TauDm=[mean(TauDx(:,1:2:end),2) mean(TauDx(:,2:2:end),2)];
196
197 stdRoCm=mean(stdRoCx,2);
198 stdRoDm=mean(stdRoDx,2);
199
200 stdRpCm=[mean(stdRpCx(:,1:2:end),2) mean(stdRpCx(:,2:2:end),2)];
201 stdRpDm=[mean(stdRpDx(:,1:2:end),2) mean(stdRpDx(:,2:2:end),2)];
202
203 stdTauCm=[mean(stdTauCx(:,1:2:end),2) mean(stdTauCx(:,2:2:end),2)];
204 stdTauDm=[mean(stdTauDx(:,1:2:end),2) mean(stdTauDx(:,2:2:end),2)];
205
206 else
207
208 PulseCm=mean(PulseCx,2);
```

```
209 PulseDm=mean(PulseDx,2);
210
211 RoCm=mean(RoCx,2);
212 RoDm=mean(RoDx,2);
213
214 end
215
216
save(['C:\PhD\Model\Xalt\MAT\PPC_',num2str(order),'RCx\',ambient{aa,
1},'degC_soc_',soc{jj,1},'.mat'])
217
218
219 clearvars -except ambient soc cell aa jj kk order
220 end
221 end
```

5. The following MATLAB script was utilised to automate the parameter fitting for both 1st and 2nd order ECMs:

Note, the 'EstECMPara' function was reproduced with permission from:

W.D. Widanage, A. Barai, G.H. Chouchelamane, K. Uddin, A. McGordon, J. Marco, P. Jennings, Design and use of multisine signals for Li-ion battery equivalent circuit modelling. Part 2: Model estimation, Journal of Power Sources. 324 (2016) 61–69. https://doi.org/10.1016/j.jpowsour.2016.05.014.

The function itself is available freely for academic usage at the following web address in a Github repository: https://github.com/WDWidanage/MatlabFunctions.

```
1
2 %%
3 % Estimation options
4 options.order = 2; % Specify the order of the ECM (Number of RC
pairs)
5 options.plotFit = 0; % Set to 1 or 0 if the fitted voltage should be
plotted
6 options.ecmFitSeriesCap = 'off'; % Set to 'on' to include a series
capacitor or to
'off' to correct for any OCV change
7
8 % % Load converted maccor data
9 % load('Arbitrary file name 2019-08-15 12-41-59_876_003 - 003.mat');
10 %
11 % % Plot and check current and voltage response
12 % figure
```

```
% subplot(2,1,1)
% plot(data.TestTime/3600,data.Amps,'. -')
% xlabel('Time (h)'); ylabel('Current (A)')
% subplot(2,1,2)
% plot(data.TestTime/3600,data.Volts,'. -')
% xlabel('Time (h)'); ylabel('Volts (V)')

                %                  [~,idxRelax]                  =
find_exc_segments(data.Amps,'plotSeg',0,'timeVec',data.
TestTime/3600);

[~,idxRelax] = find_exc_segments(data.Amps);


%% Perform paramter estimation for each discharge and charge pulse

% Pulses start from 3rd index. 9 discharge pulses 8 charge pulses
countD = 0; % Loop counter
for ii = 0:2:17 % Process the discharge pulses
countD = countD + 1;
idxRng = [idxRelax(2+ii,1):idxRelax(2+ii,2)];
timeVecTmp = data.TestTime(idxRng);
timeVec = timeVecTmp - timeVecTmp(1);
currVec = -data.Amps(idxRng);
volVec = data.Volts(idxRng);

if isempty(volVec(volVec <= 2.7)) == 1

% Estimate ECM parameters for the discharge pulses
          [thetaOpt,          paraInfo,          vFit]          =
EstECMPara(timeVec,currVec,volVec,options);

% Extract the ECM parameters for each pulse
RoD(countD,1) = thetaOpt(1); % Ro
 RpD(countD,1:options.order)  =  thetaOpt(2:options.order+1);  %  R1,
R2,...
TauD(countD,1:options.order) = thetaOpt(options.order+2:end); % Tau1,
Tau2,...

% Extract the paramter uncertainities
stdRoD(countD,1) = paraInfo.stdTheta(1); %
Ro
                  stdRpD(countD,1:options.order)                  =
paraInfo.stdTheta(2:options.order+1); %
R1, R2,...
                 stdTauD(countD,1:options.order)                  =
paraInfo.stdTheta(options.order+2:end);
% Tau1, Tau2,...
```

```
51 PulseD(countD,1) = max(currVec);
52
53 RmsD(countD,1)=1000*rms(vFit-volVec);
54
55 else
56
57 countD = countD - 1;
58
59 end
60
61
62 end
63
64 countC = 0; % Loop counter
65 for ii = 1:2:15 % Process
66 countC = countC + 1;
67 idxRng = [idxRelax(2+ii,1):idxRelax(2+ii,2)];
68 timeVecTmp = data.TestTime(idxRng);
69 timeVec = timeVecTmp - timeVecTmp(1);
70 currVec = -data.Amps(idxRng);
71 volVec = data.Volts(idxRng);
72
73 if isempty(volVec(volVec >= 4.2)) == 1
74
75 % Estimate ECM parameters for the charge pulses
76           [thetaOpt,           paraInfo,           vFit]           =
EstECMPara(timeVec,currVec,volVec,options);
77
78 % Extract the ECM parameters for each pulse
79 RoC(countC,1) = thetaOpt(1); % Ro
80  RpC(countC,1:options.order)  =  thetaOpt(2:options.order+1);  %  R1,
R2,...
81 TauC(countC,1:options.order) = thetaOpt(options.order+2:end); % Tau1,
Tau2,...
82
83 % Extract the ECM parameters for each pulse
84 stdRoC(countC,1) = paraInfo.stdTheta(1); % Ro
85                    stdRpC(countC,1:options.order)                    =
paraInfo.stdTheta(2:options.order+1); % R1,
R2,...
86                   stdTauC(countC,1:options.order)                    =
paraInfo.stdTheta(options.order+2:end); %
Tau1, Tau2,...
87 PulseC(countC,1) = min(currVec);
88
89 RmsC(countC,1)=1000*rms(vFit-volVec);
90 else
91
```

```
92 countC = countC - 1;
93
94 end
95
96 end
```

Appendix C. MATLAB/Simulink ECMs: Lookup Tables

In the following tables (Tables C -1 and C – 2), the capacity values (in Ah) at different discharge C-rates and ambient temperatures are presented for air-based and oil-based parameterisation methods, respectively. These values were implemented using the lookup table blocks in MATLAB/Simulink.

Table C - 1. Values for Lookup Table: Air-based Capacity Values (in Ah)

Discharge Current [A] / **Ambient Temperature [°C]**	**0.25C**	**1C**	**3C**
−20	31.9	32.2	34.7
−10	33.2	34.2	36.3
0	38.4	36.4	37.3
25	42.3	40.6	39.5

Table C - 2. Values for Lookup Table: Oil-based Capacity Values (in Ah)

Discharge Current [A] / **Ambient Temperature [°C]**	**0.25C**	**1C**	**3C**
−20	30.7	24.6	13.3
−10	31.9	31.4	24.8
0	38.3	34.1	30.5
25	41.7	40.3	39.2

In the following tables (Tables C -3 and C – 4), the energy values (in Wh) at different discharge C-rates and ambient temperatures are presented for air-based and oil-based parameterisation methods, respectively. These values were implemented using the lookup table blocks in MATLAB/Simulink.

Table C - 3. Values for Lookup Table: Air-based Energy Values (in Wh)

Discharge Current [A] / **Ambient Temperature [°C]**	**0.25C**	**1C**	**3C**
−20	108.9	105.4	109.9
−10	113.2	115.9	118.0
0	138.7	126.9	124.5
25	156.4	148.0	140.2

Table C - 4. Values for Lookup Table: Oil-based Energy Values (in Wh)

Discharge Current [A] / **Ambient Temperature [°C]**	**0.25C**	**1C**	**3C**
−20	102.6	75.7	38.0
−10	109.4	103.8	75.7
0	138.1	117.0	101.6
25	153.7	146.0	136.7

In Tables C-5 and C-6, the data tables used to populate the look-up tables that parameterise ECM impedance parameters are illustrated. Table C-5 is for the 1st order ECM (1RC) and Table C-6 is for the 2nd order ECM (2RC). Each cell in Table C-5 is represented as follows: [R_O (in mΩ); R_{P1} (in mΩ); τ_{P1} (in seconds)]. This represents the value of the mathematically fitted impedance parameters at a particular SOC, ambient temperature and charge/discharge current. In Table C-6, each cell is represented as follows: [R_O (in mΩ); R_{P1} (in mΩ); τ_{P1} (in seconds); R_{P2} (in mΩ); τ_{P2} (in seconds)].

Table C - 5. 1st RC Model: Values for R_O, R_{P1}, τ_{P1} based on Temperature, Current and SOC [Note: Discharge is Positive]

Current [A]	-80	-60	-40	-30	-20	-10	10	20	30	40	60	80	120
Temperature [°C]	**20% SOC**												
−20	10.1; 13.6; 0.7*				10.1; 13.6; 0.7	11; 20.9; 0.7	17.6; 23.4; 2.6	16.1; 19.4; 4.3	16.1; 19.4; 4.3*				
−10	6.5; 7.4; 0.5*				6.5; 7.4; 0.5	6.8; 9.9; 0.5	9.6; 9.1; 1.4	9.3; 8; 2.2	8.6; 7.7; 2.8	8.1; 7.9; 3.4	8.1; 7.9; 3.4*		
0	3.9; 1.2; 1.7	4.1; 1.4; 1.4	4.3; 1.8; 1	4.4; 2; 0.9	4.6; 2.1; 1	4.8; 2.3; 1.1	5.1; 2.4; 1.8	5; 2.5; 2.1	4.8; 2.5; 2.3	4.7; 2.6; 2.5	4.4; 2.7; 2.9	4.2; 2.8; 3.1	4.2; 2.8; 3.1
25	1.4; 1.2; 23.9	1.4; 1.2; 22.5	1.4; 1.1; 20.6	1.4; 1.1; 19.4	1.4; 1.1; 20.8	1.4; 1.2; 21.4	1.4; 1.5; 24.7	1.4; 1.4; 21.5	1.4; 1.3; 20.4	1.4; 1.2; 20.6	1.4; 1.2; 20	1.5; 1.2; 20.3	1.5; 1.1; 20.5
Temperature [°C]	**50% SOC**												
−20	10.6; 11.8; 0.5*				10.6; 11.8; 0.5	9.9; 20; 0.4	9.4; 18.9; 0.4	10.2; 11.2; 0.5	9.6; 8.5; 0.6	9.7; 6.4; 0.9	9.1; 4.5; 1.4	9.1; 4.5; 1.4*	
−10	5; 6.5; 0.3*				5; 6.5; 0.3	4.6; 8.8; 0.2	4.9; 8.1; 0.3	5.4; 5.7; 0.3	5.4; 4.6; 0.4	5.8; 3.5; 0.7	5.8; 2.5; 1.2	5.5; 2.1; 1.6	4.9; 1.8; 2.2
0	3.6; 0.8; 1.9	3.9; 1; 1.6	4.1; 1.2; 1.2	4.2; 1.4; 1	4.5; 1.4; 1	4.3; 1.8; 0.8	4.8; 1.3; 1.9	4.7; 1.2; 2.2	4.4; 1.1; 2.2	4.2; 1; 2.4	3.9; 0.9; 3.1	3.6; 0.8; 3.5	3.2; 0.8; 4.4
25	1.3; 0.8; 22.1	1.3; 0.9; 22.3	1.3; 0.9; 20.9	1.3; 0.9; 20.1	1.3; 0.8; 17.1	1.3; 0.8; 16.3	1.3; 1.9; 40.7	1.3; 1.7; 35.6	1.3; 1.6; 36.4	1.3; 1.5; 34.8	1.3; 1.3; 30.4	1.3; 1.1; 28	1.3; 1; 25.8
Temperature [°C]	**80% SOC**												
−20	7.3; 29.3; 0.4*					7.3; 29.3; 0.4	9.2; 17.5; 0.4	9.5; 11.3; 0.5	8.9; 8.6; 0.6	8.6; 6.9; 0.7	7.9; 4.9; 0.8	7.3; 3.8; 0.9	6.4; 2.7; 1.1
−10	5.1; 8.2; 0.3*					5.1; 8.2; 0.3	7.2; 6.2; 0.7	7.1; 4.4; 0.8	6.4; 3.9; 0.8	5.9; 3.4; 0.7	5.4; 2.7; 0.8	4.9; 2.3; 0.8	4.3; 1.7; 0.8
0	3.9; 1.1; 1.5*		3.9; 1.1; 1.5	4; 1.2; 1.3	4.2; 1.3; 1.5	4.3; 1.4; 1.7	4.5; 1.7; 3.3	4.3; 1.6; 3.3	4.1; 1.4; 3	4; 1.3; 3	3.7; 1.1; 3.1	3.5; 1; 2.6	3.2; 5.1; 75.4
25	1.3; 1.8; 51.2	1.4; 2.1; 58.2	1.4; 2.2; 57.3	1.4; 2.1; 51.1	1.3; 1.8; 41.1	1.3; 1.8; 37.2	1.3; 2.1; 37.7	1.3; 1.8; 31.4	1.3; 1.5; 25.9	1.3; 1.4; 25.4	1.3; 1.2; 19.9	1.3; 1.2; 20.8	1.3; 1.2; 24.4

*Extrapolated using clip/hold from ECM values for previous current pulse.

Table C - 6. 2nd RC Model: Values for $R_O, R_{P1}, \tau_{P1}, R_{P2}, \tau_{P2}$ based on Temperature, Current and SOC [Note: Discharge is Positive]

Current [A]	-80	-60	-40	-30	-20	-10	10	20	30	40	60	80	120
Temp. [°C]	**20% SOC**												
−20	6.6; 14.8; 0.3; 9.2; 20.6*				6.6; 14.8; 0.3; 9.2; 20.6	7.2; 21.5; 0.3; 9.4; 14.7	7.3; 19.2; 4.7; 19.2; 2.5	7; 16.8; 5.5; 15.1; 2.9	7; 16.8; 5.5; 15.1; 2.9*				
−10	3.8; 8.7; 0.2; 3.3; 11.2*				3.8; 8.7; 0.2; 3.3; 11.2	3.4; 10.9; 0.2; 3.1; 3.4	3.7; 10.2; 0.2; 5.9; 4.3	4.1; 7.8; 1.9; 6.6; 3.4	3.8; 7.1; 1.9; 6.4; 3.5	3.7; 6; 0.2; 7.1; 5.4	3.7; 6; 0.2; 7.1; 5.4*		
0	2.1; 2.4; 0.1; 3.6; 48.5	2.1; 2.8; 0.1; 2.9; 33.4	2; 3.4; 0.1; 1.5; 11	1.9; 3.7; 0.1; 1.2; 5.5	2; 3.8; 0.1; 1.3; 4.4	2; 2.2; 2.7; 3.2; 1.4	2.1; 3.9; 0.1; 1.8; 4.4	2.2; 3.7; 0.1; 2; 4.7	2; 3.6; 0.1; 2.1; 4.8	2.1; 3.3; 0.1; 2.2; 5	2.2; 2.8; 0.1; 2.4; 5	2.2; 2.5; 0.1; 2.5; 4.9	2.2; 2.5; 0.1; 2.5; 4.9*
25	1.4; 0.3; 6; 2.7; 144.4	1.4; 0.3; 4.8; 2.6; 134.6	1.4; 0.3; 4.2; 2.7; 136.7	1.4; 0.3; 3.2; 2.5; 120.5	1.3; 0.3; 2.4; 2.3; 106.5	1.3; 0.2; 1.8; 1.9; 84.3	1.3; 0.4; 4.6; 2.6; 133.6	1.4; 0.4; 5; 2.8; 145.4	1.4; 0.4; 5.1; 2.9; 147	1.4; 0.4; 4.8; 3; 144.9	1.4; 0.3; 4.5; 2.9; 136.4	1.4; 0.3; 4.4; 2.8; 133.4	1.4; 0.3; 4.4; 2.7; 129.1
Temp. [°C]	**50% SOC**												
−20	5.6; 14.4; 0.2; 4.7; 8.2*				5.6; 14.4; 0.2; 4.7; 8.2	5.3; 21.9; 0.2; 5.7; 8.1	5.1; 20.6; 0.2; 5.1; 8.1	5.6; 13.6; 0.2; 4.3; 8	5.3; 10.7; 0.2; 3.8; 7.7	5.5; 8.7; 0.2; 3.8; 9.2	5.6; 6.2; 0.2; 3.6; 10.3	5.6; 6.2; 0.2; 3.6; 10.3*	
−10	2.5; 7.9; 0.1; 1.6; 4.1*				2.5; 7.9; 0.1; 1.6; 4.1	2.5; 9.6; 0.1; 1.8; 3.3	2.5; 9.2; 0.1; 1.9; 4.1	2.7; 7.3; 0.1; 1.9; 5.2	2.6; 6.4; 0.1; 1.8; 5.8	2.9; 2.9; 4.7; 4.3; 2.3	3.1; 3.3; 2.6; 2.7; 6.7	3.2; 3.4; 0.1; 2.1; 12.5	3.1; 2.6; 0.2; 2.4; 17.4
0	1.5; 2.4; 0; 0.8; 8.1	1.4; 2.8; 0; 0.8; 5.4	1.3; 3.4; 0; 0.8; 4.6	1.3; 3.7; 0; 0.8; 4.4	1.5; 3.8; 0; 0.9; 4.3	1.4; 4.1; 0; 0.9; 4.4	1.5; 3.9; 0; 1.1; 5.7	1.5; 3.6; 0; 1.1; 6.6	1.3; 3.5; 0; 1.1; 7.5	1.5; 3.1; 0; 1.1; 9.1	1.6; 2.6; 0; 1.4; 14.7	1.7; 2.2; 0.1; 1.5; 20.2	1.7; 1.8; 0.1; 1.9; 29.7
25	1.3; 0.2; 4.1; 2.1; 145.4	1.3; 0.2; 3.7; 2.1; 142.4	1.3; 0.2; 3.8; 2.1; 139.6	1.3; 0.2; 3.8; 2; 136.3	1.3; 0.2; 3.5; 1.7; 113.5	1.3; 0.3; 4.4; 1.3; 95.2	1.3; 0.3; 6; 2.6; 159.7	1.3; 0.3; 5.6; 2.6; 147.5	1.3; 0.3; 5.6; 2.7; 154	1.3; 0.3; 5.4; 2.7; 157.9	1.3; 0.3; 5.3; 2.6; 156.1	1.3; 0.3; 5.7; 2.5; 163.2	1.3; 0.3; 6.4; 2.4; 169.5
Temp. [°C]	**80% SOC**												
−20	3.5; 14.7; 1.8; 19.9; 2.1*					3.5; 14.7; 1.8; 19.9; 2.1	5.1; 18.9; 0.2; 4.8; 6.6	5.8; 13; 0.2; 5; 11.9	5.6; 10.4; 0.2; 5.9; 19.1	5.7; 8.5; 0.2; 17.9; 88.7	5.5; 6.2; 0.2; 23.3; 150	5.3; 5; 0.2; 36.9; 302.3	4.7; 3.7; 0.2; 40.7; 427.6
−10	2.6; 9.3; 0.1; 2; 3.5*					2.6; 9.3; 0.1; 2; 3.5	2.6; 8.8; 0.1; 2.9; 5.2	2.9; 7.1; 0.1; 2.5; 6	2.8; 6.1; 0.1; 2.3; 7.7	3.4; 9.3; 59; 6.6; 23.3	3.5; 3.9; 0.2; 25.1; 261	3.4; 3.2; 0.2; 37.3; 472.7	3.1; 2.5; 0.2; 51; 838.4
0	1.4; 3; 0; 0.8; 5*		1.4; 3; 0; 0.8; 5	1.3; 3.2; 0; 0.9; 4.3	1.5; 3.2; 0.1; 0.9; 4.1	1.2; 3.7; 0; 1.1; 4	1.6; 2.7; 2; 2.1; 4	1.6; 2; 4.4; 2.6; 2.1	1.5; 2.5; 2.6; 2; 4.5	1.6; 2.7; 0.1; 1.5; 9.4	2; 2.2; 0.1; 2.8; 29.7	2.2; 1.7; 0.1; 7.5; 113.5	2.1; 1.5; 0.1; 12.8; 252.6
25	1.3; 0.2; 3.9; 3.3; 177.7	1.3; 0.2; 3.4; 3.4; 174.1	1.3; 0.2; 2.6; 3.4; 162.5	1.3; 0.2; 2.5; 3.2; 154.6	1.3; 0.3; 2.9; 3.1; 162.7	1.3; 0.3; 2.8; 2.7; 127.7	1.3; 0.4; 4.3; 3.1; 152.3	1.3; 0.4; 5; 3.4; 180.3	1.3; 0.4; 5; 3.4; 176.1	1.3; 0.4; 4.9; 3.4; 179	1.3; 0.4; 5; 3.5; 182.7	1.3; 0.3; 5; 3.4; 179.3	1.3; 0.3; 5.6; 3.4; 179.4

*Extrapolated using clip/hold from ECM values for previous current pulse.